Performance assessment of a 3-D steady-state and spatial kinetics model for the CROCUS reactor

THÈSE N^{O} 8248 (2018)

PRÉSENTÉE LE 30 AVRIL 2018
À LA FACULTÉ DES SCIENCES DE BASE
LABORATOIRE DE PHYSIQUE DES RÉACTEURS ET DE COMPORTEMENT DES SYSTÈMES
PROGRAMME DOCTORAL EN ENERGIE

ÉCOLE POLYTECHNIQUE FÉDÉRALE DE LAUSANNE

POUR L'OBTENTION DU GRADE DE DOCTEUR ÈS SCIENCES

PAR

Adolfo RAIS

acceptée sur proposition du jury:

Prof. S. Haussener, présidente du jury
Prof. A. Pautz, Dr M. Hursin, directeurs de thèse
Dr P. Blaise, rapporteur
Prof. T. Kozlowski, rapporteur
Prof. H.-M. Prasser, rapporteur

ÉCOLE POLYTECHNIQUE
FÉDÉRALE DE LAUSANNE
Suisse
2018

To my parents, Nora and Carlos.

Acknowledgements

In the first place I would like to thank my thesis director, Prof. Andreas Pautz, for giving me the opportunity to study here and for the support during the course of this investigation. I would also like to express my sincere appreciation to my advisor, Dr. Mathieu Hursin, for his invaluable assistance and encouragement that made this experience stimulating and gratifying.

Several people have been of great help for the development of this work. I wish to thank Dr. Pavel Frajtag, Dr. Vincent Lamirand, Dr. Grégory Perret, M. Laurent Braun and M. Daniel Godat for their contribution to this work and assistance at the CROCUS reactor. My sincere thanks to Prof. Thomas Downar, Dr. Andrew Ward, Dr. Volkan Seker and Dr. Yunlin Xu for welcoming me at the University of Michigan and for the benefit from their expertise. I would also like to thank all my colleagues and friends in the Laboratory for Reactor Physics and Systems Behavior.

The financial support of this research by *swiss*nuclear is gratefully acknowledged.

Lastly, I would like to give a special thank to my girlfriend, Adélaïde, for her support and love.

Lausanne, 5 October 2017 A. R.

Abstract

The current tools for performing safety analyses of research reactors (RR) have been mostly developed in-house specifically for each kind of reactor and rely on simple models that yield conservative estimates. More advanced methods are used for the analysis of power reactors and may also apply to RR. However, owing to fundamental differences in reactor design and operating conditions, the adequacy of these codes for RR analysis needs to be demonstrated through verification and validation studies. The CROCUS reactor is an attractive tool for the validation of stand-alone neutronics models not only due to the absence of thermal feedback and fuel burn-up effects but also because of the peculiarities of its design.

This dissertation covers both experimental and numerical neutronics studies to evaluate the adequacy of the Serpent/PARCS code sequence for modeling the steady-state and kinetics behavior of the CROCUS reactor. The reactor presents design characteristics that raise questions about the acceptability of diffusion theory for its modeling. The PARCS model of CROCUS was developed considering several potential sources of biases. More precisely, albedo boundary conditions were used to limit the axial geometry to the grid plates where diffusion theory may lead to inaccuracies due to the presence of Cadmium layers. Proper treatment of scattering anisotropies through in-scatter correction of diffusion coefficients was also fundamental for producing accurate eigenvalues in the CROCUS reactor. A parametric study has been conducted to evaluate transport effects and the impact of energy discretization on eigenvalue and pin power distribution.

Steady-state and time-dependent experimental data have been obtained from CROCUS with the purpose of validating the computational scheme. A comprehensive evaluation of experimental uncertainties provided support for the generation of reliable experimental data. Particular focus was placed upon the development of transient experiments that involve local perturbations of the flux. Delayed neutron effects were not captured in these transients because of the tightly coupled nature of the reactor.

The comparison of PARCS simulations against experimental data indicated that control rod reactivity worth is predicted within $(4 \pm 3)\%$. PARCS radial fission rate distributions are in considerable disagreement with experimental data for the outer core region, where differences are as large as 15%. This was attributed to the fact that PARCS does not allow using adaptable mesh sizes in the radial plane, which results in a mismatch between the mesh and explicit pins of the outer core region. However, from a safety viewpoint, these biases are conservative and are located in the outer core region where the power is

low. PARCS axial fission rate profiles agree within 1% with experimental data for the bottom and mid regions for the core. On the other hand, larger deviations of about 20% were encountered for the top region, which are attributed to transport effects near the water/air interface. Finally, the investigation of neutron kinetic effects verified that the PARCS code is capable of modeling the transient experiments with spatial effects in the CROCUS reactor, where maximum differences are in the order of 5%.
Overall, the Serpent/PARCS scheme shows satisfactory performance for modeling the CROCUS reactor, except for the estimation of radial reaction rate profiles, where biases were attributed to the impossibility of adapting the mesh size to match the fuel pitch of both fuel zones.

Keywords: CROCUS reactor, high leakage, experimental reactor physics, validation, neutron diffusion, space-time kinetics, PARCS, Monte Carlo lattice physics, Serpent

Résumé

Les schémas de calculs utilisés pour effectuer l'analyse de sécurité des réacteurs de recherche (RR) ont été principalement développés en interne spécifiquement pour chaque réacteur et s'appuient sur des modèles simples qui produisent des estimations conservatives des paramètres de sécurité. Des méthodes plus avancées sont utilisées pour la modélisation de réacteurs de puissance et peuvent également être appliquées aux RR. Cependant, en raison des différences de conception et de conditions de fonctionnement, l'adéquation de ces schémas de calcul doit démontrée par le biais de processus rigoureux de vérification et de validation. Le réacteur CROCUS est un outil attractif pour la validation de modèles neutroniques autonomes non seulement en raison de l'absence de contre-réactions thermiques et d'usure du combustible, mais aussi par les particularités de sa conception.

Cette thèse décrit la mise en place d'un schéma de calcul Serpent/PARCS pour la modélisation du réacteur CROCUS en états stationnaires et transitoires. La comparaison détaillée de résultats numériques et expérimentaux, présentées dans cette thèse, en a permis sa validation. Le réacteur présente un design particulier dont la modélisation remet en cause certaines hypothèses de la théorie de diffusion. Le modèle PARCS du réacteur CROCUS a été développé pour minimiser les sources de biais. Plus précisément, des conditions aux bords de type « albédo » ont été utilisées pour limiter la géométrie axiale aux grilles de support du cœur de CROCUS. En effet, l'absorption des neutrons dans les couches de Cadmium est particulièrement difficile à modéliser correctement avec la théorie de la diffusion. Un traitement spécial de l'anisotropie du choc des neutrons avec les noyaux d'hydrogène est fondamental à la prédiction des valeurs propres du réacteur CROCUS. Une étude paramétrique a été menée à bien pour évaluer les effets des approximations de discrétisation énergétique et angulaire sur les prédictions de valeurs propres et de distribution de puissance. Des données expérimentales ont été obtenues avec CROCUS en fonctionnement stationnaire et transitoire pour valider le schéma de calcul Serpent/PARCS. Dans ce but, une évaluation rigoureuse des incertitudes expérimentales a été mené à bien. Un accent particulier a été mis sur le développement d'expériences en régime transitoire impliquant des perturbations locales du flux. Les effets de neutrons retardés sur la distribution de flux n'ont pas pu être observés durant ces transitoires en raison de la nature étroitement couplée du réacteur.

La comparaison des calculs PARCS avec les données expérimentales a indiqué que la réactivité de la barre de contrôle est prédite avec une imprécision de $(4 \pm 3)\%$. Les distributions radiales du taux de fission obtenue avec PARCS ne concordent pas avec les données expérimentales pour la région externe du cœur avec des différences allant jusqu'à 15%. Ceci a été attribué au fait que PARCS ne permet pas d'utiliser un maillage de taille adaptable dans le plan radial ce qui conduit à un décalage entre le maillage et la position réelle des crayons combustibles dans cette région. Cependant, d'un point de vue de la sécurité, ces grandes différences sont conservatives et sont localisées dans une région du cœur où la puissance est faible. Les distributions axiales de taux de fission obtenues par simulation présentent des différences inferieures a 1% par rapport aux données expérimentales pour le bas et le milieu du cœur du réacteur. De grandes déviations (près de 20%) ont été observé pour la partie supérieure du cœur à proximité de l'interface eau/air. Ces biais de calculs sont dus aux limitations de la théorie de la diffusion près des bords du model. Finalement, les expériences de cinétiques ont permis de montrer que le code PARCS est capable de modéliser les états transitoires de CROCUS où des distorsions locales du flux de neutrons sont visibles. Les différences maxima observées entre calculs et mesures sont de l'ordre de 5%.

Globalement, le schéma de calcul Serpent/PARCS a démontré des performances satisfaisantes pour la modélisation du réacteur CROCUS, hormis pour l'estimation du profil radial de taux de réactions, où les erreurs ont été attribuées aux limitations de PARCS pour la description de la géométrie de CROCUS : il est impossible d'adapter la taille du maillage pour correspondre aux positions exactes des crayons dans les deux zones du réacteur.

Mots clefs : réacteur CROCUS, fuites neutroniques, neutronique expérimentale, validation, diffusion des neutrons, cinétique spatiale, PARCS, calcul de réseau Monte Carlo, Serpent

Contents

Acknowledgements **i**

Abstract **iii**

Résumé **v**

List of figures **ix**

List of tables **xiii**

1 Introduction **1**

1.1 Background and motivation 1

1.2 Objectives and thesis organization 3

2 Theoretical background and current methods **5**

2.1 Neutron transport problem: mathematical formulation 5

2.2 Computational neutron transport 7

2.2.1 Deterministic methods 7

2.2.2 Monte Carlo methods 12

2.2.3 Deterministic vs. Monte Carlo 13

2.2.4 The diffusion approximation 14

2.3 Practical solution to full-core steady-state and kinetics problems 18

2.3.1 Spatial homogenization and group condensation 20

2.3.2 Full-core calculations: steady-state and neutron kinetics 22

2.3.3 The Serpent Code 27

2.3.4 The PARCS code 29

3 The CROCUS zero-power reactor **33**

3.1 Fuel description 35

3.2 Control rods description 38

3.3 Nuclear instrumentation 39

4 Experimental analysis **41**

4.1 Control rod reactivity worth measurements 42

4.1.1 Methods 42

4.1.2 Measurements by asymptotic period method 46
4.1.3 Measurements by inverse point kinetics method 51
4.1.4 Effect of kinetic parameters and nuclear data on reactivity worth . 54
4.1.5 Summary and discussion of results 56
4.2 Fission rate distribution measurements 57
4.2.1 Experimental procedure 57
4.2.2 Results 62
4.2.3 Evaluation of uncertainties 63
4.3 Neutron kinetics measurements 67
4.3.1 Global flux kinetic measurements 68
4.3.2 Space-time kinetics measurements 69

5 Numerical analysis 85

5.1 Serpent code modeling of the CROCUS reactor 85
5.1.1 Few-group constants generation 86
5.2 PARCS code modeling of the CROCUS reactor 95
5.2.1 Neutron kinetics modeling 100
5.3 Numerical results 101
5.3.1 Steady-state results 101
5.3.2 Parametric analysis 105

6 Experimental benchmarking 115

6.1 Control rod reactivity worth 115
6.2 Fission rate profiles 116
6.3 Neutron kinetics 118
6.3.1 Global flux transients 119
6.3.2 Space-time kinetic transients 120
6.4 Discussion of benchmarking results 122

7 Conclusions and recommendations 125

7.1 Conclusions 125
7.2 Recommendations 128

A Additional data 131

B Scripts and models 133

B.1 Serpent model of the CROCUS reactor 133
B.2 Serpent to FMFD-compatible cross-section 139

Bibliography 147

Curriculum Vitae 149

List of Figures

2.1 Multi-step computational scheme for full-core analysis 19
2.2 Simplified computation scheme for fine-mesh and coarse-mesh full-core calculations 23

3.1 Overview of the CROCUS reactor 34
3.2 Radial arrangement of the CROCUS components. Dimensions in mm. . . 35
3.3 Axial arrangement of the CROCUS components. Dimensions in mm. . . . 36
3.4 Top view of CROCUS grids and base plates. Dimensions in mm. 37
3.5 CROCUS B_4C control rods. Dimensions in mm. 38
3.6 Translateur Radial AXial (TRAX) system for in-core fission chamber scans 40

4.1 Power transient following a positive reactivity step of 0.23 $ in the CROCUS reactor 42
4.2 Asymptotic behavior of a transient following a positive reactivity step of 0.23$ 43
4.3 Asymptotic approach after positive (+0.23 $) vs. negative (-0.23 $) reactivity insertion. Analytical solution of the point-kinetics equations for the CROCUS reactor. 45
4.4 Solution for the largest root of the inhour equation in the CROCUS reactor. 45
4.5 Count rate (power) as a function of time for a typical rod withdrawal experiment 47
4.6 Exponential fitting for the asymptotic period in typical rod withdrawal experiment. 49
4.7 Typical output PDF generated from statistical sampling for the estimation of reactivity and associated uncertainty. 49
4.8 Example rod insertion measurement and reactivity estimation by inverse kinetics. 53
4.9 Reactivities calculated with kinetic parameters from JEFF-3.1.1 and ENDF/B-VII.1 nuclear data - Experiment #1a 55
4.10 In-core fission chamber (FC) scans. Radial and axial measurements 57
4.11 Effect of partial rod insertion on axial fission rate profile - Monte Carlo simulation 58

4.12 Effect of partial rod insertion on radial fission rate profile - Monte Carlo simulation . . . 59
4.13 Mobile fission chamber response versus power . . . 61
4.14 Mobile fission chamber signal's spectra at various reactor powers . . . 62
4.15 Axial fission rate distribution measurements in the CROCUS reactor for different critical water levels (h_{crit}) . . . 63
4.16 Radial fission rate distribution measurements in the CROCUS reactor . . . 63
4.17 Fission rate gradient in the radial direction. Monte Carlo simulation . . . 65
4.18 Fast control rod withdrawal and insertion transient measurements in the CROCUS reactor . . . 68
4.19 Slow control rod withdrawal and insertion transient measurements in the CROCUS reactor . . . 69
4.20 Experimental arrangement for flux perturbation measurements . . . 70
4.21 Acquisition system schematic diagram. Time-dependent flux perturbation measurements . . . 71
4.22 Schematic representation of detector radial positioning with respect to Al. guide tube . . . 72
4.23 In-core detector signal's spectra at various reactor powers . . . 73
4.24 In-core detector response versus power . . . 74
4.25 Monte Carlo simulated signals with Poisson noise . . . 76
4.26 Different filtering techniques on simulated signals . . . 77
4.27 Example of signal averaging for 100 trials . . . 79
4.28 Probability distributions of the error after signal denoising . . . 80
4.29 Local distortion measurements for different withdrawal speeds. In-core detector at h = 80 cm . . . 82
4.30 Local distortion measurements for absorber speed of 1.7 cm/s and various in-core detector positions . . . 83
4.31 Local distortion measurements for absorber speed of 1.7 cm/s and detector was fixed at h = 50 cm . . . 84

5.1 Calculation scheme for CROCUS reactor modeling . . . 86
5.2 Top and side views of full-core Serpent model of the CROCUS reactor. Geometry plots (left) and reaction rate plots (right) . . . 87
5.3 Serpent regions for cross-section homogenization in the CROCUS reactor . 89
5.4 Serpent mesh for tallying flux and fission rate . . . 93
5.5 Schematic representation of coarse and fine-mesh fission rate tallies for the generation of form functions . . . 94
5.6 CROCUS reactor control rod modeling . . . 95
5.7 Top view of PARCS model spatial discretization . . . 98
5.8 Side view of PARCS model spatial discretization . . . 99
5.9 Small absorber and detector modeling in PARCS for kinetics simulations . 101
5.10 Extent of thermal flux perturbation due to rod insertion . . . 103

5.11 PARCS and Serpent simulations of CROCUS radial ^{235}U fission rate profiles 104
5.12 PARCS and Serpent simulations of CROCUS radial neutron flux profiles . 105
5.13 Fuel/moderator inconsistencies between homogeneous (PARCS) and heterogeneous (Serpent) models 105
5.14 Impact of transport-corrected diffusion coefficient on neutron flux profiles 107
5.15 Models used for the study of in-scatter-corrected diffusion coefficients . . . 109
5.16 PARCS and Serpent simulations of CROCUS radial neutron flux profiles . 110
5.17 Multi-group diffusion pin power comparison for 2D CROCUS model . . . 112
5.18 Diffusion vs. SP$_3$ pin power comparison for 2D CROCUS model 114

6.1 Calculated vs. measured axial ^{235}U fission rate profiles 117
6.2 Calculated vs. measured axial radial ^{235}U fission rate profiles 118
6.3 Shape of radial ^{235}U fission rate 118
6.4 Calculated vs. measured results for fast control rod withdrawal and insertion transient 120
6.5 Calculated vs. measured results for slow control rod withdrawal and insertion transient 120
6.6 Calculated vs. measured results for space-time kinetic transient - Global flux data 121
6.7 Calculated vs. measured results for space-time kinetic transient - Local flux data 122
6.8 Calculated vs. measured results for space-time kinetic transient - Local/global flux ratio 123

List of Tables

3.1 CROCUS reactor fuel rod information 36

3.2 Materials data for structural components in the CROCUS reactor 37

3.3 B_4C control rods data. Guide tube not included 39

3.4 Data for CROCUS nuclear instrumentation 39

4.1 Reactivity worth by AP method - Rod withdrawal experiments 50

4.2 Reactivity worth by IK method - Rod insertion experiments 53

4.3 Reactivity worth by IK method - Rod withdrawal experiments 54

4.4 CROCUS kinetic parameters from JEFF-3.1.1 & U^{235} thermal from JEF/DOC-920 55

4.5 Summary of reactivity worth measurements 56

4.6 Statistical uncertainty after signal denoising 81

4.7 Uncertainty due to in-core detector's axial position 81

5.1 Two-group axial albedos for the CROCUS reactor 92

5.2 CROCUS adjoint-weighted effective kinetic parameters from Serpent - IFP method & JEFF-3.1.1 nuclear data 96

5.3 Models and parameters for the CROCUS full-core reactor calculations . . 101

5.4 Eigenvalue comparison 102

5.5 Control rod reactivity worth comparison 102

5.6 Impact of transport-corrected diffusion coefficient on CROCUS k_{eff} 106

5.7 Comparison of diffusion coefficients for the CROCUS reactor. In-scatter corrected vs. out-scatter approximation 108

5.8 Impact of transport-corrected diffusion coefficient on k_{eff} for various core sizes. 108

5.9 Impact of energy-group structure on k_{eff} - Simplified 2-D model of CROCUS.111

5.10 Impact of SP_3 multi-group solutions on k_{eff} - Simplified 2-D model of CROCUS. 113

6.1 Summary of reactivity worth measurements 116

A.1 CROCUS kinetic parameters from ENDF/B-VII.1 & U^{235} thermal fission products from Tuttle (1975) 131

A.2 Mobile fission chamber (Photonis CFUF34) response versus power 131

1 Introduction

1.1 Background and motivation

Research reactors are essential tools for education and training, medical isotopes production, but more importantly for supporting the nuclear power plant industry through experiments. They play an important role for testing advanced reactor materials, validation of computer codes and nuclear data libraries, and studying phenomena taking place in commercial power reactors. The CROCUS reactor [1] is a zero-power reactor located at the EPFL Lausanne campus in Switzerland. It is operated by the Swiss Federal Institute of Technology Lausanne (EPFL) and is the main object of study of the present work.

The operation of research reactors like CROCUS is characterized, as opposed to commercial reactors, by numerous modifications that are needed to satisfy the dynamic experimental demands. In particular, for the CROCUS reactor, three new experimental programs are scheduled for the forthcoming years [2]. Because of these activities, the regulatory body requires the operating organization to demonstrate that the experiments can be carried out without compromising the reactor safety. The current methods for transient and accident analysis of research reactor are diverse, but they commonly include the use of simple models that provides conservative estimates [3]. A good example is the PARET code [4] which uses one-dimensional heat transfer and fluid equations coupled with point-reactor kinetics models.

Regulatory bodies may require the use of updated computer codes that incorporate new developments and yield more accurate results. Computer codes used for commercial reactors have the potential to satisfy these needs, however, their application to research reactors must be demonstrated due to fundamental differences in design and operating conditions. The previous statement is particularly valid for materials, fuel composition, system pressure, core geometry and power amongst other differences. The applicability of industry-adopted computer codes to research reactor analysis must be demonstrated through the verification and validation of computational schemes. This requires the assessment of simulation results against reference simulations and relevant experimental data. The CROCUS reactor is attractive precisely for the validation of isolated neutronics effects due to the absence of thermal feedback and fuel burn-up.

The neutronics analysis of commercial light water reactors is typically done with nodal diffusion codes. They are widely used because of their high efficiency to evaluate the steady-state and transient behavior of the neutron flux in a reactor. PARCS [5] is an example of a three-dimensional nodal diffusion code that solves the space-energy-dependent neutron kinetics equations. This type of codes simplifies the transport problem with the use of neutron diffusion theory, also by reducing the core into unit cells that are spatially homogeneous and also by solving the equations for few-energy groups. The process where the heterogeneous components of the reactor are converted into homogeneous ones is performed in the step preceding the full-core calculation. This first step is typically referred to as lattice calculation and involves the use of a lattice physics code such as CASMO [6]. Nodal diffusion codes are suitable for many commercial power reactors types, however, they can present limited accuracy for certain applications such as for high-leakage reactors and systems with regions encountering sharp changes in absorption or scattering properties. The accuracy of these diffusion methods is mainly governed by the homogenization process and the optimal definition of diffusion coefficient, which remains as of today unclear and has long been a subject of debate.

The CROCUS reactor presents some of the situations where the acceptability of the diffusion-based methods is questioned, such as large losses due to neutron streaming and the presence of Cadmium absorbers. Also, at a lattice calculation level, traditional codes for producing homogenized data, like CASMO, require each homogenization region to be modeled separately with reflective boundary conditions. Such a thing is not possible in the CROCUS reactor because the complexity of the geometry in the radial plane does not allow a natural subdivision of the core in simple subsections. This issue can be overcome with the use of Monte Carlo based lattice physics codes such as Serpent [7] that allow to produce homogenized data from the full-core geometry. The Serpent code is not only adequate for this task, but also for providing full-core Monte Carlo solutions that can be used as a reference for verification studies.

The PARCS code has been chosen for the modeling of the CROCUS reactor since it represents the state-of-the-art for diffusion calculation in thermal reactors. Also, the Serpent code has been chosen for the generation of the homogenized data required by PARCS. It is therefore desired to demonstrate the applicability of the Serpent/PARCS code sequence for the neutronics modeling of the CROCUS reactor. This is expected to be accomplished with numerical studies and most importantly by comparison of simulations against experimental data addressing static and transient neutronics effects.

1.2 Objectives and thesis organization

The main objective of this thesis is to assess the performance of the Serpent/PARCS computational scheme for the modeling of CROCUS reactor using steady-state and time-dependent experimental data. To achieve this goal it is first required to obtain experimental data from the CROCUS reactor. The experimental campaign targets the generation of reliable data for the validation of neutronics models. It is particularly desired to develop experimental techniques that address local time-dependent phenomena for the validation of space-time kinetic models. Likewise, the accomplishment of the end objective requires the development of Serpent/PARCS computational models for the steady-state and space-time neutron kinetics analysis of the reactor. With this in mind, it is expected to investigate the key parameters needed to produce accurate PARCS results.

The present thesis is organized into seven chapters. This first chapter provides background information, the motivation, and objectives of the work. Chapter 2 introduces the theoretical framework that provides support for the present research. More precisely, Chapter 2 describes relevant methods for steady-state and transient neutronics modeling of nuclear reactors. The choice of computer codes for modeling the CROCUS reactor is also discussed in Chapter 2. Chapter 3 provides detailed information about the CROCUS nuclear facility. Chapter 4 covers the measurement of steady-state and time-dependent experimental data in CROCUS, and thus addresses the objective of producing reliable data for the validation of neutronics models. In Chapter 5, the neutronics modeling of the reactor is presented together with numerical results and a parametric analysis that focuses on the key parameters needed to produce accurate results. Chapter 6 reports the comparison between PARCS simulations and the experimental data, which is used to evaluate the performance of the computational scheme. The conclusions of this work and recommendations for future research are documented in Chapter 7.

2 Theoretical background and current methods

2.1 Neutron transport problem: mathematical formulation

The primary goal of nuclear reactor analysis is to predict, for any time t, the distribution of neutrons in space, angle, and energy. This information is fundamental as neutrons are responsible for maintaining the fission chain reaction, and therefore for releasing energy through fission. From the observation of the neutron population's characteristics, one can determine, amongst other things,

- the amount of power generated at any given time at any location in the reactor,
- the level of fuel depletion and production of fission products,
- the degree of neutron radiation damage induced on structural components.

The neutron distribution in a nuclear reactor is well described by the *transport equation*, which is a linear form of the Boltzmann equation and whose exact analytical solution can be only found for a few simple problems. The time-dependent form of the *neutron transport equation* can be written as

$$\begin{aligned}\frac{1}{v(E)}\frac{\partial\psi}{\partial t}(\mathbf{r},E,\mathbf{\Omega},t)+\mathbf{\Omega}\cdot\nabla\psi(\mathbf{r},E,\mathbf{\Omega},t)+\Sigma_t(\mathbf{r},E,t)\psi(\mathbf{r},E,\mathbf{\Omega},t)&\\ =\int_{4\pi}\int_0^\infty \Sigma_s(\mathbf{r},E'\to E,\mathbf{\Omega}'\to\mathbf{\Omega},t)\psi(\mathbf{r},E',\mathbf{\Omega}',t)dE'd\Omega'&\\ +\frac{\chi_{pr}\left(E\right)}{4\pi}\int_{4\pi}\int_0^\infty \nu_{pr}\left(\mathbf{r},E'\right)\Sigma_f\left(\mathbf{r},E',t\right)\psi\left(\mathbf{r},E',\mathbf{\Omega}',t\right)dE'd\Omega'&\\ +\sum_{i=1}^{N}\frac{\chi_{del,i}\left(E\right)}{4\pi}\lambda_i C_i\left(\mathbf{r},t\right)+q(\mathbf{r},E,\mathbf{\Omega},t)&\end{aligned} \tag{2.1}$$

where ψ is the angular neutron flux as a function of position ($\mathbf{r}$), energy (E), direction ($\mathbf{\Omega}$) and time (t). v is the neutron velocity vector and Σ the macroscopic cross-section for each reaction.

The previous equation can be regarded as a balance of the different neutron reactions, and thus it is written in the form of (*rate of change*) + (*rate of loss*) = (*rate of gain*). Each of the terms of the transport equation represents a specific process for the loss or gain of neutrons as described below.

- Rate of change of neutron density: $\frac{1}{v(E)}\frac{\partial\psi}{\partial t}(\mathbf{r},E,\mathbf{\Omega},t)$

- Rate of loss due to leakage: $\mathbf{\Omega}\cdot\nabla\psi(\mathbf{r},E,\mathbf{\Omega},t)$

- Rate of loss due to collisions: $\Sigma_t(\mathbf{r},E,t)\psi(\mathbf{r},E,\mathbf{\Omega},t)$

- Rate of gain due to in-scattering: $\int_{4\pi}\int_0^\infty \Sigma_s(\mathbf{r},E'\to E,\mathbf{\Omega}'\to\mathbf{\Omega},t)\psi(\mathbf{r},E',\mathbf{\Omega}',t)dE'd\Omega'$

- Rate of gain due to prompt fissions: $\frac{\chi_{pr}\left(E\right)}{4\pi}\int_{4\pi}\int_0^\infty \nu_{pr}\left(\mathbf{r},E'\right)\Sigma_f\left(\mathbf{r},E',t\right)\psi\left(\mathbf{r},E',\mathbf{\Omega}',t\right)dE'd\Omega'$

- Rate of gain due to delayed neutrons: $\sum_{i=1}^{N}\frac{\chi_{del,i}\left(E\right)}{4\pi}\lambda_i C_i\left(\mathbf{r},t\right)$

- Rate of gain due to neutron source: $q(\mathbf{r},E,\mathbf{\Omega},t)$

For neutron kinetics problems, the *time-dependent neutron transport equation* (Eq. 2.1) needs to be solved together with the *delayed neutron precursor concentration equations*

$$\frac{\partial C_i}{\partial t}(\mathbf{r},t)+\lambda_i C_i(\mathbf{r},t)=\int_{4\pi}\int_0^\infty \nu_{del,i}(\mathbf{r},E')\Sigma_f(\mathbf{r},E',t)\psi(\mathbf{r},E',\mathbf{\Omega}',t)dE'd\Omega' \qquad i=1,2,...,N \quad (2.2)$$

where i represents each delayed neutron precursor group.

The neutron transport equation (2.1) constitutes the grounds of various fields of nuclear engineering such as reactor core analysis, nuclear criticality safety and shielding calculations. When this equation is coupled to the precursor equations (2.2), the whole set of equations is referred to as *space-time kinetics equations.* In nuclear reactor analysis, these equations are employed for three main purposes:

A first application involves the steady-state calculation of reactor properties such as $\mathrm{k_{eff}}$ eigenvalue and power distribution. This is usually done for different reactor configurations and various operating conditions. For steady-state problems, the *precursor concentration equations* can be ignored and the *neutron transport equation* becomes time-independent.

A second application comprises the calculation of power transients that last in the order of seconds to minutes. This type of analysis is done at a full-core level and it is governed by the *space-time kinetics equations.*

Finally, the transport equation is also employed for the calculation of fuel burn-up and buildup of fission products. These problems are considered as much slower transients than the described above as they involve changes in the core isotopic composition over more extended periods of time. These problems also require the solution of the *burnup equations* which are not presented here as there are beyond the scope of this work. The present work covers the use of the transport equation for the first two applications: (i) steady-state full-core solutions and (ii) power transient (or spatial-kinetics) calculations.

2.2 Computational neutron transport

Except for a couple of simple cases, it is not possible to find the exact solution of the neutron transport equation. Approximate solutions can be provided by two different approaches, which are usually referred to as *deterministic* and *stochastic* methods. The deterministic techniques are those where the neutron transport equation is discretized in each independent variable (space, angle, energy and time) and solved numerically. On the other hand, stochastic methods (also known as Monte Carlo) do not require to solve the transport equation; they instead simulate neutrons one at a time and use probability distributions to predict the interactions that each neutron will undergo during its lifetime. Monte Carlo transport methods have the ability to produce very accurate results but they require large computer power as compared to deterministic solutions.

While Monte Carlo techniques are generally advantageous for problems where high accuracy is needed and the computational cost can be afforded, deterministic methods show a much better performance for production calculations. In addition, time-dependent Monte Carlo simulations are in an early stage of development [8, 9]; whereas time-dependent deterministic solutions are very well established. Both approaches have been evolving for the past 60 years, and have been seen as complementary. A more in-depth comparison between both methods will be later presented.

As it will be shown later, the solution of the neutron transport problem with deterministic and Monte Carlo methods is of relevance to this work and in particular for the neutronics analysis of the CROCUS reactor. The sections below will attempt to provide general information about these methods. Amongst the various deterministic methods, focus will be given to the neutron diffusion theory.

2.2.1 Deterministic methods

As mentioned above, deterministic methods are based on numerically solving the discretized transport equation. The derivatives and integrals appearing in the continuous form of the transport equation must also be replaced by a corresponding discrete representation. Different techniques have been developed to cope with the complex dependence of the transport equation on its seven independent variables (three spatial, one for energy, two angular and one for time).

Angular dependence

Many of the methods available for solving the transport equation have been developed to handle the angular dependency. There are three techniques for approximating the angular variable:

- Continuous angle expansion: *spherical harmonics* ($\mathrm{P_N}$) method
- Discrete angle representation: *discrete-ordinates* ($\mathrm{S_N}$) method and *method of characteristics* (MOC)
- Integration over all angles assuming isotropy: *collision probability method* (CPM)

Details on the above-listed methods are beyond the scope of this work, and therefore they are not described here. However, it is worth mentioning that the $\mathrm{P_1}$ method (1st order spherical harmonics) is closely related to the *diffusion theory* as it will be described later (see p. 14).

It is also relevant to note that a less accurate but more straightforward method than the $\mathrm{P_N}$ approximations is the so-called simplified spherical harmonic ($\mathrm{SP_N}$) approximation [10]. Numerical techniques that are appropriate for diffusion problems can generally be easily extended to these equations because the $\mathrm{SP_N}$ approximation takes a similar form than the diffusion equations. The $\mathrm{SP_N}$ method provides an efficient solution technique for full-core calculations as higher angular order relations are used to “enhance” the diffusion solutions.

In particular, the $\mathrm{SP_3}$ approximation was used in this work to study the transport effects in full-core calculations as it considers a higher order angular flux moment than diffusion theory.

Technicalities concerning the $\mathrm{P_N}$, $\mathrm{S_N}$, MOC and CPM methods can be found in literature from Lewis and Miller [11], Larsen and Morel [12], Askew [13] and Askew [14], respectively.

Energy dependence

Having discussed the most common approaches to handle the angular dependence in the transport equation, one can proceed with the treatment of the energy dependence. This is typically done with the standard *multigroup approximation* [15]. The multigroup formulation differs from the original transport equation (Eq. 2.1) in that the energy variable is discrete rather than continuous, so all the integrals over the energy variable can be replaced by sums over the energy groups. The choice of the number of groups and group structure (energy boundaries between each group) depends on each specific problem. For each group, the neutron cross-sections are represented as constants (multigroup cross-sections) that are computed by flux-weighting the continuous energy cross-sections on each energy interval. However, at this calculation stage, the flux spectrum (that is used as weighting function) is unknown and therefore it is required to use an approximated (or guessed) flux

$$\Sigma_g \cong \frac{\displaystyle\int_{E_g}^{E_{g-1}} \Sigma(E)\ \phi_{\text{approx}}(\mathbf{r}, E)\ dE}{\displaystyle\int_{E_g}^{E_{g-1}} \phi_{\text{approx}}(\mathbf{r}, E)\ dE} \tag{2.3}$$

On top of that, the neutron cross-sections can be extremely complicated functions of the energy variable and thus the biggest challenge of the multigroup approximation is to accurately calculate the multigroup cross-sections.

Space dependence

Different techniques are available to treat the spatial dependence of the transport equation. *Fine-mesh finite-differences*, *nodal methods*, and *finite elements* are the most common approaches. While finite difference and nodal methods are relatively easy to implement on Cartesian spatial grids, other discretization methods, such as finite element, are advantageous for non-Cartesian grids (triangular, tetrahedral, or unstructured). Because the PARCS code employs both finite difference and nodal methods, only these methods will be briefly introduced below. Details about finite element methods are provided by Zienkiewicz et al. [16].

The spatial dependence of the transport equation was early treated with classical *finite difference* schemes. This method consists of approximating the spatial derivatives of the flux by divided differences of various orders obtained from a truncated Taylor expansion. Given that a low-order truncation error is introduced, finite-differences schemes require a fine mesh spacing for acceptable accuracy. The mesh size should be around the smallest group-wise diffusion length[1], even if the geometry can be defined using a larger mesh size [17]. For that reason, fine-mesh finite-difference solutions generally treat each fuel pin separately.

There are two varieties of the finite difference method: the mesh-corner and mesh-centered finite differences. The latter has been the most widely used in production codes. The mesh-centered finite differences method assumes that the average neutron flux in a region is equal to the neutron flux at the center of that region. The set of finite-difference equations can be obtained, for example, by integrating the diffusion equation over each mesh cell. The resulting differential terms of the integrated equation are replaced with finite-difference relations obtained from the first two terms of the Taylor-expanded neutron flux. The equations resulting from the finite difference relationships are presented in various classic textbooks as the numerical solution of the neutron diffusion equation. In particular, the textbook by Hébert [18] provides the different finite differences formulations for diffusion problems.

---

[1] the thermal diffusion length in the CROCUS reactor core is ∼ 1.8 cm

The posterior development of *nodal methods* [19] resulted in a more computationally efficient approach to tackle the spatial discretization. Because these methods allow the reactor core to be discretized in larger regions (nodes) achieving the same or greater accuracy than with classical finite difference schemes, they have been extensively used in the nuclear reactor community. However, in order to achieve acceptable accuracy, nodal techniques need to employ a higher order spatial treatment within each mesh than classical finite difference schemes.

Nodal methods have been evolving over the years and therefore there exist different classes [20]. Only those based on the *transverse integration procedure* will be discussed here as they are the ones implemented by the PARCS code. Although they have been developed in the mid-1970s, they are considered as modern nodal methods, and they are still used today by most advanced nodal codes [21]. Essentially, this type of nodal methods approximates the multi-dimensional transport equation by a coupled system of one-dimensional (1-D) transport equations as it will be later shown. The diffusion approximation is presented in detail on page 14, and will be used here to describe the transverse integrated nodal methods.

Transverse integrated nodal methods convert the 3-D diffusion equation into a system of three 1-D equations coupled through a transverse leakage term. For example, the steady-state form of the diffusion equation can be integrated over the y- and z- directions to yield the transverse integrated equation for the x- direction

$$-D_g^m \frac{d^2}{dx^2}\bar{\phi}_{gx}^m(x) + \Sigma_{rg}^m \bar{\phi}_{gx}^m(x) - \bar{q}_{gx}^m(x) = -\bar{L}_{gx}^m(x) \tag{2.4}$$

where $\bar{\phi}_{gx}^m$ is the transverse-integrated flux in the x-direction in node m, $\bar{q}_{gx}^m$ is the transverse-averaged source, and $\bar{L}_{gx}^m$ is the transverse leakage term. The transverse-integrated flux and the transverse leakage term can be computed as

$$\bar{\phi}_{gx}^m(x) = \frac{1}{\Delta y \Delta z} \int_{y^m-\Delta y/2}^{y^n+\Delta y/2} \int_{z^m-\Delta z^n/2}^{z^m+\Delta z/2} \phi_g^m(x,y,z) \tag{2.5}$$

$$\bar{L}_{gx}^{m}(x) = -\frac{D_g^m}{\Delta z \Delta y}\left[\int_{z^m-\Delta z/2}^{z^m+\Delta z/2} dz \frac{\partial}{\partial y}\phi_g^m(x,y,z)\Big|_{y^m-\Delta y/2}^{y^m+\Delta y/2} + \int_{y^m-\Delta y/2}^{y^m+\Delta y/2} dy \frac{\partial}{\partial z}\phi_g^m(x,y,z)\Big|_{z^m-\Delta z/2}^{z^m+\Delta z/2}\right] \tag{2.6}$$

where Δy, and Δz are the node dimensions the y- and z-directions, respectively. The transverse leakage term ($\bar{L}_{gx}^{m}$) accounts for the neutrons leaving the node in the transverse directions. The majority of the modern transverse-integrated nodal methods employ an approximation which uses quadratic polynomials to describe this term. Then, equation 2.6 can be approximated as

$$\bar{L}_{gx}^{m}(x) = L_{0gx}^{m} + p_1(x)L_{1gx}^{m} + p_2(x)L_{2gx}^{m} \tag{2.7}$$

where p_j is a polynomial of order j. One-dimensional equations in the y- and z-directions are derived in an analogous manner and they can all be extended to the time-dependent form of the neutron diffusion equation (2.24). This set of 1-D equations are solved to satisfy the *node balance condition*

$$\frac{1}{\Delta x}\left(J_{gx+}^{m} - J_{gx-}^{m}\right) + \frac{1}{\Delta y}\left(J_{gy+}^{m} - J_{gy-}^{m}\right) + \frac{1}{\Delta z}\left(J_{gz+}^{m} - J_{gz-}^{m}\right) + \Sigma_{rg}^{m}\bar{\phi}_g^m = \bar{q}_g^m \tag{2.8}$$

where the plus (+) and minus (-) subindices denote the right directed and left directed faces of the node m.

It is possible to solve the one-dimensional equations (2.4) with a polynomial expansion of the 1-D nodal fluxes $\bar{\phi}_{gx}^{m}(x)$ (typically in a 4th order) using the Nodal Expansion Method (NEM), or even analytically using the Analytic Nodal Method (ANM). An excellent review of transverse integrated nodal methods is that of Lawrence [22]. The paper by Sutton and Aviles [20] provides an extension to time-dependent problems and a good summary of methods for solving the neutron diffusion equation.

Time dependence

Last but not least, for time-dependent problems (space-time reactor kinetics) the time variable also needs to be discretized. This is a relevant matter with respect to the subject of this thesis. The simplest solution is to use the *forward-difference* (explicit) scheme. While it requires low computational effort, a small time-step must be used to obtain a reliable result. A coarser time-step in the explicit scheme might lead to numerical instabilities. These instabilities can be solved by employing *backward-difference* (implicit) schemes. The implicit scheme has the advantage that it can provide the unconditional numerical stability that allows for larger time steps. The time step size is usually limited by the accuracy of the solution (due to truncation error) rather than by numerical stability. The downside of the implicit scheme is that it requires a longer computation is required because a matrix inversion is carried out at each time step. Another class of implicit schemes is the *theta-difference* method, which is generally stable but also requires the inversion of a matrix leading to longer computational times. The theta-difference method can be reduced, for particular values of theta, to the forward-difference, backward-difference or even the Crank-Nicolson schemes [23].

Different approximations to the solution of time-dependent neutron transport problem (i.e. point reactor kinetics, space-time kinetics) will be discussed later in Section 2.3.2 (p. 22).

More specifics on classical and modern deterministic techniques for solving the neutron transport problem can be found in textbooks by Hébert [18] or Azmy and Sartori [24].

2.2.2 Monte Carlo methods

In contrast to deterministic techniques that solve the neutron transport equation, stochastic (or Monte Carlo) methods present a different approach where the neutron transport process is simulated directly without referring to the transport equation. This transport equation (used by deterministic methods) describes the average neutron behavior in a medium; however, due to the statistical nature of particle interactions, the actual neutrons behavior fluctuates around the average with a magnitude that depends on the population size. This statistical nature provides a logical reason for using stochastic sampling or Monte Carlo methods to simulate neutron transport processes. Monte Carlo methods are said to be stochastic because they rely on random numbers to simulate and track neutrons moving through a certain domain from their birth to death. As a consequence, Monte Carlo results are slightly different if the same problem is run several times.

The Monte Carlo method is the most accurate but also the most computer-intensive technique for solving the neutron transport problem. The essential idea behind this method is to simulate millions or billions of random neutron histories and to average results to determine the behavior of neutrons [25, 26]. Random numbers are used in each neutron history to sample appropriate probability distributions for travel distances between collisions, type of reaction after collision, scattering angles and so on. The following algorithm exemplifies the Monte Carlo technique to simulate a neutron history:

1. The neutron's initial energy, position, and direction are determined by sampling the source distribution.
2. The distance that the neutron will travel before colliding is sampled stochastically.
3. The material and point of collision are determined.
4. Cross section data is sampled to determine what nuclide will interact with the neutron (through a collision) and whether the collision is an absorption or a

scattering reaction.

5. If the neutron experiences an absorption reaction, the history is ended. In the case that the absorption is a fission reaction, the position of the collision is saved as a potential starting point for tracking the next generation of neutrons.
6. If the neutron experiences scattering, the outgoing scattering angle and energy are sampled from the appropriate distributions. In the case of elastic scattering, the outgoing energy is determined by conservation of energy and momentum.
7. With the energy, position, and direction after the collision, the procedure is repeated for successive collisions until the neutron is absorbed or leaks out from the system.

Because Monte Carlo results are generated stochastically, they are distributed randomly and are represented by the mean value and its associated uncertainty (i.e., variance). A Monte Carlo result reported without its associated uncertainty is meaningless. This uncertainty is related to the number of neutron histories used for simulating the transport problem. The standard deviations associated with the mean value varies inversely to the square root of the number of histories [25]. However, in criticality calculations, a low uncertainty level does not necessarily ensure good results; convergence of the source distribution also needs to be assessed for a reliable calculation [27].

Monte Carlo results, such as the reaction rate over a specific volume, need to be collected through the course of the simulation. This process is known as tallying or scoring [26]. One of the most serious drawbacks of Monte Carlo techniques is precisely related to the collection of information averaged over a very small volume, or worse, at a point. For a finite number of histories, the variance of the result will rise rapidly as the volume decreases, since few if any of the particles will collide or even pass through the volume. Ultimately, the results will become unreliable as one approaches the point limit since for a given number of N histories the most likely result will be that no particles contribute to the tally [11].

2.2.3 Deterministic vs. Monte Carlo

Monte Carlo methods present certain advantages over deterministic methods. To begin with, it is possible to solve problems for the exact geometry (no spatial discretization is required) and to build arbitrarily complex geometries. With deterministic methods, the geometry needs to be approximated and if the model is complex, a sophisticated mesh generation process needs to be carried out.

Monte Carlo codes can also benefit from the use of continuous-energy point-wise cross-section data directly with no need of self-shielding approximations (with exception of the unresolved resonance region where probability tables need to be used). This means that they be employed to solve problems with extremely complex energy-dependence cross-section data. As opposed to Monte Carlo, deterministic methods require an extra step in the calculation scheme to generate multi-group resonance-treated cross-sections that take into account the valleys and peaks in the resonance region. This can be accomplished by performing ultra-fine group calculations.

One of the fundamental advantages of Monte Carlo methods is that few approximations are made to simulate the transport process. The continuous treatment of energy, as well as space and angle, reduces discretization errors such as those resulting from the use of multigroup approximations. If the geometry of the system and the probability distributions that govern the transport process are known, results contain only statistical errors. Very accurate results can be therefore obtained, provided that enough neutron histories are run. This is the reason why Monte Carlo methods are used to study non-standard situations and to verify deterministic results.

Monte Carlo methods are also very versatile and are applicable to any reactor type. Due to the several approximations made to solve the transport equation, deterministic methods are, in general, more restricted to specific reactor types.

On the other hand, deterministic methods can also be advantageous. The clearest advantage is that, for certain applications, accurate deterministic solutions can be obtained very quickly. Monte Carlo techniques are much slower and resource-intensive because they rely on repeated random sampling.

As earlier mentioned, Monte Carlo methods provide results that are collected stochastically through events (such as collisions) taking place in the volume of interest. This is a serious shortcoming of these methods since they are extremely time-consuming when detailed information (e.g. flux) is desired in small regions. Monte Carlo methods are more efficient for estimating global parameters such as criticality eigenvalue than for local parameters such as the response of detector located in the core periphery (i.e., far from the source). Contrarily, deterministic methods provide good knowledge of the average behavior everywhere.

Last but not least, deterministic methods can provide a solution to reactor kinetics problems. Time-dependent Monte Carlo transport methods are being developed [8, 7, 9], however, preliminary results are limited and remain highly computationally expensive.

2.2.4 The diffusion approximation

Monte Carlo and deterministic transport methods are not best suited for full-core calculations because they need large computational effort and memory. What is done instead, is to use *neutron diffusion theory* to simplify the problem by nearly eliminating the angular dependence from the transport equation. This simplification reduces substantially the final number of unknowns in a full-core problem. For this reason, the *diffusion approximation* is the simplest method for solving the neutron transport problem and has been widely used since the early development of nuclear reactors.

The diffusion approximation can be derived from the transport theory by first reducing the angular dependency [15]. This can be done by integrating the transport equation over angle, which yields the neutron balance in the system, and can be expressed as

$$\frac{1}{v}\frac{\partial \phi}{\partial t}(\mathbf{r},E,t) + \nabla \cdot \mathbf{J}(\mathbf{r},E,t) + \Sigma_t(\mathbf{r},E,t)\phi(\mathbf{r},E,t) = \int_0^\infty \Sigma_s(\mathbf{r},E' \to E,t)\phi(\mathbf{r},E',t)dE' + Q(\mathbf{r},E,t) \tag{2.9}$$

The previous equation is known as the *neutron continuity equation.* In this equation, the production from fission reactions is included in the sources term $Q(\mathbf{r},E,t)$.

The continuity equation has two unknowns, the scalar flux $\phi(\mathbf{r},E,t)$ and a newly introduced variable: the net current $\mathbf{J}(\mathbf{r},E,t)$. This implies that integrating over angle is not sufficient to simplify the problem because a new unknown has appeared. It is therefore required to introduce a relation between $\phi(\mathbf{r},E,t)$ and $\mathbf{J}(\mathbf{r},E,t)$ that limits the angular variation of $\phi(\mathbf{r},E,t)$. An elegant way to accomplish this is to expand the angular dependence of the angular flux ψ using spherical harmonics. As a matter of fact, this type of expansion is used to derive the P_N equations as described in the previous section (2.2.1). If we retain the first two terms, the expansion yields the P_1 approximation, which assumes that the angular flux is a linear function of angle

$$\psi(\mathbf{r},E,\mathbf{\Omega},t) \approx \frac{1}{4\pi}\left[\phi(\mathbf{r},E,t) + 3\mathbf{\Omega}\cdot\mathbf{J}(\mathbf{r},E,t)\right] \tag{2.10}$$

The previous equation is known as the linearly anisotropic flux approximation which, in practical terms, implies that the flux is nearly isotropic. The P_1 equations are then given by

$$\frac{1}{v}\frac{\partial \phi}{\partial t}(\mathbf{r},E,t) + \nabla \cdot \mathbf{J}(\mathbf{r},E,t) + \Sigma_t(\mathbf{r},E,t)\phi(\mathbf{r},E,t) = \int_0^\infty \Sigma_{s0}(\mathbf{r},E' \to E,t)\phi(\mathbf{r},E',t)dE' + Q_0(\mathbf{r},E,t) \tag{2.11}$$

$$\frac{1}{v}\frac{\partial \mathbf{J}}{\partial t}(\mathbf{r},E,t) + \frac{1}{3}\nabla\phi(\mathbf{r},E,t) + \Sigma_t(\mathbf{r},E,t)\mathbf{J}(\mathbf{r},E,t) = \int_0^\infty \Sigma_{s1}(\mathbf{r},E' \to E,t)\mathbf{J}(\mathbf{r},E',t)dE' + Q_1(\mathbf{r},E,t) \tag{2.12}$$

Where Eqs. 2.11 and 2.12 are the zeroth and first-moment P_1 equations respectively.

Note that the zeroth moment equation corresponds to the continuity equation (Eq. 2.9). Σ_{s0} and Σ_{s1} are the isotropic and linearly anisotropic components of the differential cross section characterizing elastic scattering. They are approximated as a sequence of terms in a Legendre polynomial expansion and they are typically referred to zeroth and first scattering moments, respectively [15].

To derive the diffusion approximation from the P_1 equations (Eqs. 2.11 and 2.12), further assumptions need to be made. By assuming that all neutron sources are isotropic and that the neutron current $\mathbf{J}$ varies slowly in time, it is possible to arrive to *Fick's law* for neutrons

$$\mathbf{J}(\mathbf{r},E,t) = -D(\mathbf{r},E,t)\nabla\phi(\mathbf{r},E,t) \tag{2.13}$$

Fick's law constitutes the basis of the diffusion approximation as it expresses that neutrons tend to diffuse from regions of high to lower neutron densities. In this equation, $D(\mathbf{r},E,t)$ is the *diffusion coefficient* which can be approximated in several ways. The most general form of the diffusion coefficient is given by

$$D(\mathbf{r},E,t) = \frac{1}{3\Sigma_{tr}(\mathbf{r},E,t)} \tag{2.14}$$

where Σ_{tr} is the so-called *transport cross-section* and can take different forms. The different definitions of the transport cross-section deserve detailed discussion and is addressed in the following section (p. 17).

Fick's law (Eq. 2.13) can be used to replace the net current ($\mathbf{J}$) in the continuity equation (Eq. 2.9) to finally arrive at the continuous-energy time-dependent diffusion equation

$$\begin{aligned}\frac{1}{v(E)}\frac{\partial\phi}{\partial t}(\mathbf{r},E,t) - \nabla\cdot D(\mathbf{r},E,t)\nabla\phi(\mathbf{r},E,t) + \Sigma_t(\mathbf{r},E,t)\phi(\mathbf{r},E,t)&\\ = \int_0^\infty \Sigma_s(\mathbf{r},E'\to E,t)\phi(\mathbf{r},E',t)dE'&\\ + \chi_{pr}(E)\int_0^\infty \nu_{pr}\left(\mathbf{r},E'\right)\Sigma_f\left(\mathbf{r},E',t\right)\phi\left(\mathbf{r},E',t\right)dE'&\\ + \sum_{i=1}^{N}\chi_{del,i}(E)\lambda_i C_i(\mathbf{r},t) + q(\mathbf{r},E,t)&\end{aligned} \tag{2.15}$$

The detailed derivation of the diffusion approximation can be found in classic textbooks such as Duderstadt and Hamilton [15].

The neutron diffusion theory provides a valid mathematical description of the neutron behavior when the problem satisfies the assumptions made in the derivation of the diffusion approximation. These assumptions are (1) the neutron flux has a weak (linear) angular dependence, (2) neutron sources -including fission- are isotropic, and (3) the neutron current varies slowly in time as compared to the mean time between neutron-nuclei collisions. As a matter of fact, only the first of these approximations is restrictive since a weak angular dependence can be associated with neutron fluxes having a weak spatial dependence. This assumption is violated in the following cases:

(i) near boundaries or interfaces where material properties change abruptly over distances comparable to a mean free path,

(ii) near localized sources,

(iii) in strongly absorbing media.

It is important to keep these limitations in mind as we apply the diffusion approximation to the analysis of nuclear reactors, in particular for the CROCUS reactor.

Transport cross-section variants

The transport cross section can be regarded as a correction accounting for anisotropies in the scattering collision process.

The transport cross-section can be derived from the P_1 equations (Eqs. 2.11 and 2.12) and can be formally written as [15]

$$\Sigma_{tr}(\mathbf{r},E) = \Sigma_t(\mathbf{r},E) - \frac{\displaystyle\int_0^\infty \Sigma_{s1}(\mathbf{r},E' \to E)\mathbf{J}(\mathbf{r},E')dE'}{\mathbf{J}(\mathbf{r},E)} \tag{2.16}$$

where $\Sigma_{s1}(\mathbf{r},E' \to E)$ is the first moment scattering cross-section from E' to E. The previous equation represents the rigorous definition of P_1 transport cross-section and implies that the P_1 scattering cross-sections are current-weighted. In the context of P_1 equations, the neutron current can be represented by the first moment of the angular flux (ϕ_1), which leads to the so-called *in-scatter method* for the calculation of transport cross-sections. However this method results impractical because the evaluation of the P_1 component of the angular flux (ϕ_1) requires a prior detailed transport calculation [28].

Different approximations can be made on Equation 2.16 for a more efficient evaluation of transport cross-sections. The most elemental (non-corrected) form of the transport cross-section is given in the case where isotropic scattering is assumed in the laboratory reference frame (LAB), which implies that $\Sigma_{s1}(\mathbf{r},E,t) = 0$. In such a case, the transport correction takes the form of

$$\Sigma_{tr}(\mathbf{r},E) = \Sigma_t(\mathbf{r},E) \tag{2.17}$$

The previous equation is known as P_0 *transport cross-section* because it consider only the zeroth moment (P_0 component) of the scattering and neglects higher orders. Unfortunately, the assumption of isotropic scattering is very weak, particularly for low mass number nuclei scatterers such as hydrogen in light water reactors. Several methods were developed to correct this P_0 *transport cross-section* by accounting for anisotropy in the scattering process. This correction is precisely the reason why the transport cross-section was introduced for computing diffusion coefficients.

The most usual approach to account for scattering anisotropy without having to deal with the *in-scatter method* is to simplify Equation 2.16 by assuming that the in-scatter and out-scatter sources are equal

$$\int_0^\infty \Sigma_{s1}(\mathbf{r}, E' \to E)\mathbf{J}(\mathbf{r}, E')dE' \approx \int_0^\infty \Sigma_{s1}(\mathbf{r}, E \to E')\mathbf{J}(\mathbf{r}, E)dE' \tag{2.18}$$

This approximation –known as the *out-scatter approximation*– can be used to factor out the neutron current ($\mathbf{J}$) from the integral in Equation 2.16. This yields the *out-scatter transport-corrected-P_0 transport cross-section*

$$\begin{aligned} \Sigma_{tr}(\mathbf{r}, E) &= \Sigma_t(\mathbf{r}, E, t) - \Sigma_{s1}(\mathbf{r}, E) \\ &= \Sigma_t(\mathbf{r}, E) - \overline{\mu}_0\Sigma_{s0}(\mathbf{r}, E) \end{aligned} \tag{2.19}$$

where $\overline{\mu}_0$ is the average cosine scattering angle and Σ_{s0} the zeroth moment (P_0) scattering cross-section.

The *out-scatter approximation* neglects the anisotropic contribution to energy transfer in a scattering collision. This a reasonable assumption in the thermal energy region where the neutrons are in quasi-equilibrium with the nucleus, however at higher energies, the scattering becomes more anisotropic, and the assumption loses validity. This is the reason why the out-scatter (Eq. 2.19) and in-scatter methods (Eq. 2.16) show the most significant discrepancies in the fast energy region. The work by Liu et al. [29] compares the two methods and confirm the differences for high neutron energies. For the analysis of light water reactors and in particular for high-leakage systems like CROCUS, the in-scatter method is preferred.

Alternative approaches to treat anisotropic scattering can be derived from the *in-scatter method*. In these methods, the current spectrum ($\mathbf{J}$) in Equation 2.16 can be approximated for example by the scalar flux (ϕ_0) or by the ratio of the scalar flux to the total cross-section (ϕ_0/Σ_t). A good review of methods for treating anisotropic scattering can be found the work by Yamamoto et al. [28].

2.3 Practical solution to full-core steady-state and kinetics problems

Monte Carlo transport methods have the ability to produce very accurate results, however, full three-dimensional Monte Carlo solutions demand excessive computational task, with the added inconvenience that time-dependent simulations are in an early stage of development [8, 9].

Three-dimensional heterogeneous full-core deterministic transport is also computationally impractical due to the large number of unknowns (up to 10^{13}) that result from the discretization of the transport equation. An alternative method to reduce the computer requirements is that one followed by codes such as DeCART [30], nTRACER [31] and MPACT code[2] [33] where the transport equations are solved only in the radial plane and diffusion theory (or simplified transport) solutions are used to provide axial coupling. Unfortunately, full-core solutions using this approach remain computationally expensive.

What is done instead for a more practical approach is to reduce the spatial resolution of the problem and to simplify the energy dependence by solving the equations for few-energy groups. The spatial detail is reduced by partitioning the core into unit cells that are spatially homogeneous. The basic idea behind this simplification is to replace the heterogeneous components of the reactor (such fuel pins or fuel assemblies) with homogeneous ones. This process is referred to as *homogenization and group condensation*.

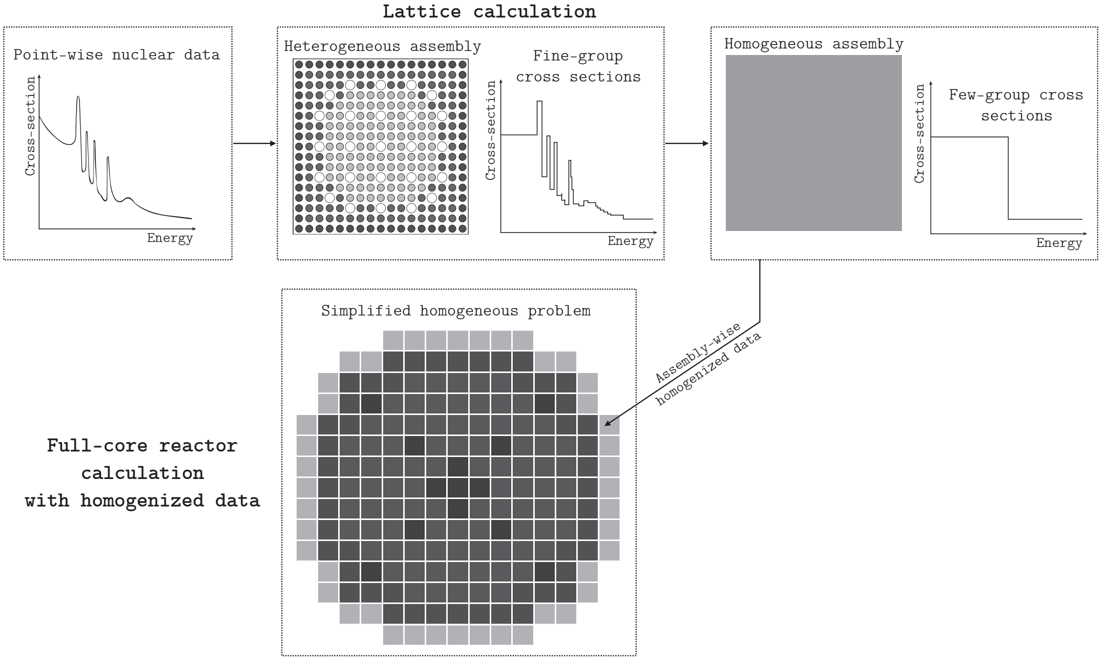
Lattice calculation
Point-wise nuclear data
Cross-section
Energy
Heterogeneous assembly
Fine-group cross sections
Cross-section
Energy
Homogeneous assembly
Few-group cross sections
Cross-section
Energy
Assembly-wise homogenized data
Simplified homogeneous problem
Full-core reactor calculation with homogenized data

Figure 2.1 – Multi-step computational scheme for full-core analysis

The general procedure for solving the full-core problem is then based on various stages of calculations interconnected together. This is shown schematically in Figure 2.1 where the starting point is the generation of spatially-homogenized few-group cross-sections for each reactor sub-unit. This first step is known as a *lattice calculation*. These homogenized few-group cross-sections are later used in the second calculation step that typically consists of using diffusion or simplified transport methods for solving the homogenized (simplified) full-core problem.

---

[2] The MPACT code also provides 3-D full-core heterogeneous transport solutions, however they demand prohibitive computer power [32]

The sections below will discuss first some details about *homogenization and group condensation* theory and secondly some practical methods for dealing with *full-core steady-state and time-dependent solutions*. The computer codes and methods that were chosen in this thesis for both purposes are also briefly introduced.

2.3.1 Spatial homogenization and group condensation

The *lattice calculation* is the first stage of the calculation scheme and involves the solution of the steady-state transport problem over a pin-cell or a fuel assembly. At the start of this procedure, continuous-energy microscopic cross-sections are pre-processed to produce multigroup cross-sections in hundreds of energy groups. In the case of employing a Monte Carlo code for the lattice calculation, continuous-energy cross-section data can be used directly during the transport calculation. Once the fine-group cross-section library is generated, the materials in each pin-cell (or fuel assembly) of the reactor are homogenized and cross-sections are further collapsed into few-energy groups (typically to two groups for light water reactors). The result of the lattice calculation are few-group spatially-homogenized data (such as macroscopic cross-sections) that are used in the following step of the calculation scheme: the full-core calculation. There is no unique process for spatial homogenization since it is possible to preserve different quantities[3]. There has been extensive debate about the proper manner in which homogenization should be done [34].

Because the homogenization process involves replacing heterogeneous components with homogeneous ones, correction factors need to be introduced in order to nearly reproduce the heterogeneous solution. The generalized equivalence theory (GET) [35] and the superhomogenization (SPH) equivalence technique [36] are the most common approaches.

The generalized equivalence theory (GET) [35] was introduced as a homogenization technique applied to nodal methods[4]. The GET method uses the traditional *flux-volume weighting* to obtain the homogeneous cross-sections, which can be computed as:

$$\Sigma_g^{\text{hom}} = \frac{\displaystyle\int_{E_g}^{E_{g-1}} \int_V \Sigma(\mathbf{r}, E)\phi^{\text{het}}(\mathbf{r}, E)dV dE}{\displaystyle\int_{E_g}^{E_{g-1}} \int_V \phi^{\text{het}}(\mathbf{r}, E)dV dE} \tag{2.20}$$

---

[3] The most relevant quantities that need to be preserved are the surface group-wise neutron currents, the average group-wise reaction rates and the multiplication factor [17]

[4] Modern nodal methods are described in page 9

where ϕ^{het} is the scalar flux in the heterogeneous system. The integration is carried out over the homogenized volume V and energy group g.

Interface flux discontinuity factors (f_g^S) are then defined as follows to preserve leakage rates

$$f_g^S = \frac{\displaystyle\int_{E_g}^{E_{g-1}} \int_S \phi^{\text{het}}(\mathbf{r}, E) dS dE}{\displaystyle\int_S \phi_g^{\text{hom}}(\mathbf{r}) dS} \tag{2.21}$$

where ϕ_g^{hom} is the group-g homogeneous flux. The integration is carried out over the interface surface S of the homogenized volume.

Since these interface discontinuity factors are defined for each surface, several of them are assigned to each homogeneous node. Therefore, each factor carries information about orientation. Finally, the formulation of interface currents can be obtained in different manners depending on the method used for the full-core calculation (for example finite-difference diffusion).

Fine-mesh (pin-by-pin) solutions require a different homogenization approach. The super-homogenization (SPH) technique [36] is well suited since it is based on the conservation of pin-by-pin average reaction rates. The main idea behind the SPH method is to preserve the reaction rates of the heterogeneous problem by using factors that adjust the homogenized cross-sections.

Homogeneous cross-sections (Σ_g^{hom}) can be calculated using traditional flux-volume weighting (Eq. 2.20). However, if the boundary conditions in the homogenized system are different from those in the heterogeneous system, reaction rates are not preserved. Therefore, SPH factors (μ_g) are introduced to correct the homogenized cross-sections

$$\mu_g = \frac{\displaystyle\int_{E_g}^{E_{g-1}} \int_V \phi^{\text{het}}(\mathbf{r}, E) dV dE}{\displaystyle\int_V \phi_g^{\text{hom}}(\mathbf{r}) dV} \tag{2.22}$$

Then, the SPH correction is applied as

$$\Sigma_g^{\text{hom-SPH}} = \mu_g \cdot \Sigma_g^{\text{hom}} \tag{2.23}$$

Since the neutron flux in the homogenized system (ϕ_g^{hom}) depends on the SPH-corrected homogenized cross-sections ($\Sigma_g^{\text{hom-SPH}}$), the SPH factor set ($\mu_{g,i}$) needs to be obtained through iterative calculations.

Spatial homogenization and group condensation has traditionally been done with deterministic transport codes such as CASMO [6] and HELIOS [37]. Any of the transport methods discussed in Section 2.2 can be used for the lattice calculation stage. Even Monte Carlo techniques can be now used for the generation of homogenized data. In the past decade there has been considerable progress precisely on using Monte Carlo techniques for spatial homogenization and group condensation purposes [26, 38]. Monte Carlo offers several advantages over traditional deterministic methods; some of which are described in the comparison between deterministic and Monte Carlo methods (see p. 13). In the particular case of the CROCUS reactor, Monte Carlo lattice calculations are of great advantage due to the complicated assembly design and the impossibility to subdivide the core into repeatable units (such as fuel assemblies). The Serpent code [39] is a good example of a Monte Carlo code that can produce homogenized data for the full-core calculation. It has been chosen primarily for the generation of few-group constants and kinetic data for the CROCUS reactor, and secondly to provide full-core steady-state reference solutions for some numerical benchmarks. Section 2.3.3 provides a brief description of the code.

A review of lattice calculation techniques and homogenization theory has been published by Knott and Yamamoto [40].

2.3.2 Full-core calculations: steady-state and neutron kinetics

The last stage in the multi-step computational approach is the full-core calculation. At this level, continuous-energy microscopic cross-sections have already been reduced to few-group macroscopic cross-sections that are problem-dependent. Because spatial homogenization was performed during the lattice calculation stage, full-core spatial detail is reduced to homogeneous unit blocks. If the full-core solutions are provided by finite difference schemes (i.e., spatial discretization with low order polynomials), these unit blocks are typically represented by pin-cells. The use of coarse-mesh and nodal methods (i.e., discretization with higher order polynomials) allow the choice of much coarser unit blocks such as fuel assemblies. Figure 2.2 illustrates the differences between typical fine-mesh and coarse-mesh full core computational schemes.

Although not strictly limited to diffusion-like methods, diffusion theory or simplified transport methods such as SP$_3$ [41] are the simplest approaches to solve the full-core level problem. The problem is solved typically for few-energy groups and is represented, for example, by the multi-group form of the time-dependent diffusion equations

$$\frac{1}{v_g}\frac{\partial \phi_g}{\partial t}(\mathbf{r},t) = \nabla \cdot D_g(\mathbf{r},t)\nabla\phi_g(\mathbf{r},t) - \Sigma_{rg}(\mathbf{r},t)\phi_g(\mathbf{r},t) + q_g(\mathbf{r},t) \qquad g = 1, ..., G. \quad (2.24)$$

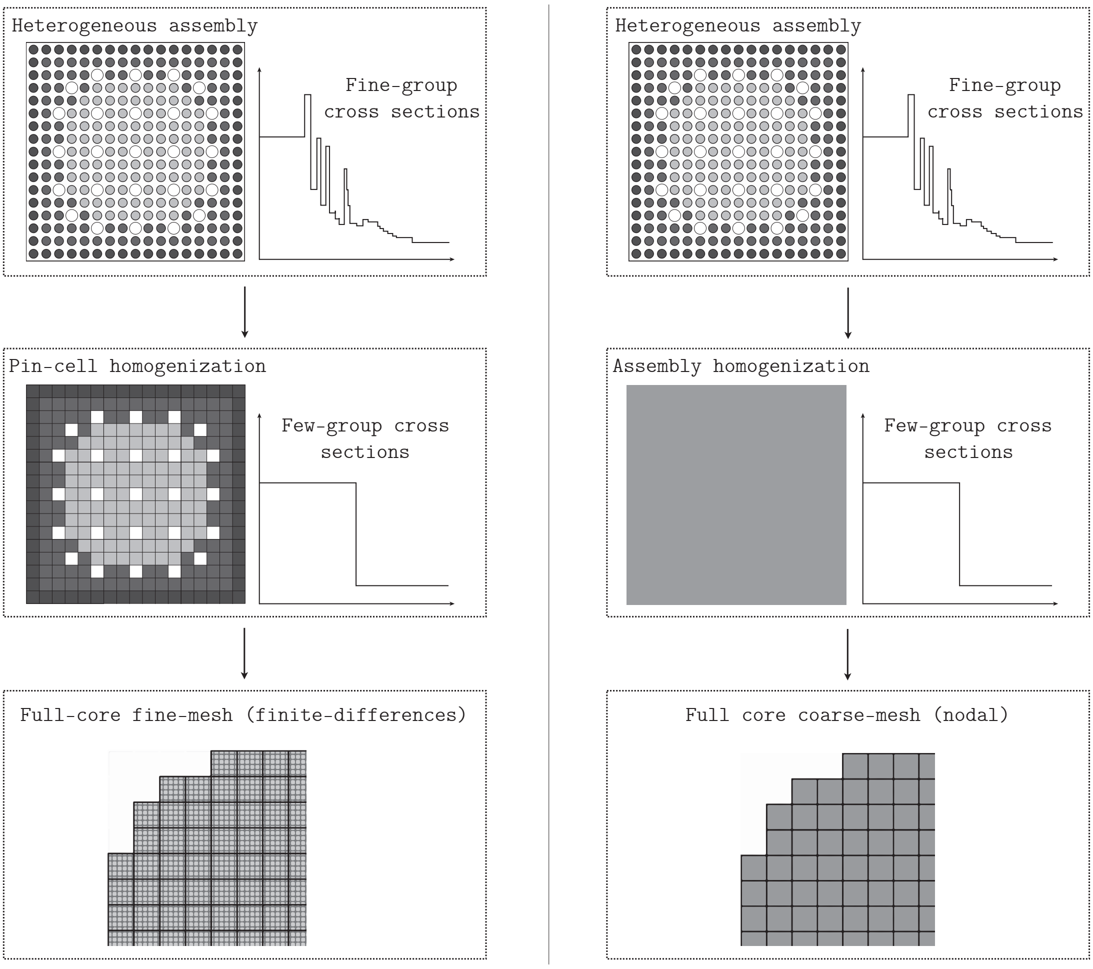
Heterogeneous assembly
Fine-group cross sections
Pin-cell homogenization
Few-group cross sections
Full-core fine-mesh (finite-differences)
Heterogeneous assembly
Fine-group cross sections
Assembly homogenization
Few-group cross sections
Full core coarse-mesh (nodal)

Figure 2.2 – Simplified computation scheme for fine-mesh and coarse-mesh full-core calculations

where g is the energy group index, $\Sigma_{rg} \equiv \Sigma_{tg} - \Sigma_{sgg}$ is the *removal cross-section* defined as the difference between the total cross-section and the in-group scattering cross-section. q_g is the group-g source representing the scattering transfer matrix, prompt fission source and delayed neutron source.

The spatial discretization methods mentioned above allow transforming the multi-group diffusion (or simplified transport) equations into a matrix system that can be solved by standard numerical analysis techniques. These techniques are well described in the textbook by Hébert [18].

The methods that allow the calculation of steady-state parameters can also be extended to calculate the time evolution of neutron flux distribution [17]. This can be achieved by adding the time derivative and delayed neutron precursor source terms to the steady-state diffusion (or transport) equations and coupling them to the delayed neutron precursor equations (Eq. 2.2, p. 6). This whole set of equations are known as *space-time kinetics* *equations*.

There are several approaches to solve the time-dependent problem [20]. The most relevant with respect to the subject of this thesis are *point-reactor kinetics approximation*, *space-time factorization methods* and *direct space-time kinetics methods*.

Point-reactor kinetics approximation

In the fifties, the lack of reliable numerical methods and limited computer power encouraged the development of computer-efficient methods to solve the time-dependent transport problem. The point-reactor kinetics approximation is one of the earliest methods [42] based on the factorization of the neutron flux into the product of two functions

$$\phi(\mathbf{r}, E, \mathbf{\Omega}, t) = \Psi_0(\mathbf{r}, E, \mathbf{\Omega}) \cdot p(t) \tag{2.25}$$

where $\Psi_0(\mathbf{r}, E, \mathbf{\Omega})$ is the position- energy- and angle-dependent *shape function* calculated at $t = 0$, and $p(t)$ the flux *amplitude function* that depends only on time.

The assumption that the neutron flux varies in amplitude without changing its spatial distribution implies that the reactor can be conceptually reduced to zero-dimensions in space, that is a point. Even though this assumption may not be valid for all reactor types and problems, the point-reactor kinetics approximation has had strong physical relevance and is still an important utility for nuclear engineering, in particular for tightly coupled systems.

The derivation of the point-reactor kinetics equations can be done in several different ways, however this is beyond the scope of this work. It can be found in classic textbooks such as Duderstadt and Hamilton [15] or Ott and Neuhold [43].

In the case of an initially critical reactor, the most traditional form of the *point-reactor kinetics equations* is given by

$$\dot{p}(t) = \frac{\rho(t) - \beta(t)}{\Lambda(t)} p(t) + \sum_{i}^{N} \lambda_i C_i(t) \tag{2.26}$$

$$\dot{C}_i(t) = \frac{1}{\Lambda(t)} \beta_i(t) p(t) - \lambda_i C_i(t), \qquad i = 1, 2, ..., N. \tag{2.27}$$

where $p(t)$ is the instantaneous power being generated in the reactor, $C_i(t)$ is the delayed neutron precursor population for the ith group, N the number of delayed neutron groups, λ_i the decay constant of ith group delayed neutron precursors, β_i the effective delayed neutron fraction for the ith group, $\beta(t) = \sum_i^N \beta_i(t)$ the total effective fraction, $\rho(t) = [k(t) - 1]/k(t)$ the reactivity, and $\Lambda(t)$ the mean neutron generation time.

Equations 2.26 and 2.27 are a set of N+1 coupled equations that describe the time-dependence of the neutron population (or power) in the reactor and the decay of the delayed neutron precursors respectively.

It is important to differentiate the physical from the effective delayed neutron fraction. The *physical delayed neutron fraction* is simply the fraction of neutrons emitted from the radioactive decay of certain precursors of the fission products. Because delayed neutrons appear with somewhat lower energies than do the prompt fission neutrons, in a thermal reactor they undergo a more favorable slow down process which results in a higher probability of inducing thermal fissions. To take account for this effect, the physical delayed neutron fraction can be corrected to produce the *effective delayed neutron fraction.* The calculation of effective delayed neutron fraction is typically performed employing the adjoint flux as a weighting function. This allows accounting for the spatial and energy-dependence of the emitted neutrons. This which is rigorously presented in the textbook by Ott and Neuhold [43]. The adjoint flux is typically referred to as neutron importance function which is subject of study in the field of perturbation theory [17]. Having stated the differences between the effective and physical delayed neutron data, it is important to bear in mind that the former ones should be used to account for the spatial and spectral effects.

The major limitation of the point-reactor kinetics model is in the assumption that the neutron flux shape is calculated at $t = 0$ and remains constant in time. This assumption is valid for transients where flux perturbations are uniform across the core or for tightly coupled small reactors, where the flux shape remains fairly invariant during a transient. For rapid transients where spatial effects are important, one needs to rely on spatial-kinetics treatment, which is governed by the coupled time-dependent diffusion (or simplified transport) and precursor concentration equations.

Space-time factorization kinetics

More sophisticated methods were developed in the late fifties to account for the deficiencies in the point-reactor kinetic approximation. Many of these methods are also based on the space-time factorization of the neutron flux. However it is important to note that, as compared to the point-reactor kinetic model, the shape function is allowed to vary in time

$$\phi(\mathbf{r}, E, \mathbf{\Omega}, t) = \Psi(\mathbf{r}, E, \mathbf{\Omega}, t) \cdot p(t) \tag{2.28}$$

where $\Psi(\mathbf{r}, E, \mathbf{\Omega}, t)$ is the position-, energy-, and time-dependent *shape function* and $p(t)$ the time-dependent *amplitude function.*

The incentive for using these techniques is that in many situations the shape function is only weakly dependent on time, and thus it can be computed or updated on a less frequent basis than the amplitude function. Because the shape function is considerably more computationally expensive to calculate than the amplitude function, space-time factorization methods can often produce results with less computer resources than direct methods (described next) with minimal accuracy losses.

The most elemental of these space-time factorization methods is the so-called *adiabatic approximation* [44]. In this method, the *time-dependent shape function* $\Psi(\mathbf{r}, E, \mathbf{\Omega}, t)$, determining the spatial distribution of the neutron flux, is computed from solutions of the static problem. The amplitude function $p(t)$ is found from the solution of the point-reactor kinetics approximation.

The adiabatic method is essentially an extension of the point-reactor kinetics model because the shape function is not only calculated at $t = 0$ but also updated at different times along the transient. Because the time-dependent changes are reflected in the spatial distribution of the flux, the adiabatic approximation is expected to produce significantly better results than the point-reactor kinetics approximation. However, one cause of inaccuracies in this approach is that delayed neutrons are not taken into account for the solution of the shape function. In other words, the neutron flux distribution is determined in absence of delayed neutrons. This approximation may become weak for large and weakly coupled cores undergoing fast perturbations, where the flux shape slowly approaches its perturbed static state. Stacey [17] referrers to this retardation in the establishment of the flux as delayed neutron holdback effect.

A series of similar but more elaborate approximations known as *quasi-static* and *improved quasi-static* approximations were later developed to account for the effect delayed neutrons on the flux shape. These methods are presented in detail in the textbook by Ott and Neuhold [43].

Direct space-time kinetics

The most straightforward techniques for solving the space-time kinetics equations are those referred to as direct space-time kinetics methods. These methods first discretize the time-dependent multigroup diffusion and associated precursor equations in space to form a coupled set of equations in time. The equations can then be solved using different time discretization schemes to finally obtain the space- and time-dependent behavior of the neutron flux.

The PARCS code [45, 46] is a good example of a three-dimensional neutron kinetics code that can solve the time-dependent problem using direct methods. It has been chosen for the 3-D steady-state and time-dependent modeling of the CROCUS reactor. Section 2.3.4 provides a brief description of the code.

2.3.3 The Serpent Code

Serpent [39] is a three-dimensional continuous-energy Monte-Carlo code that has been specifically designed for lattice physics applications. The Serpent code has been developed at VTT Technical Research Center of Finland and it is now being extended to a multitude of other applications including time-dependent and coupled multi-physics simulations [47]. It has been used in the present work primarily for the generation of few-group constants and kinetic data for the CROCUS reactor, and secondly to provide full-core steady-state reference solutions for some numerical benchmarks.

In general, cross-section homogenization are performed using a sub-region of the core such as a fuel assembly using periodic of reflective boundary conditions; which assumes that the sub-region can be decoupled from the other regions of the core. This configuration produces inaccuracies in spatial and energy dependence of the neutron flux, which are later translated as inaccuracies of homogenized parameters. This problem can be corrected by introducing artificial leakage into the system with leakage models such the B_1 fundamental mode [48]. The problem can be also solved, and in a more accurate manner, if the full-scale geometry is used to spatially homogenize the cross-sections and generate delayed neutron data for 3-D spatial kinetics solutions. In most cases, this is impractical due to the high computational cost that results from full-scale Monte Carlo transport calculations. Fortunately, the small size of the CROCUS reactor core and the absence of fuel burn-up effects reduce the computational cost and therefore make full-core Monte Carlo calculations feasible.

The Serpent code uses a universe-based geometry model for describing structures. Universes also define the regions where spatial homogenization and energy collapsing take place. By using the full-core Serpent model of the reactor, the exact neutron flux spectrum is used for the flux-volume weighting of cross-section and there is no need to rely on leakage models. The whole few-group constants data is produced in multiple universes within a single run.

The Serpent code approach for spatial homogenization and energy condensation to few-energy groups is handled in two steps [49]

(1) In the first place, fine-group homogenized cross-sections (Σ_h^{hom}) and fluxes (ϕ_h^{hom}) are calculated using the standard flux-volume weighting

$$\Sigma_h^{\mathrm{hom}} = \frac{\displaystyle\int_{E_h}^{E_{h-1}} \int_V \Sigma(\mathbf{r},E)\phi^{\mathrm{het}}(\mathbf{r},E)dVdE}{\displaystyle\int_{E_h}^{E_{h-1}} \int_V \phi^{\mathrm{het}}(\mathbf{r},E)dVdE} \tag{2.29}$$

$$\phi_h^{\text{hom}} = \int_{E_h}^{E_{h-1}} \int_V \phi^{\text{het}}(\mathbf{r}, E) dV dE \tag{2.30}$$

where h is the index for the fine-group structure. The integrals in Equations 2.29 and 2.30 are obtained using standard Monte Carlo tallies.

(2) Secondly, the fine-group cross-sections are flux-weighted to be condensed into a coarser energy group structure

$$\Sigma_g^{\text{hom}} = \frac{\sum\limits_{h \in g} \Sigma_h^{\text{hom}} \phi_h^{\text{hom}}}{\sum\limits_{h \in g} \phi_h^{\text{hom}}} \tag{2.31}$$

As earlier mentioned, if the spatial homogenization is carried out over a sub-assembly with reflective boundary conditions, leakages models can be used to account for the non-physical infinite-lattice approximation and to condense cross-sections with a corrected spectra.

Equations 2.29 to 2.31 can be used as the standard approach to derive the total, absorption fission cross-section and inverse neutron velocities. On the other hand, group transfer scattering matrices are generated using an analog estimator [49]. The generation of delayed neutron data represents an area where a great deal of effort needs to be made [50] and is later discussed. However, as Leppänen et al. [26] stated in his work, the real challenge of Monte Carlo few-group constant generation is in the calculation of transport cross-sections (or diffusion coefficients).

Diffusion coefficients

Serpent uses two approaches to estimate diffusion coefficients from flux-weighted homogenized parameters. The first one is based on calculating transport cross-section deriving from the P_1 equations as described in Section 2.2.4. The rigorous definition of the P_1 transport cross-section requires the evaluation of current integrals to weight the P_1 scattering cross-sections. However, this is difficult to achieve in Monte Carlo simulations [49] and therefore, the Serpent code needs to rely on the out-scatter approximation to compute transport-corrected-P_0 transport cross-section. In that case, the diffusion coefficients are given by

$$D_g(\mathbf{r}) = \frac{1}{3\left[\Sigma_{t,g}(\mathbf{r}) - \overline{\mu}_0 \Sigma_{s0,g}(\mathbf{r})\right]} \tag{2.32}$$

where $\overline{\mu}_0$ is the average cosine scattering angle and $\Sigma_{s0,g}$ the zeroth moment (P_0) group scattering cross-section. The cosine scattering angle is obtained from the direction vectors of the incident and emitted neutron in the scattering event and $\Sigma_{s0,g}$ from the group transfer scattering matrix.

The second approach used by the Serpent code to estimate diffusion coefficients is related to the solution of the B_1 leakage model. Because cross-sections have been homogenized using the full-core geometry, the use of leakage models are irrelevant to this work, and will not be discussed here. More details concerning Serpent's methods for spatial homogenization and group condensation can be found in a publication by Leppänen et al. [49].

Delayed neutron data

The importance of using adjoint-weighted delayed neutron data has been already stated in Section 2.3.2, hence the generation of physical kinetic parameters is not discussed here.

The deterministic approach for producing adjoint-weighted parameters requires the explicit solution for the adjoint flux which is a difficult task for continuous-energy Monte Carlo codes. For this reason, there exist different methods developed for Monte Carlo codes to calculate importance-weighted kinetic parameters without the need for an explicit solution of the adjoint flux. Each of the techniques yields a slightly different result as shown in the paper by Leppänen et al. [50].

One of the methods implemented in Serpent that accounts for delayed neutron importance has been initially proposed by Meulekamp and van der Marck [51]. The method consists in approximating the β_{eff} as the ratio of the average number of fissions generated by delayed neutrons to the average number of fissions generated by all neutrons.

Recently, the Serpent code has implemented a more accurate approach based on the iterated fission probability (IFP) method [52]. Specifics about the IFP method exceeds the scope of this work, however, the theory and implementation in Serpent can be found in the publication by Leppänen et al. [50]. The current limitation of the iterated fission probability method is that it produces core-averaged kinetic parameters instead of a set of parameters for each homogenized region.

Other methods for calculating kinetic parameters are available in Serpent, however, the iterated fission probability produces the best results [50], and for this reason, it was chosen for the kinetic modeling of the CROCUS reactor.

2.3.4 The PARCS code

One of the main objectives of the present work is to employ advanced diffusion codes that have been adopted by industry for the modeling of non-conventional research core reactors like CROCUS. PARCS [45, 46] is a multi-dimensional diffusion kinetics code developed by the U.S. Nuclear Regulatory Commission (NRC) for the full-core analysis of commercial power reactors. It represents, as of today, the state-of-the-art for diffusion calculations in thermal reactors.

PARCS has been extensively used for the analysis of commercial light water reactors (LWR), and it is precisely for this application where verification and validation efforts have been made [53, 54, 55]. The extension of the PARCS code to the analysis of small high-leakage systems like CROCUS is interesting not only for research reactors but also for small modular reactors (SMR) applications. However, PARCS performance for these kind of reactors has not been exhaustively examined yet. For the reason stated above, the PARCS code has been selected for the 3-D steady-state and time-dependent modeling of the CROCUS reactor.

Early versions of PARCS were limited to a two-group nodal diffusion scheme. Later developments implemented other solution kernels such as time-dependent multi-group diffusion and simplified P_3 solvers [46]. The PARCS code is essentially a nodal code, however, it also provides the ability to solve the neutron diffusion equation using the classical finite difference method (FDM), which is more suitable for finer mesh structures such as the one in the CROCUS reactor. The PARCS code can be coupled to an external thermal-hydraulics code for calculations with cross sections feedback, however, as earlier stated, this is not necessary for the CROCUS reactor due to the low power that limits the thermal feedback effects.

Spatial treatment

To solve the three-dimensional multigroup diffusion equations, PARCS employs a transverse integration procedure (described in Section 2.2.1) where the thee-dimensional equations are converted into three one-dimensional equations coupled through a transverse leakage terms. The resulting set of 1-D equations can be solved using various high order methods such as the analytic nodal method (ANM), the nodal expansion method (NEM) or a hybrid combination of both.

PARCS nodal solutions are implemented within the framework of the nonlinear coarse mesh finite difference (CMFD) iterative solution scheme introduced by Smith [56]. In the CMFD method, a coarse level finite difference discretization scheme is used to solve the diffusion problem. The coarse mesh solution is updated by a high order nodal method after a given number of iterations to improve the CMFD accuracy. The CMFD is essentially an acceleration scheme designed to minimize memory requirement and computing time associated with the higher-order nodal methods above mentioned.

In addition to nodal methods, PARCS implements the classical fine-mesh finite difference (FMFD) scheme for the spatial discretization of the three-dimensional diffusion problem. The coarse mesh finite difference (CMFD) or coarse mesh rebalancing (CMR) strategies can be used to accelerate global FMFD solution. The FMFD solver is designed for three-dimensional pin-by-pin diffusion calculations where the explicit representation of pin cells is required.

Time-dependent solutions

To solve the time-dependent equations, the PARCS code first initializes the transient by solving the steady-state core condition. Even though this can be accomplished by solving a steady-state fixed source problem, most time-dependent analyses are based on an initial condition achieved by an eigenvalue calculation because the external source is meaningful only for low power physics test conditions. The eigenvalue is determined during the initial steady-state calculation and remains constant during the transient calculation.

The PARCS code treats the temporal dependence in a manner that results in a fixed source problem, which is formulated by employing the analytic precursor integration, the theta method temporal differencing, and the CMFD spatial differencing. Once the problem is initialized by the eigenvalue calculation, the transient calculation begins by constructing the transient fixed source and solving it at the first time point, which is then repeated at each subsequent time step.

Although PARCS is essentially a diffusion code with multi-group capabilities, it also provides simplified P_3 (SP_3 transport solutions implemented in the FMFD kernel. Time-dependent SP_3 solutions are therefore also available in PARCS for situations where transport effects are significant and diffusion theory loses validity.

The following PARCS solvers have been used the present work. The CMFD-only (i.e., CMFD with no nodal update) kernel was used to provide two-group diffusion solutions and the FMFD kernel was used to provide multigroup diffusion and multigroup SP_3 solutions. The reason for using the CMFD-only kernel instead of the FMFD kernel for two-group diffusion solutions is that the later does not allow to use detectors and albedo boundary conditions which are needed for the CROCUS modeling. In addition, the nodal update option was not required as the spatial mesh size is in the order of the smallest group-wise diffusion length, which allows achieving numerical and spatial convergence for the CROCUS solution.

3 The CROCUS zero-power reactor

The present work has been based on the CROCUS zero-power reactor [1] for carrying out a variety of reactor physics experiments for the validation of computational models. This chapter provides detailed information about the CROCUS facility, which is required, on one side as a basis for the description of the experimental activities, and on the other side for the description of the computational studies. The experimental and computational analyses of the CROCUS reactor are presented in Chapters 4 and 5, respectively.

CROCUS is a light-water-moderated nuclear reactor located at the EPFL Lausanne campus in Switzerland. It is operated by the Laboratory for Reactor Physics and Systems Behaviour (LRS) of the Swiss Federal Institute of Technology Lausanne (EPFL). The reactor power is limited to a maximum of 100 W, producing practically no heat which allows it to be classified as a *zero-power reactor*. The magnitude of the neutron flux reaches approximately 2.5×10^7 neutrons/cm^2/s at the center of the core for a reactor power of 1 W.

The CROCUS reactor core presents a nearly cylindrical shape with a diameter of approximately 58 cm and a height of 100 cm. The distinct feature of the reactor is its core composed by two radial fuel zones which are arranged in two different square lattices as illustrated in Figure 3.1.

The core reactivity is controlled by a variation of the water level with an accuracy of ±0.1 mm (equivalent to ±0.4 pcm) or by means of two control rods containing natural boron carbide (B_4C) sintered pellets located symmetrically within the outer fuel region as shown in Figure 3.1b.

Light water (H_2O) is used as neutron moderator. The outer fuel zone is surrounded by light water up to a diameter of 130 cm, which serves as neutron reflector. The core and reflector are contained within an aluminum water tank with a thickness of 1.2 cm and diameter of 132.4 cm. The water temperature is adjusted and kept at approximately 20 °C by a hydraulic circuit system.

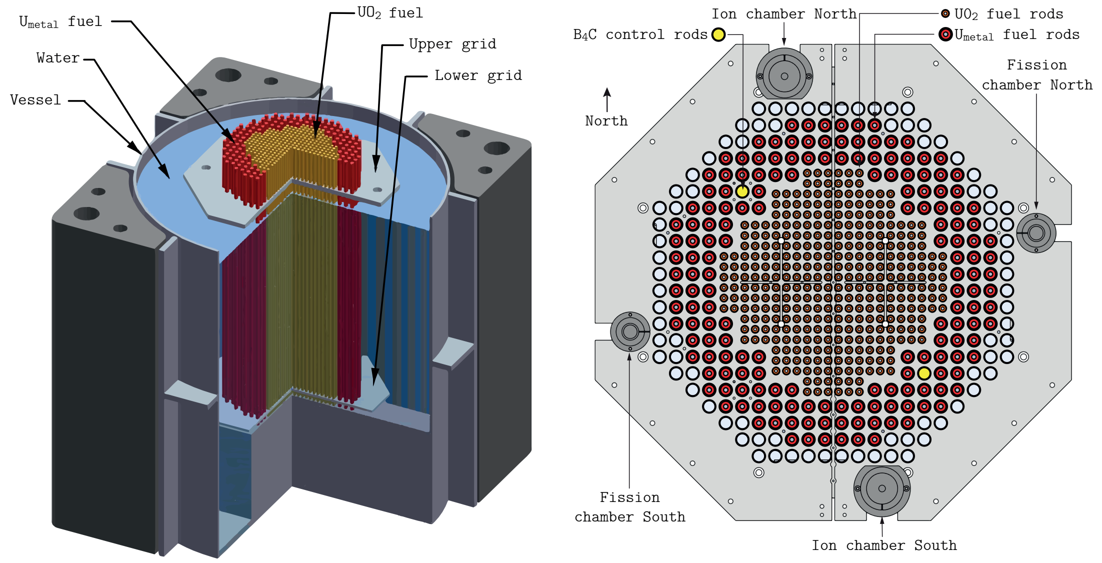

(a) Core structure and internals: isometric view (b) Upper grid and fuel lattices: top view

Figure 3.1 – Overview of the CROCUS reactor

There are two grid plates (as shown in Figure 3.1a) that are used to arrange the fuel in the different lattice structures and to keep them in a vertical position. The upper grid plate is fixed to a solid stainless steel structure to prevent the radial displacement of the upper core region. This metallic structure is not shown in the figures and not included in the description either because it is located far enough from the reactor core and thus has negligible influence on the reactor's reactivity . Figure 3.1a shows an overview of the main reactor structure and components.

The essential nuclear instrumentation is composed by four detection channels (see Fig. 3.1): two pulse channels (fission chambers) and two current channels (ionization chambers) which are used for safety and core monitoring purposes, repetitively. The four detectors are located in the core periphery and are kept in place through supports attached to the upper grid plate.

The reactor possesses six independent shut down mechanisms allowing it to be brought to a sub-critical state in less than one second. There are two cruciform shaped cadmium (Cd) blades at the core center and four safety tanks operated by a valve system that allow to decrease the moderator level.

A biological shield is placed around the reactor to protect operating personal from the radiation released during the reactor's operation. This concrete enclosure has a ground area of 6.5 m x 7 m and is 6.1 m high. The thickness of the walls is 130 cm. A lateral door with the same thickness, weighting 14 tons, allows the access inside the cavity for the operating personal. At the top, a 50 tons movable cover can leave an aperture of 2 m by 3 m over the core to handle the core using a polar crane.

Because of the low power of the CROCUS reactor, the behavior of the neutron population inside the core is virtually not influenced by thermal effects. An additional advantage of the low neutron flux levels is that fuel burn-up effects can also be neglected. Given that the neutronics phenomena can be addressed in an isolated manner (without thermal feedback and fuel burn-up effects), zero-power reactors like CROCUS provide an optimal and powerful mean to validate stand-alone neutronics codes.

3.1 Fuel description

As mentioned earlier, the CROCUS reactor core presents two different kinds of fuel rods. The central core region is fueled with 336 UO_2 fuel rods (1.806 wt.%-enriched) that are arranged in a square lattice with a pitch of 1.837 cm. The peripheral region is loaded with 176 U-metal fuel rods (0.947 wt.%-enriched) with a pitch of 2.917 cm. The U-metal fuel rods have a larger diameter than the UO_2 ones. A two-fold rotational symmetry is achieve with this fuel arrangements. Although several other arrangements are possible in the CROCUS reactor, the one previously described is the only one used for the present work.

The UO_2 and U-metal fuel rods use an aluminum cladding to contain the fuel pellets. The cladding is kept in vertical position by means of the upper grid and lower grid plates, which are spaced 100 cm apart. Helium is used to fill the gap between the fuel pellets and

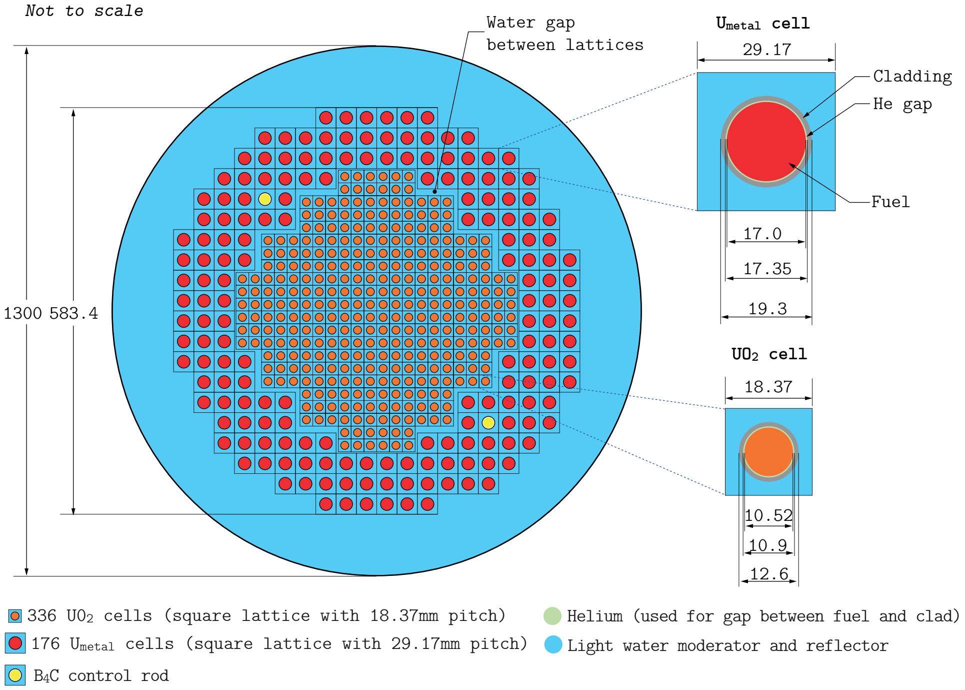
Not to scale
Water gap
between lattices
1300
583.4
U_{metal} cell
29.17
Cladding
He gap
Fuel
17.0
17.35
19.3
UO_2 cell
18.37
10.52
10.9
12.6
336 UO_2 cells (square lattice with 18.37mm pitch)
176 U_{metal} cells (square lattice with 29.17mm pitch)
B_4C control rod
Helium (used for gap between fuel and clad)
Light water moderator and reflector

Figure 3.2 – Radial arrangement of the CROCUS components. Dimensions in mm.

aluminum cladding. Springs at the top of the fuel rod are used to keep the fuel pellets together (see Fig. 3.3).

Both grid plates contain a 0.50 mm thick cadmium layer that are used to limit the thermal flux in the axial direction. The active part of the fuel has a length of 100 cm and begins at the top surface of the lower cadmium layer. All fuel rods sit on an aluminum base plate, which is fixed to a core support structure. The lower grid is screwed to the base plate using spacers of 2.15 cm (see Figure 3.3).

The radial and axial arrangement of the fuel rods are shown in Figure 3.2 and 3.3 respectively. Figure 3.4 shows the dimensions for the base and grid plates. Tables 3.1 and 3.2 provide specific information about the fuel rods and structural components of the reactor core.

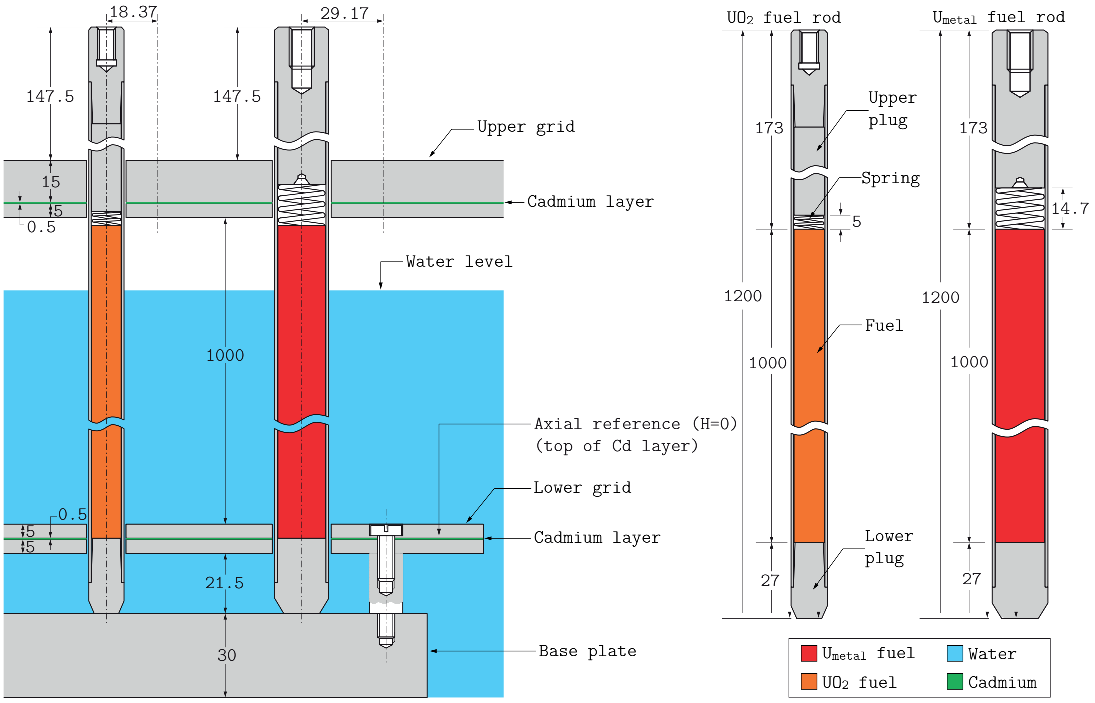
18.37
29.17
147.5
147.5
Upper grid
15
5
0.5
Cadmium layer
Water level
1000
Axial reference (H=0)
(top of Cd layer)
Lower grid
0.5
5
5
Cadmium layer
21.5
30
Base plate
UO2 fuel rod
Umetal fuel rod
173
173
Upper plug
Spring
5
14.7
1200
1200
Fuel
1000
1000
Lower plug
27
27
🟥 Umetal fuel
🟦 Water
🟧 UO2 fuel
🟩 Cadmium

Not to scale - Only relevant dimensions are shown

Figure 3.3 – Axial arrangement of the CROCUS components. Dimensions in mm.

Table 3.1 – CROCUS reactor fuel rod information

	UO_2	$U_{\textbf{metal}}$
Fuel diameter [mm]	10.52	17.00
Internal cladding diameter [mm]	10.90	17.35
External cladding diameter [mm]	12.60	19.35
Fuel lattice pitch [mm]	18.37	29.17
^{235}U enrichment [wt. %]	1.806	0.947
Fuel density [g/cm^3]	10.556	18.677

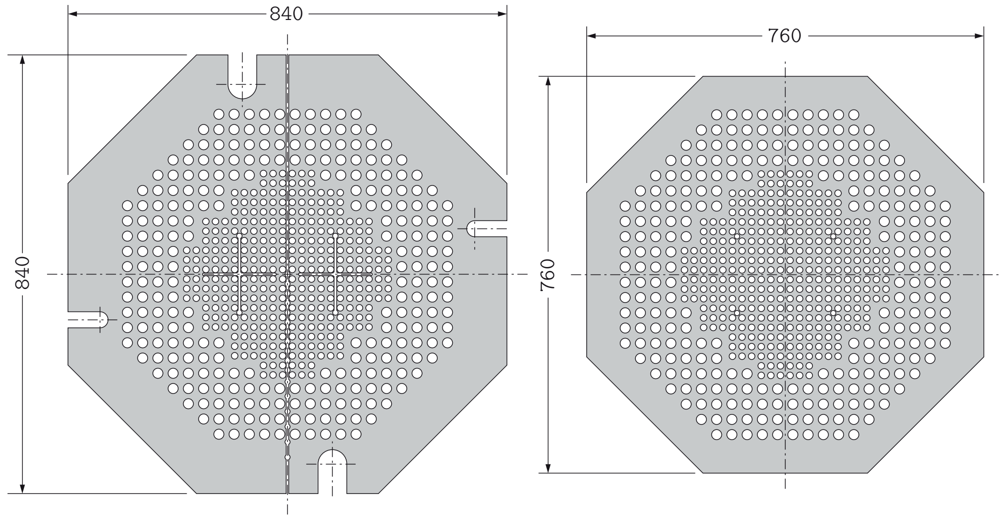

Upper grid plate

Lower grid plate

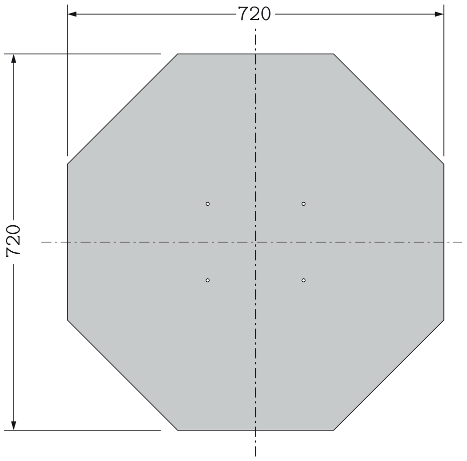

Base plate

Figure 3.4 – Top view of CROCUS grids and base plates. Dimensions in mm.

Table 3.2 – Materials data for structural components in the CROCUS reactor

Component	Material	Density [g/cm^3]
Base plate and grid plates Fuel cladding Fuel rod plugs	Aluminum	2.70
Cadmium layers	Cadmium	8.65
Springs	Fe - Cr - Ni - Mn 70.35 - 19.15 - 8.50 - 2.00 (%)	7.82
Moderator	Light water	9.98×10^{-1}
Fuel rod filler gas	Helium	1.64×10^{-4}
Material above water level	Air	1.20×10^{-3}

3.2 Control rods description

Two B_4C control rods can be used in the CROCUS reactor to be able to adjust the reactor power without having to vary the moderator level. The reactor is typically operated with both control rods withdrawn, in which case the critical moderator level is approximately 952 mm. Alternatively, critical state can be reached with a maximum moderator level of 1000 mm. In such a case, the control rods need to be partially inserted to compensate for the reactivity excess. The reactivity worth of each control rod is about 175 pcm (or 0.23 $).

An automatized system allows to move the control rods with a precision below 1 mm at different speeds. The rods can be inserted or withdrawn from the core in less than one second. The drop speed of the control rod is essentially limited by gravity.

Each control rod consists of a pile of natural B_4C pellets contained within a thin stainless steel tube (0.46 mm thick) as illustrated in Figure 3.5. This thin inner tube is protected by an outer 2 mm thick stainless steel tube that holds the entire control rod. The control rod is suspended from a cable and is inserted into the aluminum guide tubes that are identical to the cladding used for the U-metal fuel rods. Two Teflon rings surround the outer (thick) stainless steel tube on the top and bottom to allow a smooth gliding between surfaces and to avoid horizontal oscillations. Table 3.3 provides detailed information about the control rods. The geometrical and material information for the guide tube are the same than for the U-metal rods.

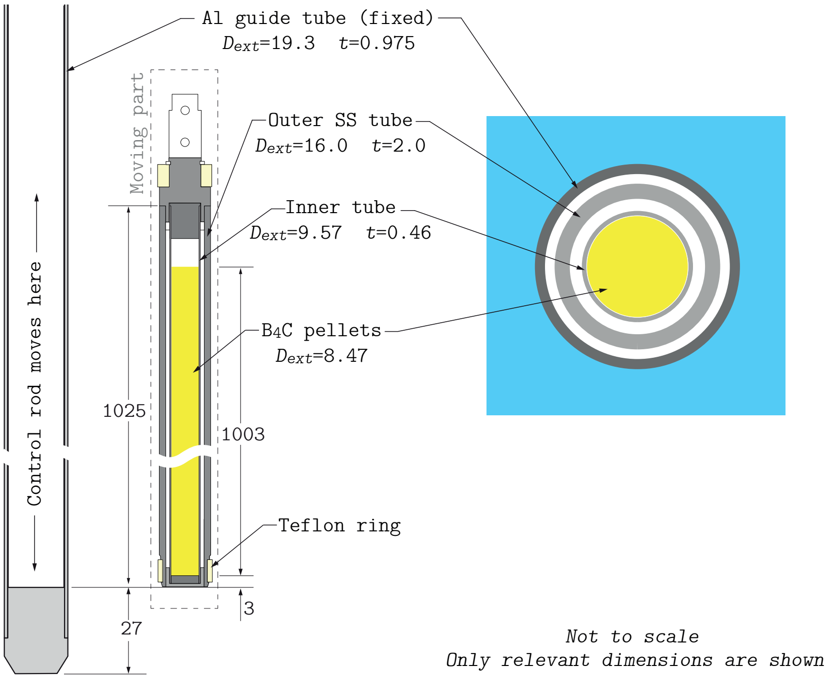

Not to scale
Only relevant dimensions are shown

Figure 3.5 – CROCUS B_4C control rods. Dimensions in mm.

Table 3.3 – B_4C control rods data. Guide tube not included

	B_4C pellets	Inner tube	Outer tube
Material	^{10}B(19.9%) ^{11}B (80.1%) ^{12}C (98.9%)^{13}C (1.1%)	SS[†] 316	SS 316
External diameter [mm]	8.47	9.57	16
Thickness [mm]	-	0.46	2.00
Height [mm]	1003[‡]	1024	1025
Density [g/cm^3]	1.79	8.10	8.1

[†] Stainless steel, [‡] stack of pellets

3.3 Nuclear instrumentation

Out-of-core detectors

As mentioned earlier, the reactor possesses four main out-of-core neutron detection channels. Two Photonis CFUM21 fission chambers are used in pulse mode primarily for safety purposes but also for core monitoring. These detectors are double deposit ^{235}U fission chambers with a sensitivity of 0.01 cps/nv[1].

The second series of detectors consists of two Merlin Gerin CC54 ^{10}B-coated compensated ionization chambers that are used in current mode for core monitoring. While the main purpose of the ^{10}B-coated electrodes is to detect neutrons, they also interact with the field of gamma radiation. To compensate for this effect, a second electrode insensitive to neutrons is used to detect the gamma photons and to remove the gamma-generated currents from the main signal. These ionization chambers have a sensitivity of 3×10^{-5} nA/nv. Table 3.4 provides detailed data for these four out-of-core detectors.

Table 3.4 – Data for CROCUS nuclear instrumentation

	Ionization chambers	Fission chambers
Active deposit	^{10}B (92 wt. % enriched)	^{235}U (> 90 wt. % enriched)
Surface density [mg/cm^2]	1	0.07
Sensitive length [mm]	355	120
Sensitive surface [cm^2]	769	N/A
Inner electrode ϕ_{ext} [mm]	25	N/A
Outer electrode ϕ_{ext} [mm]	36	25.4
Coordinates* (x, y, h) [cm]	-8.60, 36.35, 47.65 (IC-1) 8.60, -36.35, 47.65 (IC-2)	35.80, 8.70, 9.9 (FC-1) -35.80, -8.70, 9.9 (FC-2)

*Coordinates for center of sensitive part, ϕ_{ext}: external diameter

---

[1] nv = neutron flux measured in neutrons/cm^2/sec.

In-core detectors

In addition to the four detectors earlier mentioned, an in-core miniature fission chamber (Photonis CFUF34) is used for local flux measurements. The fission chamber is allowed to move axially and radially within the active core and reflector regions. The sensitive part of the detector has a diameter of $\phi = 4.7 \pm 0.5$ mm, a sensitive length of 27 mm and is loaded with approximately 1 mg of ^{235}U ($\sim$ 100 wt%-enriched). The chamber is filled with a mixture of Argon (96 %) and Nitrogen (4 %) at a pressure of 1500 kPa. The detector is used in pulse mode, where the sensitivity to thermal neutrons is of 0.001 cps/nv. The detector is mounted at the end of a vertical shaft, which is suspended from rails running parallel to the central slit in the upper grid plate (see Fig. 3.6).

A computerized system, known as TRAX (french acronym for Translateur Radial AXial), controls the radial and axial movement of the miniature fission chamber with a precision of 1 mm. In the axial direction, the chamber can move from top to bottom, and in the radial direction, the displacement is limited to the central slit as shown in Figure 3.6.

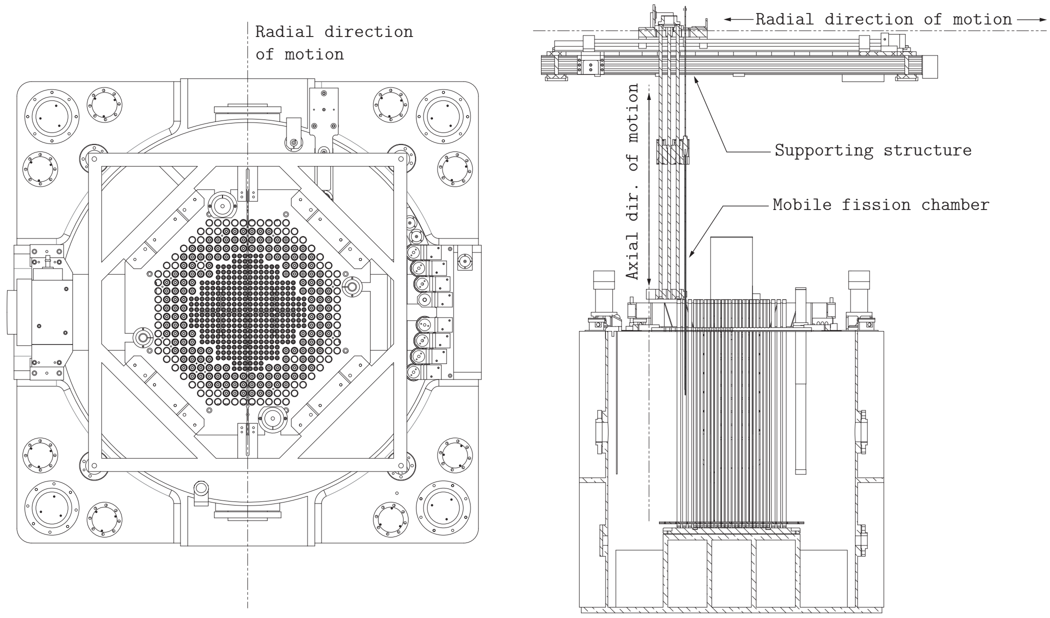

Figure 3.6 – Translateur Radial AXial (TRAX) system for in-core fission chamber scans

4 Experimental analysis

Numerical studies on reactor physics have always been a key tool for research and industry. Today, more sophisticated simulations are possible as a result of the continuous and enormous advances in computing power seen over the past decades. These simulations often rely on validated computer codes or techniques to verify results and computational schemes. The high-fidelity and accuracy of Monte Carlo methods provide a logical basis for code verification. However experimental studies are still of paramount importance to validate the consistency between computational results and experimental observations.

In the present work, it is of particular interest to estimate the accuracy of the Serpent/PARCS scheme for the steady-state and transient modeling of the CROCUS reactor. This can be achieved by comparing the computational results with experimental data. In an attempt to do so, a series of experimental measurements were carried out focusing on the estimation of static parameters such as fission rate profiles and control rods reactivity worth. A second experimental phase focused on time-dependent experiments that involve not only the measurement of global flux amplitude variations but also space-time effects. The latter was expected to be addressed through the measurement of local time-dependent flux perturbations induced by the movement of a small neutron absorber inside the CROCUS reactor core.

This chapter is organized into three sections. The first one focuses on the measurements of control rod reactivity worth, the second one on fission rate profiles and the third one on the measurement of neutronics transients. Each section describes the experimental setup and methods, discusses the evaluation of uncertainties and presents relevant results. The analysis and discussion of experimental results are reserved for Chapter 6, where measured data is compared against computer simulations. The computational models of the CROCUS reactor are reported in Chapters 5.

4.1 Control rod reactivity worth measurements

The first series of experiments consisted of measuring the reactivity worth of the control rods using two different dynamic techniques. The *asymptotic period method* was employed for the measurement of reactivity resulting from the removal of control rods (i.e., positive reactivities) and the *inverse kinetics method*[1] was used for the same experiments and also for the case in which the rods are inserted (i.e., negative reactivities). Both techniques are said to be dynamic [57, 58] because they rely on the measurement of time-dependent data and they both derive from the *point-reactor kinetics* approximation as described in Section 2.3.2.

4.1.1 Methods

Asymptotic period

The simplest type of kinetic measurement is to induce a reactivity change ($\Delta\rho$) in the reactor by removing or inserting a control rod. In the case of a control rod removal, the result is a positive reactivity insertion ($\Delta\rho > 0$) as shown in Figure 4.1. This example illustrates the power evolution in a time scale of milliseconds following a step change in reactivity, which represents an infinitely fast rod withdrawal.

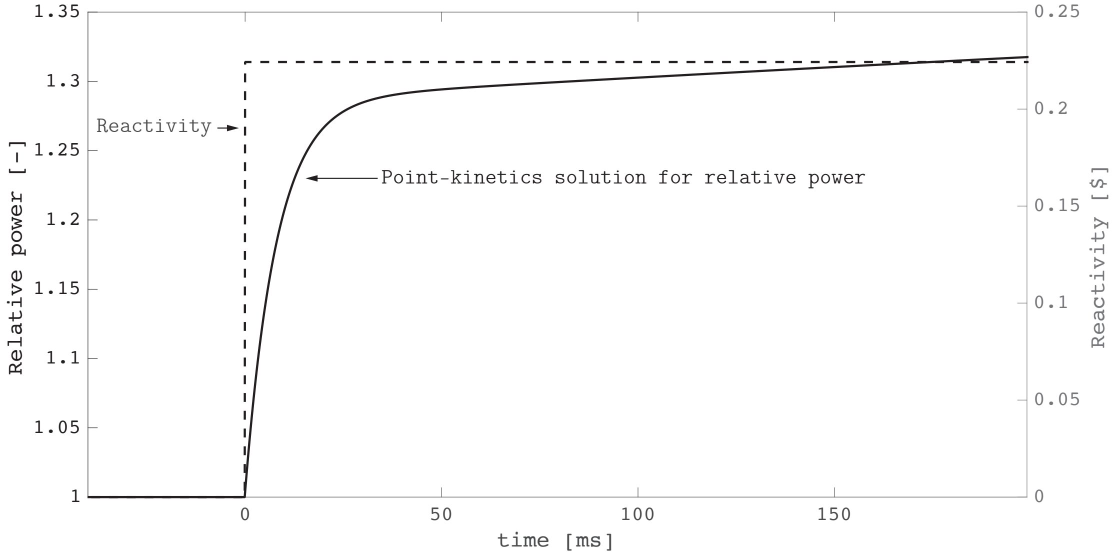

Figure 4.1 – Power transient following a positive reactivity step of 0.23 $ in the CROCUS reactor

If the reactor power is low enough to neglect temperature feedbacks effects[2], a constant positive reactivity of smaller magnitude than the β –such as shown in Figure 4.1– will cause the neutron population to rise exponentially with a stable period (T). To be more precise, after a very rapid initial transient[3], the power rise will asymptotically approach a stable period. The asymptotic behavior is illustrated in Figure 4.2, where the power evolution following a reactivity insertion of 0.23 \$ is shown on a larger time scale than in Figure 4.1. The transient behavior can be described in terms of power by the analytic solution of the point-reactor kinetics equations [43]

---

[1] Formally called *inverse point-kinetics* to differentiate from the *inverse spatial-kinetics*

[2] This was indeed the case for the reactivity effect measurements conducted at the CROCUS reactor.

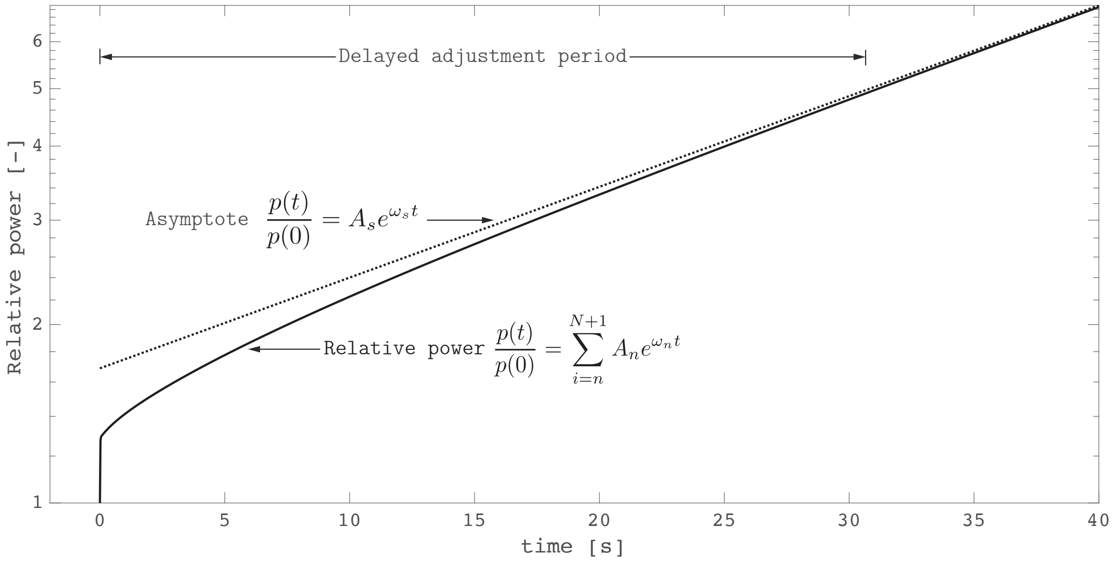

Figure 4.2 – Asymptotic behavior of a transient following a positive reactivity step of 0.23\$

$$\frac{p(t)}{p(0)} = \sum_{i=n}^{N+1} A_n e^{\omega_n t} \tag{4.1}$$

where N is the number of delayed neutron groups and ω_n are the N+1 roots that yield from the so-called *inhour equation.* The inhour equation is derived from the point-reactor kinetics equations and can be written as

$$\rho(\omega) = \omega \cdot \left(\Lambda + \sum_{i=1}^{N} \frac{\beta_i}{\omega + \lambda_i} \right) \tag{4.2}$$

The largest root of the inhour equation is known as inverse reactor period $\omega_1 = \omega_s = T^{-1}$, where the index s stands for *stable.*

The contribution from the exponential terms in Equation 4.1 that are driven by the other roots (ω_n, $n > 1$) die off after a delayed adjustment period, after which the power is governed only by the largest root exponential term, leading to the asymptotic behavior of the neutron population

---

[3] Approximately 10 ms for the CROCUS reactor, based on the prompt inverse period $\omega_p = \frac{\rho - \beta}{\Lambda}$

$$\frac{p(t)}{p(0)} \approx A_s e^{\omega_s t} \tag{4.3}$$

Figure 4.2 shows an example of the rapid initial transient referred to a as *prompt jump*, and the delayed adjustment period where the power asymptotically approaches the stable exponential growth driven by the largest root of the inhour equation. The curves in Figure 4.2 are given by the analytical solution of the point-kinetics equations using kinetic parameters from the CROCUS reactor. The delayed adjustment period to approach a stable exponential behavior can be approximately computed as $1/(\omega_1 - \omega_2)$ where ω_1 and ω_2 are the two largest roots of the inhour equation [43]. In the case of the CROCUS reactor, this period is of about 30 seconds.

The *asymptotic period technique* is ideal for studying this kind of reactivity effects because it essentially relates the stable reactor period ($T = \omega_s^{-1}$) to the worth of the control rod (ρ). From the measurement of the stable period one can use the inhour equation (4.2) to estimate the perturbation's reactivity worth.

The asymptotic period method has, however, certain limitations. First of all, the method is practically limited to positive reactivities, since for negative ones, the (negative) asymptotic period is dominated by the decay time of the longest living delayed neutron precursor ($-\frac{1}{\omega_1} \rightarrow \frac{1}{\lambda_{\text{longest}}} \approx 80$ s) and it is relatively insensitive to the value of reactivity [15]. From a rigorous standpoint, this method could be potentially employed for the control rod insertion experiments in the CROCUS reactor (i.e. small negative reactivities). However there are two major constraints: the first one is related to the transition time (or delayed adjustment time) before the power level reasonably approaches a stable behavior. Figure 4.3 shows that, in the CROCUS reactor, the stable asymptotic behavior is approached much faster in the case of a positive reactivity insertion than for the negative case for the same magnitude of reactivity. Given the dynamics of the reactor, the asymptotic period method could be used for control rod insertion experiments provided that (1) the power measurements are recorded for a long time after the rod drop to allow the exponential decay to become stable and dominated by the negative reactor period ($T^- = -105$ s), and (2) the initial power before the rod drop is high enough to provide reasonable counting statistic during the measurement period.

The second limitation of using the asymptotic period for the measurement of negative reactivities was already briefly mentioned and it is related to the solution of the inhour equation (Eq.4.2). The stable reactor period is given by the largest root of the inhour equation, which is shown in Figure 4.4. From the figure it is possible to see that a reactivity insertion of -0.23\$ and +0.23\$ corresponds to a reactor period (inverse of largest root) of -105 s and 28 s respectively. From the figure it is also clear that for negative reactivities, the solution of the inhour equation is very sensitive to the value of reactor period, and thus a small error in the measurement of the reactor period will propagate as

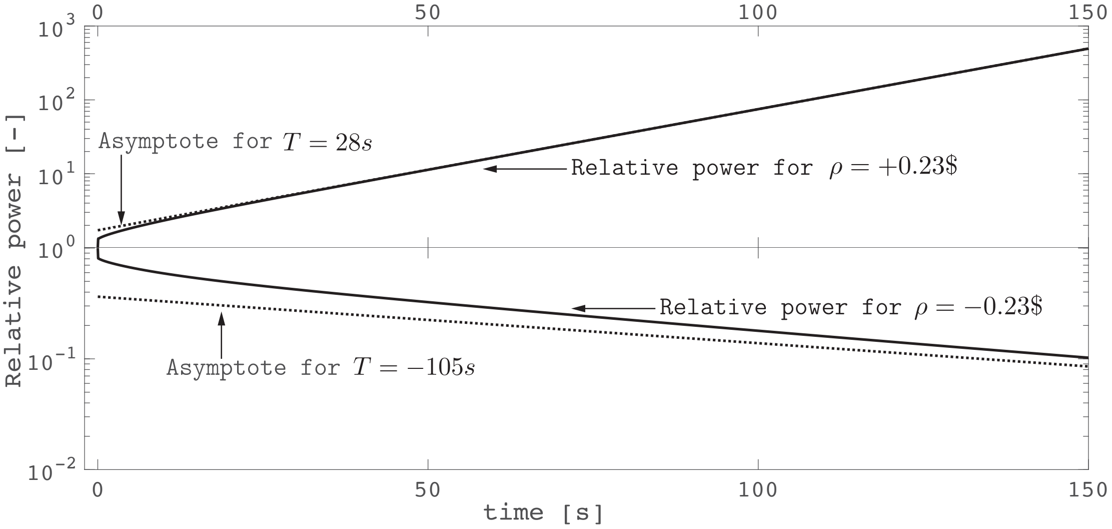

Figure 4.3 – Asymptotic approach after positive (+0.23 \$) vs. negative (-0.23 \$) reactivity insertion. Analytical solution of the point-kinetics equations for the CROCUS reactor.

a large error in the estimation of reactivity.

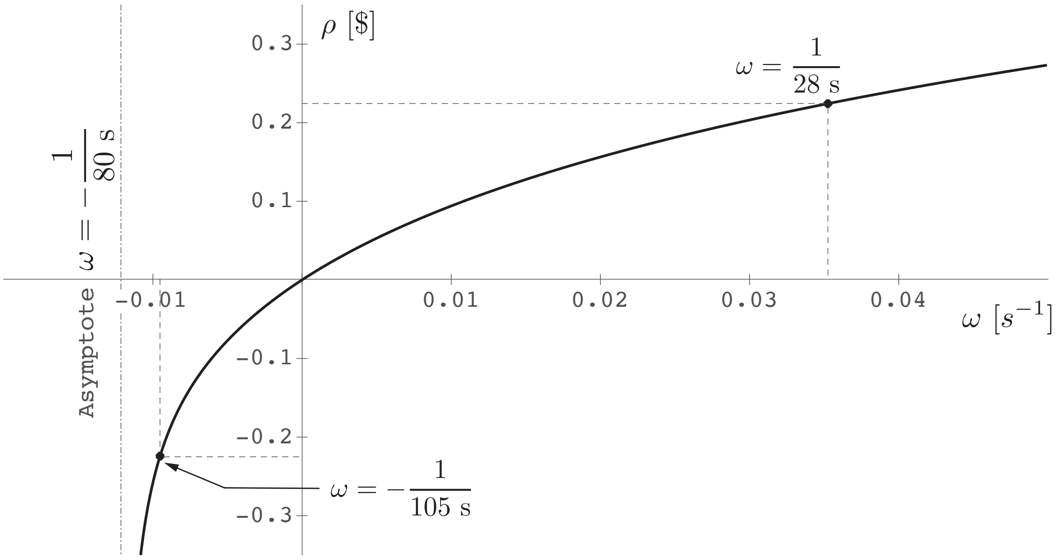

Figure 4.4 – Solution for the largest root of the inhour equation in the CROCUS reactor.

Another limitation of the asymptotic period method is that, for reactivities close to 1 \$ (i.e., reactor close to prompt supercritical state), the assumption of time-invariant shape function ($\Psi(\mathbf{r}, E)$) and time-invariant kinetic parameters ($\beta_i(t) = \beta_i$, $\Lambda(t) = \Lambda$) might not be valid. Therefore, this method is, in practice, limited to a reactor in a delayed supercritical state and moderate reactivities insertions ($0 < \rho \ll \beta$).

Inverse point kinetics

A more general method for estimating reactivity is the inverse point kinetics technique, where an on-line estimate of the reactivity $\rho(t)$ is possible to be obtained from the measurement of an instantaneous power signal $p(t)$.

The inverse point kinetics method is derived from the point-reactor kinetics approximation by reformulating the equations to solve $\rho(t)$ in terms of $p(t)$. For a reactor with no external source, the inverse kinetics equation can be written as [43]:

$$\rho(t) = \beta + \Lambda \frac{\dot{p}(t)}{p(t)} - \frac{1}{p(t)} \sum_{i=1}^{N} \lambda_i \beta_i \int_{-\infty}^{t} p(t') e^{-\lambda_i (t-t')} dt' \tag{4.4}$$

The *inverse point kinetics* (IK) method can be used for the measurement of any type of reactivity insertion, especially for negative reactivities where the asymptotic period method presents limitations as mentioned above. Examples of the application of the IK method are provided in Section 4.1.3

4.1.2 Measurements by asymptotic period method

Experimental procedure

The asymptotic period method was employed only for the measurement of reactivity resulting from the removal of control rods. During these experiments, the reactor power was measured with two ^{235}U fission chambers (Photonis CFUM21) located in the reflector region near the core periphery as depicted in Figure 3.1. Details about these detectors have been included in Section 3.3 (p. 39). The detectors' signal was acquired and digitalized by a multichannel scaling (MSC) counter which is computer-controlled and allows to record the detectors count rate as a function of time. An integration time (a.k.a. dwell time) of 200 or 400 ms was typically used, although in some cases, the integration time was increased up to 1 s. The acquisition system has a total of 8192 channels, which provided enough time span for the measurements. For the described CROCUS reactor detection system, the work published in OECD/NEA [59] showed that at powers greater than 40 W, an effect known as pulse pile-up[4] could alter the count rate to neutron flux ratio of these detectors. Accordingly, the power level during the experiments was limited to a maximum of 30 W.

Both control rods are almost identical in composition and geometry and are symmetrically placed in the core; therefore their reactivity worth should be similar. However, since experiments were performed by removing only one rod at a time, they will be differentiated as follows: SE control rod for the one located on the South East side of the core and NW control rod for the one located on the North West side of the core.

---

[4] This occurs when multiple pulses overlap and cannot be discriminated as individual counting events.

All control rod removal measurements were started with the reactor critical at about 100 mW and the start-up source withdrawn. The power level was selected as low as possible to allow sufficient range for the exponential growth before reaching the operational limit, but high enough to provide reasonable counting statistics. Given that CROCUS is a zero-power reactor with a maximum operating power of 100 W, reactivity feedbacks effects resulting from heat generation were neglected.

To begin each measurement, the reactor was brought to critical with only one of the two B_4C control rods completely inserted. The measured critical water level was typically of 991 mm at 20.0 °C. The inserted control rod was completely removed at full speed (i.e., $< 1\,\mathrm{s}$). The power was allowed to increase up until a range of 10–30 W at which point both control rods were inserted bringing the reactor into a subcritical state to lower the power level. The power evolution following the reactivity insertion was recorded by the acquisition system and saved for later post-processing. A typical experiment lasted in the order of 200 s and produced data as shown in Figure 4.5. Count rate uncertainty was estimated assuming a Poisson distribution of the total counts per integration time step; therefore the standard deviation follows the law $\sigma = \sqrt{\text{counts}}$. Details concerning the assumption of Poisson statistics for neutron counting will be presented later. The uncertainty band shown in Figure 4.5 is only visible at low power (see zoomed area). The detectors' power calibration factor is approximately 2500 cps/W [60].

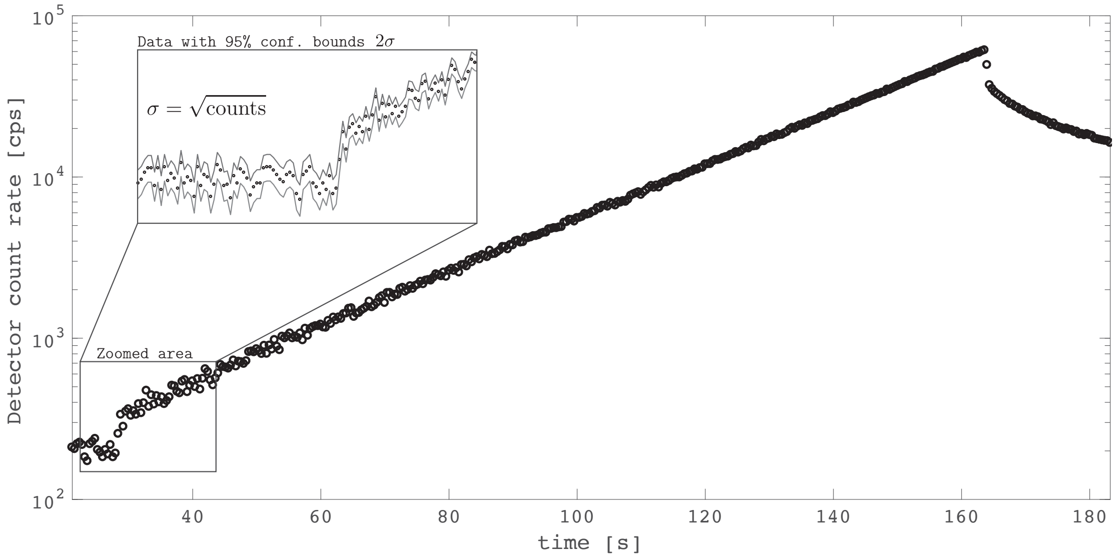

Figure 4.5 – Count rate (power) as a function of time for a typical rod withdrawal experiment

To estimate the control rod worth, the stable inverse periods were obtained by fitting an exponential curve into the experimental data. The least-squares method was used to fit a single-term exponential. The first 40 seconds of the transient were skipped in the fitting to ensure that the exponential growth is mostly governed by the stable period. The adjusted coefficient of determination $\overline{R}^2$ was employed to evaluate the goodness of fit.

The inverse reactor period ($\omega = T^{-1}$) and the reactor kinetic parameters ($\beta_i, \lambda_i, \Lambda$) are the input quantities that are used to estimate the reactivity worth through a physical model represented by the inhour equation. All these input quantities introduce uncertainty in the estimation of reactivity worth. Random sampling methods were used to obtain the expected reactivity value $\mathbb{E}(\rho)$ and its associated uncertainty $u(\rho)$. To do so, a Matlab® script was written to process the experimental data in the following manner:

1. The inverse reactor periods ω (resulting from the exponential fit), the kinetic parameters $\beta_i, \lambda_i, \Lambda$, and associated uncertainties $u(\omega), u(\beta_i), u(\lambda_i), u(\Lambda)$[5] were loaded into the script.
2. Using the mean values and associated uncertainties, independent normal distributions of $S = 10^5$ samples were generated for each input quantity $\omega, \beta_i, \lambda_i, \Lambda$.
3. The probability density functions (PDF) for each input quantity were propagated through the inhour equation using *random sampling* (a total of S trials) to obtain a PDF for the reactivity.
4. The expected reactivity value $\mathbb{E}(\rho)$ was computed as the arithmetic mean of all samples from the output probability distribution.

$$\mathbb{E}(\rho) = \tilde{\rho} = \frac{1}{S}\sum_{k=1}^{S} \rho_k$$

5. The associated standard uncertainty $u(\rho)$ was computed from the output PDF variance.

$$u(\rho) = \sqrt{\sigma^2(\rho)} = \sqrt{\frac{1}{S-1}\sum_{k=1}^{S}(\rho_k - \tilde{\rho})^2}$$

Given that the previous technique is performed with a finite number of samples, the value of $\tilde{\rho}$ and $\sigma^2(\rho)$ are just estimations of the mean and variance that converge to the true values as the number of samples S tends to infinity. The uncertainty in the estimation of the mean follows the law $\sigma(\tilde{\rho}) = \sigma(\rho)/\sqrt{S}$ and therefore decreases with a rate proportional to $\sqrt{S}$. Uncertainty propagation through random sampling was also applied to other experiments as it will be later described.

Figures 4.6 and 4.7 provide examples of the experimental data post-processing (using the Matlab® script) for the estimation of control rod worth by asymptotic period method.

---

[5] Uncertainties on kinetic parameters taken from JEF/DOC-920: [61]

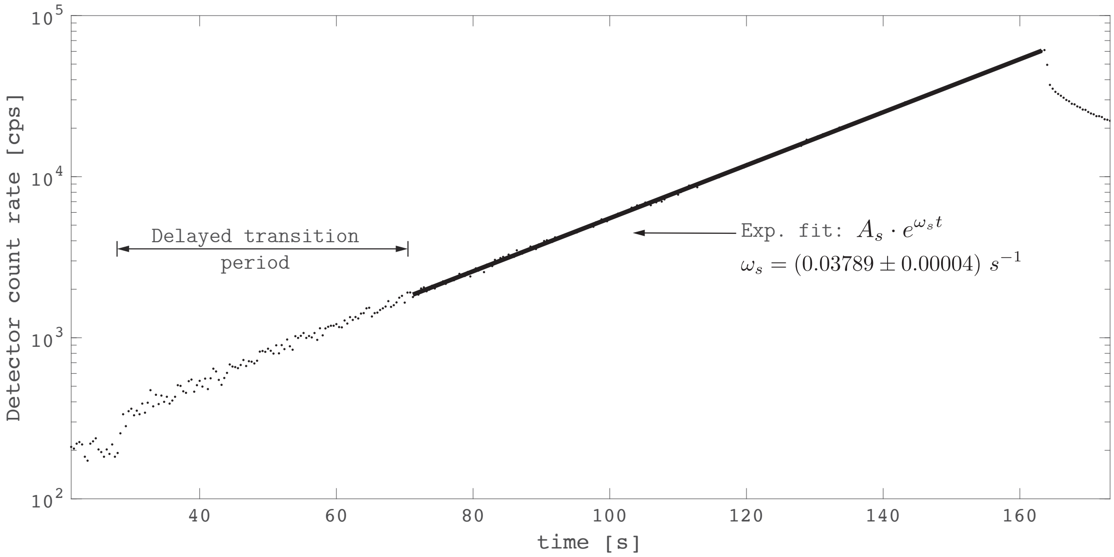

Figure 4.6 – Exponential fitting for the asymptotic period in typical rod withdrawal experiment.

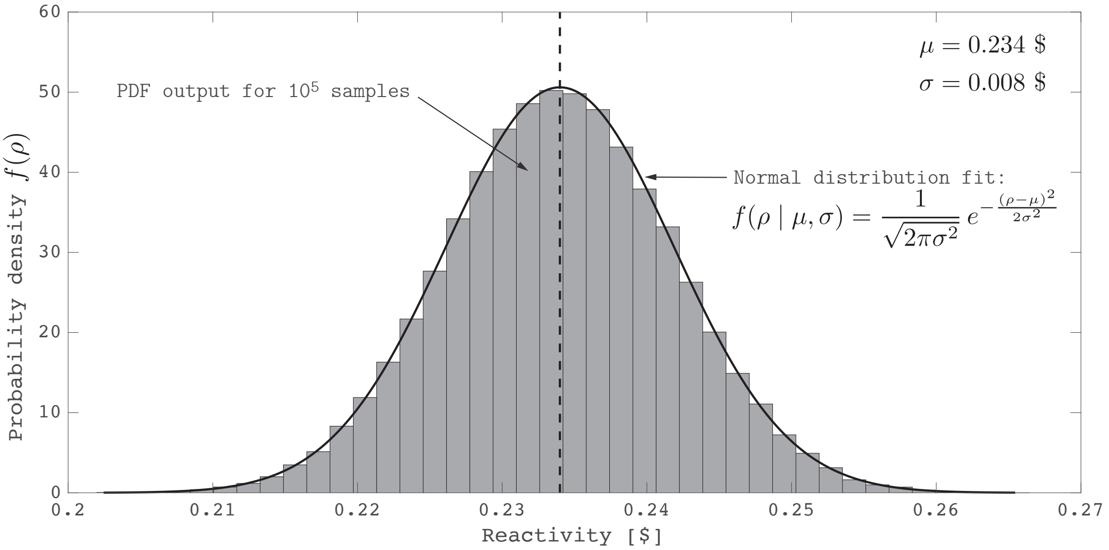

Figure 4.7 – Typical output PDF generated from statistical sampling for the estimation of reactivity and associated uncertainty.

Results

All reactivity worth results were obtained using the CROCUS reactor kinetic parameters listed in Table 4.4 (Section 4.1.4, p. 54). They were computed by the MCNP5-1.6 code using the JEFF-3.1.1 nuclear data library [60]. The uncertainties on the kinetic parameters were obtained from JEF/DOC-920 [61]. It was assumed no correlation between input uncertainties.

The measurements for control rod withdrawal were repeated 18 times for the South East (SE) control rod, and three times for the North West (NW). The difference in the amount of measurements was due to time constraints related to the availability of the reactor for experiments. Table 4.1 shows the full list of measurements by the asymptotic period method. The notation used to identify each run is X_i where X is a number denoting the experimental run and i represents the detector used for the run. For example, *1a* and *1b* correspond to measurements with the North and South fission chambers, respectively, for the first experimental run. A summary and discussion of the results are presented in Section 4.1.5 (p. 56).

The results shown in Table 4.1 are reported with two uncertainty values. These uncertainties were evaluated by statistical methods (i.e. derived from observed frequency distributions) and are reported with a coverage factor $k = 1$, providing a confidence level of approximately 68%. The first value that follows the ± sign represents the combined standard uncertainty (total uncertainty) and it was computed by random sampling propagation on the kinetic parameters and the inverse reactor period. This uncertainty will be denoted by "u_T" and may be used (a) for the comparison between predictions from computer codes and experimental values or (b) for comparing experimental values

Table 4.1 – Reactivity worth by AP method - Rod withdrawal experiments

Run #	Control rod	Detector	Inverse period [s^{-1}]	Reactivity worth* [\$]
1a	SE	FC North	0.0379 ± 0.0003	0.234 ± 0.008 (0.001)
1b	SE	FC South	0.0378 ± 0.0003	0.234 ± 0.008 (0.001)
2b	NW	FC South	0.0378 ± 0.0006	0.234 ± 0.008 (0.002)
3a	SE	FC North	0.0366 ± 0.0003	0.229 ± 0.008 (0.001)
3b	SE	FC South	0.0367 ± 0.0003	0.230 ± 0.008 (0.001)
4a	NW	FC North	0.0389 ± 0.0006	0.238 ± 0.008 (0.002)
4b	NW	FC South	0.0389 ± 0.0006	0.238 ± 0.008 (0.002)
5a	SE	FC North	0.0372 ± 0.0003	0.232 ± 0.008 (0.001)
5b	SE	FC South	0.0372 ± 0.0003	0.232 ± 0.008 (0.001)
6a	SE	FC North	0.0373 ± 0.0003	0.232 ± 0.008 (0.001)
6b	SE	FC South	0.0374 ± 0.0003	0.232 ± 0.008 (0.001)
7a	SE	FC North	0.0374 ± 0.0003	0.232 ± 0.008 (0.001)
7b	SE	FC South	0.0374 ± 0.0003	0.232 ± 0.008 (0.001)
8a	SE	FC North	0.0374 ± 0.0003	0.232 ± 0.008 (0.001)
8b	SE	FC South	0.0373 ± 0.0003	0.232 ± 0.008 (0.001)
9a	SE	FC North	0.0374 ± 0.0003	0.232 ± 0.008 (0.001)
9b	SE	FC South	0.0373 ± 0.0003	0.232 ± 0.008 (0.001)
10a	SE	FC North	0.0374 ± 0.0003	0.232 ± 0.008 (0.001)
10b	SE	FC South	0.0374 ± 0.0003	0.232 ± 0.008 (0.001)
11a	SE	FC North	0.0373 ± 0.0003	0.232 ± 0.008 (0.001)
11b	SE	FC South	0.0375 ± 0.0003	0.232 ± 0.008 (0.001)

*Value after the ± sign: combined standard uncertainty (u_T). Value in parenthesis: sample standard deviation (σ_{exp}).

calculated with different kinetic parameters. On the other hand, the uncertainty value in parenthesis represents the experimental uncertainty, therefore it will be denoted by "σ_{exp}". It was computed as the standard deviation of each set of measurements for the SE and NW control rods,

$$\sigma_{\text{exp}} = \sigma(\rho_i) = \sqrt{\frac{1}{N-1}\sum_{i=1}^{N}(\rho_i - \tilde{\rho})^2} \tag{4.5}$$

where N is the number of measurements (or experimental runs) for each control rod, ρ_i the reactivity value for each measurement and $\tilde{\rho} = \frac{1}{N}\sum_{i=1}^{N}\rho_i$ is the mean value. The uncertainty given by Equation 4.5 provides an idea of the uncertainty associated with the measuring process; however it does not take into account the influence of the kinetic parameters' uncertainty. The value given by Equation 4.5 may be employed for the comparison between experimental values that have been calculated with the same kinetic parameters. Note that the uncertainty estimation does not consider the correlation between runs within each set of measurements. The reported uncertainty values are therefore lower than if this correlation had been taken into account.

4.1.3 Measurements by inverse point kinetics method

Experimental procedure

The inverse kinetic method was used for the estimation of control rod worth from control rod withdrawal ($\Delta\rho > 0$) and control rod insertion experiments ($\Delta\rho < 0$).

The experimental procedure for the control rod withdrawal measurements was already explained in the previous section (4.1.2). With respect to the control rod insertion measurements, they were all carried out adopting the procedure that follows. The reactor was brought to critical at powers between 10 and 15 W with both control rods and the start-up source withdrawn. The measured critical water level was typically of 952 mm at 20.0 °C. One control rod was completely inserted at full speed (< 1 s), and the power was allowed to decrease below 100 mW. The detection and acquisition system was the same as the one used for the control rod withdrawal measurements.

Since the control rod withdrawal and insertion experiments were performed having the reactor start-up source withdrawn, the inverse kinetics equation with no source (Eq. 4.4) was employed to estimate the reactivity worth as a function of the reactor power $p(t)$ (or detectors' count rate) and the reactor kinetic parameters $\beta_i, \lambda_i, \Lambda$. A Matlab® script was written to solve the inverse kinetics equation and to estimate the reactivity worth and associated uncertainty using random sampling techniques. The script processes the experimental data in the following manner:

1. The power signal $p(t)$ given by the detectors' count rate was down-sampled to 1 Hz (integration time of 1 s) to increase the number of counts per channel (hence reduce the statistical uncertainty) and to normalize all experimental data to a single sampling rate.

2. An algorithm allowed to select the time interval $[t_i, t_f]$ after the rod insertion/withdrawal where the power signal $p(t)$ provides good counting statistics and the resulting reactivity function $\rho(t)$ is reasonably invariant in time (see Fig. 4.8). The time interval was used to average the time-dependent reactivity $\langle\rho\rangle = \frac{1}{t_f - t_i}\int_{t_i}^{t_f} \rho(t)dt$ and it was computed as follows:

   (a) For the rod withdrawal case, the time interval begins when the count rate exceeds 1×10^3 cps (∼400 mW) and finishes 5 seconds before the end of the exponential growth.

   (b) For the rod insertion case, the time interval begins 5 seconds after the rod drop and finishes when the count rate drops below 1×10^3 cps (∼400 mW).

3. Independent probability distributions of S samples were randomly generated for the input parameters. A Poisson distribution was used for the power $p(t)$ and normal distributions were used for the kinetic parameters $\beta_i, \lambda_i, \Lambda$.

4. The probability density functions (PDF) for each input quantity were randomly propagated through the inverse kinetics equation to obtain a PDF for the reactivity. The reactivity output PDF is contained within a matrix of size $T \times S$, where T is the length of the power signal sampled at 1 Hz during the time interval $[t_i, t_f]$ and S is the number of random samples.

5. The expected reactivity value was computed as the arithmetic mean of all samples from the output probability distribution $\mathbb{E}(\rho) = \tilde{\rho}$. The associated standard uncertainty was computed as the standard deviation of the output PDF $u(\rho) = \sigma(\rho)$.

Figure 4.8 shows an example of the power response following a rod insertion and the calculated reactivity by inverse kinetics. The figure also shows the time interval $[t_i, t_f]$ where the reactivity was averaged to obtain an estimate of the reactivity worth. The uncertainty propagation by random sampling yields a probability density function for the reactivity similar to that one showed for the asymptotic period method in Figure 4.7.

Results

Measurements for control rod insertion were repeated three times for the South East (SE) control rod, and six times for the North West (NW). Table 4.2 shows the full list measurements using the inverse kinetics method. Uncertainties were calculated in an equivalent way than for the asymptotic period measurements. They are expressed with a coverage factor of $k = 1$, providing a confidence level of $\sim 68\%$.

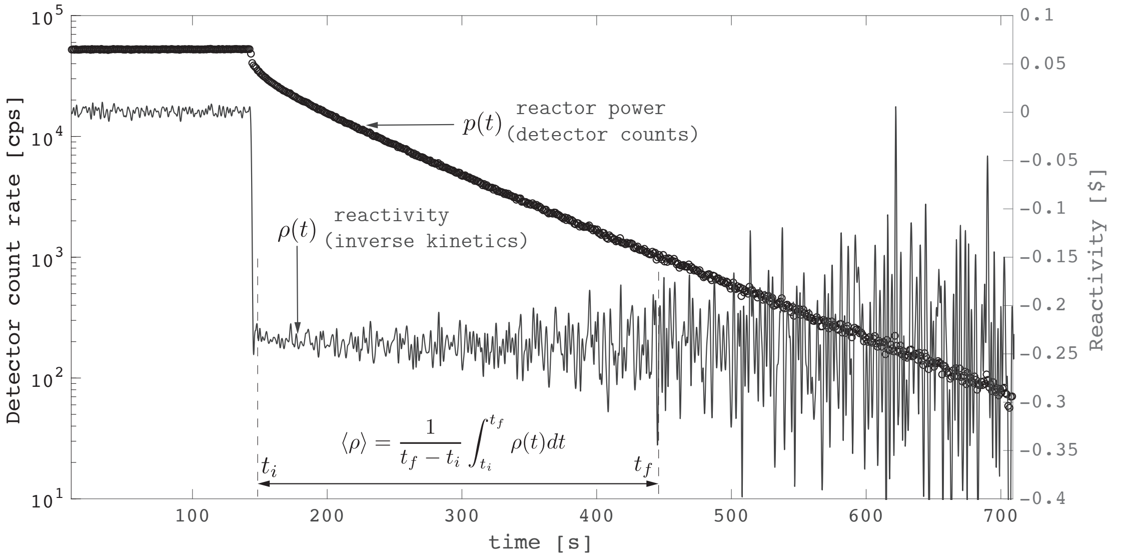

Figure 4.8 – Example rod insertion measurement and reactivity estimation by inverse kinetics.

Table 4.2 – Reactivity worth by IK method - Rod insertion experiments

Run #	Control rod	Detector	Reactivity worth* [$]
12a	NW	FC North	-0.233 ± 0.023 (0.005)
12b	NW	FC South	-0.228 ± 0.031 (0.005)
13b	SE	FC South	-0.235 ± 0.014 (0.003)
14a	NW	FC North	-0.232 ± 0.013 (0.005)
14b	NW	FC South	-0.233 ± 0.015 (0.005)
15a	SE	FC North	-0.241 ± 0.015 (0.003)
15b	SE	FC South	-0.239 ± 0.016 (0.003)
16a	NW	FC North	-0.240 ± 0.013 (0.005)
16b	NW	FC South	-0.240 ± 0.014 (0.005)

*Result expressed as: $\rho \pm u_T$ (σ_{exp}).

It is worthwhile noting that the experimental conditions for rod insertion experiments were not always optimal because, in some cases, the reactor power before the rod drop was not high enough to provide good counting statistics. The experimental run #12 (see Table 4.2) exemplifies the case where the initial power before the rod insertion was low (in the order of 1 W). Due to the low power, the detectors' signal –that is proportional to the power $p(t)$– carried a large statistical noise that was propagated towards the final estimation of reactivity. The whole set of rod insertion experiments was executed at lower power ranges (15 to 0.4 W) than the withdrawal ones (0.4 to 30 W), and therefore all reactivity values from rod insertion measurements carried larger uncertainties than their withdrawal counterparts.

The measurements for control rod withdrawal (presented in the previous section) were also used to estimate the reactivity worth by inverse kinetics. These results are listed in Table 4.3 and summarized in Section 4.1.5.

Table 4.3 – Reactivity worth by IK method - Rod withdrawal experiments

Run #	Control rod	Detector	Reactivity worth* [$]
1a	SE	FC North	0.232 ± 0.007 (0.001)
1b	SE	FC South	0.233 ± 0.008 (0.001)
2b	NW	FC South	0.233 ± 0.008 (0.002)
3a	SE	FC North	0.229 ± 0.007 (0.001)
3b	SE	FC South	0.229 ± 0.008 (0.001)
4a	NW	FC North	0.236 ± 0.007 (0.002)
4b	NW	FC South	0.236 ± 0.009 (0.002)
5a	SE	FC North	0.230 ± 0.007 (0.001)
5b	SE	FC South	0.231 ± 0.008 (0.001)
6a	SE	FC North	0.231 ± 0.008 (0.001)
6b	SE	FC South	0.231 ± 0.007 (0.001)
7a	SE	FC North	0.231 ± 0.007 (0.001)
7b	SE	FC South	0.230 ± 0.007 (0.001)
8a	SE	FC North	0.231 ± 0.008 (0.001)
8b	SE	FC South	0.231 ± 0.008 (0.001)
9a	SE	FC North	0.232 ± 0.007 (0.001)
9b	SE	FC South	0.232 ± 0.008 (0.001)
10a	SE	FC North	0.232 ± 0.007 (0.001)
10b	SE	FC South	0.232 ± 0.008 (0.001)
11a	SE	FC North	0.231 ± 0.007 (0.001)
11b	SE	FC South	0.231 ± 0.008 (0.001)

*Result expressed as: $\rho \pm u_T$ (σ_{exp}).

4.1.4 Effect of kinetic parameters and nuclear data on reactivity worth

The effect of nuclear data libraries on the estimation of reactivity worth was investigated. Nuclear libraries need to be chosen for the calculation of kinetic parameters that are later used for the reactivity estimation by asymptotic period (AP) or inverse kinetics (IK) methods.

The experiment #1*a* for control rod withdrawal (see Table 4.3) was used as an example to quantify the reactivity dependence on the kinetic parameters. The reactivity worth was estimated using the inverse kinetics method and the following kinetic parameters

(a) Calculated by MCNP5-1.6 using the JEFF-3.1.1 nuclear data library with associated uncertainties taken from U^{235} thermal fission from JEF/DOC-920 [61].

(b) Calculated by MCNP5-1.6 using the ENDF/B-VII.1 nuclear data library with associated uncertainties taken from U^{235} thermal from Tuttle [62].

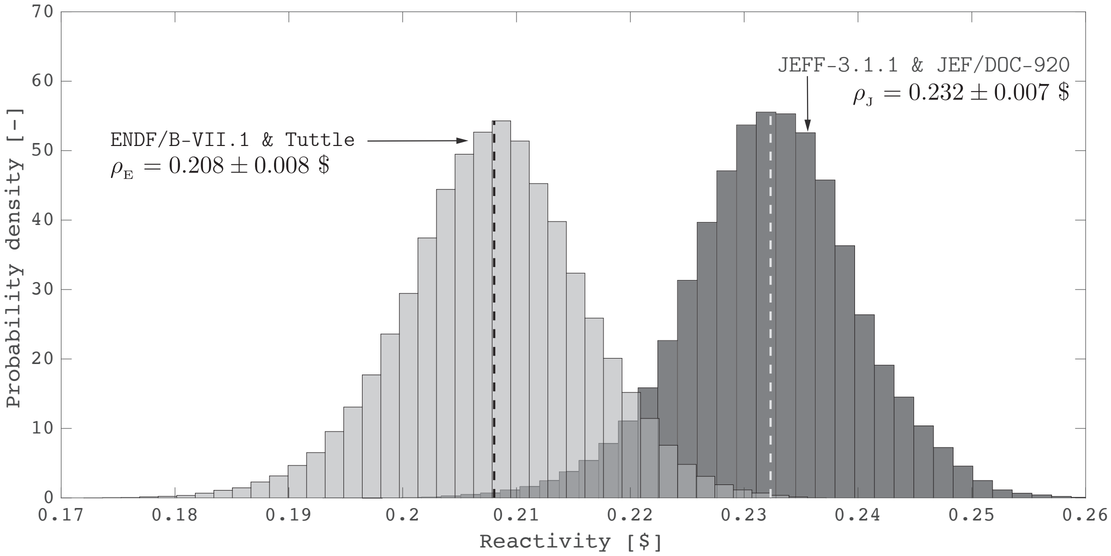

Figure 4.9 – Reactivities calculated with kinetic parameters from JEFF-3.1.1 and ENDF/B-VII.1 nuclear data - Experiment #1a .

Table 4.4 – CROCUS kinetic parameters from JEFF-3.1.1 & U^{235} thermal from JEF/DOC-920

λ_i [s^{-1}]	β_i *	σ_{λ_i} [%]	σ_{β_i} [%]	Λ [s^{-1}]
1.247×10^{-2}	2.300×10^{-4}	0	12.80	4.751×10^{-5}
2.829×10^{-2}	1.110×10^{-3}	0	4.42	
4.252×10^{-2}	6.400×10^{-4}	0	9.85	
1.330×10^{-1}	1.440×10^{-3}	0	11.68	
2.925×10^{-1}	2.460×10^{-3}	0	1.99	
6.665×10^{-1}	8.000×10^{-4}	0	4.98	
1.635	6.600×10^{-4}	0	1.97	
3.555	2.400×10^{-4}	0	41.48	

*Effective delayed neutron data

Figure 4.9 illustrates the difference of reactivities derived from JEFF-3.1.1 and ENDF/B-VII.1 nuclear data. In relative terms, results obtained with the two libraries differ by about 10 %, which is larger than the 2σ uncertainty. The work by Perret [63] suggests that kinetic parameters derived from the JEFF-3.1.1 library are more reliable than those obtained from the ENDF/B-VII.1 library. This conclusion was reached after comparing the average period $\sum_i \beta_i/\lambda_i$ obtained from both libraries against that one obtained by Tuttle [62]. Consistent conclusions were reached after the comparison of experimental and Monte Carlo calculated values for the reactivity worth [64]. This work pointed out that the differences between experimental and computer simulated values were lower with use of the JEFF-3.1.1 library than with the ENDF/B-VII.1 library.

Therefore, the kinetic parameters from JEFF-3.1.1 were chosen for all the reactivity measurements, and are listed in Table 4.4. The kinetic parameters from ENDF/B-VII.1 are shown in the Appendix A (Table A.1). A difference between the kinetic parameters from the two libraries resides in the delayed neutron group structure: the ENDF/B-VII.1 library uses the traditional 6-group structure, whereas the JEFF-3.1.1 library uses eight groups.

In conclusion, this study revealed that the reactivity results are highly dependent on the reactor kinetic parameters. More specifically, the dependence is on the choice of nuclear data library used for the calculation of kinetic parameters. This effect was observed for the reactivity estimation by the asymptotic period (AP) and inverse kinetics (IK) methods.

4.1.5 Summary and discussion of results

Table 4.5 summarizes the reactivity worth from control rod withdrawal and insertion experiments. The reactivity worth estimates are taken as the arithmetic mean of the total number of evaluations ($\bar{\rho}$) for each measurement set. The experimental uncertainty was computed as the standard error of the mean (SE), where $SE = \sigma_{\text{exp}}/\sqrt{N}$.

Table 4.5 – Summary of reactivity worth measurements

Control rod withdrawal experiments

Control rod	No. of measurements	Worth* [$] (AP)	Worth* [$] (IK)
SE	18	0.232 ± 0.008 (0.0003)	0.231 ± 0.008 (0.0002)
NW	3	0.236 ± 0.008 (0.0013)	0.235 ± 0.008 (0.0010)

Control rod insertion experiments

Control rod	No. of measurements	Worth* [$] (IK)
SE	3	-0.238 ± 0.015 (0.002)
NW	6	-0.234 ± 0.019 (0.002)

*Result expressed as: $\rho \pm u_T$ (SE). AP: asymptotic period - IK: inverse kinetics

Results from Table 4.5 indicate that the asymptotic period (AP) and the inverse kinetic (IK) methods yield similar total uncertainties that are in the order of 3% of the reactivity value. Results suggest that both methods are equivalent for evaluating reactivities.

The comparison between the SE and NW rods' results suggests that both control rods have slightly different reactivity worth. Their worth difference resulted in ~ 0.004 $ (or 3 pcm) and fell outside the 2σ uncertainties. Note that the standard error of the mean (value in parenthesis) is considered in this analysis instead of the total uncertainty because the reactivity worth values were computed with the same kinetic parameters.

4.2 Fission rate distribution measurements

The second series of experiments consisted in measuring relative fission rate distributions in the axial and radial directions. This section reports the experimental procedure including the characterization of the acquisition system, the measurements results and the evaluation of uncertainties.

4.2.1 Experimental procedure

The measurements were performed using an in-core miniature size fission chamber (Photonis CFUF34) and an out-of-core fission chamber (Photonis CFUM21). The out-of-core detector is the same as used for the reactivity worth measurements. Details about these detectors have been included in Section 3.3 (p. 39).

The position of the miniature fission chamber is controlled by the system described in Section 3.3 as TRAX (Translateur Radial AXial) that allows vertical and radial displacement of the chamber with a precision of ±1 mm. In the axial direction, the chamber can move from top to bottom of the core. In the radial direction, the displacement can be extended from the radial center of the core to the reflector region. However, all fission chamber movements are contained within a single plane located in the central water gap between the fuel rods as shown in Figure 4.10. A full 3-D fission rate mapping of the core is therefore not possible with the current system.

In spite of the small size of the detector, it introduces reactivity changes as it moves

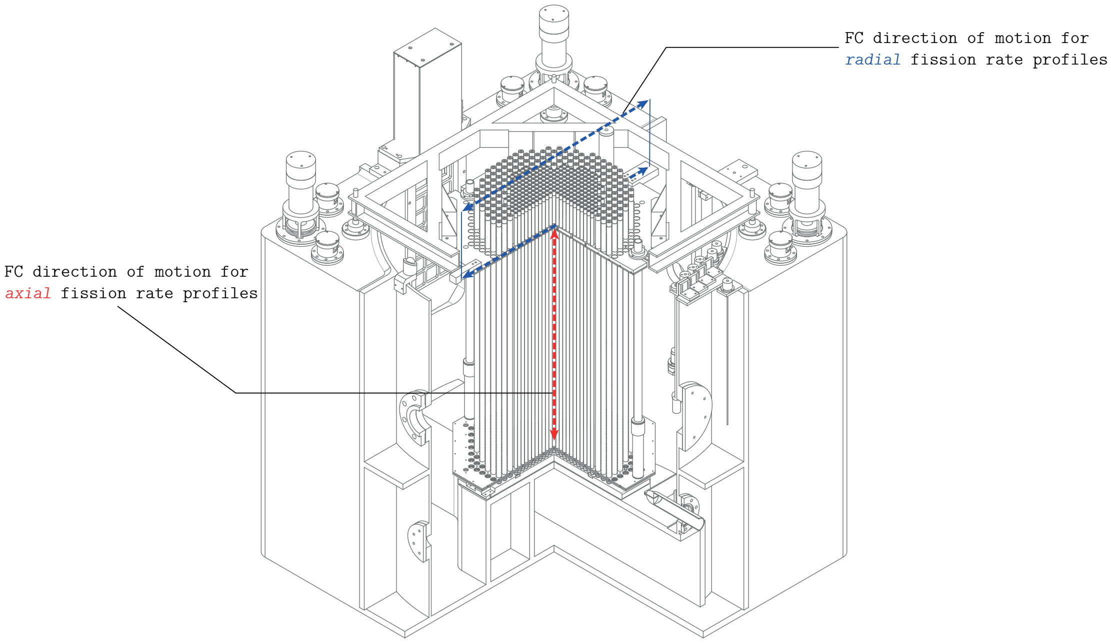
FC direction of motion for
radial fission rate profiles
FC direction of motion for
axial fission rate profiles

Figure 4.10 – In-core fission chamber (FC) scans. Radial and axial measurements

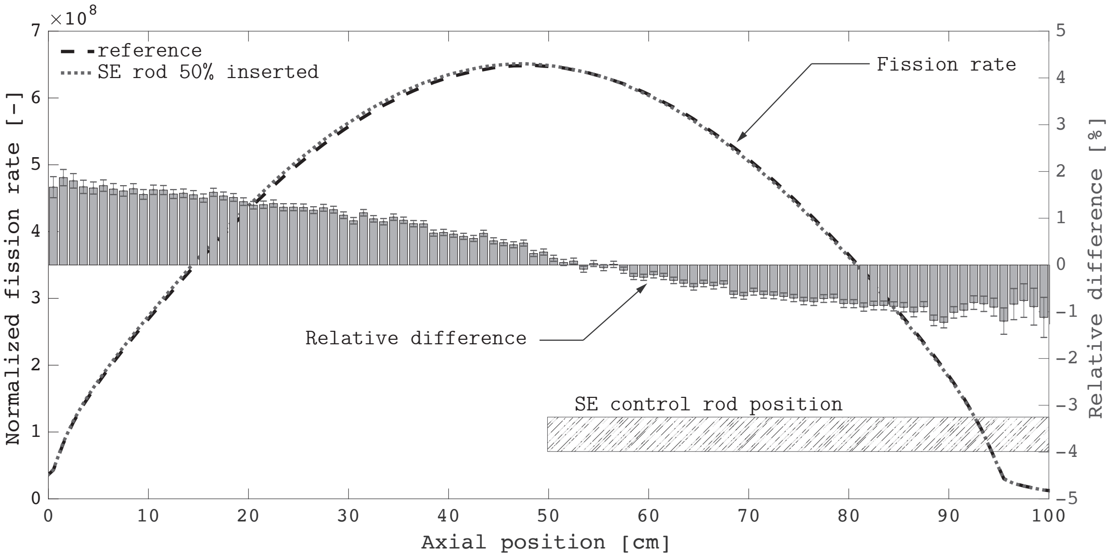

Figure 4.11 – Effect of partial rod insertion on axial fission rate profile - Monte Carlo simulation

inside the core. This effect can be compensated by adjusting the critical water level or by moving the control rods to preserve the reactor at a critical state. However, since the fission rate profiles are water-level-dependent, the level must remain constant during the experiment. In this context, reactivity changes introduced by the mobile chamber need to be compensated by moving one of the control rods. Monte Carlo simulations were run to investigate whether the partial insertion of the control rod alters the shape of the fission rate profiles. The first set of Monte Carlo profiles were obtained for the case where no rods are inserted, and the second set of profiles were obtained for the case in which the South East control rod is partially (50 %) inserted. The Serpent code was used for these simulations. A total of 9900 active cycles of 10^6 source neutrons each were run to achieve relative statistical uncertainties on the tallies below 0.5 % (1σ confidence). The relative difference between the two cases was computed as $d_{\%} = (R_f - R_{f,\mathrm{ref}})/R_{f,\mathrm{ref}} \cdot 100$ where R_f denotes *fission rate* and the *reference* corresponds to the case where no rods are inserted. Uncertainties on the relative difference were propagated using the classical law of propagation based on first-order Taylor expansion [65].

The Monte Carlo simulations (shown in Figures 4.11 and 4.12) revealed that for the axial profiles, the partial insertion of the control rod produced a shape tilt of the order of 1 % at the top region of the core with respect to the axial midpoint ($h = 50$ cm), and a distortion of about 2 % at the bottom region. The simulations for the radial profiles showed that the shape distortion due to partial rod insertion are in the order of 1 %. Even though these shape distortions are not very significant, they were taken into account for the estimation of experimental uncertainty as it will be shown later (see p. 63). Having quantified the impact, the South East control rod was used to compensate for the chamber's reactivity changes. Note that the Monte Carlo simulations were taken as a conservative bound

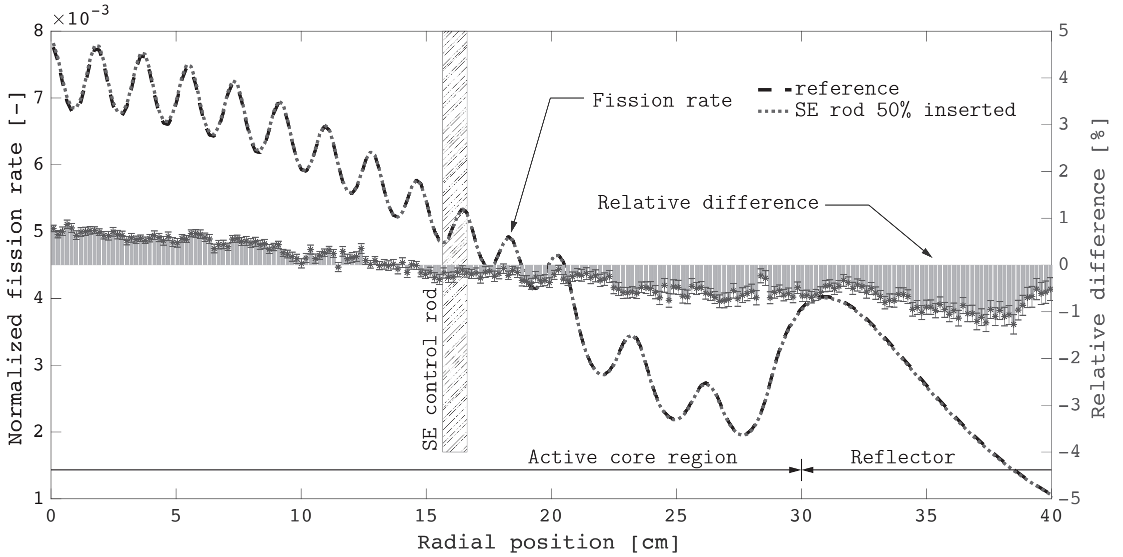

Figure 4.12 – Effect of partial rod insertion on radial fission rate profile - Monte Carlo simulation

estimate since they express the case where the South East control rod is inserted 50 % whereas in reality (during the experiments), the rod was only inserted between 30% and 40 %.

During the course of the measurements, the reactor presented small power variations in time for two main reasons:

(a) In practice it is not possible to preserve the critical state in time. Hence, the reactor was either in a slight subcritical or supercritical condition.

(b) The critical state of the reactor was altered when the fission chamber was moved to a new position. The reactor was brought back to a critical state by means of the SE control rod, however, at a slightly different power.

These power variations were accounted for by normalizing the readings from the mobile fission chamber (R_f^{mob}) with respect to those taken from the out-of-core fission chambers (R_f^{ref}) located in the reflector region at a distance of about 37 cm from the radial center. Note that the active core region is extended up to a radius of 30 cm. Therefore, these reference chambers can detect the global variations of the neutron flux (or fission rate), but they are insensitive to the local perturbations caused by the mobile fission chamber. All mobile chamber's fission rate readings were normalized in the following way

$$\widehat{R}_f(\mathbf{r},t) = \frac{R_f^{\mathrm{mob}}(\mathbf{r},t)}{R_f^{\mathrm{ref}}(t)} \tag{4.6}$$

To run the axial profile measurements, the mobile fission chamber's radial position was fixed at $r = 0$ (radial center of the core). The axial center of the chamber's sensitive part was taken as the reference point for the position of the fission chamber. Measurements were typically taken in steps of 5 cm along the axial direction for a total of 19 positions. At each position, two measurements of 30 seconds each were taken and were later averaged. The first set of measurements was carried out for a critical water level of 970 mm, and the second set of measurements for a critical water level of 1000 mm. The purpose of performing measurements at two different water level is to determine if differences in the axial profile can be resolved experimentally.

The radial profile measurements were performed having the reactor critical with a water level of 960 mm at a power of about 0.8 W. The power level was selected to operate in the linear range of the detector and at the same times as high as possible to provide good counting statistics. Characterization of the detector response was made prior to executing the experiments and is presented below. The South East control rod was again used to compensate for the reactivity changes introduced by the fission chamber. The radial measurements were initiated fixing the mobile fission chamber's axial position at $h = 50$ cm (axial mid-plane). Measurements were taken starting from the radial center of the core ($r = 0$) and were extended to the reflector region in steps of 1 cm. In the area near the water gap between fuel lattices (r = 20 cm), the step size was decreased to 0.5 cm to improve the spatial resolution. The radial scans were performed only for one half of the core taking advantage of the reactor's rotational symmetry.

Fission chamber response

Fission chambers are a class of neutron detectors that contain a fissionable material deposited on the detector's electrode. Neutrons interact with the fissionable material inducing fissions. The fission products ionize the chamber filling gas producing ion-electron pairs. The high voltage between the electrodes allows collecting the charges that are later converted into an electrical signal (current pulses). In this experience, the mobile fission chamber (Photonis CFUF34) is used in pulse mode[6], which implies that the detector's output signal are defined and separated pulses that can be counted individually as events. However, in this mode, the acquisition system has a limited maximum count rate at which the proportionality with the neutron flux is lost. This breakup point takes place when pulses begin to overlap (pile-up occurs), and pulses cannot be longer counted as individual events.

Because the count rate varies significantly as the detector moves across and along the core, the proper evaluation of reaction rate profiles requires a linear relationship between the count rate and the magnitude of the neutron flux. This issue does not concern the reference fission chamber (Photonis CFUM21) since its position is fixed and also because it exhibits a linear response up to powers of about 40 W (as discussed in Section 4.1.2); limit that is far beyond the power range used during the present experiments.

---

[6] Other modes, such as fluctuation (a.k.a. Campbelling) can be used for higher fission rates.

Preliminary measurements have been made to assess the range of linear response for the mobile fission chamber acquisition system, which consisted of

- a miniature size fission chamber (Photonis CFUF34)
- a charge preamplifier (Tennelec TC 174)
- a high voltage supply (Tennelec TC 952)
- a voltage amplifier (Tennelec TC 243)
- a timer (Tennelec TC 534)
- pulse amplitude discriminator and counter (Tennelec TC 533)

The linearity of the above listed acquisition system was evaluated by measuring the detector's counts for different reactor powers. The measurements were carried out with the detector located at the radial and axial center of the core, point at which the magnitude of the neutron flux is maximum. The reference power was measured from one of the two safety channels (Photonis CFUM21 out-of-core fission chambers). The linearity measurements are illustrated in Figure 4.13 and show the clear departure from linearity at powers near 1 W. The raw measured data is shown in the Appendix A (Table A.2).

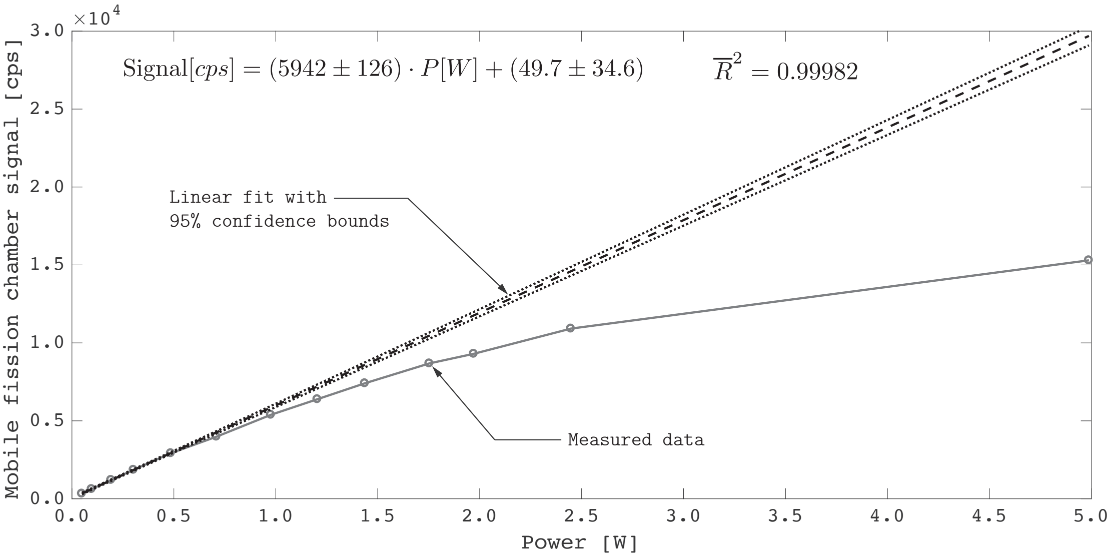

Figure 4.13 – Mobile fission chamber response versus power

In addition, a pulse-height-analysis test (a.k.a. charged-particle spectroscopy) was run to complement the linearity test. The goal of this second experiment was to investigate the behavior of the detector signal's spectrum at different powers. For these series of measurements, the counter and timer systems were replaced by a multi-channel pulse-height analyzer (Ortec 926 MCB). A spectrometry software (Ortec MAESTRO) was employed to process the multi-channel analyzer data. The detector was located at the same position as in the previous linearity test (core center). The same amplifier shaping time was used for this spectral study (2 μs). The results of this second test are shown in Figure 4.14 and were obtained for an acquisition time of 180 seconds. The spectra were normalized with respect to their integrals starting from channel no. 600 to exclude the background noise. The results are consistent with the previous linearity test as they evidence that the detector's spectrum is distorted and spreads towards higher energies (i.e. higher channel numbers) for reactor powers over 1 W. This phenomenon arises from the fact that, at powers over 1 W, pulse pile-up manifests which increases the mean height of the pulses.

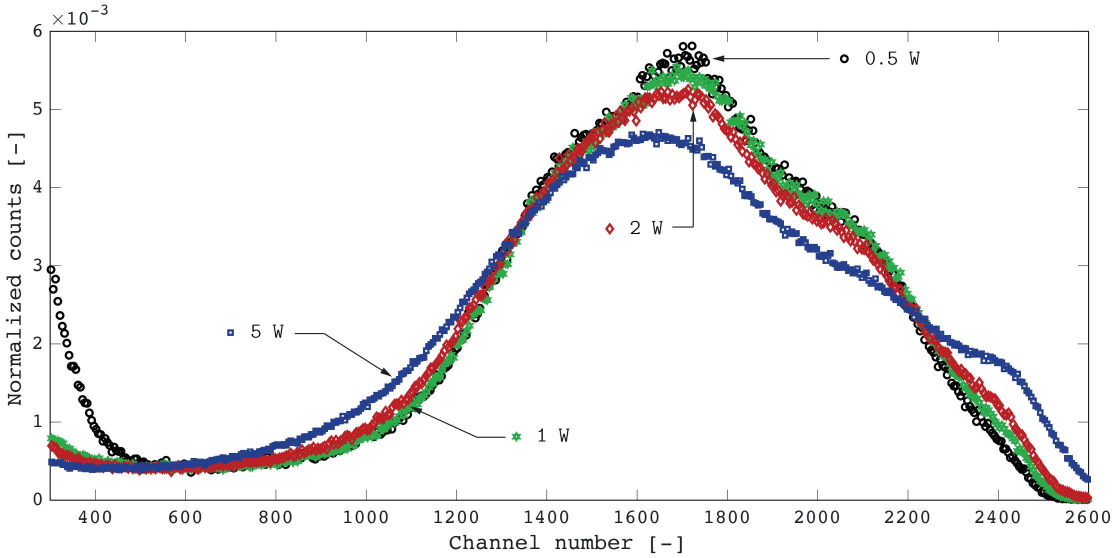

Figure 4.14 – Mobile fission chamber signal's spectra at various reactor powers

The spectral information provided by the pulse-height-analysis confirmed the hypothesis that the mobile fission chamber should be operated at count rates below 6000 cps – equivalent to a power of 1 W when the detector is placed in the core center–. This limitation is associated with the acquisition system electronics but not necessarily with the detector itself. According to the manufacturer, the fission chamber can operate up to 1×10^6 cps in pulse mode[7], which is far beyond the limit that was found for the entire acquisition chain by the linearity and pulse height tests.

4.2.2 Results

Figure 4.15 shows the results for the two sets of axial measurements and Figure 4.16 shows the results of the measurements along the radial direction. Note that the spline curves shown in the plots are simply employed for the sake of connecting each pair of measured data points, yet they have no physical meaning. Uncertainties bars shown in both plots are the combined (total) standard uncertainty (u_T) and are expressed with a coverage factor of $k = 1$ to provide a confidence level of approximately 68 % (1σ). A complete description of the uncertainty sources and propagation of uncertainties are presented in Section 4.2.3.

---

[7] Source: Photonis CFUF34 data sheet

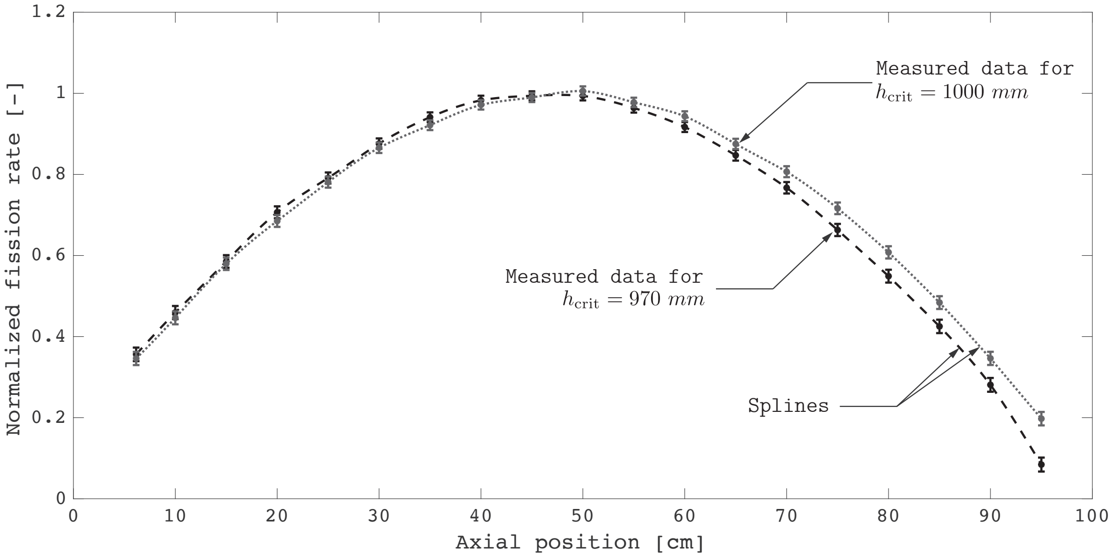

Figure 4.15 – Axial fission rate distribution measurements in the CROCUS reactor for different critical water levels (h_{crit})

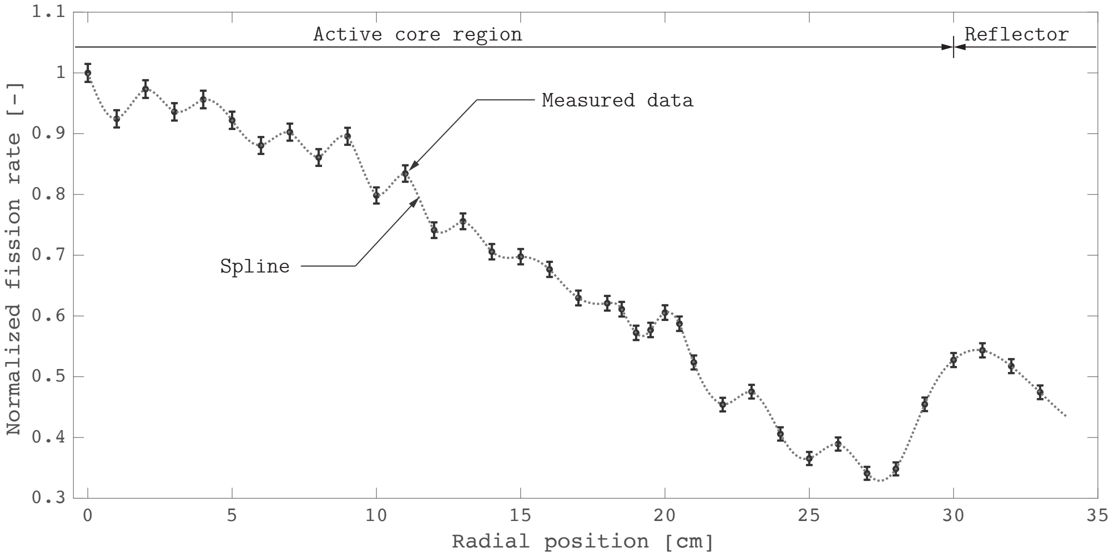

Figure 4.16 – Radial fission rate distribution measurements in the CROCUS reactor

4.2.3 Evaluation of uncertainties

The evaluation of uncertainties has been done following the *The Guide to the expression of Uncertainty in Measurement* [65]. The potential sources of uncertainty listed below have been identified, quantified and propagated to compute the total uncertainties for each $\widehat{R}_i$ measured data point[8], where i denotes a different axial or radial position

- **Detectors' signal.** The uncertainty associated with the detectors' signal was estimated assuming that the detectors' counts approximately follow a Poisson distribution. In accordance with Poisson statistics, the standard uncertainty (1σ) for the counts is given by: $u_{\text{counts}} = \sqrt{\text{counts}}$

  The relative fission rate $\widehat{R}_i$ (defined in Eq. 4.6) is computed as the ratio of the *mobile* to the *reference* fission chamber's readings; hence its standard uncertainty can be obtained using the classical law for error propagation, assuming no correlation between terms (zero covariance)

  $$u_{\text{counts}}(\widehat{R}_i) = \widehat{R}_i \cdot \sqrt{\left(\frac{\sqrt{\text{counts}^{\text{mob}}}}{\text{counts}^{\text{mob}}}\right)^2 + \left(\frac{\sqrt{\text{counts}^{\text{ref}}}}{\text{counts}^{\text{ref}}}\right)^2}$$

- **Shape tilt due to partial rod insertion.** As shown by the Monte Carlo simulation, the partial insertion (50 %) of a control rod produces a maximum tilt of about 2 % and 1 % in the axial and radial directions respectively. Results could have been corrected for this effect because the bias is known. However due to time constraints, the tilts were considered as part of the experimental uncertainty. A conservative but reasonable estimate for the uncertainty associated with this effect is given by:

  $$u_{\text{tilt}}(\widehat{R}_i) = \widehat{R}_i \cdot 2\% \qquad \text{for the axial profiles}$$
  $$u_{\text{tilt}}(\widehat{R}_i) = \widehat{R}_i \cdot 1\% \qquad \text{for the radial profiles}$$

- **Detector's position.** The mobile fission chamber's positioning system has a stated precision of ±1 mm. By assuming that all values of the uncertainty within this band are equally probable (i.e. they follow a rectangular distribution), the standard uncertainty on the position can be computed as $u(x_i) = \frac{1\text{ mm}}{\sqrt{3}}$ [65], where x is the spatial variable (radial or axial).

  Given that the profiles are not flat, the fission rate changes significantly with position, in particular for the radial case where the magnitude of the gradient (or slope) is appreciable as it is shown in Figure 4.17. The position's uncertainty contribution to the fission rate distribution can be calculated through the spatial derivative (or gradient) deriving from the classical law for error propagation

  $$u_{\text{pos}}(\widehat{R}_i) = \left|\frac{d\widehat{R}}{dx}\right| \cdot u(x_i)$$

  For the axial case, the gradient was calculated by fitting the measured data to a single-term sinusoidal and evaluating the derivative of this function. As expected, the uncertainty contribution is negligible in the axial center (where the derivative is zero) and increases towards the extremes.

---

[8] In this section, the notation for fission rate is simplified to $\widehat{R}$, which is otherwise denoted as $\widehat{R_f}$

In the radial direction, the fuel/moderator heterogeneities are much stronger than for the axial case. The spatial resolution of the measured data is not high enough to resolve such heterogeneities, and therefore we needed to rely on a higher resolution Monte Carlo simulation to compute the gradient as shown in Figure 4.17.

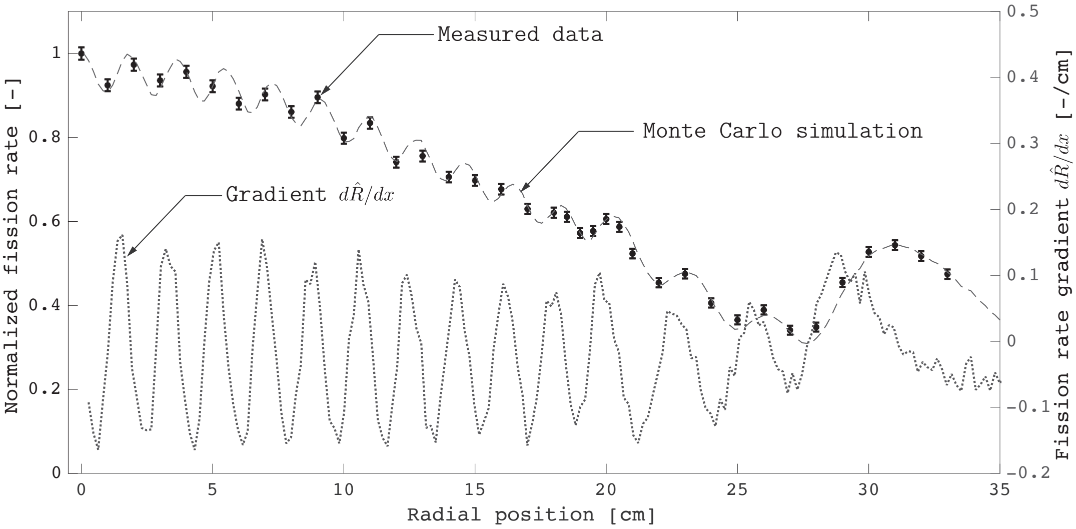

Figure 4.17 – Fission rate gradient in the radial direction. Monte Carlo simulation

The fission rate spatial derivative was then approximated by divided finite differences:

$$\frac{d\widehat{R}}{dx} = \frac{\widehat{R}_{j+1} - \widehat{R}_j}{x_{j+1} - x_j}$$

where j denotes each mesh used to tally the fission rate in the Monte Carlo simulation. Since the resulting radial gradient is highly fluctuating with the position, the envelope curve of the gradient was used as a conservative estimate for the derivative.

- **Local distortion due to the presence of the detector**: An additional potential source of uncertainty comes from the fact that the local fission rate (or neutron flux) is distorted due to the interaction of the neutron field with the detector's materials. This effect has not been quantified in the present work due to time constraints and hence it is not included in the uncertainty analysis.

All uncertainties sources quantified above are assumed independent from each other and need to be combined to produce a *total uncertainty* for the measurement. The general approach to do so is to take the square root of the sum of the squares

$$u_{\mathrm{T}}(\widehat{R}_i) = \sqrt{\left[u_{\mathrm{counts}}(\widehat{R}_i)\right]^2 + \left[u_{\mathrm{tilt}}(\widehat{R}_i)\right]^2 + \left[u_{\mathrm{pos}}(\widehat{R}_i)\right]^2} \tag{4.7}$$

4.3 Neutron kinetics measurements

Much numerical work has been done in the field of neutron reactor kinetics since the early development of nuclear reactors. However, there is a recognized need to perform relevant transient measurements for testing numerical methods and codes. Unfortunately, little work has been carried out in this subject, in particular for spatial-dependent kinetics.

The most noteworthy of the kinetic experiments have been the Special Power Excursion Reactor Test (SPERT) experiments [66] which provides data on rapid positive transients. However, much of the SPERT transient data do not specifically concern space-time effects. They rather involve feedback effects between the neutronics and thermal-hydraulic behavior of the reactor. Therefore, proper modeling of these experiments requires the use of coupled neutron kinetics/thermal-hydraulics codes. Experiments performed on the Transient Reactor Test Facility (TREAT) [67] also address neutron kinetics with thermal feedback effects.

Experimental evidence addressing space-time effects without significant thermal feedback has been much more limited in open literature. Some of the available publications have reported on transient experiments [68, 69] designed to emphasize the delayed neutron holdback effect. This effect is the delay in the establishment of the asymptotic flux shape following a fast perturbation such as a rod insertion [17]. This is most pronounced in large and weakly coupled cores where space- and time-dependent effects such as transient flux tilts are easily observed. In small tightly coupled reactors like CROCUS, transient flux tilts with delayed neutron holdback are more difficult to observe.

Most of the experimental work related to neutron kinetics on small zero-power reactors concerns noise analysis. An example is a work performed on the NORA reactor [70, 71] to develop the reactor transfer function using noise techniques. In the context of accelerator driven systems (ADS), the MUSE-4 experimental data [72] was used to account for space and time effects on the determination of reactivity [73].

The lack of transient experimental data on zero-power reactors encouraged the development of a last experimental phase in the CROCUS reactor with the objective of measuring global kinetic data and most importantly, space-dependent kinetics effects. A series of time-dependent measurements were performed in the CROCUS reactor. The first set of transient experiments were initiated by the movement of control rods and intended to produce data for global flux amplitude variations, where the reactor can be regarded as a point. These experiments will be hereafter referred to as *global flux kinetics measurements*. The second set of measurements aiming to capture spatial effects were initiated by the movement of a small neutron absorber inside the CROCUS reactor core. These experiments will be hereafter referred to as *space-time kinetics measurements*.

This section is organized into two major parts. The first one deals with global flux kinetics measurements, and the second one with measurements of space-time kinetics effects.

4.3.1 Global flux kinetic measurements

These transient measurements were performed using the same experimental arrangement than for the control rod reactivity worth measurements described in Section 4.1 (p. 42). The detection of global flux amplitude variations was done by means of out-of-core fission chambers.

Two different control rod initiated transients were measured: the first one characterized by fast insertion and withdrawal speeds and the second one by slow ones. The fast transient sequence consists of

1. The reactor is at a critical state with one control rod fully inserted
2. At $t = 0$ s the rod is completely withdrawn at full speed (~ 2 m/s)
3. The positive reactivity addition produces an exponential reactor power rise
4. At $t = 137.3$ s the control rod is completely inserted at full speed (~ 2 m/s)

Figure 4.18 shows the experimental data for this transient.

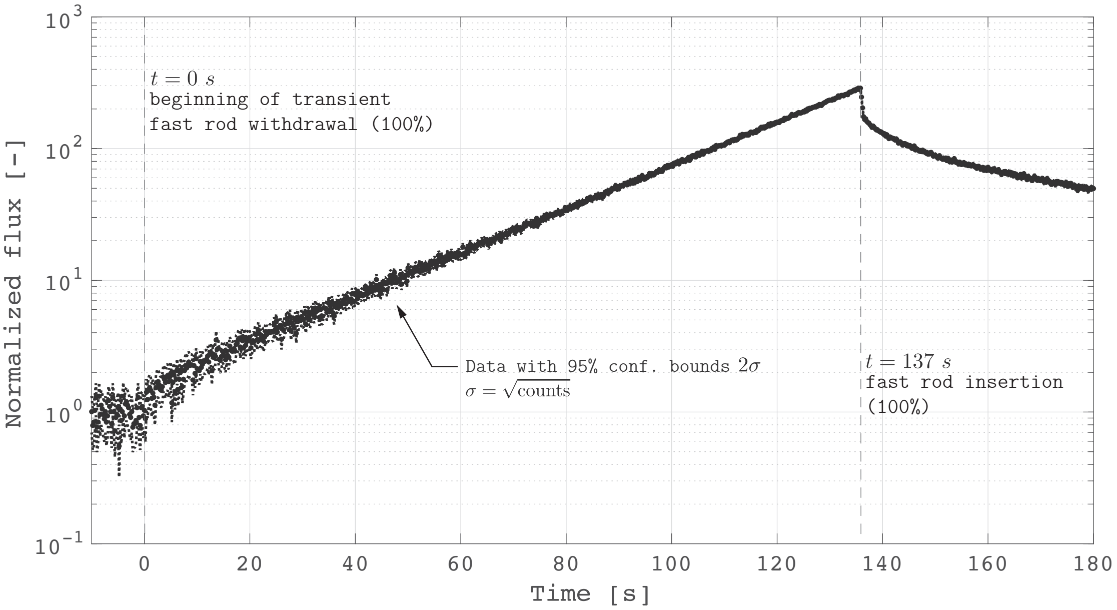

Figure 4.18 – Fast control rod withdrawal and insertion transient measurements in the CROCUS reactor

The second transient is characterized by the following sequence of events

1. The reactor is at a critical state with one control rod 50% inserted
2. At $t = 0$ s the rod starts to be removed at low speed (1.47×10^{-2} m/s)
3. At $t = 34$ s the rod reaches its fully withdrawn position
4. The control rod remains out of the for a period of 100 seconds while the power

continues to increase

5. At $t = 134\ s$, the rod begins its insertion at low speed ($1.47 \times 10^{-2}\ m/s$)
6. At $t = 202\ s$, the rod reaches its fully inserted position

The experimental data for this transient are displayed in Figure 4.19.

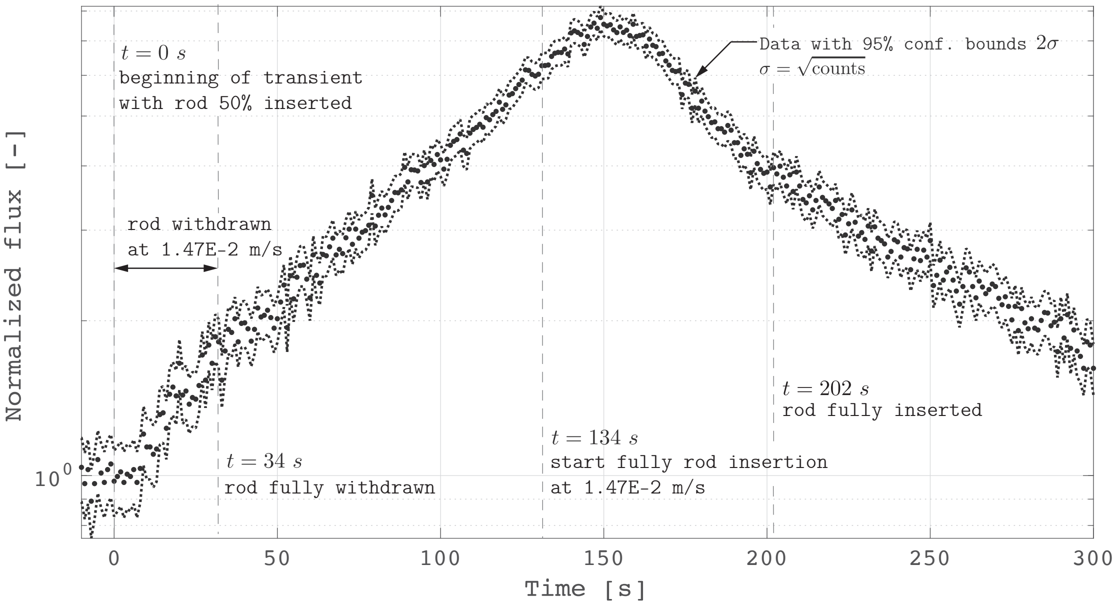

Figure 4.19 – Slow control rod withdrawal and insertion transient measurements in the CROCUS reactor

4.3.2 Space-time kinetics measurements

The objective of these experiments is to capture the spatial flux perturbation from the movement of a small neutron absorber along the axial direction of the core. This required a specific experimental setup that was not part of the standard for the CROCUS operation. The specific experimental arrangement is described below along with the experimental procedure.

This section also reports, on page 72, a characterization of the acquisition system and detector response that was made prior to executing the experiments. The signal processing techniques for reducing the statistical noise are also reported on page 74, followed by a description of uncertainty propagation on page 79. The measurement results are presented on page 81.

Experimental procedure

The small neutron absorber piece was built from a 1 mm thick cadmium sheath rolled onto a Plexiglas cylinder as shown in Figure 4.20. The absorber has an effective length of

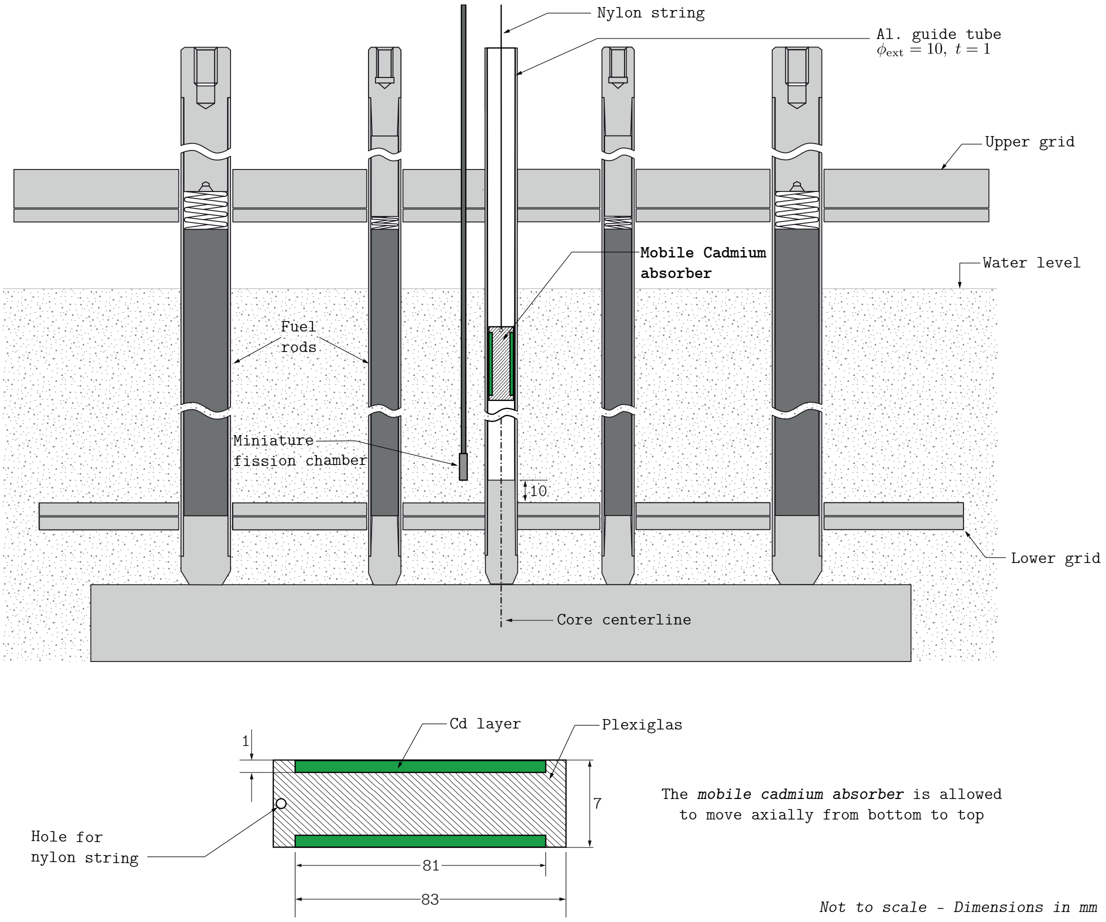
Nylon string
Al. guide tube
$\phi_{\text{ext}} = 10,\ t = 1$
Upper grid
Mobile Cadmium absorber
Water level
Fuel rods
Miniature fission chamber
10
Lower grid
Core centerline
Cd layer
Plexiglas
1
7
The mobile cadmium absorber is allowed to move axially from bottom to top
Hole for nylon string
81
83
Not to scale - Dimensions in mm

Figure 4.20 – Experimental arrangement for flux perturbation measurements

81 mm and an outer diameter of 7 mm. While the cadmium sheath's thickness is reported with an uncertainty of 0.05 mm, the active length and diameter have been measured with an uncertainty of 1 mm (1σ). The latter uncertainty value is related to the cadmium rolling process that resulted in small imperfections.

The idea behind the experimental design was to maximize the absorber's reactivity worth to length ratio. The reactivity worth of the piece at the axial center of the core resulted of approximately -0.13 \$ (or -100 pcm), which is almost 60% of the B_4C control rods worth for a piece that is 12 times smaller in length.

The absorber piece was suspended from a nylon string and inserted into an empty (air-filled) aluminum guide tube with a thickness of 1 mm and an outer diameter of 10 mm. The aluminum guide tube was located in the radial center of the core. The absorber was allowed to move axially from bottom to top by means of a stepping motor that is coupled to the nylon string through a pulley. The motor is computer-controlled, providing speed adjustment and positioning with a precision better than 0.5 mm. The absorber piece can be withdrawn in less than 0.2 seconds. The maximum insertion velocity is, naturally, larger than the withdrawal one since it is limited by gravity and the eventual friction between the absorber and guide tube. The absorber piece's position and withdrawal speed were calibrated using the computer software that controls the motor.

The specific purpose of these experiments was to capture *local spatial variations of the flux* relative to the global variations induced by the departure from a critical state. The global behavior of the flux –as it may be described by the point-reactor kinetics approximation– can be measured by the out-of-core detectors that are located in the reflector region, approximately seven centimeters away from the active core. The in-core fission chamber –located once centimeter away from the absorber's guide tube– can measure the local distortion of the flux, but also the global power amplitude variations induced by the departure from criticality. Hence, the time-dependent local distortion can be "isolated" by calculating the ratio of the in-core (i-c) to the out-of-core (o-c) detectors' readings:

$$\widehat{\phi(t)}_{\text{local}} = \frac{\phi(t)_{\text{i-c}}}{\phi(t)_{\text{o-c}}} \tag{4.8}$$

The acquisition system for the time-dependent measurements comprises two main detectors (in-core and out-of-core) and their associated electronics. Figure 4.21 shows a schematic representation of the acquisition chain. The preamplifier and amplifier associated to the out-of-core detector (Photonis CFUM21) were in-house developed and remained unchanged with respect to the previous fission rate distribution measurements (discussed in Section 4.2). A high-speed PCI-bus multi-channel scaler (Ortec MCS-pci) collected the signal from the amplifier's output to record the count rate as a function of time.

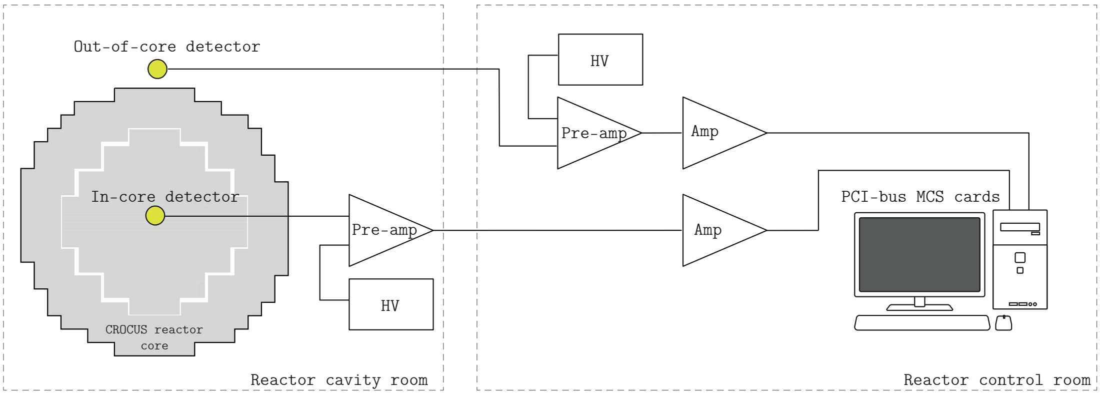

Figure 4.21 – Acquisition system schematic diagram. Time-dependent flux perturbation measurements

For the in-core measurements, the miniature-size fission chamber (Photonis CFUF34) was one more time employed but with differently associated electronics. The detector's output signal was connected to a high voltage supply and a charge preamplifier (Ortec 142A). The preamplifier signal was shaped and amplified by a voltage shaping amplifier

(Canberra 2022). The amplifier's output was connected to a second PCI-bus MCS card. The integration time of the multi-channel scalers can be set at a minimum of 100 ns, with a maximum number channels of 65536. This is more than sufficient for the time resolution and span needed in these experiments. A LabVIEW software [60] was used to control the MCS cards and to record the data. The MCS cards and the LabVIEW software allow synchronized acquisition from multiple signals.

The counting system (MCS cards and software) had been previously developed and installed for neutron noise measurements in the CROCUS reactor [60].

The transients were initiated by withdrawing the absorber piece at different speeds. Integration times between 5 ms to 400 ms were used for the measurements that lasted between 10 and 60 seconds depending on the withdrawal speed. The measurements started with the reactor at the following conditions:

- stable critical state,
- power level of approximately 1 W,
- critical water level of 1000 mm,
- absorber located at the bottom of the core,
- detector fixed at r = 15 mm and various axial positions.

The fact that the detector was fixed at r = 15 mm implies that the distance between the aluminum guide tube and the detectors is of 7.65 mm as illustrated in Figure 4.22.

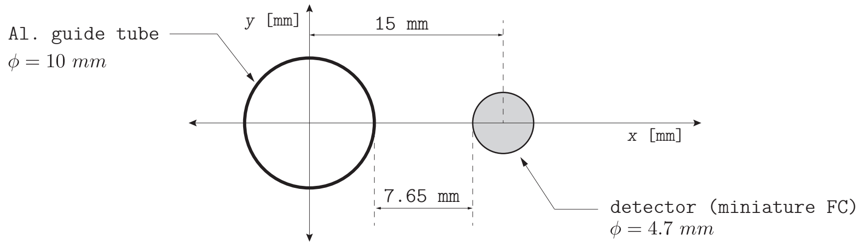

Figure 4.22 – Schematic representation of detector radial positioning with respect to Al. guide tube

The axial center of the absorber's active part was set as the reference point for its position. Therefore, h = 5.35 cm is the lower achievable axial level when it is lowered to the bottom of the core (recall Fig. 4.20).

In-core detector response

These measurements need to be carried out in the range of power where the detection system provides a linear response with respect to neutron flux. Even though the detectors are the same than those used for the fission rate distribution measurements (see p. 60), some components of the acquisition system for in-core detection were modified. The preamplifier (Tennelec TC 174) and amplifier (Tennelec TC 243) were replaced by more modern ones (Ortec 142A and Canberra 2022). These changes motivated the reassessment of the in-core detection system response. As mentioned earlier, the out-of-core detector (Photonis CFUM21) exhibits a linear response up to powers of about 40 W hence it was not included in this analysis.

A pulse-height charged-particle spectroscopy test was performed to analyze the detector signal's spectrum at different powers. To do so, the output of the voltage amplifier (Canberra 2022) was connected to a multi-channel pulse-height analyzer (Ortec 926 MCB). A spectrometry software (Ortec MAESTRO) was employed to process the multi-channel analyzer data. The detector was located at the core center (r = 0, h = 50 cm) which corresponds to the point of maximum neutron flux. The amplifier shaping time was fixed to 1 μs. Pulse-height spectra were measured and recorded for 180 seconds at various powers. Figure 4.23 shows the different spectra generated at 0.5, 1.1, 2 and 5 W, which were normalized with respect to their integrals starting from channel no. 400 to exclude the background noise. From these integrals (representing the total counts) and the acquisition time, it was possible to calculate data for the detector counts rate as a function of power. The count rate vs. power curve is shown in Figure 4.24.

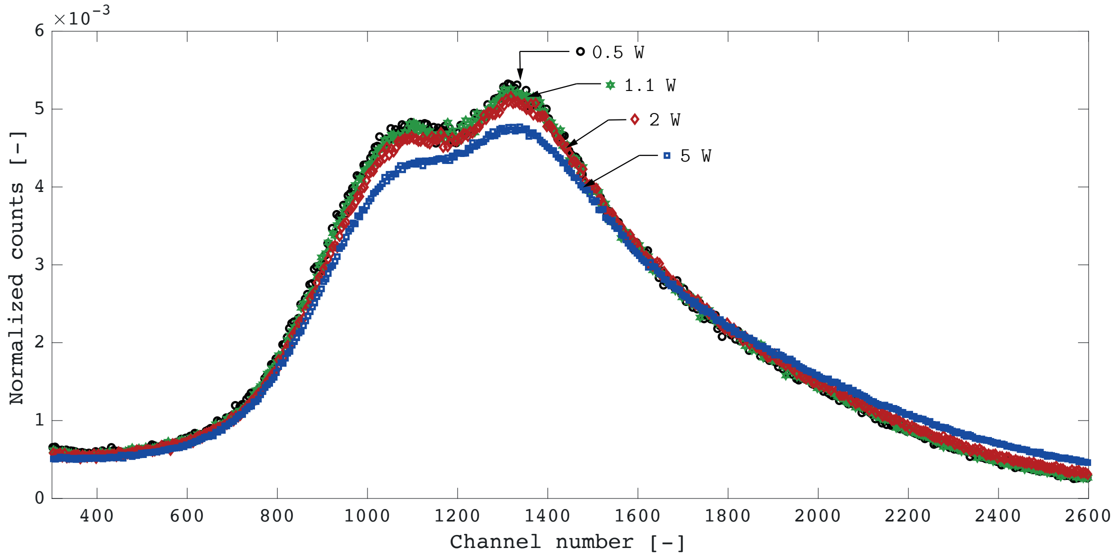

Figure 4.23 – In-core detector signal's spectra at various reactor powers

Results from the pulse-height spectroscopy and linearity test (Figures 4.23 and 4.24) suggest that the signal does not manifest significant pulse pile-up at powers below 2 W. In particular, the spectroscopy results show an improvement with respect to the electronics previously used (recall Figure 4.14). With the currently associated electronics, is it then reasonable to operate the detector at count rates below 9000 cps (or a power level around 1.5 W if the detector is located in the center of the core).

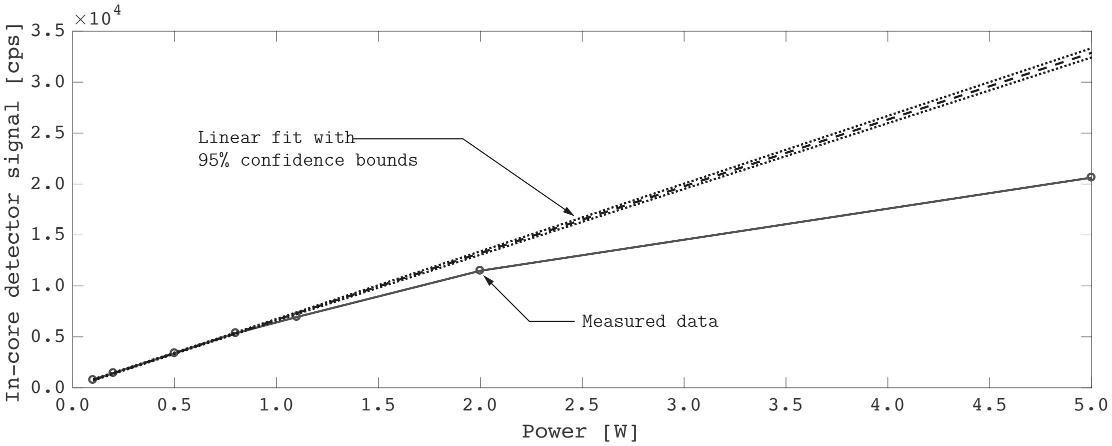

Figure 4.24 – In-core detector response versus power

Noise reduction

Due to the linearity constraints described earlier, the experiments had to be run at low power levels which derived in large statistical uncertainty associated with the measurements. Therefore, noise reduction techniques were employed to treat the in-core and out-of-core detectors signals. The techniques applied in this work to improve the quality of the measurements include *signal filtering* and *signal averaging* and are described below.

Prior to describing the noise reduction techniques, it is required to briefly discuss about the statistical uncertainty associated with neutron detection.

Poisson statistics play a fundamental role in the description of uncorrelated events occurring randomly in time, such as the disintegration of radioactive nuclei. The detection of neutrons in a nuclear reactor does not strictly follow a Poisson distribution because neutrons born from the same fission chain are time-correlated. As a matter of fact, this non-Poisson nature of fission-born neutrons is used for neutron noise measurements [74]. However, for the purposes of the present work (i.e., noise reduction and uncertainty estimation), the deviation from the Poisson statistics is small enough (in the order of few percents) to approximate the neutron counting events as a Poisson process.

Having assumed that neutron counting can be described as a Poisson process, the measured signal $N(t, \Delta t)$ will fluctuate around the mean with a magnitude of $\sqrt{N(t + \Delta t)}$, where N denotes the number of events (counts) that occur in the integration time Δt. This implies that the fluctuation (or noise) is signal-dependent and the signal-to-noise ratio (SNR) is improved only if the number of events increase ($\text{SNR} = N/\sqrt{N} = \sqrt{N}$). For a given reactor power, this derives in a trade-off between temporal resolution and noise, because the statistical noise can be reduced only at the expense of increasing the integration time.

Signal filtering

Different noise filtering techniques were tested on artificial data. A reference signal was generated from Monte Carlo simulations to reproduce noise-free experimental data for the flux perturbation measurements. The simulated data intends to replicate a typical experiment where the absorber piece is withdrawn from bottom to top at a speed of 1.7 cm/s. A series of steady-state Serpent code simulations were run for different absorber's positions. In each run, the reference signal is computed as the ratio of two detector tallies (fission rate) following equation 4.8. For simplicity, this reference signal will be hereafter denoted by $X_{\text{ref}}(t) = \phi(t)^{\text{Monte Carlo}}_{\text{i-c}} / \phi(t)^{\text{Monte Carlo}}_{\text{o-c}}$, where *i-c* and *o-c* are the in-core and out-of-core detectors. The actual transient is then approximated by a series of instantaneous Monte Carlo steady-state criticality calculations using the so-called *adiabatic approximation* discussed in Section 2.3.2. Thirty-two steady-state calculations were computed for different absorber axial positions ($z_i,\ i = 1, ..., 32$). The results were expressed in the time domain through the position and speed as $t_i = \dot{z} \cdot z_i$, where $\dot{z}$ is the absorber speed. The computational cost of this set of simulations was very large as the calculation time was approximately 2400 CPU hours to resolve the transient with 32 points, achieving a statistical uncertainty in detector tallies of 1%.

A Matlab® script was written to process the simulated data and to test some denoising techniques. Noise was added to the signals by assuming that the detector counts are Poisson-distributed and that the experiment is run at a power level of 1 W. At that power, the in-core and out-of-core detectors yield a count rate of 6000 and 2500 cps respectively. Because the reference signal is defined as the ratio of two Monte Carlo detectors tallies $X_{\text{ref}}(t) = \phi(t)^{\text{Monte Carlo}}_{\text{i-c}} / \phi(t)^{\text{Monte Carlo}}_{\text{o-c}}$, noise was not added directly to the reference signal, but rather to each of the signals resulting from the Monte Carlo simulation. The final noisy signal is computed as:

$$X_{\text{noisy}}(t) = \frac{\phi(t)^{Monte\ Carlo}_{\text{i-c}} + Pois\left[\phi(t)^{\text{Monte Carlo}}_{\text{i-c}}\right]}{\phi(t)^{\text{Monte Carlo}}_{\text{o-c}} + Pois\left[\phi(t)^{\text{Monte Carlo}}_{\text{o-c}}\right]} \tag{4.9}$$

where *Pois*(λ) is a function delivering Poisson-distributed noise following a expected value of λ.

Figure 4.25 shows an example of the simulation for reference and noisy signals at different sampling rates. The figure clearly shows that the magnitude of the noise increases with increasing time-resolution.

Having mentioned the importance of the sampling rate, the filters were tested on a noisy signal generated at a sampling rate of 200 Hz (i.e., an integration time of 5 ms), which was the typical sampling rate used for the actual measurements. The noisy signal will be referred to as "unfiltered."

A frequency-domain analysis was first performed on the *reference* and *unfiltered* signals using fast Fourier transforms (FFT). This analysis revealed that, for the simulated experiment, the transient is represented in the frequency domain below 0.2 Hz. Therefore, according to the *Nyquist sampling theorem* [75], the signal can be discretized to a minimum

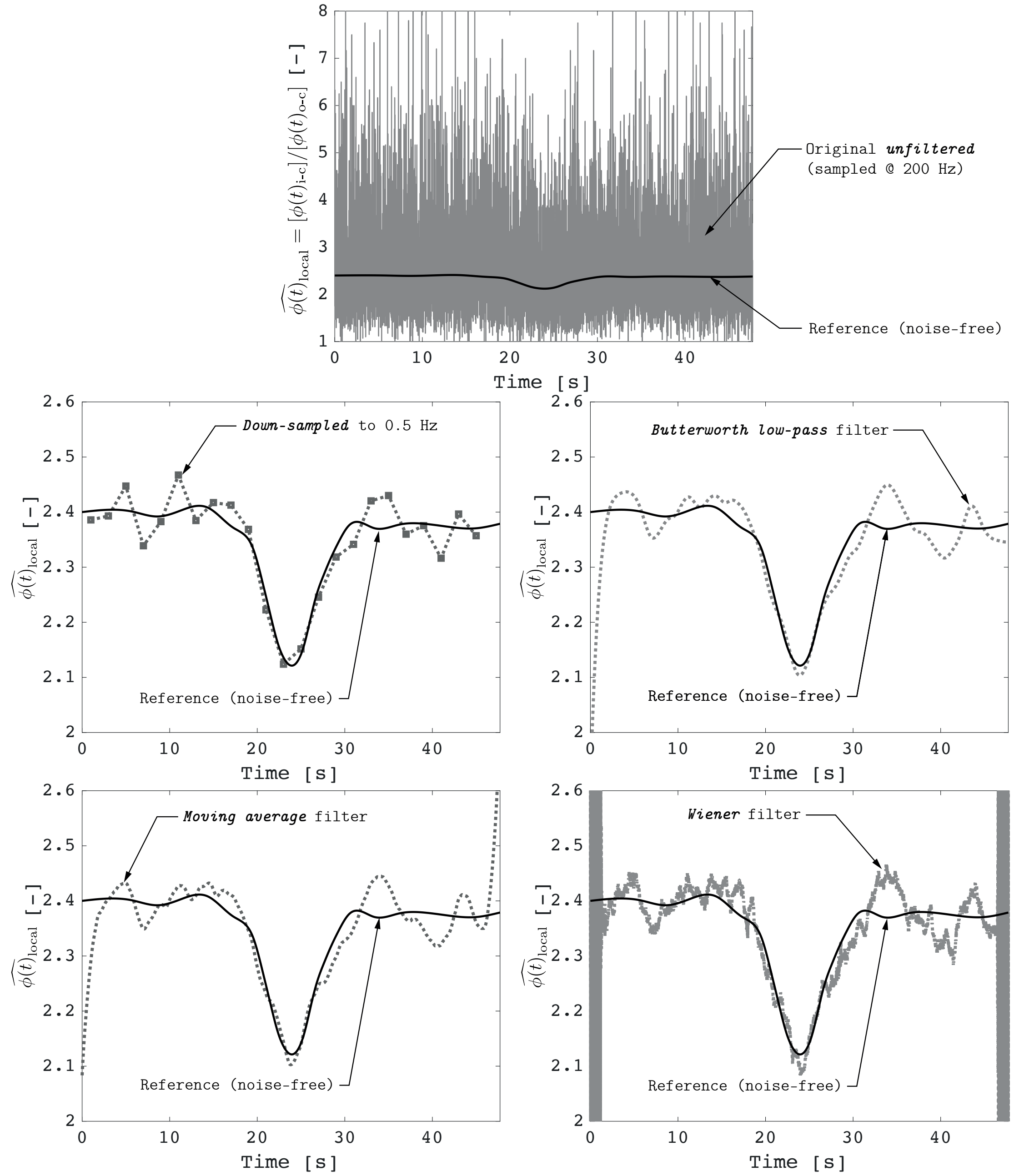

Figure 4.26 – Different filtering techniques on simulated signals

while leaving the low ones. The cut-off frequency was selected to 0.2 Hz. This filter introduces a frequency-dependent time shift (or phase distortion) that was automatically corrected by a built-in Matlab® function (`filtfilt`) that eliminates the non-linear phase distortion. The 1000 trial test on this filter yielded a mean SNR of 37.5 ± 1.5 dB. The detailed description of each filtering technique is beyond the scope of this work but can be found in textbooks by Oppenheim [75] or Smith et al. [76].

A moving average filter was also tested. The filter was set up using 500 points for the

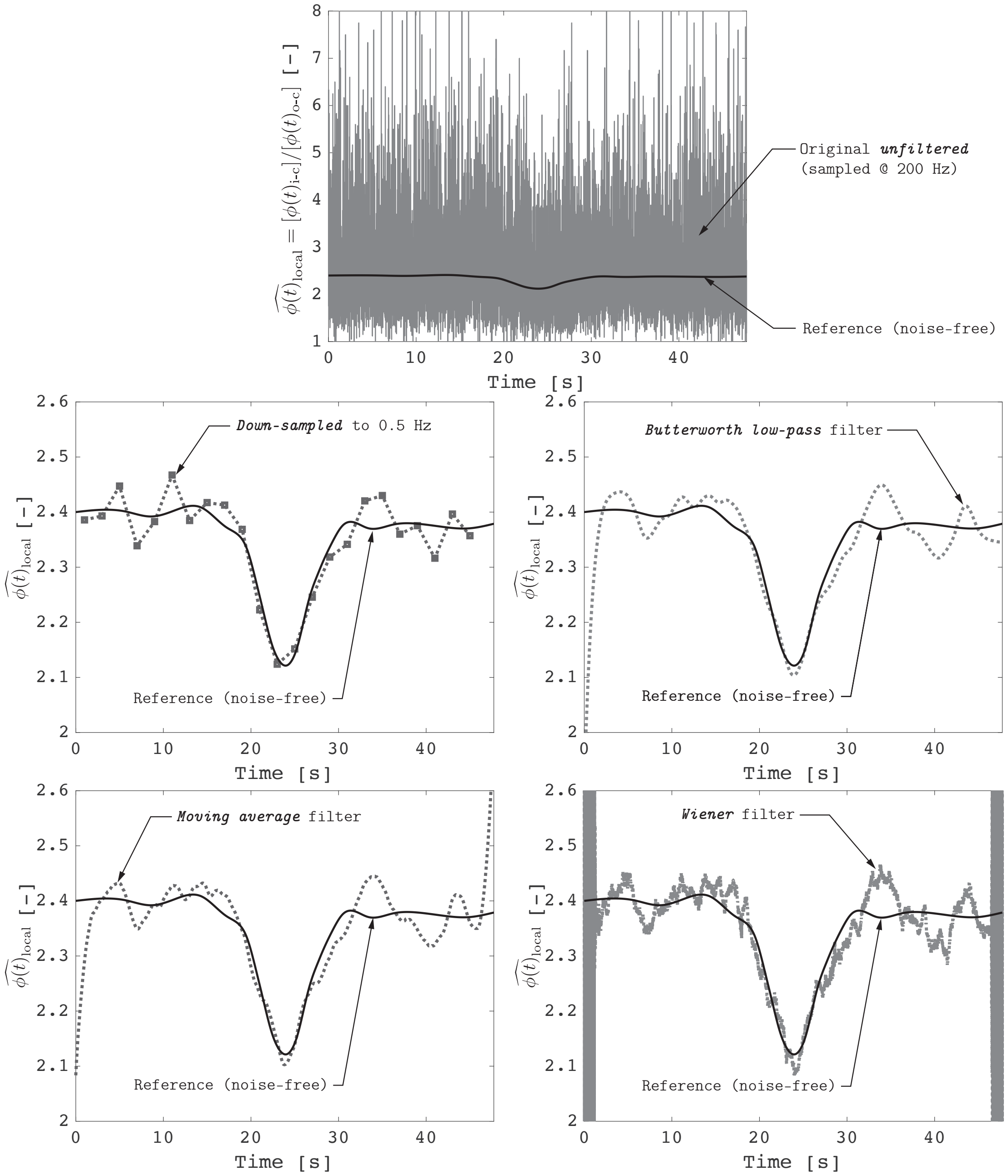

Figure 4.26 – Different filtering techniques on simulated signals

while leaving the low ones. The cut-off frequency was selected to 0.2 Hz. This filter introduces a frequency-dependent time shift (or phase distortion) that was automatically corrected by a built-in Matlab® function (`filtfilt`) that eliminates the non-linear phase distortion. The 1000 trial test on this filter yielded a mean SNR of 37.5 ± 1.5 dB. The detailed description of each filtering technique is beyond the scope of this work but can be found in textbooks by Oppenheim [75] or Smith et al. [76].

A moving average filter was also tested. The filter was set up using 500 points for the averaging, which is equivalent to smoothing the signal over a period of 500 × 5 ms = 2.5 s. The 1000 trial test on this filter yielded a mean SNR of 38.3 ± 1.5 dB.

Lastly, an adaptive Wiener filter was also tested on the unfiltered data. The 1000 trial test on this filter yielded a mean deviation of 35.2 ± 1.0 dB.

Figure 4.26 shows the reference, unfiltered and filtered signals using the various techniques mentioned above. While the down-sampling technique yields the lowest performance in terms of signal to noise ratio, the low-pass and moving average techniques yield the best results. The adaptive Wiener filter seems to show lower performance than the latter two. Note that the parameters for each of these filters need to be optimized for each particular problem.

The moving average filter was selected in this work to reduce the statistical noise of the in-core and out-of-core detectors. This filter was used in conjunction with the *signal averaging* technique whenever multiple measurements were made possible.

Signal averaging

Let us consider a measured time-dependent signal that is corrupted by random noise such as the one coming from the in-core detector used in the present experiences. If we are able to repeat that measurement N times, it is then possible to sum the set of N signals and divide them by N to obtain an average with improved signal-to-noise ratio. Even though this technique is quite simple to implement, certain conditions need to be met before applying it:

- Naturally, it is required to repeat the time-dependent experiment more than once to be able to compute the average. This was indeed possible for some of the time-dependent measurements carried out in the CROCUS reactor.
- The temporal position of each signal must be accurately known for a proper time-synchronization. For every time-dependent measurement, the start of the transient was recorded with an uncertainty of 0.5 seconds.
- The noise associated to the signal has to be stochastic because its random nature allows to canceled out the noise in the averaging process. Given that, in this work, the total counts per integration time step can be reasonably assumed to be Poisson distributed, the noise associated to the measured signals have a large stochastic component that allows to implement this technique.

Figure 4.27 provides an example of a time-dependent signal (Reference) that has been measured with associated Poisson noise with a SNR of 30 dB (Single trial). The measurement was repeated 100 times to improve the signal-to-noise ratio to 50 dB using the *signal averaging* technique (100 trials average). The SNR improvement is given by $\mathrm{SNR}_N = N \cdot \mathrm{SNR}_{\mathrm{single}}$ or alternatively in decibels as $\mathrm{SNR}_{\mathrm{N,dB}} = 10 \cdot \log_{10}(N) \cdot \mathrm{SNR}_{\mathrm{single,dB}}$, where N is the number of trials.

The example shown above represents only a simulation and has no relation with the experiments. For the actual measurements, this technique has been applied using a total of nine samples as it will later shown, which improves the SNR by 10 dB.

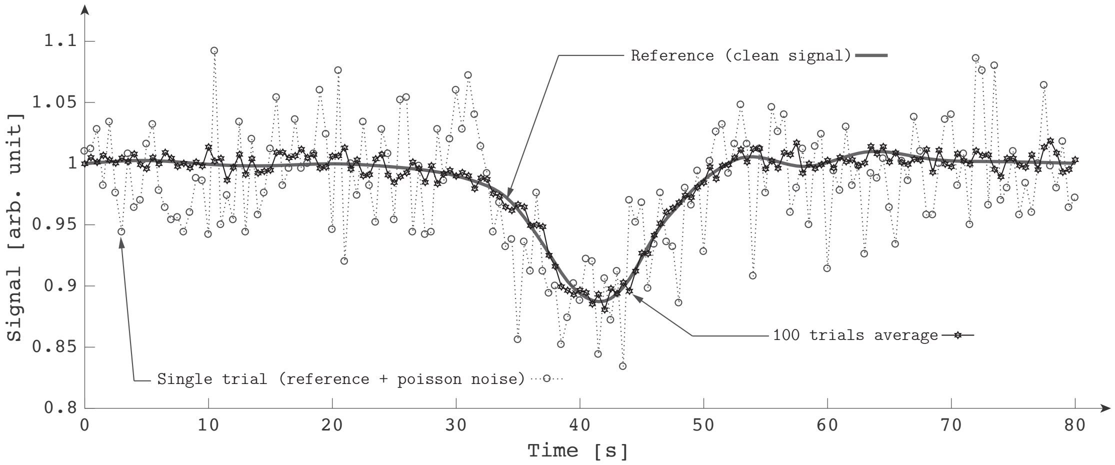

Figure 4.27 – Example of signal averaging for 100 trials

Evaluation of uncertainties

A. Statistical uncertainty. Provided that signal denoising is performed in an optimum way where the amplitude of the noise is reduced as much as possible while retaining the shape of the signal, the statistical uncertainty can be then reduced without introducing a bias.

The statistical uncertainty after denoising was evaluated by a Matlab® script in the following manner:

1. The reference (noise-free) signal was generated as explained in the signal filtering section.
2. A total of S noisy signals were generated in a loop using Poisson statistics and following equation 4.9.
3. Each of these S signals were filtered using the Moving average, Butterworth low-pass and adaptive Wiener filter.
4. The deviation (or error) of these filtered signals from the reference signal was computed as:

$$d_{\%}(t_i) = \frac{X_{\text{filtered}}(t_i) - X_{\text{ref}}(t_i)}{X_{\text{ref}}(t_i)} \cdot 100$$

5. The probability distributions of the deviations –as computed from the previous equation– provide information about the uncertainty and a potential bias due to

filtering. The standard uncertainty was computed as the square root of the variance when the curves followed a normal distribution. The mean value and shape of the distribution provides information about the bias.

6. The same approach taken in items 1 to 5 was followed to assess the uncertainty due to signal averaging in addition to filtering. Before filtering, each of the S signals had been previously averaged in a nested loop using N noisy signals. In other words, from N noisy signals, we obtain one averaged signal that is later filtered; and the procedure is repeated S times.

Figure 4.28 shows the probability distributions of the relative deviations $d_{\%}$ of the filtered signals with respected to the reference. The probability distributions were obtained for $S = 1000$ trials. On the right-hand side of the figure, results are shown for the case where the moving average filter is applied after performing signal averaging over 9 signals. The distribution no. 5 (green) corresponds to the case where the signal is over filtered, resulting in a bias (or systematic error). The shape of the distribution shows a clear departure from the normal one, indicating that the error is no longer random. If the filters are properly applied (i.e. being optimized), the probability distributions follow a normal shape and the mean value tends to zero. The uncertainties (taken as the square root of the variances) and mean values are listed in Table 4.6. The mean values listed in the Table in conjunction with the shape of the distribution, express that the deviation (or error) is random and that there is no bias.

B. In-core detector's position. The in-core detector's position influences the accuracy of the measured data such as shown for the Reaction rate distribution measurements. The contribution of detector's axial position to the uncertainty in the time-dependent measurements was computed in Section 4.2.3. For this calculation, it was assumed that the detector positioning system has a precision of ±1 mm. Results are shown in Table

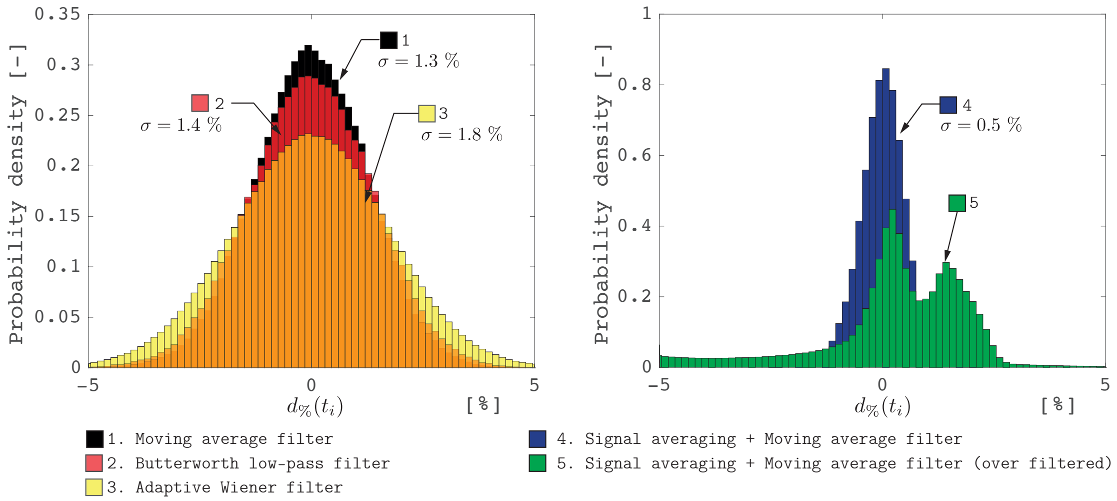

Figure 4.28 – Probability distributions of the error after signal denoising

Table 4.6 – Statistical uncertainty after signal denoising

Denoising technique	Std. uncertainty σ [%]	Mean $\mu \pm \sigma_\mu$ [%]†
Moving average filter	1.3	-0.02 ± 0.04
Butterworth low-pass filter	1.4	-0.01 ± 0.04
Adaptive Wiener filter	1.8	-0.02 ± 0.05
Averaging + moving avg. filter	0.5	-0.01 ± 0.02

$^\dagger\sigma_\mu = \frac{\sigma}{\sqrt{S}}$, $S = 1000$ trials

4.7.

Table 4.7 – Uncertainty due to in-core detector's axial position

Axial position [cm]	50	45	40	35	30	25	20
Axial position [cm]	50	55	60	65	70	75	80
Uncertainty [%]	0.0	0.1	0.2	0.3	0.3	0.4	0.5

When the detector is located in the axial center, the contribution of detector position to the uncertainty is minimal because the gradient of the neutron flux is almost zero. This is reflected in Table 4.7.

C. Other sources of uncertainty. The uncertainty on the detector's radial position represents a potential source of uncertainty for the time-dependent measurements because the measured distortion ($\widehat{\phi(t)}_{\text{local}}$) is reduced as the detector moves away from the absorber piece's line of motion. This source of uncertainty has not been quantified in the present work, however it could be assessed through a set of Monte Carlo simulations.

Also, as discussed in the Reaction rate distribution measurements (Section 4.2.3), an additional potential source of uncertainty comes from the fact that the local neutron flux is distorted due to the interaction of the neutron field with the detector's materials. This effect has not been quantified in the present work either and could also be assessed by means of Monte Carlo simulations.

Results

The first set of measurements was performed to identify the maximum speed of the absorber at which the transient can be resolved from the statistical noise. For these measurements, the mobile absorber was initially placed at the axial mid-plane (h = 50 cm) and the detector was located 30 cm higher (h = 80 cm). The radial position of the detector was fixed to r = 15 mm for all measurements as indicated earlier. The transients started after withdrawing the absorber at speeds of 17.3 ± 0.9 cm/s, 8.7 ± 0.3 cm/s, 3.47 ± 0.06 cm/s and 1.74 ± 0.03 cm/s. An integration time of 400 ms was used for these measurements. The uncertainties on the speeds represent the standard uncertainty (1σ) with a coverage factor of $k = 1$. They were computed using the standard law for

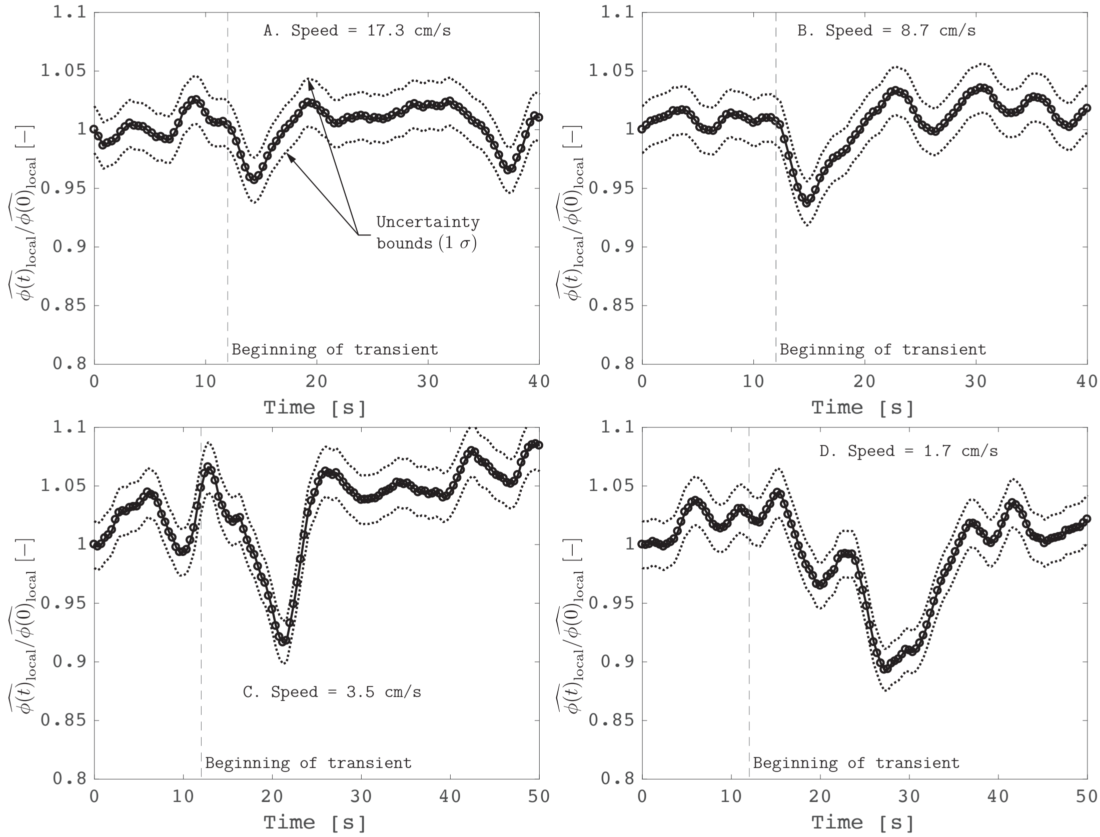

Figure 4.29 – Local distortion measurements for different withdrawal speeds. In-core detector at h = 80 cm

uncertainty propagation, with an uncertainty in the time measurements of 0.5 s and equally probable (rectangular) distributions.

The results for the first series of measurements are shown in Figure 4.29 and suggest that the distortion is reasonably discriminated from the signal's noise for speeds below 3.5 cm/s. In the plot *A* –top left, corresponding to an absorber speed of 17.3 cm/s–, the second depression observed near $t = 37$ s was caused by the lowering of the piece to its initial position (h = 50 cm). The beginning of the transient has been measured with an uncertainty of ±1 s. Note that the plots in the bottom (*C* and *D*) are displayed in a larger time scale because the experiments were performed at lower speeds.

A second series of measurements were taken for different in-core detector positions along the axial direction. The mobile absorber was initially placed at the bottom of the core (h = 5.35 cm), and later withdrawn at a speed of 1.7 cm/s. At that speed, it takes in the order of 55 seconds for the absorber to move from bottom to top of the core. The measurements were carried out for the in-core detector located at h = 15, 32.5, 50, 67.5 and 85 cm. Figure 4.30 shows the results in separated plots (A, B, C, D and E) and also as a whole (F). The plots illustrate how the measured flux distortion is shifted towards

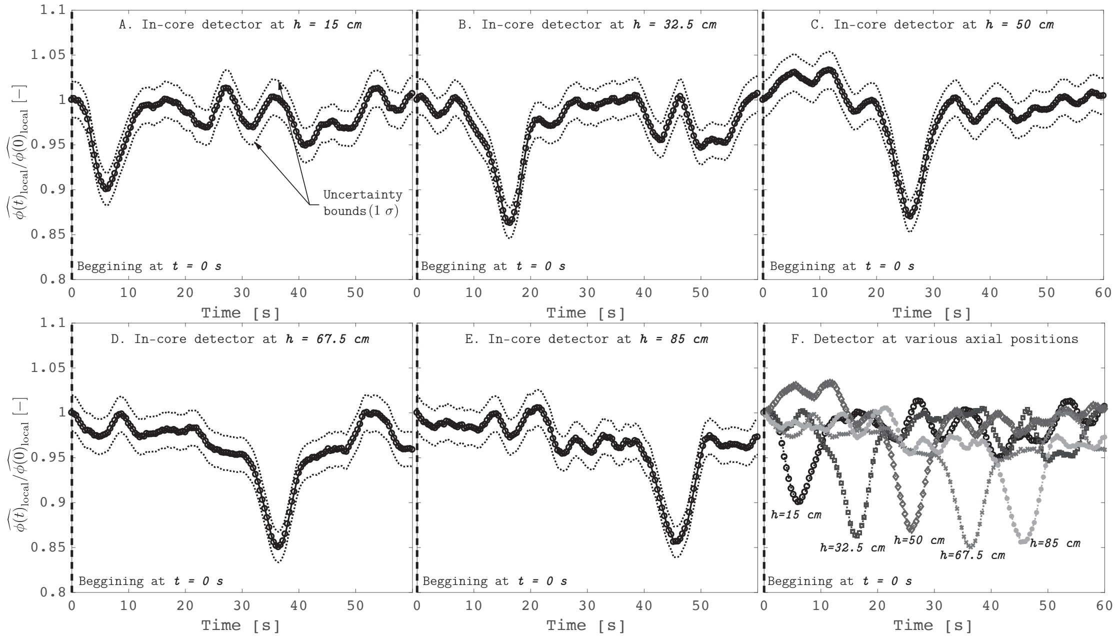

Figure 4.30 – Local distortion measurements for absorber speed of 1.7 cm/s and various in-core detector positions

larger times as the detector is moved to the top of the core. The plots show no clear evidence of the optimal detector position for better distortion discrimination.

Given that the previous series of measurements were affected by statistical noise, the last series of measurements attempted to improve the quality of the measured signal. Several measurements were repeated under the same conditions (i.e., same absorber speed and detector position) to reduce the noise using the *signal averaging technique*. For these measurements, the mobile absorber was initially placed at the bottom of the core (h = 5.35 cm), and later withdrawn at a speed of 1.7 cm/s. The in-core detector was fixed at h = 50 cm (axial center).

A total of nine measurements were repeated following the same experimental procedure and were synchronized in time. Because the signal averaging technique can be only applied to signals with random noise, the average signal was first computed from the unfiltered signals. The average signal was later filtered using a moving average filter.

Figure 4.31 shows the individual measurements (left) and the average resulting from the nine measurements (right). The transients started at t = 0 s. The individual measurements shown in the figure were filtered using a moving average filter. The uncertainty bounds for the individual runs were not plotted for the sake of clarity. The average signal represents a clear improvement in terms of signal quality and uncertainty reduction.

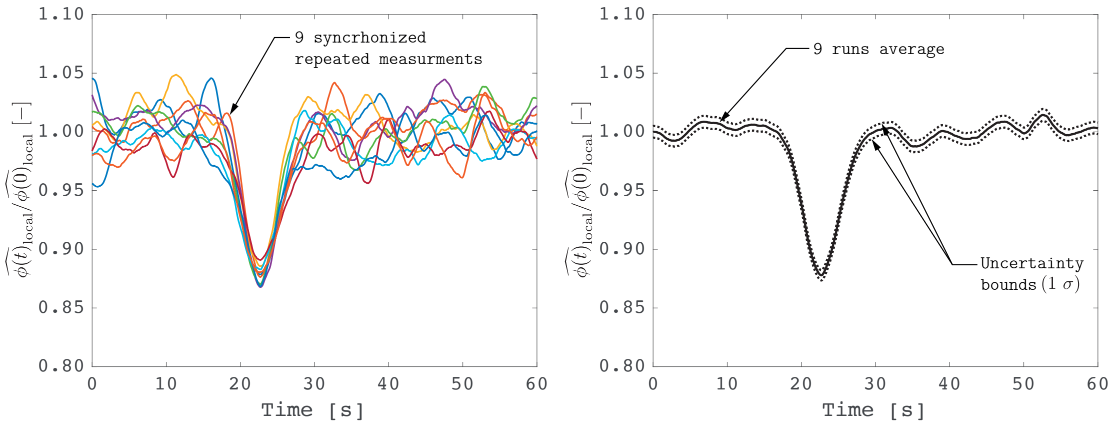

Figure 4.31 – Local distortion measurements for absorber speed of 1.7 cm/s and detector was fixed at h = 50 cm

5 Numerical analysis

As outlined earlier, the PARCS code has been chosen for the 3-D steady-state and time-dependent modeling of the CROCUS reactor. Details about the code have been discussed in Section 2.3.4 (p. 29).

The few-group macroscopic cross sections and delayed neutron data required by the PARCS code were generated by the Serpent code [26]. Serpent is a three-dimensional continuous-energy Monte Carlo code that has been specifically designed for lattice physics applications. The Serpent code has also been used in this work for full-core steady-state calculations. The entire calculation scheme for the modeling of the CROCUS reactor is depicted in Figure 5.1.

This chapter is divided into three sections. A first part describes the few-group constant parameters generation and full-core modeling with the Serpent code, a second part presents the PARCS code modeling of the CROCUS reactor and a third part presents some computational results with Serpent and PARCS codes. The comparison of the simulation results against experimental data is presented in Chapter 6.

5.1 Serpent code modeling of the CROCUS reactor

The Serpent code has been primarily used for group constant and delayed neutron data generation. The relatively small size of the CROCUS reactor made full-core three-dimensional reactor calculations feasible. These full-core calculations were also used as a reference for the comparison against PARCS steady-state solutions.

The Serpent model of the CROCUS reactor has been built in detail with no major approximations. It comprises all reactor components within the water tank including the supporting structure below the core and main nuclear instrumentation. Figure 5.2 shows the geometry and reaction rate plots for the full-core Serpent model of the CROCUS reactor. The exterior surfaces of the aluminum grid plates were used as computational

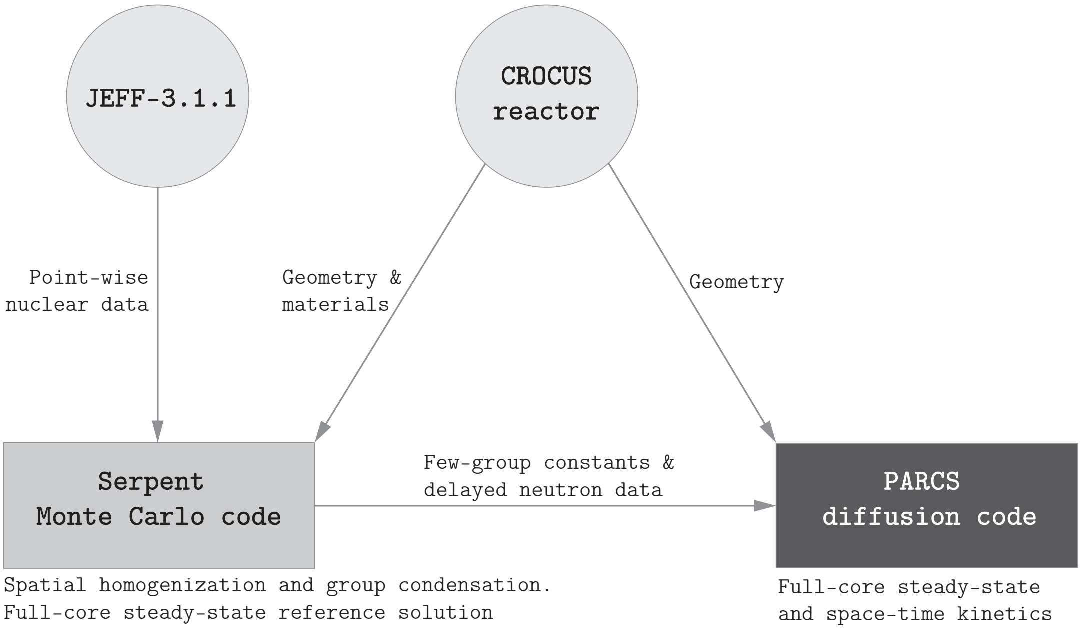
JEFF-3.1.1
CROCUS reactor
Point-wise nuclear data
Geometry & materials
Geometry
Serpent Monte Carlo code
Few-group constants & delayed neutron data
PARCS diffusion code
Spatial homogenization and group condensation. Full-core steady-state reference solution
Full-core steady-state and space-time kinetics

Figure 5.1 – Calculation scheme for CROCUS reactor modeling

boundaries for the radial and bottom directions. The top boundary is defined by the end of the fuel rods as shown in Figure 5.2. Vacuum boundary conditions were imposed on all external surfaces.

The Serpent code version 2.1.27 and the JEFF-3.1.1 nuclear data library were used for the simulations. A typical full-core calculation was run using 10^4 cycles of 10^6 neutrons each to achieve eigenvalue estimates within ± 0.7 pcm. The calculation time for a run with this number of neutron histories was approximately 1600 CPU hours on a 2.93 GHz machine (i.e. using a single processor). The nuclear data was evaluated at 300 K. The thermal scattering data for hydrogen in light water was taken from the JEFF-3.1 library and was evaluated at 294 K.

To improve Serpent results accuracy, probability tables were used to sample cross section data in the unresolved energy resonance regions. The input file for the Serpent model of the CROCUS reactor is listed in Appendix B.1.

5.1.1 Few-group constants generation

The input parameters used by the PARCS code to compute steady-state and transient solutions for the CROCUS reactor are:

1. Transport cross-sections $\Sigma_{tr,G}$ (or alternatively, diffusion coefficients D_G)
2. Absorption cross-sections $\Sigma_{a,G}$

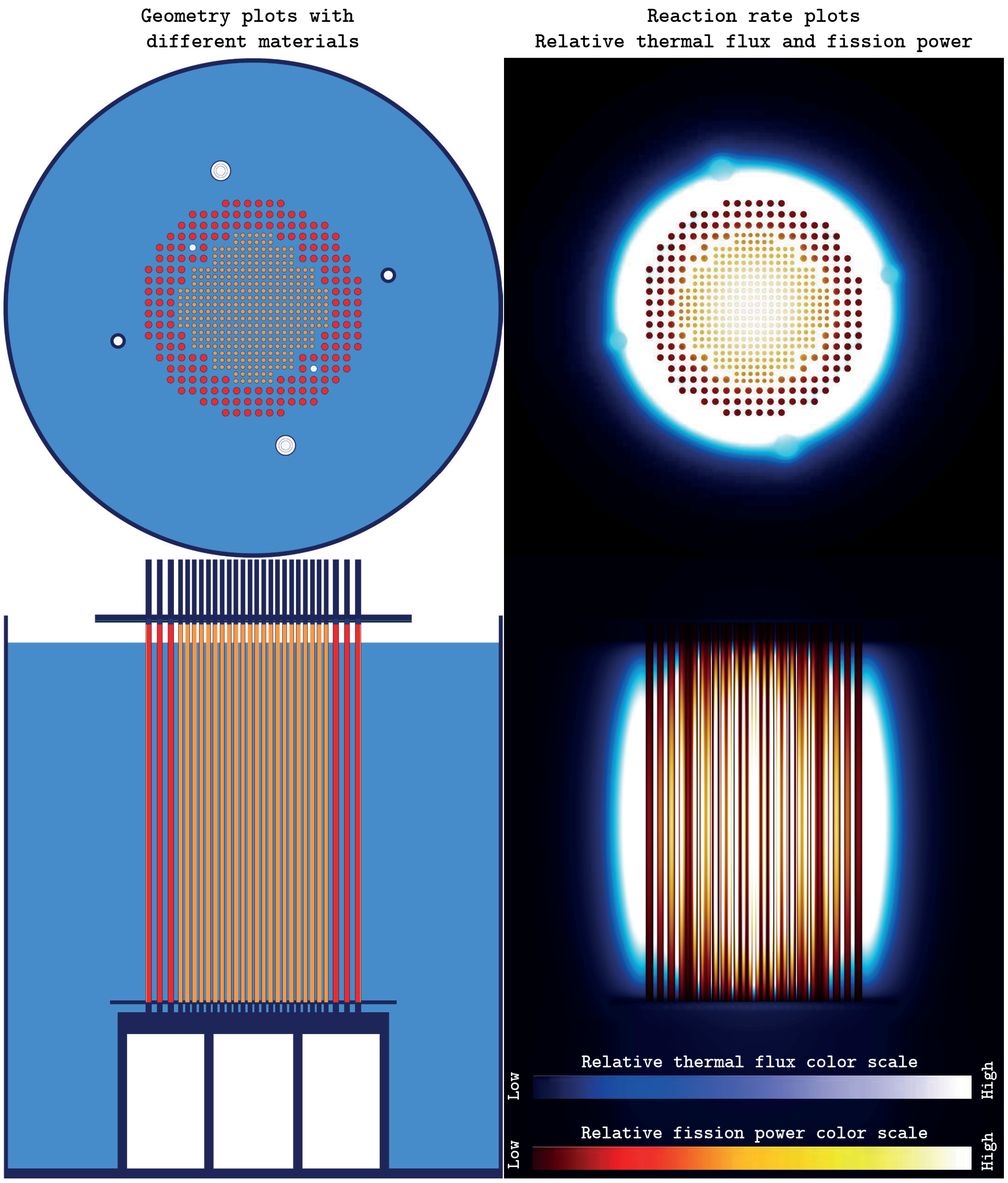

Geometry plots with different materials

Reaction rate plots
Relative thermal flux and fission power

Relative thermal flux color scale
Low
High
Relative fission power color scale
Low
High

Figure 5.2 – Top and side views of full-core Serpent model of the CROCUS reactor. Geometry plots (left) and reaction rate plots (right)

3. Fission cross-sections $\Sigma_{f,G}$
4. Average number of neutrons released per fission ν
5. Group-to-group scattering cross-sections $\Sigma_{s,GG'}$
6. Fission spectrum χ_G
7. Energy release per fission κ

8. Effective delayed neutron fraction β_i
9. Decay constant of delayed neutron precursors λ_i
10. Inverse neutron velocities v_G^{-1}
11. Albedos β_G
12. Detector cross-sections $\Sigma_{det,G}$
13. Form functions FF

While items 1 to 6 are needed for solving the multi-group diffusion equations, items 8 to 10 are employed in time-dependent problems to solve the delayed neutron precursor concentration equations. The energy released by fission is used to normalize the absolute value of neutron flux. Finally, each of the items from 11 to 13 are employed to set boundary conditions, for detectors modeling and for the reconstruction of heterogeneous quantities from homogenized solutions, respectively.

The parameters listed above were generated with the Serpent Monte Carlo code because, recalling the discussion on the use of Monte Carlo codes for lattice physics application, the main advantages of using the Serpent code for this purpose are:

- Few-group constants can be generated from the full-core geometry rather than from the traditional 2-D assemblies with reflective boundary conditions.
- The full-core transport calculation can be used as a reference steady-state solution.

The Serpent code uses universes to describe geometries and also to define the regions where spatial homogenization and energy collapsing take place. The whole few-group constants data can be produced for multiple universes within a single run. Almost all of the parameters needed by PARCS can be extracted directed from the Serpent output file, with exception of the detector cross-sections, form functions, and albedos that require additional treatment with user-defined tallies.

The group-wise macroscopic cross-sections were homogenized using seven non-overlapping universes defined within the full-core geometry of the reactor as shown in Figure 5.3. The choice of each universe was based on homogenizing over regions where material properties are already rather homogeneous, namely UO_2 cells with water, U-metal cells with water, water reflector, control rod cells with water, UO_2 cells with air, U-metal cells with air, and control rod cells with air. It should have been possible to further subdivide these regions, for example by defining an inner and outer UO_2 fuel region, and also an inner and outer U-metal region such that the core is represented by four concentric ring-shaped regions. Likewise, the reflector region could have been represented by concentric universes.

However, this has not been tested in the present work. Each color in Figure 5.3 represents a different homogenization universe. These universes were deliberately defined to match the PARCS mesh structure. The homogenization region was axially limited by the lower and upper grid plates where partial currents were tallied for the estimation of albedos.

The few-group constants were converted into a PARCS-readable format using the GenPMAXS v6.1.3co code [77]. The GenPMAXS code was specifically built as an interface between various lattice physics codes and PARCS. It provides cross-section data in PMAXS file format, which allows PARCS to perform steady-state, transient and core-depletion calculations. There are other ways to input cross-section data into the PARCS code, however the PMAXS format is the most extended one because it allows to use almost all PARCS capabilities.

As it will be specified in the following section (p. 95), two solution kernels were used in PARCS: the coarse-mesh finite difference (CMFD) and the fine-mesh finite difference (FMFD) kernels. While cross-section data for the CMFD kernel was provided in the form of PMAXS files, the FMFD kernel requires a specific format and does not support PMAXS files. A Matlab® script was written to convert Serpent's output to FMFD-formatted cross-section data (see Appendix B.2). This script can generate multi-group cross-section data, however it does not produce kinetic parameters because time-dependent simulations were not run with the FMFD solver.

The following sections address specifics about correction of diffusion coefficients, generation

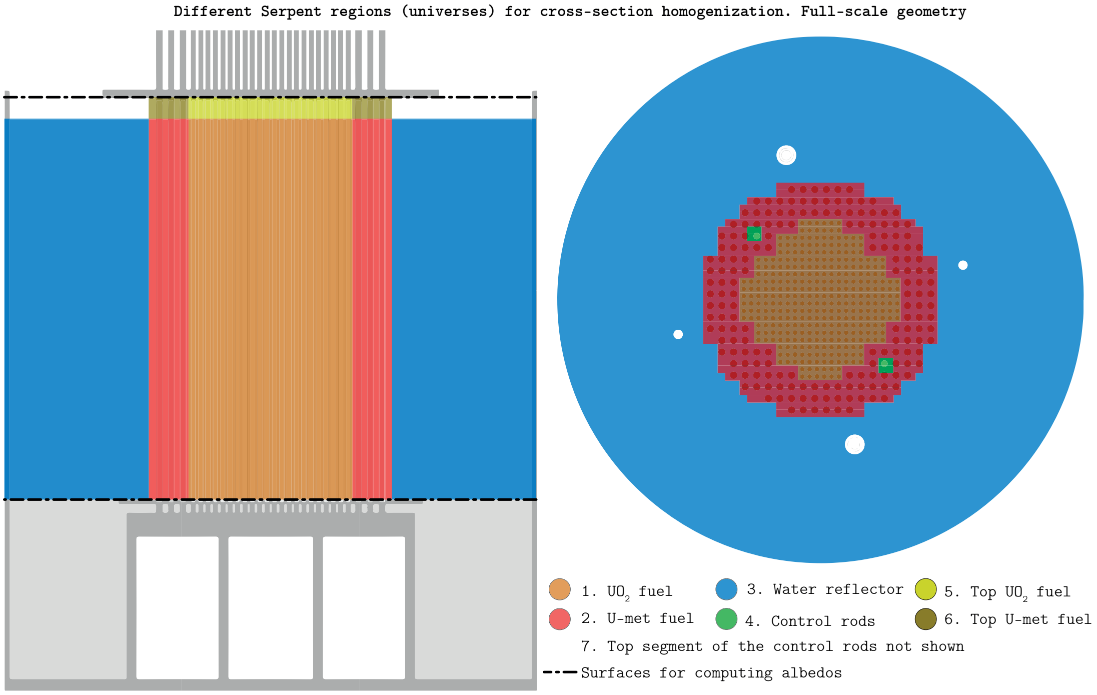
Different Serpent regions (universes) for cross-section homogenization. Full-scale geometry
1. UO$_2$ fuel
2. U-met fuel
3. Water reflector
4. Control rods
5. Top UO$_2$ fuel
6. Top U-met fuel
7. Top segment of the control rods not shown
Surfaces for computing albedos

Figure 5.3 – Serpent regions for cross-section homogenization in the CROCUS reactor

of albedos, detector cross-sections, form functions, control rod cross-sections and kinetic parameters.

In-scatter correction of diffusion coefficients

As discussed in Section 2.3.3 (p. 27) Serpent code uses two approaches to estimate diffusion coefficients. The first method is derived from the P_1 equations and uses the *out-scatter approximation* to obtain the transport cross-sections. A second definition is derived from the B_1 equations to correct diffusion coefficients based on an artificial leakage spectrum. Because the full-scale geometry was used to generate few-group constants for the CROCUS reactor, leakage models were not needed and therefore leakage-corrected diffusion coefficients were not implemented. The following section focuses only on the first approach.

Various manners to derive transport cross-section from the P_1 equations have been presented in Section 2.2.4, amongst which the in-scatter and out-scatter methods deserve special consideration in the present context. With the exception of a few lattice physics codes such as CASMO [6] and HELIOS [37], many codes rely on the out-scatter method for the generation of diffusion coefficients. The out-scatter method yields acceptable results for most for most reactors, however it has been reported that this approximation leads to important errors in light water reactors (LWR) with large neutron leakages [78, 29]. These errors are attributed to the fact that the out-scatter approximation does not properly treat scattering anisotropy at high neutron energies.

Herman et al. [79] developed a correction method that accounts for the out-scatter method's deficiencies in the treatment of scattering anisotropy. Because in LWRs the hydrogen bound to water is the main responsible for this anisotropy[1], the method was initially applied to the ^{1}H isotope, however it can be extended to any isotope. This correction is applicable to Monte Carlo codes and allows to generate diffusion coefficients consistent with the in-scatter method. The approach is equivalent to that one used by CASMO [6] and has been recently implemented in the second version of the Serpent Monte Carlo code (Serpent 2).

The idea behind this method is to correct the transport cross-section of the isotope responsible for the scattering anisotropy such as Hydrogen, if we are dealing with a LWR. This is achieved by first generating transport cross-sections that treat in-scattering without approximations to later obtain an *energy-dependent transport-to-total correction curve.* The transport and total cross-sections can be obtained from a fixed-source problem of a one-dimensional homogeneous slab of this isotope. The simplicity of this problem allows to obtain the diffusion coefficient directly with no approximations. Then, the transport-to-total correction curve is computed as follows

---

[1] as seen from the laboratory (LAB) reference frame

$$f_i(E) = \frac{1}{3D(E)} \cdot \frac{1}{\Sigma_{t,i}(E)} = \frac{\Sigma_{tr,i}(E)}{\Sigma_{t,i}(E)} \tag{5.1}$$

where i stands for isotope used in the slab problem. Note that no other isotope is present in the homogeneous slab problem and that the energy dependence in Eq. 5.1 is in practice handled using a very fine energy group structure.

This curve can be later used by the lattice code (Serpent) to perform the in-scattering correction on the out-scatter-approximated transport cross-sections. The general procedure is the following one:

- The lattice code computes the total and non-corrected transport cross-sections of the isotope i: $\Sigma_{t,i}(E)$ and $\Sigma_{tr,i}(E)$
- The lattice code computes the total and non-corrected transport cross-section for all other isotopes: $\Sigma_{t,all}(E)$ and $\Sigma_{tr,all}(E)$
- The lattice code corrects the transport cross-sections of the isotope i using the pre-computed correction curve:

  $$\Sigma_{tr,i}^{IC}(E) = \Sigma_{t,i}(E) \cdot f_i(E)$$

  where the superscript IC indicates that the cross-section has been in-scatter corrected.
- The lattice code removes the non-corrected isotope i component from the transport cross-section of all other isotopes and adds the corrected transport cross-section of isotope i:

  $$\Sigma_{tr,all}^{IC}(E) = \Sigma_{tr,all}(E) - \Sigma_{tr,i}(E) + \Sigma_{tr,i}^{IC}(E)$$

Herman [81] showed that this correction yields transport cross-sections consistent with the in-scatter approximation. A numerical study addressing the impact of this correction for the CROCUS reactor and also for different reactor core sizes will be presented later in Section 5.3.

Albedos

Albedos are used to establish general boundary conditions for the solution of the multigroup diffusion equations. The albedo factors (β_G) essentially represent the ratio of in-going to out-going group-wise currents in a boundary surface.

$$\beta_G = \frac{J_G^-}{J_G^+} \tag{5.2}$$

Albedo factors set to zero ($\beta_G = 0$) represent zero incoming current (a.k.a., void) boundary conditions whereas albedos set to one ($\beta_G = 1$) represent reflective boundary conditions.

To set albedo boundary conditions, the PARCS code requires the user to input an albedo-dependent function (α_G). This function is used by the code to relate the neutron current to the neutron flux and is computed as follows [18]:

$$\alpha_G = \frac{1}{2} \cdot \frac{1 - \beta_G}{1 + \beta_G} \tag{5.3}$$

Albedos were computed by tallying Serpent's group-wise partial currents at the following surfaces:

1. X-Y plane at the top of lower grid plate

2. X-Y plane at the bottom of upper grid plate

The previously listed planes were used to compute albedos because they represent the axial limits of the volume used for cross-section homogenization. Since different water levels were used to run simulations, albedos had to be computed for the various water levels. Table 5.1 shows different albedo values (β_G) for water levels of 952.2 mm and 960 mm.

Detector cross-sections

PARCS detectors have been used to model the response of a fission chamber that moves along and across the core and reflector region. The Serpent code was used to generate detector cross-sections. They were computed as the ratio of group-wise ^{235}U fission rates to neutron fluxes.

Table 5.1 – Two-group axial albedos for the CROCUS reactor

	Top boundary β_G		Bottom boundary β_G	
Water level [mm]	Fast	Thermal	Fast	Thermal
952.2	0.290	0.053	0.452	0.358
960.0	0.294	0.055	0.452	0.358

$$\Sigma_{det,G} = \frac{\displaystyle\int_V \int_{E_i}^{E_{i+1}} \Sigma_f^{^{235}U}(\mathbf{r},E)\phi(\mathbf{r},E)\; dE\; dV}{\displaystyle\int_V \int_{E_i}^{E_{i+1}} \phi(\mathbf{r},E)\; dE\; dV} \tag{5.4}$$

The fission rates and neutron fluxes were tallied following the mesh is shown in Figure 5.4. The mesh has a length equivalent to the PARCS mesh size (i.e., 1.837 cm as it will be described later on page 95) and a width equivalent to the fission chamber diameter (0.47 cm) which was presented in the experimental section (4.2).

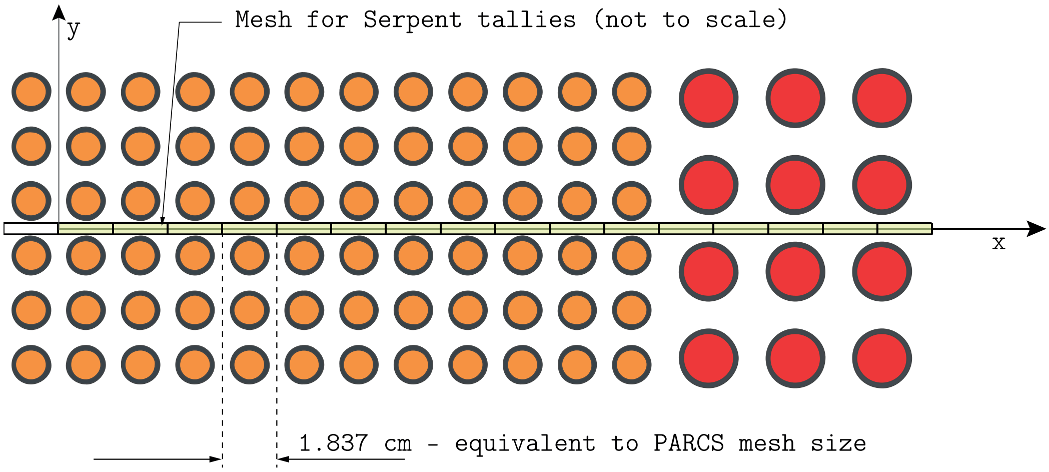
y
Mesh for Serpent tallies (not to scale)
x
1.837 cm - equivalent to PARCS mesh size

Figure 5.4 – Serpent mesh for tallying flux and fission rate

Form functions

Even though PARCS is able to model fission rate profiles through the use of detectors, they only provide cell-wise information. Form functions (FF) can be used as follows to reconstruct within-cell heterogeneities from homogeneous (cell-wise) solutions,

$$R_f^{\text{het}}(\mathbf{r}) = R_f^{\text{hom}}(\mathbf{r}) \cdot FF(\mathbf{r}) \tag{5.5}$$

where R_f stands for fission rate.

The Serpent code was employed to compute these form functions. The homogeneous fission rate (R_f^{hom}) was approximated as the average fission rate in a volume of length equivalent to the PARCS mesh size and width equivalent to the fission chamber diameter (0.47 cm). This meshing is represented in Figure 5.4.

The heterogeneous fission rate (R_f^{het}) was computed in a similar way, but for a much finer spatial discretization. To tally the heterogeneous fission rate, each of the meshes shown in Figure 5.4 was subdivided in the x-direction into 10 smaller meshes (length of 0.1837 cm), while the width (y-dimension) was kept constant.

The form functions were then computed as

$$FF(m) = \frac{R_f^{\text{het}}(m)}{R_f^{\text{hom}}(i)} \tag{5.6}$$

Where i and m represent the indices for coarse (1.837 cm) and fine (0.1837 cm) meshes, respectively. Figure 5.5 shows a schematic representation of the fission rates tallied within a coarse mesh. These fission rates were calculated over the entire energy spectrum, therefore the form functions are not group-wise parameters.

The form functions were used for heterogeneous fission rate reconstruction and covered the radial direction from the center of the core ($r = 0$ cm) to the reflector region ($r = 66.1$ cm).

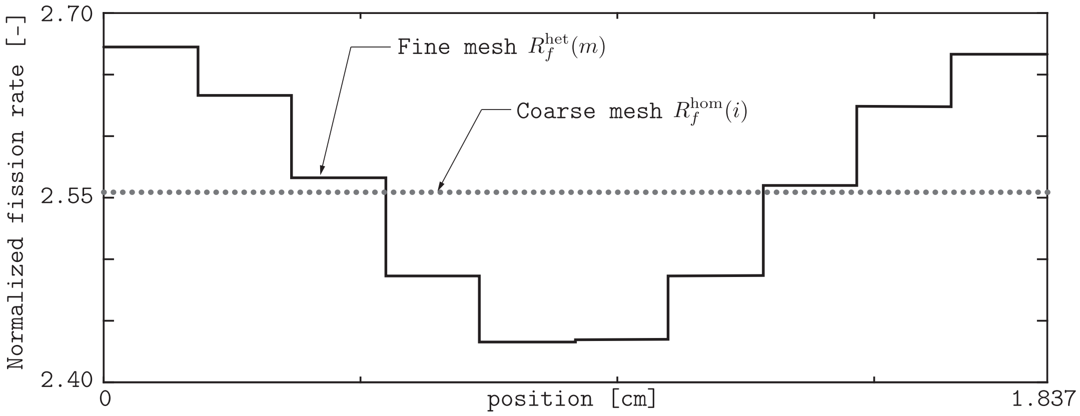

Figure 5.5 – Schematic representation of coarse and fine-mesh fission rate tallies for the generation of form functions

Control rods

The control rods were modeled using 2 by 2 meshes as shown in Figure 5.6. The cross-section data consist of two branch cases: a reference one corresponding to the unrodded state, and second one corresponding to the rodded state. The latter was generated from an additional full-core Serpent calculation having one control rod fully inserted.

Since the extent of the perturbation caused by the insertion of the control rod goes further away than the four radial meshes used to model each rod, the outer lattice fuel (U-metal fuel) cross-sections need to account for this perturbation as well. Therefore, the cross-sections for the outer lattice fuel are also represented by:

- A reference branch in which control rods are withdrawn
- A second branch case in which the control rods are fully inserted, which accounts for the perturbation induced by the proximity to the control rods.

Figure 5.6 illustrates the approach taken for modeling the control rods. The figure shows a quarter core only for the sake of clarity. Control rod cross-section data were generated using the full 3-D core model.

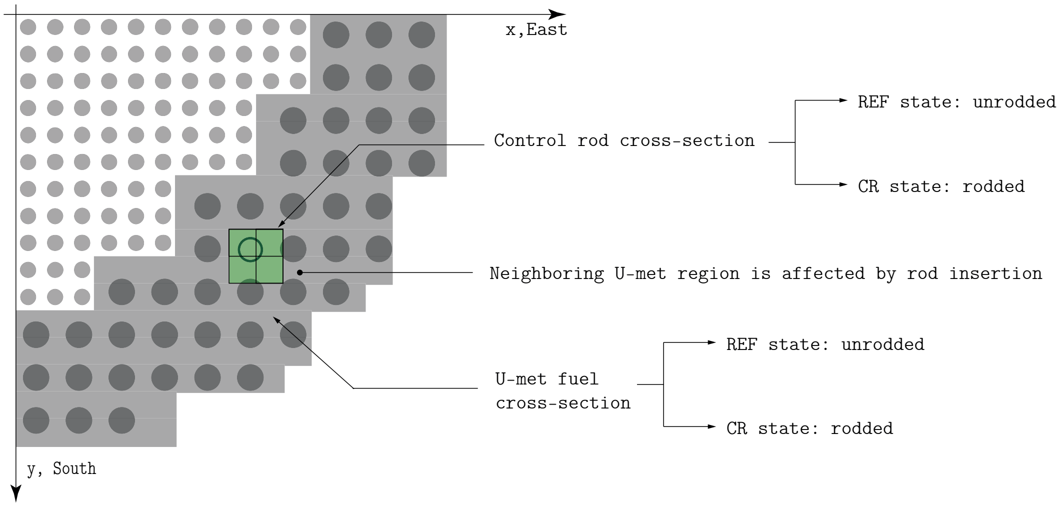
x,East
Control rod cross-section
REF state: unrodded
CR state: rodded
Neighboring U-met region is affected by rod insertion
U-met fuel
cross-section
REF state: unrodded
CR state: rodded
y, South

Figure 5.6 – CROCUS reactor control rod modeling

Kinetic parameters

The Serpent code was also used to produce the kinetic parameters required by PARCS for time-dependent simulations. Adjoint-weighted effective delayed neutron data were calculated using the iterated fission probability (IFP) method [52]. Because the IFP method calculates the kinetic parameters over the entire geometry, a single set of kinetic parameters were generated for the whole reactor. The kinetic data are listed in Table 5.2. Note that the table presented earlier in the experimental section (Chapter 4) provides kinetic parameters computed by the MCNP5 code.

5.2 PARCS code modeling of the CROCUS reactor

The use of PARCS for modeling the CROCUS reactor is challenging due to the small size of the core that leads to large neutron leakage, the presence of regions with high neutron absorption (Cadmium layers), and the incongruence of the two fuel lattices.

Table 5.2 – CROCUS adjoint-weighted effective kinetic parameters from Serpent - IFP method & JEFF-3.1.1 nuclear data

λ_i [s^{-1}]	β_i	Λ [s^{-1}]
1.247×10^{-2}	2.270×10^{-4}	4.763×10^{-5}
2.829×10^{-2}	1.094×10^{-3}	
4.252×10^{-2}	6.481×10^{-4}	
1.330×10^{-1}	1.434×10^{-3}	
2.925×10^{-1}	2.455×10^{-3}	
6.665×10^{-1}	8.066×10^{-4}	
1.635	6.715×10^{-4}	
3.555	2.513×10^{-4}	

PARCS has been built as a nodal diffusion code that can provide full-core solutions with the same accuracy as traditional fine-mesh finite difference diffusion codes but at a much lower computational cost. The advantage of advanced nodal codes such as PARCS derives from the fact that the reactor can be discretized using a much coarser mesh (such as an entire fuel assembly) than that one used by finite difference schemes. In the CROCUS reactor, the core cannot be subdivided into simple repeatable subsections because of the incongruence between the two fuel lattices. It is then natural to utilize a pin-by-pin spatial discretization, where nodal methods are no longer of advantage.

Two solution kernels were used in PARCS. The coarse mesh finite difference (CMFD) kernel was used to provide the main solutions and the fine-mesh finite difference (FMFD) kernel was employed only for a parametric analysis presented in Section 5.3.2 (p. 105). It is worth recalling the differences between the two solution kernels. While the CMFD was implemented as acceleration scheme for nodal and fine-mesh solutions, the FMFD is a standard finite difference solver intended to provide pin-by-pin solutions. In the CMFD method, a finite difference discretization is used to solve the diffusion problem, which is updated by a high order nodal method after a given number of iterations to improve the CMFD accuracy. However, provided that the spatial mesh is fine enough, the CMFD solution can converge in space without the need of a nodal method. The use of CMFD with no nodal update will be referred to as CMFD-only. In this work this is the preferred method because it can provide fine-mesh finite difference solutions using the regular PMAXS cross-section files. The CMFD-only kernel also allows to use certain PARCS features that the FMFD kernel does not such as the use of detectors and albedo boundary conditions. The PARCS modeling of the CROCUS reactor has been therefore performed using a two-group finite difference solver (CMFD-only) in Cartesian geometry. All PARCS results were run using this solver unless otherwise stated.

As described in Section 3 (p. 33), there are two radial fuel zones arranged in two different fuel squared lattices, an inner one with a pitch of 1.837 cm and an outer one with a pitch of 2.917 cm. The spatial discretization for the PARCS solution has been chosen to match the inner fuel pins for two reasons: (1) from a safety standpoint accurate pin power prediction in the inner lattice is of greater importance than for the outer lattice, and (2) accurate fine-mesh finite difference solutions require the mesh spacing to be in the order of the smallest group-wise diffusion length ($\sim$ 1.8 cm for the CROCUS reactor). In a previous publication [82], two PARCS models were built to represent both fuel regions: a first model used a finer mesh equivalent to the UO_2 fuel pitch, and a second one a larger mesh equivalent to the U-metal fuel pitch. This scheme was discarded because of the limitations to predict power in the inter-lattice region and because the most relevant phenomena take place in the core center.

The mesh structure used in the current PARCS model consists of 72 x 72 x 54 meshes in the x-th, y-th and z-th directions respectively. A mesh spacing of 1.837 cm (equivalent to the UO_2 fuel pitch) is used in the radial plane whereas a spacing of 1.857 cm is used in the axial direction. To model the reactor at a water level[2] of 95.22 cm, the axial meshing for the fuel region surrounded by air needs to be reduced to 1.593 cm. The reactor meshing includes explicit modeling of the radial reflector. Because the reference for water level is set to the top of the lower Cadmium layer and the PARCS model begins 0.5 cm higher (i.e., at the top of the lower grid plate as defined by the planes used to calculate albedos), this difference needs to be subtracted to calculate the water level in PARCS. Accordingly, the fuel region under water is defined following a structure of 51/meshes $\times$ 1.857 = 94.71 cm and the air region as 3/meshes $\times$ 593 = 4.78 cm, which yields a total fuel length of 99.49 cm. Figure 5.7 shows the radial discretization of the active core region. The colors represent different homogenized cross-section sets. The reflector meshes are not shown in the figure.

Figure 5.7 illustrates the agreement between the meshing and fuel pins in the inner lattice region and also the mismatch between the meshing and fuel pins in the outer lattice region. The figure also shows that the control rods were modeled using 2 x 2 meshes for each control rod. Details concerning the spatial homogenization process are presented in Section 5.1.

The axial meshing with the different cross-section sets and model boundaries are shown in Figure 5.8. While in the radial direction the model is extended to the water reflector periphery, in the axial direction the model was limited by the grid plates. By cutting the reactor geometry at the grid plates, the number of spatial mesh points is largely reduced and also problem convergence is tightened. Albedo boundary conditions (β_G) were used to relate the incoming and the outgoing fluxes at the axial boundaries. The albedo functions (α_G) were computed by the Serpent code as described in Section 5.1. Zero-incoming current boundary conditions were imposed to represent the external radial boundaries.

---

[2] the entire axial mesh structure varies for different water levels. A level of approximately 95.22 cm corresponds to the basic configuration with all the control rods withdrawn.

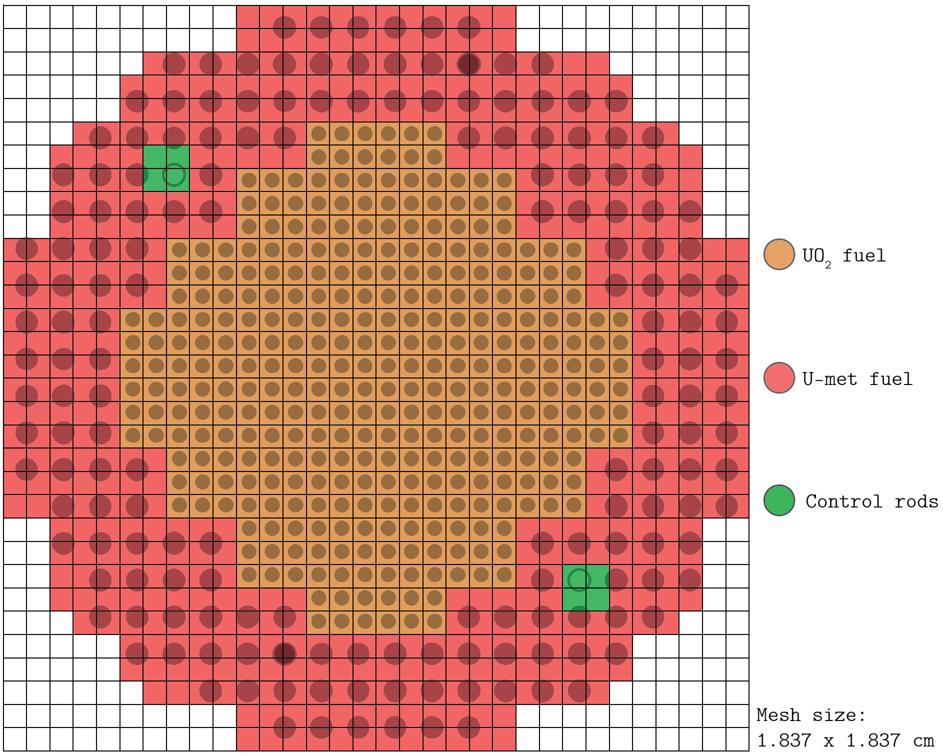

Figure 5.7 – Top view of PARCS model spatial discretization

The use of the finite difference (CMFD-only) kernel over nodal methods for PARCS solutions is based on the following reasons:

- Numerical stability issues are observed when using nodal solvers.
- Albedo boundary conditions for rectangular geometries can be used only with the finite difference kernel.
- As seen in Figure 5.8, the air on top of the water reflector was replaced by dummy regions to avoid numerical convergence issues caused by the low air cross-section values. Dummy regions are only supported by the finite difference solver, which is another reason for choosing this solver over the nodal ones.
- The mesh size used for CROCUS modeling is in the order of the smallest group-wise diffusion length ($\sim$ 1.8 cm) and allows spatial convergence of the finite difference solution [83].

However, the use of the finite difference (CMFD-only) kernel presents several limitations such as:

- Multi-group diffusion theory is not supported.

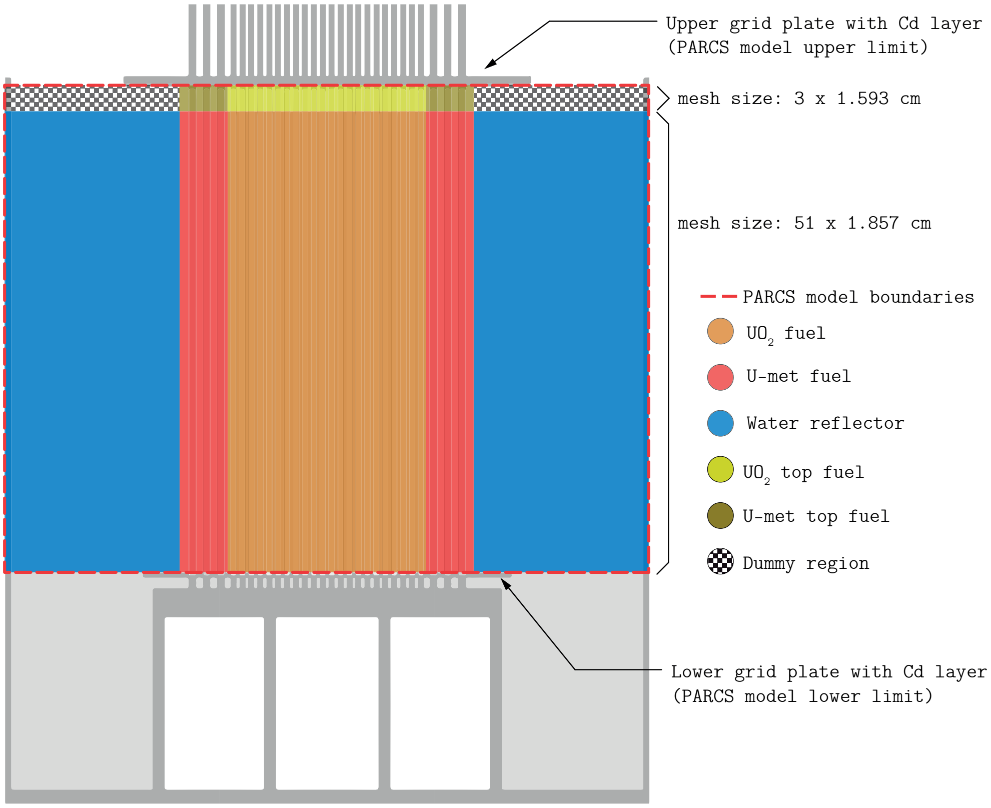
Upper grid plate with Cd layer
(PARCS model upper limit)
mesh size: 3 x 1.593 cm
mesh size: 51 x 1.857 cm
PARCS model boundaries
UO$_2$ fuel
U-met fuel
Water reflector
UO$_2$ top fuel
U-met top fuel
Dummy region
Lower grid plate with Cd layer
(PARCS model lower limit)

Figure 5.8 – Side view of PARCS model spatial discretization

- Interface Discontinuity Factors cannot be implemented.

- The SP$_3$ transport solution is not implemented.

A two-group energy structure has been used for steady-state and time-dependent solutions. Section 5.3.2 documents an analysis of the group-structure performed over a 2-D model of the CROCUS reactor using the fine-mesh finite difference (FMFD) kernel. This section also addresses transport effects by comparing diffusion to an SP$_3$ transport solution.

Neutron leakage is important in the CROCUS reactor due to the small size of the core. Leakage effects have been partially accounted for with the use of an in-scatter correction of diffusion coefficients as explained in Section 5.1.1. A numerical study addressing the impact of this correction for the CROCUS reactor and also for different reactor core sizes will be presented later in Section 5.3.

The PARCS code provides the ability to simulate detector responses, which are computed as

$$R_i = V_i \sum_G \Sigma_{\mathrm{det,G}} \cdot \bar{\phi}_{i,G} \tag{5.7}$$

where $\bar{\phi}_{i,G}$ is the Gth group mesh-averaged flux in mesh i and $\Sigma_{\mathrm{det,G}}$ is the detector cross-section. These cross-sections were read from the PMAXS files and were generated by the Serpent code as discussed in Section 5.1.1.

PARCS detectors were used to compute fission rate profiles. These responses are mesh-averaged (Equation 5.7) and even though a fine spatial mesh is used, they cannot capture the heterogeneities within the mesh. These heterogeneities were reconstructed from the PARCS homogeneous solution with the use of form functions (FF):

$$R_f^{\mathrm{het}}(\mathbf{r}) = R_f^{\mathrm{PARCS}}(\mathbf{r}) \cdot FF(\mathbf{r}) \tag{5.8}$$

5.2.1 Neutron kinetics modeling

The solution of time-dependent problems in PARCS is provided through the direct solution of space-time kinetic equations. The core conditions that initialize the transient problem are obtained with the solution of the eigenvalue problem.

While the kinetic parameters are core-averaged values, the neutron inverse velocities are space-dependent, i.e., a set of group-wise inverse velocities is assigned to each homogenized region. The inverse velocities were calculated by Serpent and homogenized by flux-volume weighing over each region as described in Section 2.3.3.

The transient consisted in moving either the control rods or the small absorber piece as described in the experimental section (Sec. 4.3). The modeling of the first type of transients is trivial and is therefore not described.

The simulation of transients initiated by the movement of a small neutron absorber was done as follows. The absorber was modeled in PARCS as one mesh cell of 1.837 by 1.837 cm in the center of the core as shown in Figure 5.9. In the axial direction, the absorber was modeled with a length of 8.1 cm. The cross-section data for the absorber had been generated accordingly with the full-core Serpent model. PARCS detectors were used to replicate the response of the out-of-core and in-core fission chambers. The in-core detector response was represented by the average fission rate of two cells near the core center as illustrated in Figure 5.9. The out-of-core detector response was represented by the average fission rate at a cell in the reflector region at a distance of seven centimeters from the core.

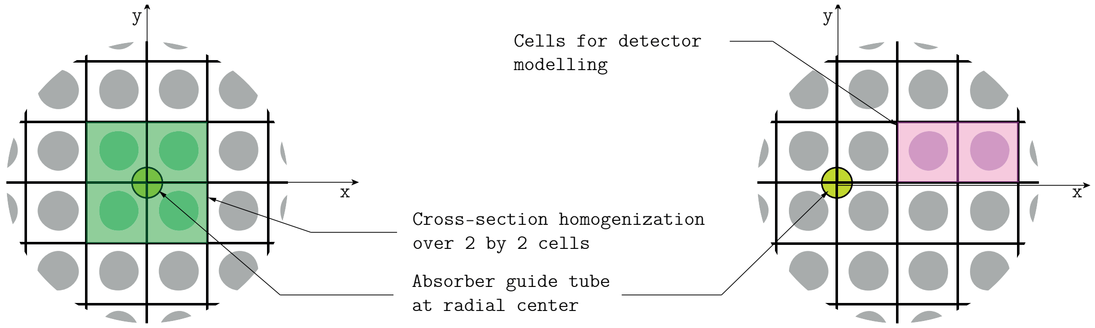
y
x
Cells for detector modelling
Cross-section homogenization over 2 by 2 cells
Absorber guide tube at radial center
y
x

Figure 5.9 – Small absorber and detector modeling in PARCS for kinetics simulations

5.3 Numerical results

5.3.1 Steady-state results

This section deals with the steady-state analysis and verification of PARCS results against Serpent Monte Carlo simulations. The comparison between PARCS and Serpent was done for eigenvalue, control rod reactivity worth, neutron fluxes and ^{235}U fission rate distributions. The comparison is based on the choices described in the preceding sections and is summarized in Table 5.3.

Table 5.3 – Models and parameters for the CROCUS full-core reactor calculations

Nuclear data library	JEFF-3.1.1
Lattice physics code	Serpent v2.1.27
Theory	Monte Carlo
Geometry	Exact heterogeneous, 3-D
Energy structure	Continuous-energy
Full-core calculation code	PARCS v32m19
Theory	Diffusion
Geometry	Homogenized pin-by-pin, 3-D Cartesian
Mesh size (x,y,z)	1.837 × 1.837 × 1.851 cm
Energy structure	Two-group
Delayed neutron precursor groups	Eight
Reactivity feedback	Not required

Given the ability of Monte Carlo codes to perform full-core steady-state calculations with a high level of detail, the Serpent solution was used as reference for the comparison. For this code-to-code comparison, a higher number of neutron histories (10^4 cycles of 10^6 neutrons each) were used in Serpent to reduce the eigenvalue statistical uncertainty to 0.7 pcm, and below 0.5% for fission rates and neutron fluxes.

Eigenvalue

The multiplication factor difference was computed as follows

$$\frac{\Delta k}{k} = \frac{k_{\mathit{eff}}^{\text{PARCS}} - k_{\mathit{eff}}^{\text{Serp}}}{k_{\mathit{eff}}^{\text{Serp}}} \tag{5.9}$$

The eigenvalue comparison between Serpent and PARCS is shown in Table 5.4. Considering the limitations of diffusion theory for high leakage system like CROCUS, good eigenvalue agreement was achieved. The difference was of -418 pcm with respect to the Serpent solution. The effect of core size in the prediction of the eigenvalue is reflected in the diffusion coefficient study presented in the parametric analysis section (5.3.2).

	k_{eff}	$\frac{\Delta k}{k}$ [pcm]
Serpent (reference)	$1.00166 \pm 0.7 \times 10^{-5}$	
PARCS - 2G diffusion	0.99747	-418

Table 5.4 – Eigenvalue comparison

Reactivity worth

The integral control rod reactivity worth was also compared with Serpent in Table 5.5. The worth values have been computed as

$$\Delta\rho = \rho_u - \rho_r = \frac{k_u - k_r}{k_u k_r} \tag{5.10}$$

where k_u and k_r are the effective multiplication factors for the unrodded and rodded cases, respectively.

	Control rod reactivity worth [pcm]
Serpent (reference)	170 ± 1
PARCS - 2G diffusion	171
PARCS - 2G diffusion (no neighboring correction)	159

Table 5.5 – Control rod reactivity worth comparison

PARCS estimate for reactivity worth agrees within 1 pcm with respect to Serpent. This high level of agreement was achieved after considering the effect of the rod insertion on the neighboring fuel area. This is also reflected in Table 5.5, where it is shown that PARCS reactivity worth differs by 11 pcm (or 6%) with respect to Serpent if the neighboring fuel is not taken into account.

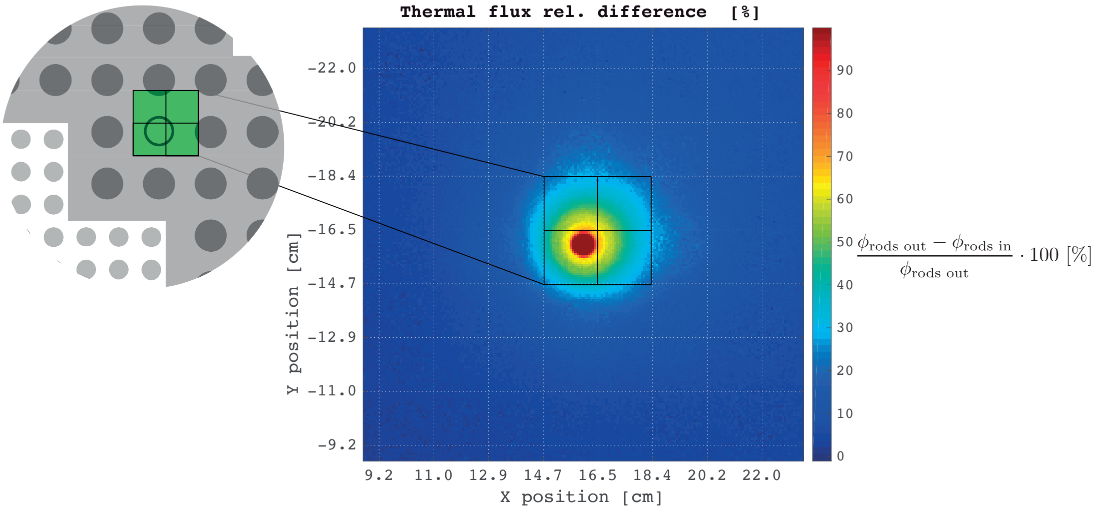

Figure 5.10 – Extent of thermal flux perturbation due to rod insertion

Figure 5.10 shows the extent of the thermal flux perturbation due to rod insertion[3]. The control rods cross-sections are represented by a 2x2 mesh, which encompasses most of the perturbed area. However, if the perturbation induced on the neighboring meshes (of up to 40%) is neglected, the difference of PARCS estimate with respect to Serpent increases from 1 pcm to 11 pcm (or 0.5% to 6%) as shown in Table 5.5. The procedure for accounting for this effect is explained in detail in Section 5.1.

Steady-state neutron flux and fission rate distributions

As earlier mentioned, PARCS detectors and form functions were used for the reconstruction of heterogeneous fission rate from homogenized solutions. The PARCS homogeneous and reconstructed solutions will be hereafter referred to as *PARCS homogeneous* and *PARCS reconstructed*, respectively.

Figure 5.11 shows the comparison of relative ^{235}U fission rate distributions between the PARCS and Serpent codes. The relative difference shown in the figure was calculated between the *PARCS reconstructed* fission rate and the Serpent reference. The *PARCS homogeneous* solution (in circles) was added to the figure to highlight the difference with the reconstructed profiles. All profiles were obtained from a radial slice of the core mid-plane. The profiles start at the radial center of the core ($r = 0$) and finish in the reflector region. Each profile was normalized with respect to their integral under the curve.

The difference between codes for radial fission rate profiles does not exceed 3% in the

---

[3] The figure is flipped across the horizontal axis $(x, y) \to (x, -y)$

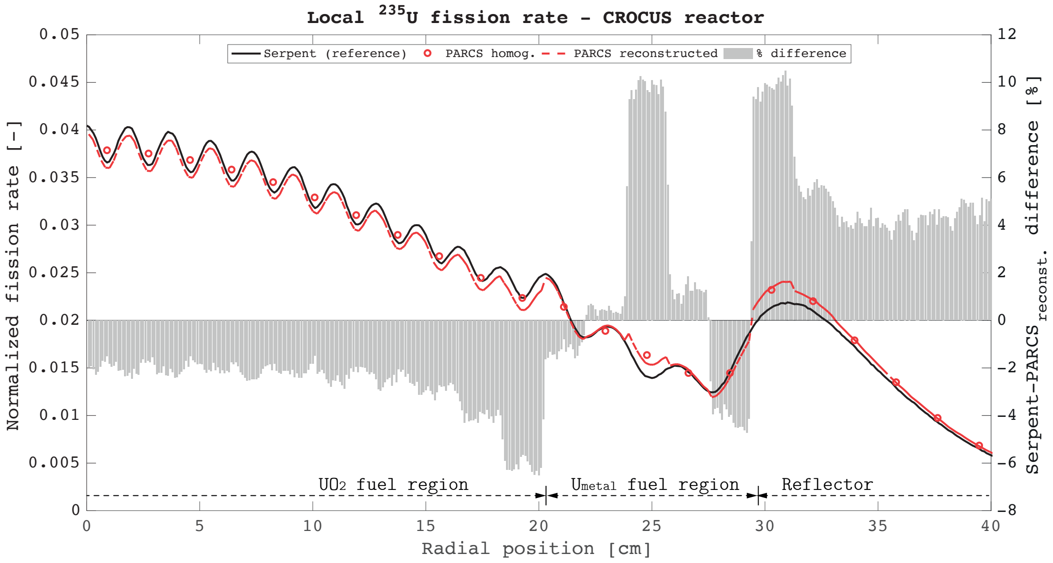

Figure 5.11 – PARCS and Serpent simulations of CROCUS radial ^{235}U fission rate profiles

central region of the core. As expected, larger differences were found in the UO_2 /U-metal fuel lattices interface ($r = 20.2$ cm), at the outer fuel lattice where the PARCS mesh and explicit fuel pins are incongruent, and near the core periphery ($r = 29.17$ cm).

Comparison at a coarser mesh level was done for thermal and fast fluxes, with no reconstruction for the PARCS profiles. With respect to Serpent profiles, the neutron fluxes were tallied using a mesh structure that matches that one of PARCS (i.e. mesh size of 1.837 cm x 1.837 cm x 1.857 cm). Due to the relatively large size of the mesh, the resulting Serpent profiles will be referred to as *Serpent coarse*.

Figure 5.12 shows the thermal and fast neutron flux radial profiles predicted by the PARCS and Serpent codes. The *Serpent continuous* profiles were obtained with a finer mesh and were included in the figure to emphasize the difference with respect to coarser-mesh-averaged solutions. All profiles were obtained from a radial slice of the core mid-plane. They were also normalized with respect to the integral under each curve.

The right axis in Figure 5.12 shows the relative differences between PARCS and Serpent coarse-mesh-averaged fluxes. Differences in the inner fuel region ($r < 20$ cm) are within 5% and 1% for the thermal and fast fluxes respectively. However, in the outer fuel lattice region, the mismatch between the PARCS meshing and fuel pins leads to higher differences. These differences can be understood by observing Figure 5.13 where the Serpent meshing for tallying neutron fluxes are compared to the PARCS meshing.

Figure 5.13 shows that each PARCS cell in the outer lattice contains the same homogeneous mixture of fuel and moderator. On the other hand, in the explicit Serpent representation, the fuel/moderator ratio varies from cell to cell. Figure 5.13 shows that cell # 3 of the Serpent model has a larger fuel/moderator ratio than its neighboring counterparts.

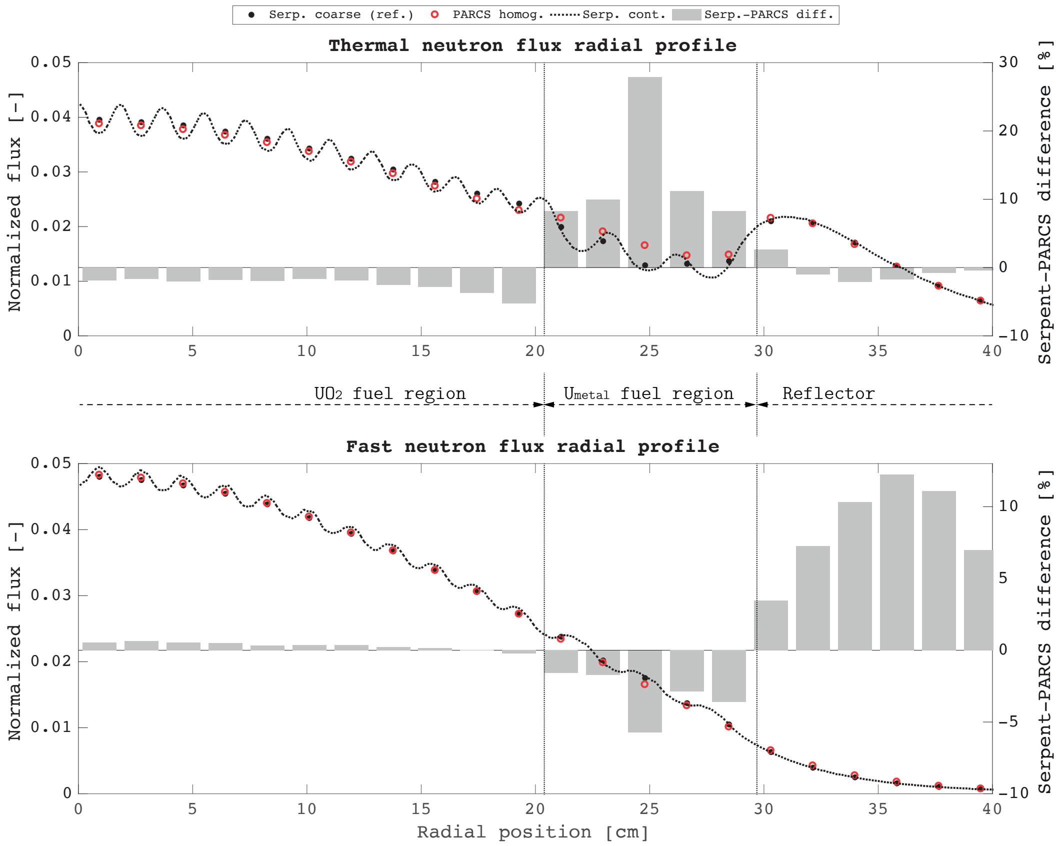

Figure 5.12 – PARCS and Serpent simulations of CROCUS radial neutron flux profiles

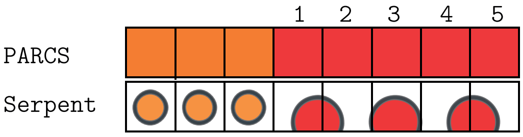

Figure 5.13 – Fuel/moderator inconsistencies between homogeneous (PARCS) and heterogeneous (Serpent) models

Therefore, the explicit Serpent model is expected to reflect, at that point, a dip in the thermal flux and a bump in the fast flux. This is reflected in Figure 5.12 in the region near $r = 25.7$ cm. Finally, concerning the fast neutron flux profiles, relative differences are high in the reflector region because more fast neutrons are slowed-down without getting absorbed in the fuel and hence the absolute value of the fast flux is small.

5.3.2 Parametric analysis

The calculation of neutronics parameters with the PARCS code is subjected to various potential sources of bias. In the context of the CROCUS reactor, special consideration was given to the transport corrections of diffusion coefficients, the discretization of the energy variable, and the use of the diffusion approximation. The purpose of this analysis is to provide and insight of the most relevant modeling parameters that may alter results in such a magnitude that differences can be resolved experientially. The impact of these parameters has been measured in terms of the eigenvalue and reaction rate profiles calculations.

In-scatter correction of diffusion coefficients

The in-scatter correction of diffusion coefficients (TRC), discussed in Section 5.1.1, has been compared against the traditional out-scatter approximation for diffusion coefficients. The acronym *TRC* will be used to make reference to those results obtained with the in-scatter correction. For the sake of simplicity, results obtained with the out-scatter approximation will be referred to as *non-corrected*.

	k_{eff}	$\frac{\Delta k}{k}$ [pcm]
Serpent (reference)	$1.00166 \pm 0.7 \times 10^{-5}$	
PARCS - no correction	0.98543	-1620
PARCS - with TRC	0.99747	-418

Table 5.6 – Impact of transport-corrected diffusion coefficient on CROCUS k_{eff}

The effect of the in-scatter correction was first investigated for the full 3-D PARCS model of the CROCUS reactor. Table 5.6 shows the comparison in terms of the eigenvalue. The last column shows the difference with respect to Serpent, which is taken as the reference. These results indicate that the in-scatter correction produces an important improvement in the eigenvalue predictions. The PARCS eigenvalues differed by approximately 1200 pcm, suggesting that the effect of this correction on core criticality is significant.

Figure 5.14 shows the comparison in terms of radial flux profiles. The relative differences between the corrected and non-corrected profiles are also plotted in the figure. Larger differences are observed for thermal flux than for the fast flux. The thermal flux predicted with the non-corrected diffusion coefficients is flatter than for the corrected counterpart.

A more in-depth analysis requires the examination of group-wise diffusion coefficient values. Table 5.7 displays them for the corrected (TRC) and non-corrected cases. Values in the Table indicate that the in-scatter correction shows the tendency to increase the thermal diffusion coefficient and to reduce the fast one. The fact that fast diffusion coefficients are reduced with the in-scatter correction may explain the differences in the eigenvalue results as neutron leakage is driven by fast neutrons. The increase of the thermal diffusion coefficient is also consistent with the eigenvalue improvement as it implies that, in the fuel/reflector interface, there is an increase of thermal neutron reflection back to the core (see the slope of thermal flux profile in Fig. 5.14 near r = 29 cm).

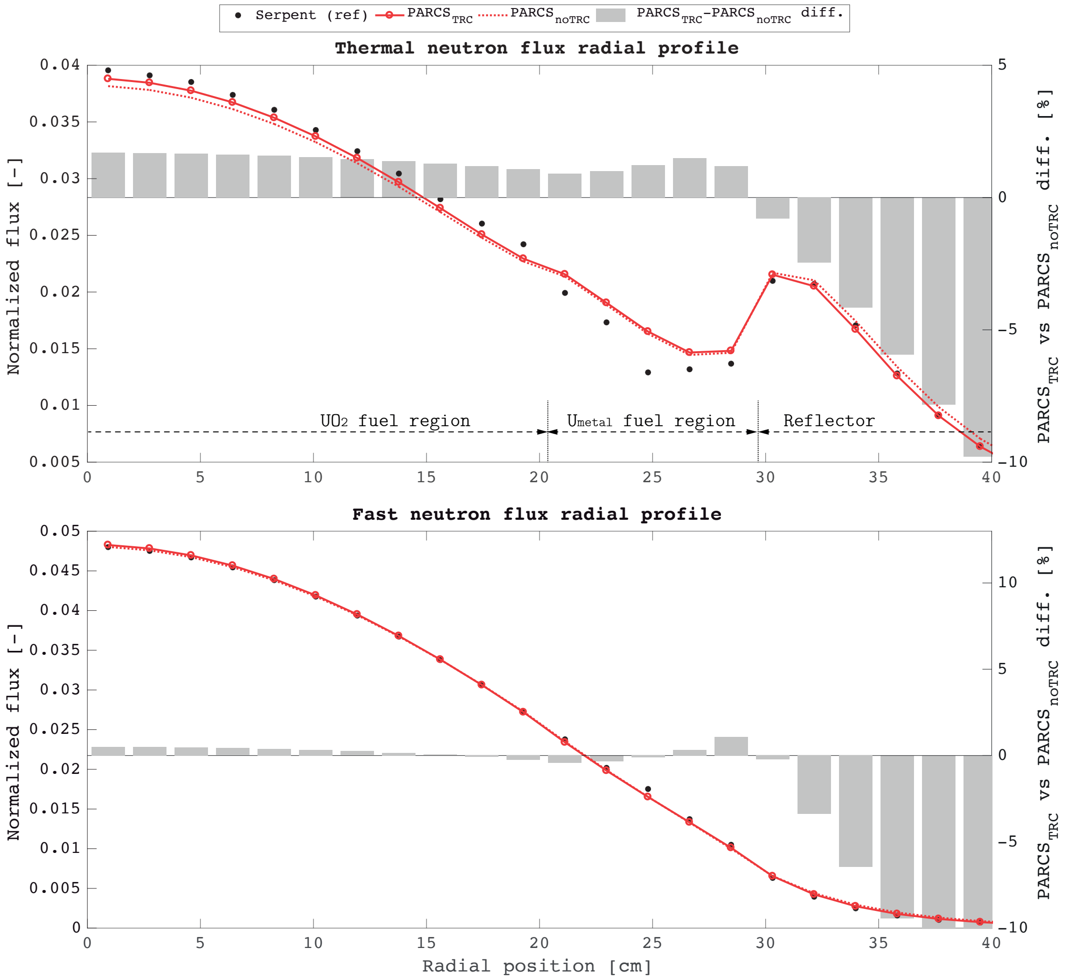

Figure 5.14 – Impact of transport-corrected diffusion coefficient on neutron flux profiles

To further study the effect of the in-scatter correction in the eigenvalue prediction, simpler models were built. The objectives of the study are:

- To verify that the improvements shown in Table 5.6 and Figure 5.14 are not due to compensation of errors.
- To determine if the impact of the in-scatter correction is more significant for smaller cores with large neutron leakage than for cores with more limited leakage.

Figure 5.15 shows the three models that were built based on a standard assembly containing 16x16 fuel pins. The assembly fuel pitch is 1.837 cm loaded with U-metal fuel and light water moderated. The same reflector thickness (29.39 cm) was used for all models and reflective boundary conditions were imposed in all three directions. Two sets of few-group constants (for fuel and reflector) were generated by Serpent using quarter-core symmetry as shown in Figure 5.15. Two-group diffusion solutions were computed using the PARCS

		Diffusion coefficient [cm]	
		Fast	Thermal
UO_2 fuel	with TRC	1.261	0.241
	no correction	1.367	0.232
	Rel. diff [%]	-7.8	4.0
U-metal fuel	with TRC	1.172	0.209
	no correction	1.251	0.201
	Rel. diff [%]	-6.3	3.9
Reflector	with TRC	1.196	0.151
	no correction	1.422	0.147
	Rel. diff [%]	-15.9	3.3

Table 5.7 – Comparison of diffusion coefficients for the CROCUS reactor. In-scatter corrected vs. out-scatter approximation

code.

	k_{eff}	$\frac{\Delta k}{k}$ [pcm]
	Model I (core width: 58.7 cm)	
Serpent (reference)	$0.95574 \pm 2 \times 10^{-5}$	
PARCS - no correction	0.94556	-1065
PARCS - with TRC	0.95359	-225
	Model II (core width: 176.3 cm)	
Serpent (reference)	$1.05662 \pm 1 \times 10^{-5}$	
PARCS - no correction	1.05548	-108
PARCS - with TRC	1.0566	-2
	Model III (core width: 352.7 cm)	
Serpent (reference)	$1.07040 \pm 1 \times 10^{-5}$	
PARCS - no correction	1.07017	-21
PARCS - with TRC	1.07046	+6

Table 5.8 – Impact of transport-corrected diffusion coefficient on k_{eff} for various core sizes.

Table 5.8 shows the Serpent and PARCS eigenvalue results for all three models. The effect of the in-scatter-corrected diffusion coefficient becomes clear for Model I (CROCUS-equivalent size), where the improvement in k_{eff} with respect to the Serpent reference is 840 pcm. For Model III (PWR-equivalent size), the transport correction seems to have a minor effect on eigenvalue, however as the core size decreases (Model II and I), this correction has a larger impact potentially due to an increase in the neutron leakage from fuel to reflector zone.

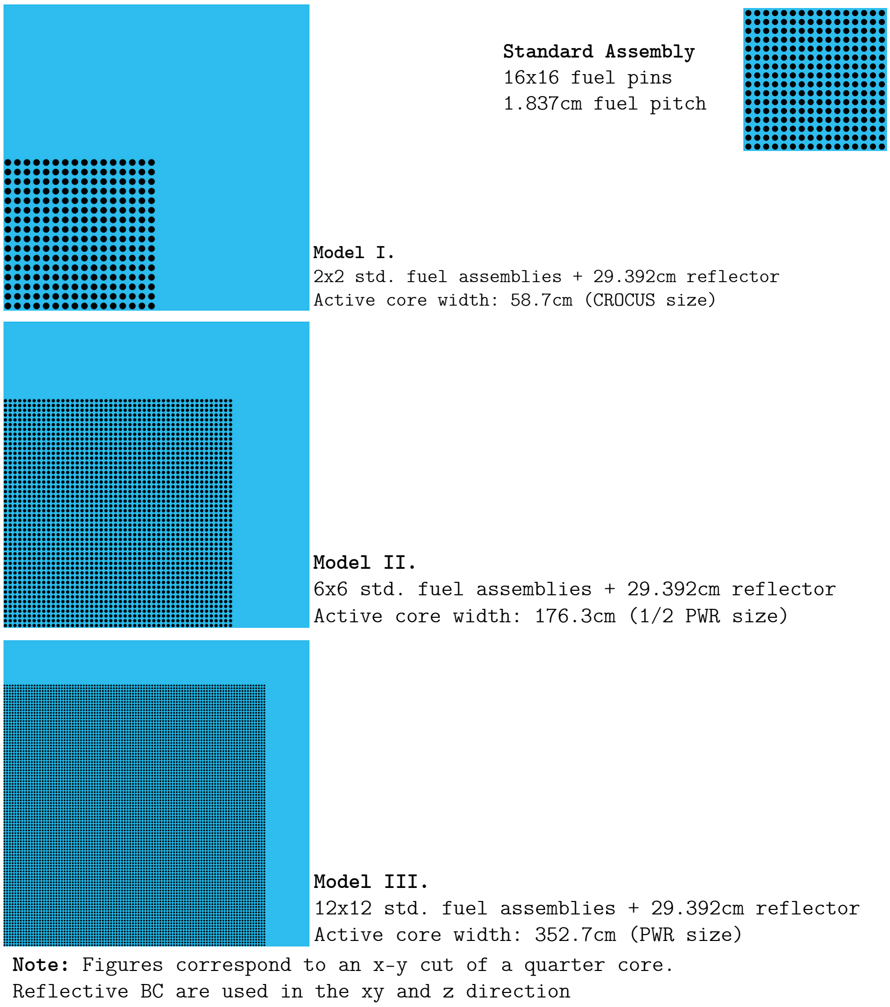
Standard Assembly
16x16 fuel pins
1.837cm fuel pitch
Model I.
2x2 std. fuel assemblies + 29.392cm reflector
Active core width: 58.7cm (CROCUS size)
Model II.
6x6 std. fuel assemblies + 29.392cm reflector
Active core width: 176.3cm (1/2 PWR size)
Model III.
12x12 std. fuel assemblies + 29.392cm reflector
Active core width: 352.7cm (PWR size)
Note: Figures correspond to an x-y cut of a quarter core.
Reflective BC are used in the xy and z direction

Figure 5.15 – Models used for the study of in-scatter-corrected diffusion coefficients

From this analysis, it is possible to conclude that in reactors with large neutron leakage like CROCUS, diffusion coefficients play a big role in producing good eigenvalues. In particular, the fast diffusion coefficient is crucial because leakage is driven by fast neutrons.

Energy group structure

As seen in the previous section, neutron leakage plays a significant role in the estimation of neutronics parameters for the CROCUS reactor. Important spectral changes may be seen in the radial plane at the fuel/reflector interface due to the large variation of neutronics properties from one region to the other. If the energy dependence of the problem is treated with a coarse energy group structure, the leakage spectrum may not be properly captured. However, this hypothesis needs to be demonstrated.

To isolate the effects of energy-group structure on PARCS steady-state calculations, it was required to simplify the CROCUS model while retaining the specificities in the radial plane. To do so, two-dimensional models based on an axial slice of the CROCUS core were built in Serpent and PARCS codes as shown in Figure 5.16. The Serpent code was also used to generate few-group constant parameters for the PARCS model. The materials and geometric dimensions remained unaffected with respect to the full 3-D CROCUS model. Reflective boundary conditions were used in all directions.

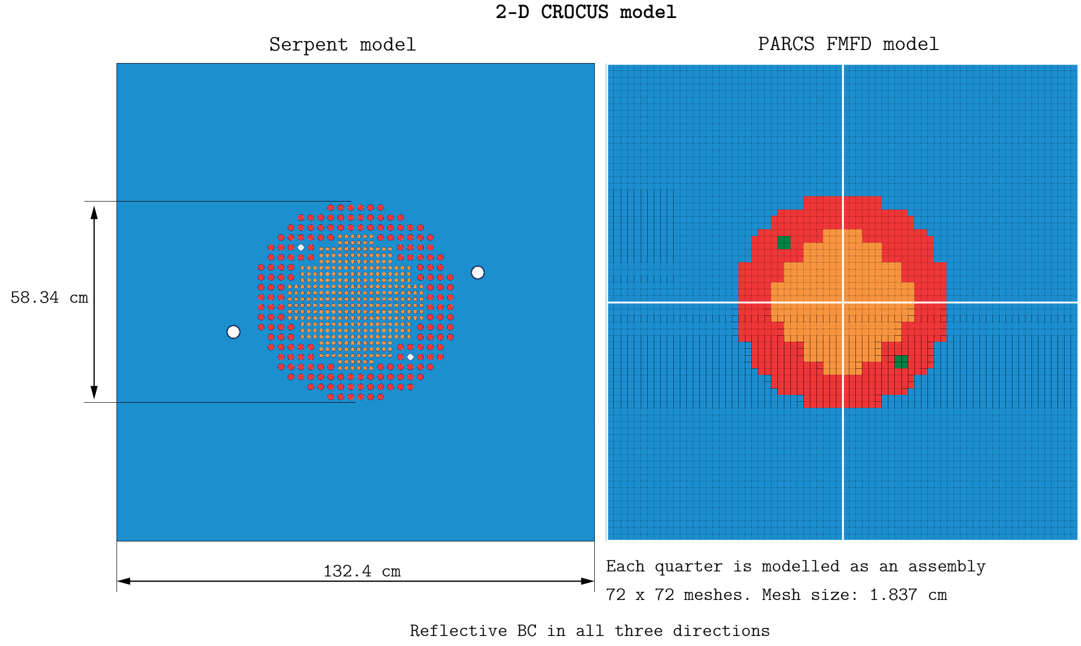
2-D CROCUS model
Serpent model
PARCS FMFD model
58.34 cm
132.4 cm
Each quarter is modelled as an assembly
72 x 72 meshes. Mesh size: 1.837 cm
Reflective BC in all three directions

Figure 5.16 – PARCS and Serpent simulations of CROCUS radial neutron flux profiles

The PARCS simulations were run using the fine-mesh finite difference (FMFD) kernel, which supports multi-group diffusion and SP_3 transport calculations. A whole block of input cards is required to run the FMFD kernel to specify pin-wise composition maps for each assembly. In particular for the 2-D CROCUS model, each quarter of the core was considered as a whole 'assembly' of 36 x 36 pins. While some of these pins within each of these quarters define a part of the active core region, some other pins are composed only of light water to represent the reflector region (see Figure 5.16).

The effect of energy group structure on PARCS solution for the 2-D CROCUS model will be first examined in terms of eigenvalue. The FMFD multi-group diffusion solver was used in the PARCS code to compute solutions for 2, 4, 8, 70, and 70 energy groups. The energy-group structures were taken from CASMO-4 [84].

Table 5.9 shows the PARCS eigenvalue estimations for different energy-group structures and their difference with respect to the Serpent reference. These results correspond to a simplified 2-D model as described above and not to the full CROCUS model. Results suggest that, for this reactor type, the eigenvalue tends to be under-predicted as the energy-group structure is refined to eight energy groups. For 8, 40 and 70 energy groups, eigenvalue estimations differ in the order of -700 pcm with respect to Serpent. Also, in the limit of 70 energy groups, the change in k_{eff} with respect to the two-group solution is limited to around 350 pcm. Given that the critical eigenvalue is an integral parameter, the two-group result can be interpreted as error compensation of local estimates that lead to a better eigenvalue prediction. The two-group diffusion solution was also computed using the CMFD-only kernel to check for consistency between PARCS models and kernels. As shown in 5.9, both kernels yield virtually the same eigenvalue result. The one pcm difference is attributed to decimal rounding.

	k_{eff}	$\frac{\Delta k}{k}$ [pcm]
Serpent (reference)	$1.03249 \pm 1.3 \times 10^{-5}$	
PARCS - 2G diffusion	1.02885	-364
PARCS - 2G diffusion (CMFD-only)[†]	1.02884	-365
PARCS - 4G diffusion	1.02677	-572
PARCS - 8G diffusion	1.02540	-709
PARCS - 40G diffusion	1.02561	-688
PARCS - 70G diffusion	1.02558	-691

[†] All other PARCS results were computed with the FMFD kernel

Table 5.9 – Impact of energy-group structure on k_{eff} - Simplified 2-D model of CROCUS.

Ideally, the effect of refining the energy-group structure should also be studied in terms of neutron flux and pin power distributions by comparison to a Monte Carlo reference. Unfortunately, this is not feasible for this model because the mismatch between fuel pins and PARCS meshing produce important biases as it was reflected in Figure 5.13. A pin power comparison was performed between PARCS solutions using the most extreme cases: 70-groups and 2-groups.

Figure 5.17 shows the radial pin power distribution differences between 70-groups and 2-groups. On the left side, differences are shown for a radial slice in the center of the core. Differences are contained within 1-2% in almost all pins across the core. Because the absolute power generated in the control rod guide tube regions is small, relative differences are expected to be larger. Note that all these simulations were run with the control rods withdrawn, therefore the control rods cross-section correspond to the case where the guide tube filled with air.

From the radial slice shown in Figure 5.17, it is possible to see that the two-group solution predicts higher power in the central region of the core. The opposite can be observed for the peripheral pins where the two-group solution predicts lower power. However, all differences are small and contained within 0.8 %.

In conclusion, results of the eigenvalue comparison for different energy group structures

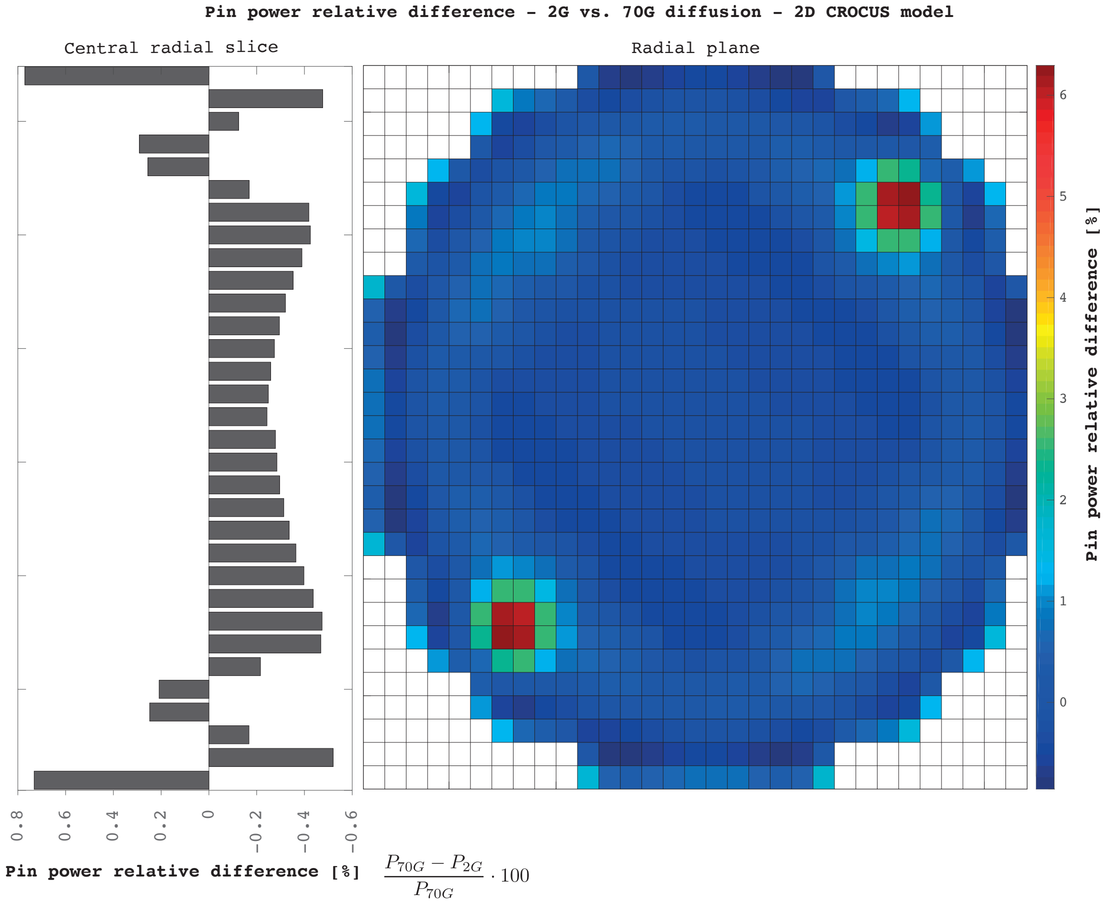

Figure 5.17 – Multi-group diffusion pin power comparison for 2D CROCUS model

are counter-intuitive as group refinement should approach continuous energy results (Serpent). The accuracy of the two-group result can be therefore attributed to the fact that the eigenvalue is an integral parameter and thus error compensation of inaccurate local estimates can lead to a better eigenvalue prediction. In terms of pin power prediction, the advantage of refining the energy group structure is not clear as differences between two and seventy groups predictions are within 3% for all fuel pins. The pin power comparison does not intend to provide arguments to understand differences in the eigenvalue as a more exhaustive analysis is required focusing on spectral changes across the core, and in particular in the fuel/reflector interface. The purpose of this comparison is rather to investigate whether the impact of group structure on pin power prediction can be reflected in the experimental comparison.

Transport effects

The impact of using the diffusion approximation was investigated using the 2-D CROCUS model described above and compared against homogeneous simplified transport (SP_3)

solutions. The objective is to observe transport effects and spatially dependent spectral effects, in particular near interfaces. To do so, the PARCS code was used to compute SP_3 solutions for 2, 4, 8, 70, and 70 energy groups. The FMFD kernel was also used for this series of simulations.

A first comparison was done in terms of eigenvalue, and a second one in terms of pin power prediction. Table 5.10 shows the PARCS eigenvalue estimations using the SP_3 transport solver. As compared to the diffusion solution (listed in Table 5.9), the SP_3 solver shows an important improvement. The most accurate solution in terms of the eigenvalue is that one computed with two-groups SP_3 where the difference with respect to Serpent is only of -15 pcm. This represents a non-negligible improvement with respect to diffusion theory solutions, where for two energy groups the difference with respect to Serpent is of -364 pcm.

	k_{eff}	$\frac{\Delta k}{k}$ [pcm]
Serpent (reference)	$1.03249 \pm 1.3 \times 10^{-5}$	
PARCS - 2G SP_3	1.03234	-15
PARCS - 4G SP_3	1.03191	-58
PARCS - 8G SP_3	1.03054	-195
PARCS - 40G SP_3	1.03103	-146
PARCS - 70G SP_3	1.03100	-149

Table 5.10 – Impact of SP_3 multi-group solutions on k_{eff} - Simplified 2-D model of CROCUS.

The effect to energy group refinement is also shown for the SP_3 eigenvalue estimations. Results are consistent with the multi-group analysis performed with diffusion theory where the eigenvalue is lowered as the energy group structure is refined from two to eight energy groups. The eigenvalue difference with respect to Serpent is maximum for eight energy groups and for further refined structures the difference remains approximately constant. This behavior was also observed in the multi-group diffusion analysis.

In terms of pin power prediction, a comparison was performed between diffusion and SP_3 for seventy and two energy groups. The results of the comparison are shown in Figure 5.18 and suggest that diffusion theory predicts flatter power profiles. The largest discrepancies are found for the 70-groups case, with differences in the order of 5 % for the peripheral pins.

Overall, results suggest that transport effects have a significant impact on pin power prediction, in particular near the fuel/water reflector interface. In terms of eigenvalue, simplified transport solutions show a clear improvement with respect to diffusion solutions. Unfortunately, the SP_3 method is not implemented in the CMFD-only kernel, which is required to provide full-core CROCUS solutions due to the reasons stated earlier in this chapter.

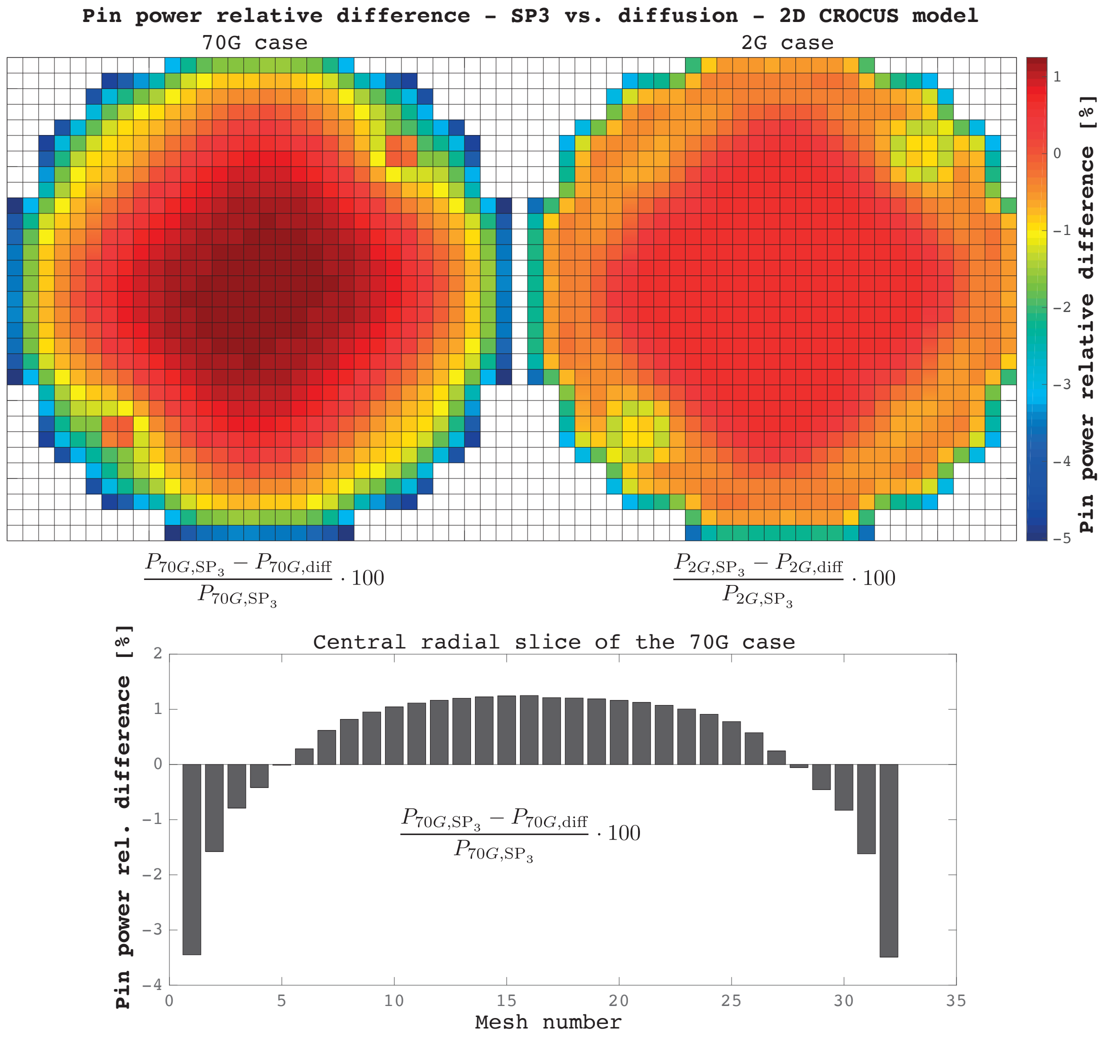

Figure 5.18 – Diffusion vs. SP$_3$ pin power comparison for 2D CROCUS model

6 Experimental benchmarking

The objective of the present section is to employ CROCUS experimental data to evaluate the performance of the Serpent/PARCS code sequence for the steady-state and kinetics modeling of the reactor. Numerical results for the steady-state simulation of the CROCUS reactor have been presented in Chapter 5. The experimental data has been obtained using the procedures described in Chapter 4.

This section is organized as follows. A first part covers the comparison of steady-state parameters, namely, fission rate profiles and control rod reactivity worth. A second part focuses on the time-dependent analysis starting with global flux kinetics effects and following by space-time kinetics.

6.1 Control rod reactivity worth

As suggested by Stacey [17], the accuracy of neutron kinetics simulations is dependent on the ability of the model to predict static characteristics. In particular, for transients involving the movement of control rods, an accurate prior prediction of control rod worth is required.

The experimental results for control rod reactivity worth were compared against those computed by the PARCS code. Table 6.1 displays the measured and computed values, which are given in dollars. PARCS results were converted to dollars using a total effective delayed neutron fraction of 7.580×10^{-3}. This value is the same one used to normalize experimental values and has been obtained with the JEFF-3.1.1 library (see Section 4.1.4). The given experimental uncertainties represent the 68% confidence interval (1 σ).

Table 6.1 also shows the relative bias between the calculated (C) and the experimentally measured (E) values which has been computed as $e_C = C/E - 1$. The uncertainty value on e_C has been computed using the classical error propagation law. It was assumed no uncertainty associated with the calculated value.

Table 6.1 – Summary of reactivity worth measurements

	Control rod reactivity worth [\$]		
Control rod	Experimental (AP*)	PARCS	Rel. bias ($C/E-1$) [%]
SE	0.232 ± 0.008	0.225	-2.9 ± 3.3
NW	0.236 ± 0.008	0.225	-4.5 ± 3.2

*Asymptotic period method - JEFF-3.1.1 library

Results from Table 6.1 indicate that the worth of the SE and NW rods are underestimated by about 3 % and 4% respectively. Differences between measured and calculated values are encompassed by the 68% (1 σ) and 95% (1 σ) confidence bands for the SE and NW rods, respectively. Hence, PARCS calculated worth are in good agreement with the measured values. This agreement will later be reflected in the evaluation of transients initiated by control rod movement.

6.2 Fission rate profiles

Measured and PARCS calculated fission rate profiles were also compared. The comparison was first done for the axial profiles. Figure 6.1 shows the axial fission rate profiles for the measurements at $h_{\text{crit}} = 970\ mm$. Each profile was normalized with respect to their integral under the curve. The differences between measured and calculated values are also displayed in the Figure and were calculated as $e_C = C/E - 1$, where C and E are the PARCS calculated and experiential values, respectively. Even though PARCS axial profiles were computed using more than 50 axial points, the axial position corresponding to each data point does not necessarily match that one of the experimental data. For that reason, an interpolation of PARCS data points was required to be able to compute differences. The uncertainty on e_C has been computed using the classical error propagation law, and provides a confidence level of about 68%. It was assumed no uncertainty associated with PARCS values.

The shape of PARCS axial profile agrees well with the experimental data for most the axial length with exception of the top region, where differences are as large as eight and twenty percent. In particular, in the bottom and central part of the core, the values agree within two percent, which is below the experimental uncertainty. Larger differences are observed in the top region of the core, which might reflect potential limitations of diffusion theory in the water/air interface. Note that the last experimental data point was measured at 950 mm. While for that point the detector was fully under water, the distance between the active part of the detector and the interface was less than 10 mm considering that half of the active length (27/2 mm) is above 950 mm. In addition, relative differences are magnified at the extremes because of the small fission rate values.

Fission rate profiles were also compared in the radial direction. As compared to the axial

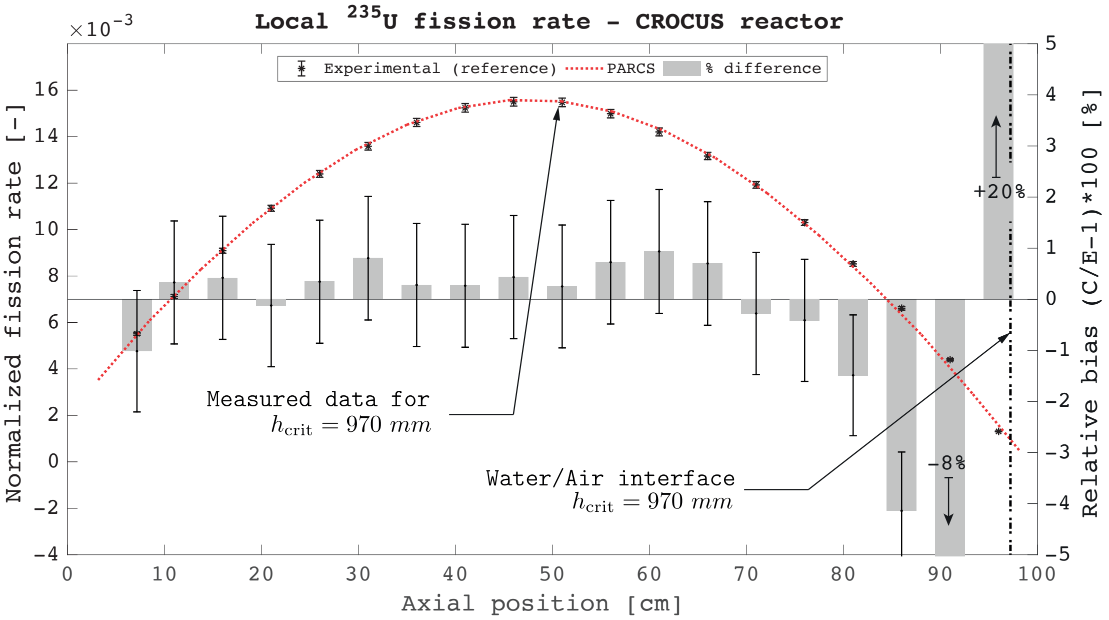

Figure 6.1 – Calculated vs. measured axial ^{235}U fission rate profiles

profiles, the radial ones present a rippled shape as described in Section 5.3 (p. 101). This adds certain complexity to the comparison since homogeneous solutions cannot capture this shape. Form functions were employed to reconstruct these heterogeneities from PARCS homogeneous solution. While the axial profiles were limited to the core, the radial profiles included a part of the reflector region.

The measured and calculated radial profiles are shown in Figure 6.2. Relative differences with associated uncertainties are also displayed in the Figure. The differences were computed as $e_C = C/E - 1$, where C is the PARCS reconstructed solution and E the experimental value. In a similar way as done for the axial profiles, an interpolation of the reconstructed solution was required to compute the difference between C and E values. The uncertainties shown in Figure 6.2 have been computed using the classical error propagation law and provide a confidence level of 68%.

Figure 6.2 shows that experimental and calculated values agree within 5% for the inner core region. The differences are enlarged near the interface between inner and outer fuel lattices ($\sim$ 20 cm), potentially due to the pin/mesh mismatch extensively discussed in the previous Chapters. The degree of agreement between measured and computed values is much lower for the outer core and reflector regions. The fact that PARCS uses a unique mesh size in the radial plane represents the most severe limitation for predicting spatial dependent quantities in the outer core region.

For a better understanding of the radial shapes, Figure 6.3 illustrates the correlation between shape and detector position. The dips take place where the detector passes nearby two fuel rods (i.e., #1, #3 and #5). At these points, there is less neutron moderation,

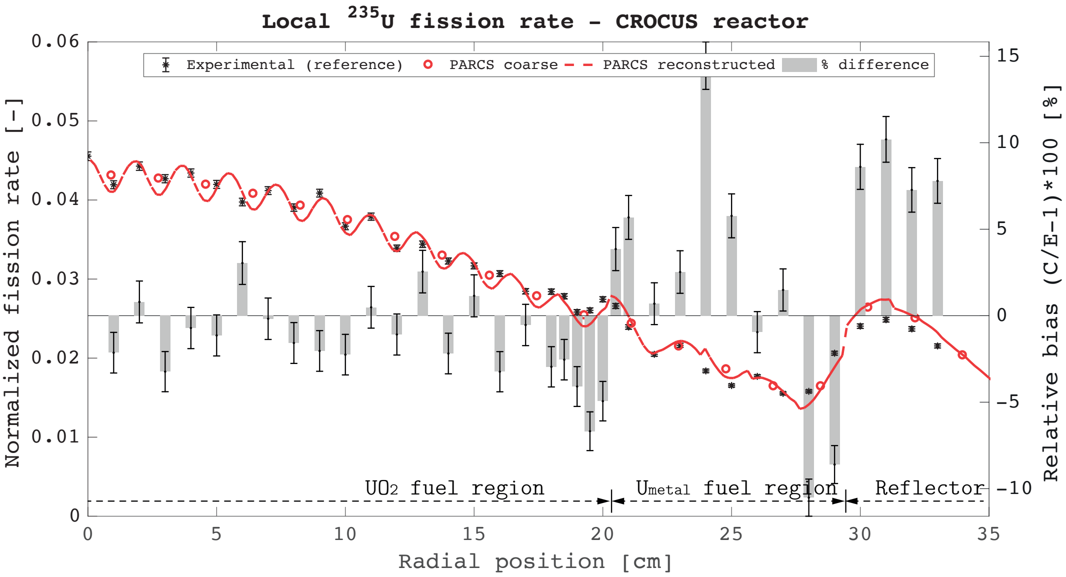

Figure 6.2 – Calculated vs. measured axial radial ^{235}U fission rate profiles

hence the magnitude of the thermal flux is lower than at points #2 and #4. Because the fission rate is proportional to the thermal flux, points #1, #3 and #5 will exhibit a local decrease of the fission rate, and points #2 and #4 a local increment. This effect is not visible in the axial direction (Fig. 6.1) because the distance between the detector and fuel rods remains constant as the detector is moved.

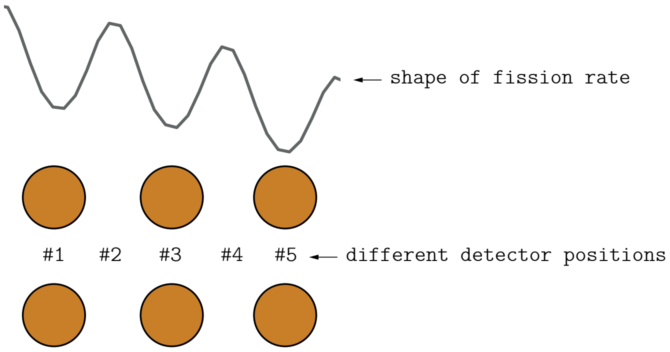

Figure 6.3 – Shape of radial ^{235}U fission rate

6.3 Neutron kinetics

So far, we have focused on the steady-state modeling of the CROCUS reactor with the Serpent/PARCS code sequence. This section deals with the performance assessment of the PARCS code for the kinetic modeling of the CROCUS reactor. The evaluation consisted in simulating different types of transients and comparing them against measured data.

The time-dependent analysis is structured as follows:

1. Transients initiated by control rods movement as described in Section 4.3.1. Because the variable of interest is the amplitude of the global flux (i.e., the reactor can be seen as a point), there are no spatial effects involved and thus they can be considered as simple transients and hence the first step for neutron kinetics modeling. The temporal variation of the flux amplitude is typically measured by out-of-core detectors.

2. Transients initiated by the movement of a small neutron absorber inside the CROCUS reactor core as described in Section 4.3.2. The calculation of these transients presents a larger degree of difficulty as compared with the ones mentioned above because spatial effects are considered with the use of local, or in-core detectors.

6.3.1 Global flux transients

These transients are characterized by the experimental cases detailed in Section 4.3.1 and briefly described below.

The first transient sequence consists of a fast rod withdrawal at $t = 0$, which is followed by fast rod drop at $t = 137.3\ s$. Measured and calculated results for this transient are shown in Figure 6.4 along with their relative differences. The curves were normalized with respect to their respective values at $t = 0$. Experimental points are scattered at the beginning of the transient because of the low counting statistics. The Figure shows that during the first 60 seconds of the power increase period, PARCS results closely follow the measured data. However, as the transient advances, the differences between PARCS and measured data increase up to 10%. Naturally, differences are magnified as the power continues to rise. Overall, PARCS shows the tendency to slightly underestimate the global power level, which is consistent with the underestimation of control rod worth shown in the static results.

The second transient sequence is characterized by a slow withdrawal and posterior insertion of a control rod. The control rod is 50% inserted for $t < 0$. At $t = 0$, the rod starts to be removed at low speed (1.47×10^{-2} m/s), and the rod reaches the fully withdrawn position at $t = 34\ s$. The control rod remains out for a period of 100 seconds, and finally at $t = 134\ s$, the rod is 100% inserted in the core.

Calculated and measured results for this transient are displayed in Figure 6.5. Differences between calculated measured results are within 10% for the whole transient. PARCS results exhibit small deviations with respect to the measured data at times greater than 100 s for the positive reactivity insertion period. The same power under-prediction trend can be observed in this and the previous (faster) transient.

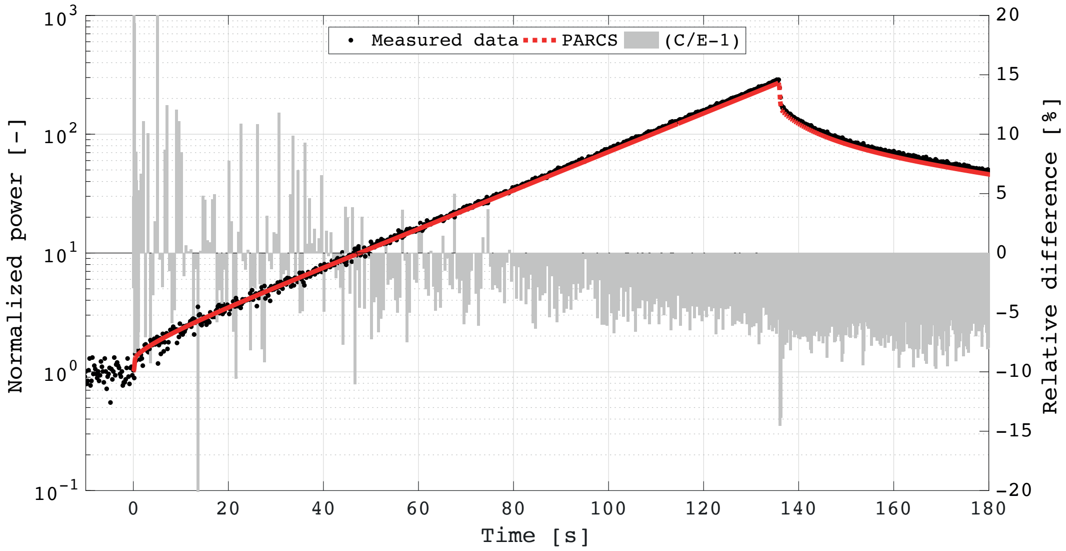

Figure 6.4 – Calculated vs. measured results for fast control rod withdrawal and insertion transient

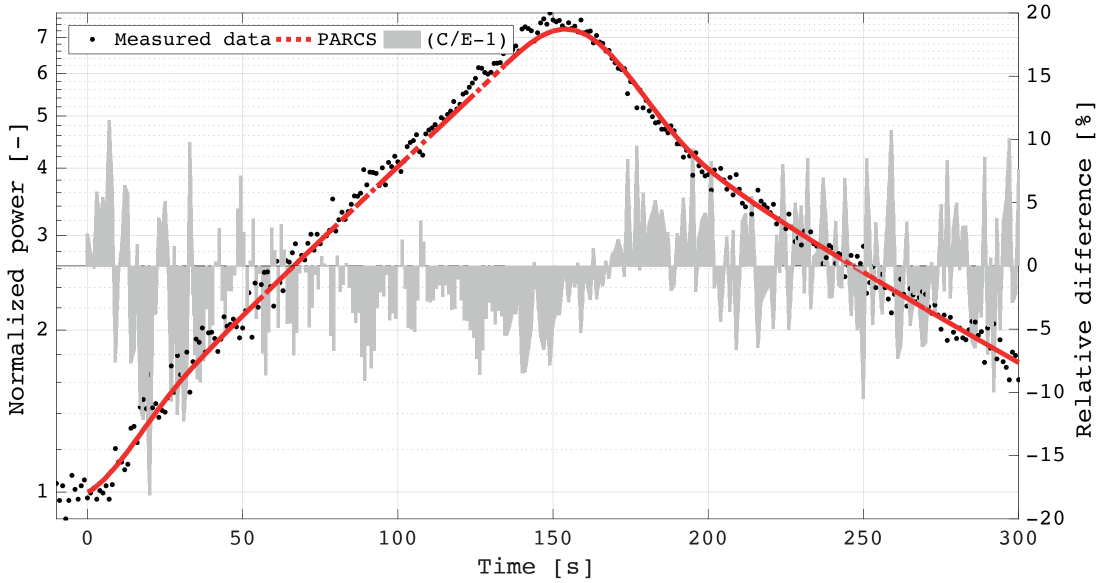

Figure 6.5 – Calculated vs. measured results for slow control rod withdrawal and insertion transient

Overall, the analysis of the control rod-initiated transients suggests that the global flux responses predicted by PARCS are consistent with experimental data.

6.3.2 Space-time kinetic transients

The purpose of this section is to study PARCS code performance for space-time kinetics modeling in the CROCUS reactor. The study focuses on the comparison between PARCS

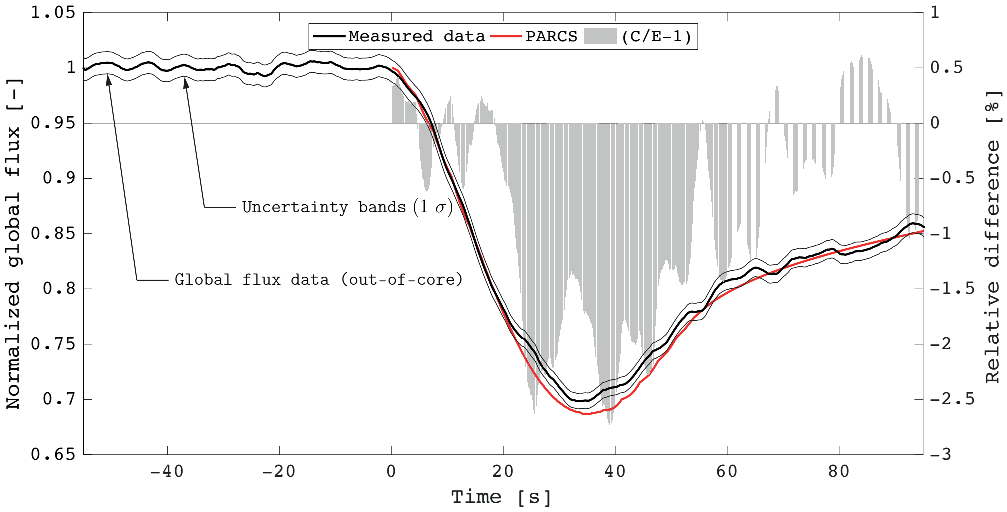

Figure 6.6 – Calculated vs. measured results for space-time kinetic transient - Global flux data

simulations and transient experimental data that capture spatial effects.

The transients were initiated by the movement of a small neutron absorber along the axial direction of the core as described in Section 4 (p. 41). The spatial distortion introduced by the movement of the absorber was measured by an in-core fission chamber located nearby the piece's path of motion. An out-of-core detector recorded the global flux amplitude variations induced by the departure from criticality. The PARCS modeling of these transients is documented in Section 5.2.1 (p. 100).

Although spatial effects are the main focus of the present study, the transients will be examined from different perspectives. The first simulations aimed at reproducing the global flux changes introduced by the absorber's movement. The comparison between calculated and measured data for these simulations is shown in Figure 6.6. The transient curves were normalized with respect to their respective values at $t = 0$. Relative differences calculated as $e_C = C/E - 1$ are also shown in the plot. During the first 20 seconds, PARCS results closely follow experimental data. However, small deviations of about 2.5% are observed between 20 and 40 seconds.

The same experiment was further analyzed focusing on the spatial effects. This time, experimental data was measured with the in-core detector, which captures the spatial distortion and also the global flux changes. Figure 6.7 displays the comparison between PARCS and experimental data and their relative differences. The curves in Figure 6.7 are similar to those shown in the previous one (Fig. 6.6) with the difference that a pronounced negative peak is observed near 25 seconds. This peak is precisely related to the local distortion measured when the absorber approaches the detector. In a similar way than for Figure 6.6, PARCS simulation closely follows experimental data for the first 20 seconds.

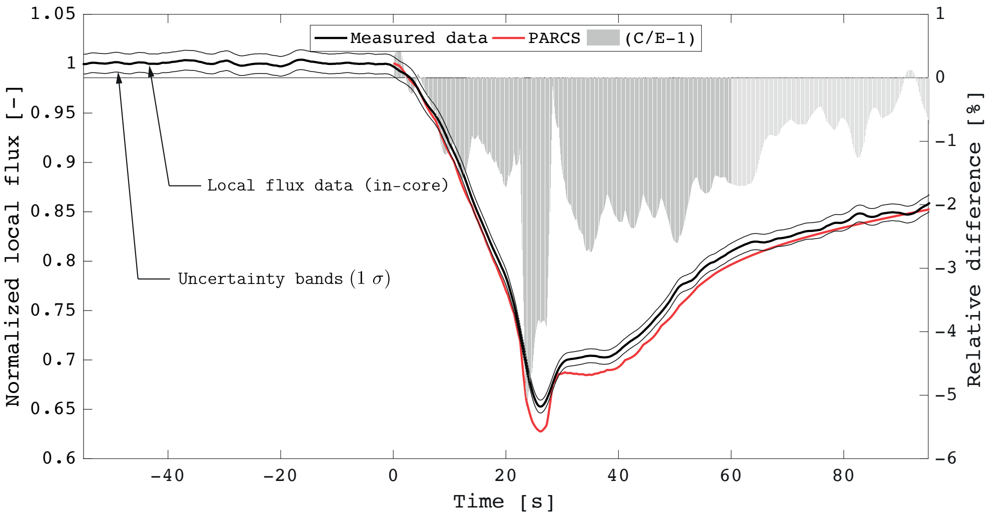

Figure 6.7 – Calculated vs. measured results for space-time kinetic transient - Local flux data

However, PARCS simulations deviate from experimental data at times between 20 and 30 seconds. At longer times, PARCS results start to approach the measured data.

As above mentioned, the in-core detector captures the spatial distortion as well as the global flux changes. The spatial effect can be detached from the global effect by computing the ratio of local to global responses shown in Figures 6.7 and 6.6, respectively. The experimentally measured and PARCS calculated ratios are displayed in Figure 6.8 along with their relative differences. These curves were normalized with respect to their respective values at $t = 0$ as done in the previous transient plots. The ratios reflect the effect seen by the in-core detector that is not seen by the out-core one, and can be regarded as the time-dependent deformations of the local flux. Close agreement is observed between calculated and measured ratios, and suggest that PARCS adequately captures spatial effects for these kinetic transients, where maximum differences are in the order of 5%.

6.4 Discussion of benchmarking results

As stated earlier, the accuracy of kinetic simulations is dependent on the ability of the model to predict static characteristics. The comparison between calculated and experimental data for control rod reactivity worth shows that PARCS closely predicts the experimental values with differences below $(4.5 \pm 3)\%$. With respect to the comparison of fission rate distributions, PARCS results manifest considerable disagreement with radial experimental data for the outer core region. This is attributed to the fact that PARCS does not allow using adaptable mesh sizes in the radial plane, which results in the repeatedly mentioned fuel pins/mesh mismatch. It is this author's opinion that this represents the most important limitation of the PARCS code for modeling the CROCUS

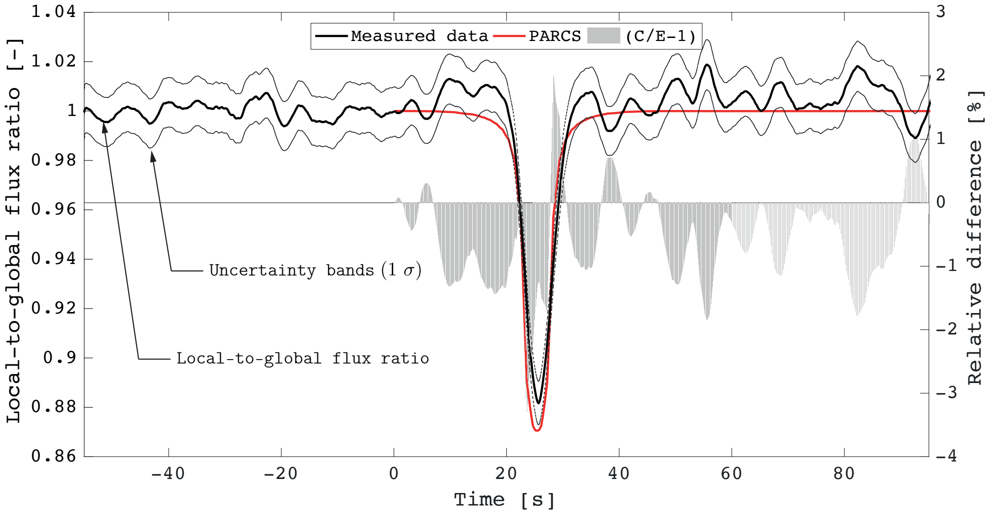

Figure 6.8 – Calculated vs. measured results for space-time kinetic transient - Local/global flux ratio

reactor. This constraint did not allow to discriminate whether differences with respect to experimental data can be attributed to potential sources of biases such as energy group structure or transport effects. Concerning the axial fission rate profiles, PARCS results agree with experimental data for the bottom and mid regions for the core, however larger deviations are encountered for the top region. This may be attributed to transport effects in the surroundings of the water/air interface.

The comparative analysis for neutron kinetic problems has verified that the PARCS code is capable of modeling the transient experiments with spatial effects in the CROCUS reactor. In particular, the experiments addressing global flux changes are well predicted by PARCS. Proper treatment of delayed neutrons data, as well as the accurate prediction of static reactivity curves, are probably a fundamental prior condition to ensure good results for this type of transients.

The modeling of transients with spatial effects deserve particular examination. Because of the compact size of CROCUS reactor core relative to the diffusion length [17, 15], neutronic responses of the reactor are tightly coupled and the effect of delayed neutron on the flux shape is insignificant. In other words, changes in the flux shape appear almost promptly with no time delay. Although these transient experiments were analyzed with direct space-time diffusion methods, the insignificant contribution of delayed neutron on the flux shape would allow to treat these experiments using the adiabatic approximation discussed in Section 2.3.2. This implies using steady-state diffusion theory or even Monte Carlo transport to predict the shape function (i.e., the local to global ratio shown in Figure 6.8), and point-reactor kinetics for the amplitude function (i.e., global flux). In the context of the CROCUS reactor, evaluating the shape function with a Monte Carlo code is unpractical because, to properly resolve the shape function in time, many several full-core calculations are needed with consequent large computational cost. For instance, with the Serpent code it takes approximately 2400 CPU hours on a 2.93 GHz machine to resolve the transient with 32 points (i.e., 75 CPU-hours/data point), achieving a statistical uncertainty in detector tallies of 1%. On the other hand, PARCS takes only 0.74 CPU hours to resolve the transient with 800 points (i.e., 3.3 CPU-seconds/data point), which implies that PARCS consumes 80 thousand times less CPU resources per data point.

7 Conclusions and recommendations

7.1 Conclusions

In summary, the purpose of this dissertation was to study the use of the Serpent/PARCS code sequence for the steady-state and spatial kinetics modeling of the CROCUS reactor. Reliable experimental data was generated and used for the comparison against computational results. The theoretical framework that provides support to this dissertation is discussed in Chapter 2 along with the choice of computer codes. The PARCS code, representing the state-of-the-art for diffusion calculations in thermal reactors, has been selected for the modeling of the CROCUS reactor along with the Serpent code for few-group constants generation.

The CROCUS reactor has shown to be an interesting tool for the validation of stand-alone neutronics models not only due to the absence of thermal feedback and fuel burn-up effects but also by virtue of the peculiarities in design such as two radial fuel zones, the presence of Cadmium layers and a water/air interface amongst others. The experimental and numerical studies are based upon the CROCUS reactor, whose detailed description is documented in Chapter 3.

The evaluation of steady-state and transient experimental data is covered in Chapter 4 and presented several challenges. The most relevant one is related to the non-linearity between count rate and actual neutron flux that prevented measurements from being taken at higher power to reduce the statistical uncertainty. Linearity and pulse-height-analysis tests were performed to account for these difficulties and to find the range of linear response. A second challenge that is related to the previous one was found in the treatment of time-dependent signals with low counting statistics, i.e., large associated uncertainties. The use of moving average filters indicated that they are an effective way to improve the signal-to-noise ratio. In addition, if the time-dependent experiment can be repeated multiple times, the signal averaging technique results adequate for further improving the signal's quality. The measurement of faster spatial-dependent transients than those presented in this dissertation would require measuring at higher reactor power to be able to increase the temporal resolution without compromising the signal-to-noise ratio. Ideally, this type of measurements should be performed with a combination of faster electronics and the use of signal averaging techniques. The measurement of transients that capture delayed neutron effects on the flux shape is impractical with the current core configuration and measurement system because of the tightly coupled nature of the CROCUS reactor.

The measurements of control rod reactivity worth by asymptotic period and inverse kinetic methods revealed that results are highly dependent on the choice of nuclear data libraries for the calculation of kinetic parameters. Differences between results obtained with JEFF-3.1.1 and ENDF/B-VII.1 nuclear data libraries exceed the 95% uncertainty level, which is an indication that nuclear data for kinetic parameter generation should be reassessed. It was also found that the kinetic parameters are the main responsible for the total uncertainty in the measurement by asymptotic period and inverse kinetics techniques. The comparison between experimental results has confirmed that both methods are equivalent for evaluating reactivity worth.

The CROCUS modeling approach is reported in Chapter 5. CROCUS is a high-leakage, tightly coupled reactor that presents some of the situations where the adequacy of diffusion theory is questionable. A PARCS model of CROCUS has been developed using strategies to improve the accuracy of the model. In the first place, albedo boundary conditions were used to limit the axial geometry to the grid plates, where diffusion theory may be invalid due to the presence of Cadmium layers. In addition, the diffusion coefficients were found to be a critical parameter for producing accurate eigenvalues in the CROCUS reactor. In particular, the fast group diffusion coefficient is critical as neutron leakage from the system is driven by fast neutrons. The classical out-scatter-transport-corrected diffusion coefficients tend to overestimate leakage and therefore under predict eigenvalue. The in-scatter correction of the diffusion coefficient can cope with the previous deficiencies and thus becomes fundamental for producing more accurate eigenvalues in high-leakage systems.

A numerical study addressing the impact of energy discretization was performed using a 2-D model of CROCUS. This analysis revealed that a two-group scheme produces more accurate eigenvalues than finer group structures. While seventy-group diffusion solutions underestimate eigenvalue by about 700 pcm with respect to the Monte Carlo reference, the two-group solution eigenvalue is underestimated only by 364 pcm. Given that the critical eigenvalue is an integral parameter, the better result obtained with a two-group scheme is attributed to error compensation of local estimates. Regarding pin power distributions, the group structure has shown to produce a minimal impact as the differences between two and seventy energy groups solutions were contained within 0.8%.

In addition to the group structure study, transports effects were investigated through the use of simplified transport (SP_3) solutions for the 2-D model of CROCUS. In terms of eigenvalue, results showed that the SP_3 method is able to predict k_{eff} within 15 pcm with respect to the Monte Carlo reference. This represents an improvement of about 350 pcm with respect to the two-group diffusion solutions. Concerning pin power distributions, differences between SP_3 and diffusion solutions are limited to 1% and 5% for the inner and outer core regions respectively. The SP_3 method could not be employed for 3-D full-core CROCUS calculations because the use of detectors and albedo boundary conditions is not supported by the FMFD solution kernel required for the SP_3 method. Given that differences between SP_3 and diffusion solutions are larger than the experimental uncertainties, it should have been possible to determine whether SP_3 estimates are more accurate than those obtained with diffusion theory.

The comparison between PARCS simulations and experimental data is documented in Chapter 6. Results for control rod reactivity worth show that PARCS predicts the experimental values within 4% which is covered by experimental uncertainty. This level of agreement was achieved as a result of extending the region where the control rod induces spectral changes to the whole outer fuel lattice.

The comparative assessment on fission rate distributions indicates that PARCS results are in considerable disagreement with radial experimental data for the outer core region, where differences are as large as 15%. This was attributed to the fact that PARCS does not allow using adaptable mesh sizes in the radial plane, which results in a mismatch between the mesh and actual fuel rods of the outer core region. Moreover, due to the large radial differences resulting from this incongruity, any other potential source of bias such as the energy group structure or transport effect cannot be exposed. Thus, the impossibility of using flexible mesh sizes is, perhaps, the most important limitation of the PARCS code for modeling the CROCUS reactor. Naturally, this issue can be tackled through the use of codes that have the ability to work with unstructured grids. Concerning the axial fission rate profiles, PARCS results agree within 1% with experimental data for the bottom and mid regions for the core. On the other hand, larger deviations of about 20% were encountered for the top region. The fact that large discrepancies are only seen in the data points near the water/air interface suggests that diffusion theory does not properly capture the transport effects in the interface region.

The investigation of neutron kinetic effects verified that the PARCS code is capable of modeling the transient experiments with spatial effects in the CROCUS reactor. In particular, the experiments addressing global flux changes are well predicted by PARCS. A proper treatment of delayed neutrons data and accurate prediction of static reactivity worth are a prior condition to ensure good results for this type of transients. Concerning the transients with spatial effects, PARCS results agree well with experimental data. Although these transients were analyzed with direct space-time diffusion methods, the insignificant contribution of delayed neutron on the flux shape would allow modeling these kinetic experiments using the adiabatic approximation.

7.2 Recommendations

Considering the work performed for modeling the neutronics behavior of the CROCUS reactor, it is recommended to focus future research on the following areas. First and foremost, the fact that PARCS does not allow using adaptable mesh sizes in the radial plane represents the most important limitation of the code for modeling the reactor. In order to evaluate the impact of this constraint, it is suggested to employ CROCUS cross-section data generated by the Serpent code) to benchmark PARCS results against a 3-D diffusion or transport code that allows explicit modeling of the inter-lattice water gap as well as the pin-cells of both fuel zones. Computer codes in accordance with these conditions are those that allow the use unstructured meshes through finite element of finite volume discretization schemes.

In the second place, it is also recommended to investigate the effect of refining the energy group structure by comparison of PARCS flux distributions against Monte Carlo solutions. In order to avoid introducing an unknown bias due to the fuel pins/mesh mismatch, a simpler model with single lattice arrangement is recommended to be used.

Even though the CROCUS core is rather homogeneous, the presence of a water gap in the inter-lattice region produces large spectral changes. If the homogenization process is carried out without accounting for these heterogeneities, the estimation of neutronics parameters may be subjected to inaccuracies. It is, therefore, recommended to investigate on the effect of implementing superhomogenization (SPH) factors for the correction of homogenized cross-sections. Particular focus should be given to the inter-lattice water gap and the fuel cells bordering the core periphery.

The development of the experimental setup for the space-time kinetic measurements required a great deal of time and has shown to provide reliable data. Because the computer software controlling the motor allows precise adjustment of the absorber's position, speed, and acceleration, it is recommended that future research on this area focuses on testing more complex transients such as absorber oscillations. This would allow using the experimental setup for noise techniques such as the measurement of the reactor transfer function. With that said, the use of faster detection electronics is also recommended to be able to measure data at higher reactor power and thus reduce the statistical noise.

Concerning space-time kinetics measurements, it remains an open question whether it is possible to observe the effect of delayed neutrons on the flux shape during a transient in the CROCUS reactor. Preliminary numerical studies can be used to determine if the current experimental setup allows observing such an effect by running faster transients. The analysis should be based on the comparison of direct space-time kinetic simulations against transients approximated by a series of steady-state criticality calculations (i.e., using the adiabatic approach). While direct space-time kinetics consider the effect of delayed neutrons on the flux shape, the adiabatic approach does not and thus the difference between both simulations would reveal the effect of delayed neutrons.

With reference to the radial fission rate profiles experiments, it is recommended to perform measurements with a finer spatial resolution (2 mm) to better resolve the heterogeneities in the shape. Also, a potential source of bias of these measurements comes from the fact that the local fission rate (or neutron flux) is distorted due to the interaction of the neutron field with the detector's materials. It is, therefore, recommended to investigate this effect and to perform a correction on the measured data if it is required.

A Additional data

Table A.1 – CROCUS kinetic parameters from ENDF/B-VII.1 & U^{235} thermal fission products from Tuttle (1975)

λ_i [s^{-1}]	β_i *	σ_{λ_i} [%]	σ_{β_i} [%]	Λ [s^{-1}]
0.01336	0.00024	2.4	10.5	4.768×10^{-5}
0.03259	0.00130	3.7	3.2	
0.12110	0.00125	3.5	12.7	
0.30604	0.00279	3.9	2.5	
0.86235	0.00128	8.6	9.4	
2.89645	0.00051	14.3	15.4	

*Effective delayed neutron data

Table A.2 – Mobile fission chamber (Photonis CFUF34) response versus power

Power [W]	Detector's signal [cps]	u(signal) [cps]
0.05	330	6
0.10	622	8
0.19	1208	11
0.30	1856	14
0.49	2923	17
0.71	3985	20
0.98	5388	23
1.20	6387	25
1.44	7409	27
1.75	8683	29
1.97	9300	30
2.45	10916	33
4.99	15297	39

u(signal): standard statistical uncertainty

B Scripts and models

B.1 Serpent model of the CROCUS reactor

```
% --- Serpent model of the CROCUS reactor by Adolfo Rais
% adolfo.rais@epfl.ch - March 2016
set title "CROCUS-Serpent2"

% | 1. Surface Definitions  | 2. Cell Definitions   | 3. Transformation Cards |
% | 4. Material Definitions | 5. Serpent parameters | 6. Notes and comments   |

%%%%%%%%%%%%%%%%%%%%%%%%%%%%%%%%%%%%%%%%%%%%%%%%%%%%%%%%%%%%%%%%%%%%%%%%%%%%%%%%
% --- 1. Surface Definitions

% --- 1.1 Model + Vessel
surf    1    cylz    0 0 66.2 -47 117.3  % Vessel & Model OD
surf    2    cylz    0 0 65              %-44 102.3  % Vessel ID
surf    3    pz      -47                 % Vessel bottom OS & Model bottom
surf    4    pz      -44                 % Vessel bottom OS
surf    5    pz      102.3               % Vessel top
surf    6    pz      117.3               % Model top

% --- 1.2 Structures below core and start-up source
%    Hexagonal support with re-inforcement
surf  10 hexyprism  0 0 36.0 -44.0 -5.7 % x0,y0,d,z0,z1 Outer prism
surf  11 hexyprism  0 0 33.5 -44.0 -8.7 % x0,y0,d,z0,z1 Inner prism
surf  12    px -12.5                    % Inner reinforcement
surf  13    px -10.0
surf  14    px  10.0
surf  15    px  12.5
%   Tunnel for the start-up source
surf  16 cuboid -70 70 -13 13  -44 -5.7     % Tunnel outer limit
surf  17 cuboid -70 70 -10.5 10.5 -44 -8.7  % Tunnel inner limit
%   Start-up  source (L=5.131cm, radius=1.41cm)
surf  18  cylx  0 -13.2 1.41 -2.56 2.571   % y0,z0,r,x1,x2

% --- 1.3 Base plate (Octogonal)
surf  20   octa   0 0 36 36       % x0,y0,d1,d2 replaces surf 20 and 21 in MCNP
surf  22   pz    -5.7             % bottom of base plate
surf  23   pz    -2.7             % top of base plate

% --- 1.3 Lower grid plate (Octogonal)
surf   30  octa  0 0 38 38        % x0 y0 d1 d2 replaces surf 30 and 21 in MCNP
surf   32  pz    -0.55            % bottom of lower grid
surf   33  pz    -0.05            % bottom of lower Cd (thickness 0.05 cm)
surf   34  pz     0               % top of lower Cd
surf   35  pz     0.5             % top of lower grid plate

% --- 1.4 Water level in cm (max is 100 cm)
surf   40  pz 95.22

% --- 1.5 Upper grid plate
surf   50  octa 0 0 42 42   % x0 y0 d1 d2 replaces surf 50 and 51 in MCNP
surf   52    pz 100.5       % bottom of upper grid
surf   53    pz 101         % bottom of upper Cd
surf   54    pz 101.05      % top of upper Cd
surf   55    pz 102.55      % top of upper grid

% --- 1.6 UO2 Zone
%   UO2 zone outer radial boundaries
surf   60   cuboid -20.207 20.207  -5.511  5.511   -2.7 117.3
surf   61   cuboid -16.533 16.533  -11.022 11.022  -2.7 117.3
surf   62   cuboid -11.022 11.022  -16.533 16.533  -2.7 117.3
surf   63   cuboid  -5.511  5.511  -20.207 20.207  -2.7 117.3
%   UO2 cell
surf  160   cuboid -0.9185 0.9185 -0.9185 0.9185   -200 200
%   UO2 fuel rod model
surf   161    cylz 0 0 0.526   % fuel rod outer surface
surf   162    cylz 0 0 0.545   % inner surface of cladding
surf   163    cylz 0 0 0.63    % outer surface of cladding
surf   164    pz 100           % top of fuel
surf   165    pz 100.5         % top of spring

% --- 1.7 Umetal Zone
%   Umetal zone  outer radial boundaries
surf    70    octa     0 0   32.087   32.087
surf    71    cuboid -29.17  29.17   -29.17  29.17   -2.7 117.3
%% surf    71    cuboid -32.087 32.087  -32.087 32.087    -2.7 117.3 %%
%   Umetal zone inner radial boundaries
surf   72    cuboid -20.419 20.419   -5.834  5.834  -2.7 117.3
surf   73    cuboid -17.502 17.502  -11.668 11.668  -2.7 117.3
surf   74    cuboid -11.668 11.668  -17.502 17.502  -2.7 117.3
surf   75    cuboid  -5.834  5.834  -20.419 20.419  -2.7 117.3
%   Umetal cell boundary
surf   170    cuboid -1.4585 1.4585   -1.4585 1.4585 -200 200
%   Umetal fuel rod
surf   171    cylz 0 0 0.85    % fuel rod
surf   172    cylz 0 0 0.8675  % inner surface of clad
surf   173    cylz 0 0 0.9675  % outer surface of clad
surf   174    pz 100           % top of fuel
surf   175    pz 101.47        % top of spring

% --- 1.8 Control Rod
surf  200    cylz 0 0 0.4235  % B4C pellet (rmax=0.4238cm)
surf  201    cylz 0 0 0.4325  % cladding ss - inner
surf  202    cylz 0 0 0.4785  % cladding ss - outer
surf  203    cylz 0 0 0.6     % outer ss tube - inner part
surf  204    cylz 0 0 0.8     % outer ss tube - outer part
surf  205    pz -0.4          % al bottom of fixed tube and mobile part
surf  206    pz -0.3          % top of ss
surf  207    pz 0.0           % bottom of B4C pellets
surf  208    pz 0.2           % lower ss piece
surf  209    pz 100.25        % top of B4C pellets
surf  210    pz 101.3         % top of ss tube
surf  211    pz 102           % upper ss piece

% --- 1.9 Operation monitor: Ionisation chamber
surf  300 cylz 0 0 2.75 26.95 117.3   % casing outer dim - universe limit
surf  301 cylz -8.6  36.35 2.75 26.95 117.3   % for u=31 North Ionization chamber casing outer dim
surf  302 cylz  8.6 -36.35 2.75 26.95 117.3   % for u=32 South Ionization chamber casing outer dim
surf  303 cylz 0 0 2.5 29.95 229.95        % casing inner dim - infinite in height
surf  304 pz 65.45                              % sensitive part limit
surf  305 cylz 0 0 1.80                         % outer electrode out dim
surf  306 cylz 0 0 1.75                         % outer electrode int dim
surf  307 cylz 0 0 1.25                         % inner electrode out dim
surf  308 cylz 0 0 1.20                         % inner electrode int dim

% --- 1.10 Operation monitor: Fission chamber
surf  310 cylz 0 0 2.05 1.36 117.3   %  outer dim - universe limit
surf  311 cylz 0 0 1.50                         % upper part tube/water
surf  312 cylz 0 0 1.2 26.75 226.75      % upper part inner dim - inf. in height
surf  313 cylz 0 0 1.7 5.16 26.75       % lower part inner dim
surf  314 pz 14.56                              % sensitive part limit
surf  315 cylz 0 0 1.55                         % outer electrode out dim
surf  316 cylz 0 0 1.50                         % outer electrode int dim
surf  317 cylz 0 0 1.40                         % inner electrode out dim
surf  318 cylz 0 0 1.35                         % inner electrode int dim
surf  319 cylz  35.8   8.7 2.05 1.36 117.3   %  for u=34 North FC outer dim
surf  320 cylz -35.8  -8.7 2.05 1.36 117.3   %  for u=35 South FC outer dim

%%%%%%%%%%%%%%%%%%%%%%%%%%%%%%%%%%%%%%%%%%%%%%%%%%%%%%%%%%%%%%%%%%%%%%%%%%%%%%%%
% --- 2. Cell Definitions
% --- 2.1 Model and Vessel
cell    1     0  outside  1                            % outside
cell    2     0  Al6060  -1 ((2 -5 4):(3 -4))           % vessel
cell    3     0  Air     -1 2 -6 5 #((-70 -71)  -6 23)  % air above vessel
```

```
% --- 2.2 Support Structures below core
cell    5     0  H2O      -2  16 10  -22 4   % Water around support
cell    6     0  Al6060   -2 -16 17          % Tunnel walls
cell    7     0  fill 1    -2 -17            % Tunnel
cell    8     0  Al6060   -10 11 16          % North hexagonal support walls
cell    10    0  fill 2   -11  16            % North hexagonal support inside

% --- 2.3 Base plate
cell    12  0 H2O   -2 20 -23 22      % Water around base plate
cell    13  0 Al6060 -20  -23 22      % base plate

% --- 2.4 Fuel zones
cell   15   0  fill=10   (-60:-61:-62:-63) -6 23               % UO2 fuel zone
cell   16   0  fill=3    (-72:-73:-74:-75) -6 23 (60 61 62 63) % Gap between Umetal & UO2 fuel
cell   17   0  fill=15   -70 -71 (72 73 74 75)   -6 23         % U metal fuel zone
cell   18   0  fill=3    -2 (70:71)  -6 23 #20 #21 #22 #23     % Periphery (water&grid)
cell   20   0  fill=31   -301        % Ionisation chamber North
cell   21   0  fill=32   -302        % Ionisation chamber South
cell   22   0  fill=34   -319        % Fission chamber North
cell   23   0  fill=35   -320        % Fission chamber South

%  u = 1:  Tunnel with reactor startup source
cell   30  1  Air   -18             % cylindrical source (replace by PuBe for source)
cell   31  1  Air    18             % around the source

%  u = 2:  Reinforcement for the lower support structures
cell    35   2 Air        -12      % Air between support
cell    36   2 Al6060     -13 12   % Support
cell    37   2 Air        -14 13   % Air between support
cell    38   2 Al6060     -15 14   % Support
cell    39   2 Air         15      % Air between support

%  u = 3:  Generic description of grids and water for fuel zone
%  Water/Lower grid plate/Water/Air/Upper grid plate/Air
cell    40   3 H2O      -32              % Water below lower grid
cell    41   3 Al6060   -30  32 -33      % lower grid - lower Al layer
cell    42   3 Cd       -30  33 -34      % lower grid - Cd layer
cell    43   3 Al6060   -30  34 -35      % lower grid - upper Al layer
cell    44   3 H2O      30 32 -35        % Water around lower grid
cell    45   3 H2O      35 -40           % Water between grids
cell    46   3 Air      40 -52           % Air between grids
cell    47   3 Al6060   -50  52 -53      % upper grid - lower Al layer
cell    48   3 Cd       -50  53 -54      % upper grid - Cd layer
cell    49   3 Al6060   -50 54 -55       % upper grid - upper Al layer
cell    50   3 Air       50 52 -55       % Air around upper grid
cell    51   3 Air       55              % Air above upper grid

%  u = 10: UO2 fuel lattice
lat     10    1    0 0    24 24   1.837 % <u0> <type> <x0> <y0> <nx> <ny> <p>
11 11 11 11 11 11 11 11 11 11 11 11 11 11 11 11 11 11 11 11 11 11 11 11
11 11 11 11 11 11 11 11 11 11 11 11 11 11 11 11 11 11 11 11 11 11 11 11
11 11 11 11 11 11 11 11 11 11 11 11 11 11 11 11 11 11 11 11 11 11 11 11
11 11 11 11 11 11 11 11 11 11 11 11 11 11 11 11 11 11 11 11 11 11 11 11
11 11 11 11 11 11 11 11 11 11 11 11 11 11 11 11 11 11 11 11 11 11 11 11
11 11 11 11 11 11 11 11 11 11 11 11 11 11 11 11 11 11 11 11 11 11 11 11
11 11 11 11 11 11 11 11 11 11 11 11 11 11 11 11 11 11 11 11 11 11 11 11
11 11 11 11 11 11 11 11 11 11 11 11 11 11 11 11 11 11 11 11 11 11 11 11
11 11 11 11 11 11 11 11 11 11 11 11 11 11 11 11 11 11 11 11 11 11 11 11
11 11 11 11 11 11 11 11 11 11 11 11 11 11 11 11 11 11 11 11 11 11 11 11
11 11 11 11 11 11 11 11 11 11 11 11 11 11 11 11 11 11 11 11 11 11 11 11
11 11 11 11 11 11 11 11 11 11 11 11 11 11 11 11 11 11 11 11 11 11 11 11
11 11 11 11 11 11 11 11 11 11 11 11 11 11 11 11 11 11 11 11 11 11 11 11
11 11 11 11 11 11 11 11 11 11 11 11 11 11 11 11 11 11 11 11 11 11 11 11
11 11 11 11 11 11 11 11 11 11 11 11 11 11 11 11 11 11 11 11 11 11 11 11
11 11 11 11 11 11 11 11 11 11 11 11 11 11 11 11 11 11 11 11 11 11 11 11
11 11 11 11 11 11 11 11 11 11 11 11 11 11 11 11 11 11 11 11 11 11 11 11
11 11 11 11 11 11 11 11 11 11 11 11 11 11 11 11 11 11 11 11 11 11 11 11
11 11 11 11 11 11 11 11 11 11 11 11 11 11 11 11 11 11 11 11 11 11 11 11
11 11 11 11 11 11 11 11 11 11 11 11 11 11 11 11 11 11 11 11 11 11 11 11
11 11 11 11 11 11 11 11 11 11 11 11 11 11 11 11 11 11 11 11 11 11 11 11
11 11 11 11 11 11 11 11 11 11 11 11 11 11 11 11 11 11 11 11 11 11 11 11
11 11 11 11 11 11 11 11 11 11 11 11 11 11 11 11 11 11 11 11 11 11 11 11
11 11 11 11 11 11 11 11 11 11 11 11 11 11 11 11 11 11 11 11 11 11 11 11

%  u = 11: UO2 fuel cell
cell    110   11  Al6060  162 -163           % Al-cladding
cell    111   11  Al6060  -162 -34           % bottom plug
cell    112   11  He    161 -162 34 -164     % He-gap
cell    113   11  UO2  -161      34 -164     % UO2 - fuel
cell    114   11  springUO2  -162 164 -165   % spring region
cell    115   11  Al6060   -162 165          % upper plug
cell    116   11  fill 3   163               % pin surroundings

%  u = 15: Umetal fuel lattice with 176 fuel pins and 2 CR
lat     15     1    0 0    22 22   2.917 % <u0> <type> <x0> <y0> <nx> <ny> <p>
17 17 17 17 17 17 17 17 17 17 17 17 17 17 17 17 17 17 17 17 17 17
17 17 17 17 17 17 17 17 16 16 16 16 16 16 17 17 17 17 17 17 17 17
17 17 17 17 17 17 16 16 16 16 16 16 16 16 16 16 16 17 17 17 17 17
17 17 17 17 16 16 16 16 16 16 16 16 16 16 16 16 16 16 17 17 17 17
17 17 17 16 16 16 16 16 16 16 16 16 16 16 16 16 16 16 16 17 17 17
17 17 17 16 16 16 16 16 16 16 16 16 16 16 16 16 19 16 16 16 17 17
17 17 16 16 16 16 16 16 16 16 16 16 16 16 16 16 16 16 16 16 17 17
17 17 16 16 16 16 16 16 16 16 16 16 16 16 16 16 16 16 16 16 16 17
17 16 16 16 16 16 16 16 16 16 16 16 16 16 16 16 16 16 16 16 16 17
17 16 16 16 16 16 16 16 16 16 16 16 16 16 16 16 16 16 16 16 16 17
17 16 16 16 16 16 16 16 16 16 16 16 16 16 16 16 16 16 16 16 16 17
17 16 16 16 16 16 16 16 16 16 16 16 16 16 16 16 16 16 16 16 16 17
17 16 16 16 16 16 16 16 16 16 16 16 16 16 16 16 16 16 16 16 16 17
17 16 16 16 16 16 16 16 16 16 16 16 16 16 16 16 16 16 16 16 16 17
17 16 16 16 16 16 16 16 16 16 16 16 16 16 16 16 16 16 16 16 17 17
17 17 16 16 16 16 16 16 16 16 16 16 16 16 16 16 16 16 16 16 17 17
17 17 16 16 16 18 16 16 16 16 16 16 16 16 16 16 16 16 16 17 17 17
17 17 17 16 16 16 16 16 16 16 16 16 16 16 16 16 16 16 16 17 17 17
17 17 17 17 16 16 16 16 16 16 16 16 16 16 16 16 16 16 17 17 17 17
17 17 17 17 17 16 16 16 16 16 16 16 16 16 16 16 17 17 17 17 17 17
17 17 17 17 17 17 17 17 16 16 16 16 16 16 17 17 17 17 17 17 17 17
17 17 17 17 17 17 17 17 17 17 17 17 17 17 17 17 17 17 17 17 17 17

%  u = 16: Umetal fuel cell with pin
cell  160  16  Al6060      172 -173          % cladding
cell  161  16  He  171 -172 34 -174          % gap
cell  162  16  Al6060    -172 -34            % bottom plug
cell  163  16  Umet  -171 34  -174           % fuel Um
cell  164  16  springUmet      -172 174 -175 % spring region
cell  165  16  Al6060     -172 175           % upper plug
cell  166  16  fill=3            173         % pin surroundings

%  u = 17: Umetal fuel cell wihtout pin
cell  170  17   H2O    -173  -40             % Water instead of pin
cell  171  17   Air    -173   40             % Air instead of pin
cell  172  17   fill=3  173                  % Hole surroundings

%  u = 18: Control rod North (axial position tr8)
cell  180  18  fill=20       -172        % CR inner part
cell  181  18  Al6060      172 -173      % Um pin tube
cell  182  18  fill=3         173        % tube surroundings

%  u = 19: Control rod South (axial position tr9)
cell  190  19 fill=20     -172          % CR inner part
cell  191  19 Al6060      172 -173      % Um pin tube
cell  192  19 fill=3      173           % tube surroundings

%  u = 20: Control rod inner part (2 concentric SS tubes + B4C pellets)
cell  200   20  Air  (204 205):-205                % air below/around outer SS tube
cell  201   20  SS  (203 -204 205):(-203 205 -206) % outer ss tube
cell  202   20  Air (202 -203 208 -211)            % air between tubes
cell  203   20  SS  (202 -203 206 -208)            % lower centering ss piece
cell  204   20  SS  (201 -202 206):(-201 206 -207) % inner ss tube
cell  205   20  Air -201 200   207                 % air around B4C
cell  206   20  Air -200       209 -210            % air upper B4C
cell  207   20  SS  -200       210                 % top ss rod
cell  208   20  SS   202 -203  211                 % upper centering ss piece
cell  209   20  B4C  -200       207 -209           % B4C pellets

%  Ionisation chambers
%  u = 30: Ionisation chamber
cell  300   30  Al6060     303                % Casing
cell  301   30  Air       -303  304           % Non sensitive part
cell  302   30  Air       -303 -304  305      % Around outer electrode
cell  303   30  Al6060    -303 -304 -305 306  % Outer electrode
cell  304   30  Air       -303 -304 -306 307  % Between electrodes
cell  305   30  Al6060    -303 -304 -307 308  % Inner electrode
cell  306   30  Air       -303 -304 -308      % Central sensitive part
%  u = 31: Ionisation chamber North
cell  307   31  fill=30   -300      % North IC
%  u = 33: Ionisation chamber South
cell  308   32  fill=30   -300      % South IC

%  Fission chambers chambers
%  u = 33: Fission chamber
cell  310   33    fill=3   311 -312          % Water/grid upper part
cell  311   33    Al6060   312 -311 -312      % Casing upper part
cell  312   33    Air     -312                % Inside upper part
cell  313   33    Al6060   313       312      % Casing lower part
cell  314   33    Air     -313  314           % Non sensitive lower part
cell  315   33    Air     -313 -314  315      % Around outer electrode
cell  316   33    Al6060  -313 -314 -315 316  % Outer electrode
cell  317   33    Air     -313 -314 -316 317  % Between electrodes
cell  318   33    Al6060  -313 -314 -317 318  % Inner electrode
cell  319   33    Air     -313 -314 -318      % Central sensitive part
%  u = 34: Fission chamber North
cell  320   34  fill=33   -310      % North FC
%  u = 35: Fission chamber South
cell  321   35  fill=33   -310      % South FC

%%%%%%%%%%%%%%%%%%%%%%%%%%%%%%%%%%%%%%%%%%%%%%%%%%%%%%%%%%%%%%%%%%%%%%%%%%%%%%%%
% --- 3. Transformation Cards (unverse ’trans’ and surfaces ’strans’)

%  Translation of the control rods (z=0 CR inserted, z=100 CR withdrawn)
trans   20     0  0   100  % <u> <x> <y> <z>
%  Translation for the operation monitors <CHECK> not used currently
trans   31    -8.6   36.35  0  % Ionisation chamber North
trans   32     8.6  -36.35  0  % Ionisation chamber South
trans   34     35.8    8.7  0  % Fission chamber North
trans   35    -35.8   -8.7  0  % Fission chamber South

%%%%%%%%%%%%%%%%%%%%%%%%%%%%%%%%%%%%%%%%%%%%%%%%%%%%%%%%%%%%%%%%%%%%%%%%%%%%%%%%
% --- 4. Material Definitions

mat Al6060     -2.702   rgb 192 191 192   % m1 Plugs & vessel material
13027.03c -0.98000
14028.03c -0.00551  14029.03c -0.00029  14030.03c -0.00020
26054.03c -0.00017
26056.03c -0.00276  26057.03c -0.00006  26058.03c -0.00001
29063.03c -0.00068  29065.03c -0.00032  25055.03c -0.00100
12024.03c -0.00468  12025.03c -0.00062  12026.03c -0.00071
24050.03c -0.00002  24052.03c -0.00042
24053.03c -0.00005  24054.03c -0.00001
22046.03c -7.92e-5  22047.03c -7.30e-5  22048.03c -7.38e-4
22049.03c -5.53e-5  22050.03c -5.40e-5
30000.03c -0.00150

mat He      -1.6422e-4  rgb 255 255 150         % m2 Helium
2004.03c              1

mat H2O    -0.9983   rgb 51 153 255   moder lwtr 1001  % m3 Water
1001.03c         0.6665
1002.03c         0.0001
8016.03c         0.3334

mat Cd       -8.65 rgb 0 153 0              % m4 Nat. Cadmium
48106.03c   1.25
48108.03c   0.89
48110.03c   12.49
48111.03c   12.80
48112.03c   24.13
48113.03c   12.22
48114.03c   28.73
48116.03c   7.49

mat UO2       -10.55553  rgb 255 153 50   % m5 1.086% U235
92235.03c     -0.015920
92238.03c     -0.865593
8016.03c      -0.118487

mat springUO2   -1.2    rgb 0 0 128         % m6 Spring located in the UO2 rod
26054.03c       0.04115
26056.03c       0.64546 26057.03c       0.01491 26058.03c       0.00197
24050.03c       0.00833 24052.03c       0.16046 24053.03c       0.01819
24054.03c       0.00452 28058.03c       0.05787 28060.03c       0.02229
28061.03c       0.00097 28062.03c       0.00309 28064.03c       0.00079
25055.03c          0.02

mat springUmet  -2.93   rgb 0 0 139     % m6 Spring located in the Umet rodmpirun
26054.03c       0.04115
26056.03c       0.64546 26057.03c       0.01491 26058.03c       0.00197
24050.03c       0.00833 24052.03c       0.16046 24053.03c       0.01819
24054.03c       0.00452 28058.03c       0.05787 28060.03c       0.02229
28061.03c       0.00097 28062.03c       0.00309 28064.03c       0.00079
25055.03c          0.02

mat Umet      -18.67655 rgb 250 0 0   % m7 Uranium metal
92235.03c      -0.00947
```

```
92238.03c      -0.99053

mat Al6012    -2.75    rgb 191 192 192          % m8 alu 6012 for grid plates
13027.03c -0.941
14028.03c -0.00919   14029.03c -0.00048  14030.03c -0.00033
26054.03c -0.000292  26056.03c -0.004588
26057.03c -0.000106  26058.03c -1.4e-005 29063.03c -0.0006917
29065.03c -0.0003083 25055.03c -0.0007
12024.03c -0.00702   12025.03c -0.00093  12026.03c -0.00106
24050.03c -0.00013   24052.03c -0.00251  24053.03c -0.000285
24054.03c -7.1e-005
22046.03c -1.58e-4   22047.03c -1.46e-4  22048.03c -1.48e-3
22049.03c -1.11e-4   22050.03c -1.08e-4
30000.03c -0.003
83209.03c -0.007
82204.03c -0.000165  82206.03c -0.002870 82207.03c -0.002650
82208.03c -0.006310

mat Air     -5.058e-005   rgb 250 250 250 moder lwtr 1001 % m9 Air
7014.03c         4e-005
8016.03c         1e-005
1001.03c   5.79913e-007
1002.03c       8.7e-011

mat SS  -8.1  rgb 47 79 79        % m11 Stainless steel - 316 type
24052.03c      -0.14206
24053.03c       -0.0152 24050.03c      -0.00274 28058.03c     -0.087138
28060.03c     -0.033565 28062.03c     -0.004666 28061.03c     -0.002631
12024.03c      -0.00008 12025.03c      -0.00001 12026.03c     -0.00001
25055.03c        -0.019 14028.03c       -0.0054 14029.03c       -0.0003
14030.03c       -0.0002 26054.03c      -0.03916 26056.03c       -0.63204
26057.03c       -0.0158

mat B4C -1.799  rgb 0 250 0   % m12 B4C pellet (control rods)
5010.03c        -0.1442
5011.03c        -0.6384
6000.03c        -0.2174

mat PuBe -2.695 rgb 174 0 255  % m14 Fixed source for approach to critical
94239.03c       -0.9637
4009.03c        -0.0363

%%%%%%%%%%%%%%%%%%%%%%%%%%%%%%%%%%%%%%%%%%%%%%%%%%%%%%%%%%%%%%%%%%%%%%%%%%%%%%%%
% --- 5. Serpent parameters

% --- 5.1 Thermal scattering data for light water:
therm lwtr lwj3.00t    % JEFF-3.1 Data for Serpent 1.1.0 (HinH20 at 293.60K)

% --- 5.2 Cross section data library file path:
set acelib "/afs/psi.ch/project/stars/archive/COD/SERP/SB-SERP-ACT-001-11/Libraries/jeff311/sss_jeff311u.xsdata"

% --- 5.3 Unresolved resonance probability tables
set ures 1       % ptables turned on.

% --- 5.4 Boundary condition:
set bc 1 1 1

% --- 5.5 Neutron population and criticality cycles:
%set pop 1000000  1100  100 % keff within 2 pcm
set pop 1000000 10000  100  % keff within 0.7 pcm

% --- 5.6 Geometry and mesh plots:
plot 10 1058 1314  0.9185  -66.2  66.2 -47 117.3     % YZ cut
plot 30 1000 1000  50      -66.2  66.2  -66.2  66.2  % XY cut
mesh 3 1000 1000
mesh 2 1058 1314

%%%%%%%%%%%%%%%%%%%%%%%%%%%%%%%%%%%%%%%%%%%%%%%%%%%%%%%%%%%%%%%%%%%%%%%%%%%%%%%%
% --- 6. Notes and comments

% 6.1 The hexagonal support structure below the core is not very close but not
% exaclty the same as in reality
% 6.2 The fission and ionization chambers are only composed by aluminum and air.
%                                << End of model >>
```

B.2 Serpent to FMFD-compatible cross-section

```
% Matlab script to covert SERPENT2 cross sections to fmfd format of PARCS
% Author: Adolfo Rais - E-mail: adolfo.rais at epfl.ch
% Notes. Kinetic data not avaible.

clear all; clc; close all

% Load data from Serpent output file ?<input>_res.m?
disp(’1. Select the Serpent output file’)


[FileName,PathName] = uigetfile(’*.m’,’Select the Serpent < _res.m > file’);
run(FileName);
cd(PathName);


NG = MACRO_NG(1);       % Number of energy groups
NXS = idx;           % Numnber of cross section sets

% XS reading from Serpent2 output file

% XS format: sigxx(NXS,NG) where NXS is the component and NG
% the energy group. (fast group first)
for i=1:NXS
for j=1:NG
sigtr(i,j) = TRC_TRANSPXS(i,j*2-1);                 % Transport corrected TRANSXS
siga(i,j)  = INF_RABSXS(i,j*2-1);                   % Reduced Absoption - OK
signf(i,j) = INF_NSF(i,j*2-1);                      % Nu-fission  - OK
sigkf(i,j) = INF_KAPPA(i,j*2-1)*INF_FISS(i,j*2-1)*1.6021765E-13; % Kappa-fission with MeV to Joule conversion
sigscatt(i,:)  = INF_S0(i,1:2:end);                 % Scattering matrix
%sig12corr(i,:)  = INF_S0(i,3) - INF_S0(i,5)*INF_FLX(i,3)/INF_FLX(i,1); % Up-scattering corrected down-scattering
velocity(i,j) = INF_INVV(i,j*2-1);
% chi_delay(i,j) = INF_CHID(i,j*2-1); %not used
chi_total(i,j) = INF_CHIT(i,j*2-1);
end
for j=1:(length(FWD_ANA_LAMBDA)/2-1) %iterate over delayd neutron param
lambda(i,j) = FWD_ANA_LAMBDA(i,j*2-1);
beta(i,j) = ADJ_MEULEKAMP_BETA_EFF(i,j*2-1);
end

end

% Write fmfd compatible file

%%%%%%%%%%%%%%%%%%%%%%%% FMFD file %%%%%%%%%%%%%%%%%%%%%%%%
for i=1:NXS %iterate over number of universes
filename = (sprintf(’%dG_%d_fmfd.xsec’, NG, i));
fid=fopen(filename,’w’);


fprintf(fid, [ ’     tr           ab           nuf          kaf  \n’]);
for j=1:NG  %iterate over number of groups
fprintf(fid, [ ’ %E  %E  %E  %E\n’],sigtr(i,j), siga(i,j), signf(i,j), sigkf(i,j));
end

fprintf(fid, [ ’ scat g‘->g, UPP TRI is DOWNSCAT, LOW TRI is UPSCAT  \n’]);
scattmat = reshape(sigscatt(i,:),[NG,NG]);
for j=1:NG  %iterate over number of groups
fprintf(fid, [ ’ %E ’],scattmat(:,j));
fprintf(fid, [ ’\n’]);
end

fprintf(fid, [ ’ lambda  \n’]);
fprintf(fid, [ ’ %E ’],lambda(i,:)’);
fprintf(fid, [ ’\n’]);

fprintf(fid, [ ’ beta  \n’]);
fprintf(fid, [ ’ %E ’],beta(i,:)’);
fprintf(fid, [ ’\n’]);

fprintf(fid, [ ’ velocity  \n’]);
fprintf(fid, [ ’ %E ’],velocity(i,:)’);
fprintf(fid, [ ’\n’]);

fprintf(fid, [ ’ chi_delay  \n’]);
for j=1:NG  % all zeros
fprintf(fid, [ ’ %E ’],zeros(8,1));
fprintf(fid, [ '\n']);
end

fprintf(fid, [ ' chi_total  \n']);
fprintf(fid, [ ' %E '],chi_total(i,:)');
fprintf(fid, [ '\n']);

for i=1:5 %  dtm, dtf, ddm, cra and ppm

if i == 1
fprintf(fid, [ '     dtm tr       ab           nuf          kaf\n']);
elseif i == 2
fprintf(fid, [ '     dtf tr       ab           nuf          kaf\n']);
elseif i == 3
fprintf(fid, [ '     ddm tr       ab           nuf          kaf\n']);
elseif i == 4
fprintf(fid, [ '     cra tr       ab           nuf          kaf\n']);
elseif i == 5
fprintf(fid, [ '     ppm tr       ab           nuf          kaf\n']);
end
for j=1:NG  % all zeros
fprintf(fid, [ ' %E '],zeros(4,1));
fprintf(fid, [ '\n']);
end

fprintf(fid, [ ' scat g`->g, UPP TRI is DOWNSCAT, LOW TRI is UPSCAT  \n']);

for j=1:NG  % all zeros
fprintf(fid, [ ' %E '],zeros(NG,1));
fprintf(fid, [ '\n']);
end
end


fprintf(fid, [ '  \n']);


end

fclose(fid);
%%%%%%%%%%%%%%%%%%%%%% END FMFD file %%%%%%%%%%%%%%%%%%%%%%%
```

Bibliography

[1] R Früh. Réacteur crocus, complément au rapport de sécurité: Réactivité et paramètres cinétiques, 1993.

[2] V Lamirand, Mathieu Hursin, P Frajtag, A Pautz, G Perret, and O Pakari. Future experimental programmes in the crocus reactor. In *Conference proceedings of RRFM/IGORR 2016*, number EPFL-CONF-218310, pages 284–292, 2016.

[3] International Atomic Energy Agency. *Safety Analysis for Research Reactors.* Number 55 in Safety Reports Series. International Atomic Energy Agency, Vienna, 2008. URL http://www-pub.iaea.org/books/IAEABooks/7753/Safety-Analysis-for-Research-Reactors.

[4] Carl Franklin Obenchain. Paret: A program for the analysis of reactor transients. Technical report, Phillips Petroleum Co., Idaho Falls, Idaho. Atomic Energy Div., 1969.

[5] T J Downar, D A Barber, R M Miller, C Lee, T Kozlowski, D Lee, Y Xu, J Gan, H G Joo, J Y Cho, et al. Parcs: Purdue advanced reactor core simulator. In *Proc. Int. Conf. on the New Frontiers of Nuclear Technology: Reactor Physics, Safety and High-Performance Computing*, pages 7–10, 2002.

[6] KS Smith and JD Rhodes. Casmo-4 characteristics methods for two-dimensional pwr and bwr core calculations. *Trans. Am. Nucl. Soc*, 83:294, 2000.

[7] J Leppänen. Development of a dynamic simulation mode in serpent 2 monte carlo code. Technical report, American Nuclear Society, 555 North Kensington Avenue, La Grange Park, IL 60526 (United States), 2013.

[8] Bart L Sjenitzer and J Eduard Hoogenboom. Dynamic monte carlo method for nuclear reactor kinetics calculations. *Nuclear Science and Engineering*, 175(1):94–107, 2013.

[9] High-performance monte carlo: an FP7 euratom project, 2017. URL http://www.fp7-hpmc.eu/.

[10] Ely M Gelbard. Application of spherical harmonics method to reactor problems. *Bettis Atomic Power Laboratory, WAPD-BT-20*, 1960.

[11] E.E. Lewis and W.F. Miller. *Computational methods of neutron transport.* John Wiley and Sons, Inc.,New York, NY, Jan 1984.

[12] Edward W Larsen and Jim E Morel. Advances in discrete-ordinates methodology. In *Nuclear Computational Science*, pages 1–84. Springer, 2010.

[13] JR Askew. A characteristics formulation of the neutron transport equation in complicated geometries. Technical report, United Kingdom Atomic Energy Authority, 1972.

[14] JR Askew. *Review of the status of Collision Probability Methods.* UKAEA Atomic Energy Establishment, 1972.

[15] James J Duderstadt and Louis J Hamilton. Nuclear Reactor Analysis, 1976. ISSN 02580926.

[16] Olgierd Cecil Zienkiewicz, Robert Leroy Taylor, and Robert Lee Taylor. *The finite element method*, volume 3. McGraw-hill London, 1977.

[17] Weston M Stacey. *Nuclear reactor physics.* John Wiley & Sons, 2007.

[18] A Hébert. *Applied Reactor Physics.* Presses Internationales Polytechnique, 2009.

[19] RD Lawrence and JJ Dorning. A discrete nodal integral transport theory method for multidimensional reactor physics and shielding. In *Proceedings of the ANS Conference on Advances in Reactor Physics and Shielding, Sun Valley, Idaho*, 1980.

[20] TM Sutton and BN Aviles. Diffusion theory methods for spatial kinetics calculations. *Progress in Nuclear Energy*, 30(2):119–182, 1996.

[21] Nam Zin Cho. Fundamentals and recent developments of reactor physics methods. *Nuclear Engineering and Technology*, 37(1):25–78, 2005.

[22] RD Lawrence. Progress in nodal methods for the solution of the neutron diffusion and transport equations. *Progress in Nuclear Energy*, 17(3):271–301, 1986.

[23] Jack Dorning. *Nuclear Reactor Kinetics: 1934–1999 and Beyond*, pages 375–457. Springer Netherlands, Dordrecht, 2010. ISBN 978-90-481-3411-3. doi: 10.1007/978-90-481-3411-3_8. URL http://dx.doi.org/10.1007/978-90-481-3411-3_8.

[24] Yousry Azmy and Enrico Sartori. *Nuclear Computational Science.* Springer, 2009.

[25] Ivan Lux and László Koblinger. *Monte Carlo particle transport methods: neutron and photon calculations*, volume 102. CRC press Boca Raton, Florida, 1991.

[26] Jaakko Leppänen et al. *Development of a new Monte Carlo reactor physics code.* VTT Technical Research Centre of Finland, 2007.

[27] Forrest B Brown. On the use of shannon entropy of the fission distribution for assessing convergence of monte carlo criticality calculations. In *ANS topical meeting on reactor physics (PHYSOR 2006). Canadian Nuclear Society, Canada*, 2006.

[28] Akio Yamamoto, Yasunori Kitamura, and Yoshihiro Yamane. Simplified treatments of anisotropic scattering in lwr core calculations. *Journal of nuclear science and technology*, 45(3):217–229, 2008.

[29] Zhaoyuan Liu, Kord Smith, Benoit Forget, and Javier Ortensi. A cumulative migration method for computing rigorous transport cross sections and diffusion coefficients for lwr lattices with monte carlo. Technical report, Idaho National Laboratory (INL), Idaho Falls, ID (United States), 2016.

[30] Han Gyu Joo, Jin Young Cho, Kang Seog Kim, Chung Chan Lee, and Sung Quun Zee. Methods and performance of a three-dimensional whole-core transport code decart. *PHYSOR 2004*, 2004.

[31] YS Jung. ntracer v1. 0 methodology manual. *SNURPL-CM001 (10), Seoul National University Reactor Physics Laboratory, Seoul, Republic of Korea*, 2010.

[32] Benjamin Collins, T Downar, Jess Gehin, Andrew Godfrey, Aaron Graham, Daniel Jabaay, Blake Kelley, Kevin Clarno, Kang Seog Kim, Brendan Kochunas, et al. Mpact theory manual. Technical report, Technical Report CASL-U-2015-0078-000, Consortium for Advanced Simulation of LWRs, 2015.

[33] B Kochunas, B Collins, D Jabaay, TJ Downar, and WR Martin. Overview of development and design of mpact: Michigan parallel characteristics transport code. Technical report, American Nuclear Society, 555 North Kensington Avenue, La Grange Park, IL 60526 (United States), 2013.

[34] J Dorning. Homogenized multigroup and energy-dependent diffusion equations as asymptotic approximations to the boltzmann equation. *TRANSACTIONS-AMERICAN NUCLEAR SOCIETY*, pages 313–316, 2003.

[35] Kord S Smith. Assembly homogenization techniques for light water reactor analysis. *Progress in Nuclear Energy*, 17(3):303–335, 1986.

[36] A. Hebert. A consistent technique for the pin-by-pin homogenization of a pressurized water reactor assembly. *Nuclear Science and Engineering; (United States)*, 113:3, Mar 1993. doi: 10.13182/NSE92-10.

[37] RJ Stamm'ler et al. Helios methods. *Studsvik Scandpower*, 1998.

[38] E Fridman and J Leppänen. On the use of the serpent monte carlo code for few-group cross section generation. *Annals of Nuclear Energy*, 38(6):1399–1405, 2011.

[39] Jaakko Leppänen. Serpent–a continuous-energy monte carlo reactor physics burnup calculation code. *VTT Technical Research Centre of Finland*, 4, 2013.

[40] Dave Knott and Akio Yamamoto. Lattice physics computations. In *Handbook of nuclear engineering*, pages 913–1239. Springer, 2010.

[41] Patrick S Brantley and Edward W Larsen. The simplified p 3 approximation. *Nuclear Science and Engineering*, 134(1):1–21, 2000.

[42] AF Henry. The application of reactor kinetics to the analysis of experiments. *Nuclear Science and Engineering*, 3(1):52–70, 1958.

[43] Karl Otto Ott and Robert J Neuhold. *Introductory nuclear reactor dynamics*. American Nuclear Society, 1985.

[44] AF Henry and NJ Curlee. Verification of a method for treating neutron space-time problems. *Nuclear Science and Engineering*, 4(6):727–744, 1958.

[45] HG Joo, DA Barber, G Jiang, and TJ Downar. Parcs: Purdue advanced reactor core simulator. *Purdue University, School of Nuclear Engineering, PU/NE-98-26*, 1998.

[46] T Downar, Y Seker, and N Hudson. Parcs. *US NRC Core Neutronics Simulator, THEORY MANUAL, Department of Nuclear Engineering and Radiological Sciences University of Michigan*, 2012.

[47] Ville Valtavirta et al. Development and applications of multi-physics capabilities in a continuous energy monte carlo neutron transport code. 2017.

[48] Rudi JJ Stamm'ler and Máximo J Abbate. *Methods of steady-state reactor physics in nuclear design*, volume 111. Academic Press London, 1983.

[49] Jaakko Leppänen, Maria Pusa, and Emil Fridman. Overview of methodology for spatial homogenization in the serpent 2 monte carlo code. *Annals of Nuclear Energy*, 96:126–136, 2016.

[50] Jaakko Leppänen, Manuele Aufiero, Emil Fridman, Reuven Rachamin, and Steven van der Marck. Calculation of effective point kinetics parameters in the serpent 2 monte carlo code. *Annals of Nuclear Energy*, 65:272–279, 2014.

[51] Robin Klein Meulekamp and Steven C van der Marck. Calculating the effective delayed neutron fraction with monte carlo. *Nuclear science and engineering*, 152(2): 142–148, 2006.

[52] Yasushi Nauchi and Takanori Kameyama. Development of calculation technique for iterated fission probability and reactor kinetic parameters using continuous-energy monte carlo method. *Journal of nuclear science and technology*, 47(11):977–990, 2010.

[53] Z Zhong, T Downar, and M DeHart. Benchmarking the us nrc neutronics codes newt and parcs with the venus-2 mox critical experiments. *Nuclear Mathematical and Computational Sciences: A Century in Review*, pages 6–11, 2003.

[54] Matthew T Hardgrove. *Validation and Application of TRACE/PARCS to Boiling Water Reactor Stability Analysis on the Basis of the OECD/NRC Oskarshamn-2 Benchmark*. PhD thesis, The Pennsylvania State University, 2012.

[55] Raymond C Wang, Yunlin Xu, Nathanael Hudson, and Thomas J Downar. Validation of the us nrc coupled code system triton/trace/parcs using the special power excursion reactor test iii. *Nuclear Technology*, 183(3):504–514, 2013.

[56] KS Smith. Nodal method storage reduction by nonlinear iteration. *Transactions of the American Nuclear Society*, 44, 1983.

[57] Gilles Bignan, Philippe Fougeras, Patrick Blaise, Jean-Pascal Hudelot, and Frédéric Mellier. Reactor physics experiments on zero power reactors. In *Handbook of Nuclear Engineering*, pages 2053–2184. Springer, 2010.

[58] Grégory Perret. *Amélioration et développement des méthodes de détermination de la réactivité-Maîtrise des incertitudes associées*. PhD thesis, Thèse de doctorat, Université Joseph Fourier-Grenoble I, 2003.

[59] OECD/NEA. *Kinetic Parameters and Reactivity Effect Experiments in CROCUS - International handbook of evaluated reactor physics benchmark experiments*. OECD Nuclear Energy Agency, 2009.

[60] G Perret, G Girardin, P Frajtag, and M Hursin. Decay constant and delayed neutron fraction measurements in crocus. Technical report, TM-41-14-02, 2014.

[61] Antonio D'Angelo and John L Rowlands. Conclusions concerning the delayed neutron data for the major actinides. *Progress in Nuclear Energy*, 41(1):391–412, 2002.

[62] RJ Tuttle. Delayed-neutron data for reactor-physics analysis. *Nuclear Science and Engineering*, 56(1):37–71, 1975.

[63] G Perret. Delayed neutron fraction and generation time measurements at the zero-power reactor minerve - psi results. Technical report, TM-41-14-21, 2015.

[64] Adolfo Rais. Crocus integral control rod reactivity worth measurements. *École Polytechnique Fédérale de Lausanne (EPFL)*, 2015.

[65] Bureau International des Poids et Mesures, Commission électrotechnique internationale, and Organisation internationale de normalisation. *Guide to the expression of uncertainty in measurement*. International Organization for Standardization, 1995.

[66] JE Houghtaling, M Ishikawa, JF Scott, and DI Hergorn. Temperature-dependent kinetic behavior of the spert-iii e-core. Technical report, Phillips Petroleum Co., Idaho Falls, Idaho, 1967.

[67] CE Dickerman, RD Johnson, and J Gasidlo. Kinetics of treat used as a test reactor. Technical report, Argonne National Lab., Ill.; Argonne National Lab., Idaho Falls, Idaho, 1962.

[68] WG Winn, PB Parks, NP Baumann, and CE Jewell. Multidimensional space-time nuclear reactor kinetics studies. part iii: Three-dimensional experiments. *Nuclear Science and Engineering*, 65(2):254–272, 1978.

[69] FN McDonnell, AP Baudouin, and DH Walker. Transient experiments in simulated candu reactor cores. *DISCLAIMER Portions of this document may be illegible in electronic image products. Images are produced from the best available original document.*, page 301, 1977.

[70] H Christensen, D Babala, T Bergem, S Jovanovic, E Stormark, and W Suwalski. A review of nora project noise experiments. Technical report, Institutt for Atomenergi, Kjeller (Norway), 1967.

[71] A Edward Profio. Kinetics and noise analysis of zero-power reactors: An npy-project report, 1974.

[72] F Mellier et al. The muse experiments for sub critical neutronics validation. *Final Report to the European Commission*, 2005.

[73] F. Gabrielli, M. Carta, A. D'Angelo, W. Maschek, and A. Rineiski. Inferring the reactivity in accelerator driven systems: Corrective spatial factors for source-jerk and area methods. *Progress in Nuclear Energy*, 50(2):370 – 376, 2008. ISSN 0149-1970. doi: http://dx.doi.org/10.1016/j.pnucene.2007.11.019. URL http://www.sciencedirect.com/science/article/pii/S014919700700162X. Innovative Nuclear Energy Systems for Sustainable Development of the World. Proceedings of the Second COE-INES International Symposium, INES-2, November 26-30, 2006, Yokohama, Japan.

[74] Imre Pázsit and Christophe Demazière. Noise techniques in nuclear systems. In *Handbook of Nuclear Engineering*, pages 1629–1737. Springer, 2010.

[75] Alan V Oppenheim. *Discrete-time signal processing*. Pearson Education India, 1999.

[76] Steven W Smith et al. *The scientist and engineer's guide to digital signal processing*. California Technical Pub. San Diego, 1997.

[77] A Ward, Y Xu, and T Downar. Genpmaxs. *University of Michigan*, 2013.

[78] Sooyoung Choi, Kord Smith, Hyun Chul Lee, and Deokjung Lee. Impact of inflow transport approximation on light water reactor analysis. *Journal of Computational Physics*, 299:352–373, 2015.

[79] Bryan R Herman, Benoit Forget, Kord Smith, and Brian N Aviles. Improved diffusion coefficients generated from monte carlo codes. Technical report, American Nuclear Society, 555 North Kensington Avenue, La Grange Park, IL 60526 (United States), 2013.

[80] K Smith. Nodal diffusion methods: Understanding numerous unpublished details. In *Proc. Int. Conf. PHYSOR*, 2016.

[81] Bryan Robert Herman. *Monte Carlo and thermal hydraulic coupling using low-order nonlinear diffusion acceleration*. PhD thesis, Massachusetts Institute of Technology, 2014.

[82] Adolfo Rais, Daniel Siefman, Gaëtan Girardin, Mathieu Hursin, and Andreas Pautz. Methods and models for the coupled neutronics and thermal-hydraulics analysis of the crocus reactor at efpl. *Science and Technology of Nuclear Installations*, 2015, 2015.

[83] A Rais, D Siefman, M Hursin, A Ward, and A Pautz. Neutronics modeling of the crocus reactor with serpent and parcs codes. In *Proceedings of the International Conference on Mathematics & Computational Methods Applied to Nuclear Science & Engineering, Jeju, Korea*, 2017.

[84] Malte Edenius, Kim Ekberg, Bengt H Forssén, and Dave Knott. Casmo-4, a fuel assembly burnup program, user's manual. *Studsvik0SOA-9501, Studsvik of America, Inc*, 1995.

Adolfo Rais

Rue du Simplon 24
1006 Lausanne, Switzerland

+41 76 770 72 49 | `adolfo.rais@gmail.com`
`https://www.linkedin.com/in/adolforais`

EDUCATION

- **Ph.D. Candidate in Nuclear Engineering** (2013 - present) *École Polytechnique Fédérale de Lausanne*, Switzerland. Expected graduation date: November 2017.
- **Master in Material Science and Engineering** (2012 - 2013) *Institut Polytechnique de Grenoble*, France. Graduated with highest grade average (15.98/20), ranked 1st of class 2012.
- **Master in Nuclear Engineering** (2011 - 2012) *Universitat Politècnica de Catalunya*, Barcelona, Spain. Graduated with highest grade average (9.38/10), ranked 1st of class 2011.
- **Mechanical Engineering** - Master degree level (2004 - 2009) *Instituto Balseiro*, Argentina.

RELEVANT PROFESSIONAL EXPERIENCE

Nuclear engineering research assistant at EPFL, Switzerland — Oct. 2013 - present

Experimental and computational neutronics analysis of small-core nuclear research reactors.

- Performed numerical simulations using Monte Carlo and diffusion theory codes for the steady-state and transient neutronics analysis of the CROCUS reactor.
- Designed and carried out neutronics experiments at the CROCUS nuclear reactor for the experimental benchmarking of nuclear computer codes.

Nuclear engineering research assistant at McMaster University, Canada — Mar. 2013 - Aug. 2013

Investigated and characterized thermal-hydraulic phenomena of nuclear reactors.

- Carried out thermal-hydraulics experiments in a test loop to study the critical heat flux (CHF) phenomenon under transient conditions.
- Performed experimental and code-to-code benchmarking of the TRACE thermal-hydraulics code (from U.S. Nuclear Regulatory Commission) to determine its limitations for low-operating pressure research reactors.

Junior Field/Project Engineer at Petrolera Entre Lomas S.A., Argentina — Oct. 2009 - Aug. 2011

Worked on several projects in the areas of oil and gas production and transportation.

- Executed a project to improve the production allocation of the oil&gas field and minimize losses. Performed a technical and financial feasibility assessment of advanced metering devices (coriolis flowmeters + infrared water-cut meters) at the wellheads and manifold systems. Supervised the implementation of the new metering devices.
- Performed a risk and integrity assessment of a gas-fired pipeline heater to estimate the operating conditions limits and its life cycle.
- Planned and coordinated the refurbishment of all orifice gas meters in the field.
- Carried out the sizing, selection and performance evaluation of an ultrasonic flowmeter for the oil storage plant.
- Applied root cause analysis (RCA) to solve a recurrent maintenance problem in gas compressors.
- Provided training to technicians and field operators by means of technical talks and presentations.

LANGUAGES

- **English:** Fluent (C1 level in CEFR scale)
- **French:** Fluent spoken and very good command in written (C1 and B2 levels in CEFR scale)
- **Spanish:** Native speaker

RESEARCH INTERESTS

- Physics of nuclear reactors: Explicit full-core 3-D neutron transport methods, advanced neutron kinetics/thermal-hydraulics coupling, time-dependent Monte Carlo neutron transport, neutronic transient analysis and benchmarking. Neutronics experiments for computer codes performance assessment.
- Thermal-hydraulics of nuclear reactors: Computational multiphase and multi-dimensional fluid dynamics, flow instabilities, heat transport with phase change and critical heat flux.
- High performance computing for nuclear engineering applications.

REFEREED JOURNAL PUBLICATIONS

- Rais, A., Siefman, D. J., Girardin, G., Hursin, M., & Pautz, A. (2015). "Methods and models for the coupled neutronics and thermal-hydraulics analysis of the CROCUS reactor at EFPL". Science and Technology of Nuclear Installations, vol. 2015, Article ID 237646, 9 pages, 2015. doi:10.1155/2015/237646.
- Siefman, D. J., Girardin, G., Rais, A., Hursin, M., & Pautz, A. (2015). "Full Core modeling techniques for research reactors with irregular geometries using Serpent and PARCS applied to the CROCUS reactor". Annals of Nuclear Energy , 2015, vol. 85, p. 434-443.

MANUSCRIPTS IN PREPARATION

- Rais, A., Hursin, M., Ward, A., Downar, T., & Pautz, A. "Benchmarking of the PARCS code against reactivity worth and fission rate profile experiments at the CROCUS reactor". Manuscript in preparation to be submitted to the Nuclear Science and Engineering journal of the American Nuclear Society.
- Rais, A., Hursin, M., Ward, A., Downar, T., & Pautz, A. "Benchmarking of the PARCS neutron kinetics code against time-dependent measurements at the CROCUS reactor". Manuscript in preparation.

CONFERENCE PRESENTATIONS, PROCEEDINGS AND PAPERS

- Rais, A., Siefman, D., Hursin, M., Ward, A., & Pautz, A. (2017) "Neutronics modeling of the CROCUS reactor with SERPENT and PARCS codes" in Proceedings of the International Conference on Mathematics & Computational Methods Applied to Nuclear Science & Engineering, Jeju, Korea, April 16-20, 2017
- Rais, A., Hursin, M., Perret, G., & Pautz, A. (2016) "Experimental Validation of Control Rod Reactivity Worth and Fission Rate Distributions for the CROCUS Reactor" in Proceedings of the PHYSOR 2016 International Conference on the Physics of Reactors, Jeju, Korea, April 16-20, 2017
- Rais, A., Siefman, D. J., Girardin, G., Hursin, M., & Pautz, A. (2014) "PARCS few-group homogenized parameters generation using Serpent Monte Carlo code at the CROCUS reactor" in Proceedings of the 16th Meeting of the International Group on Research Reactors (IGORR), San Carlos de Bariloche, Argentina, November 2014.
- Rais, A., Hamidouche, T., & Novog, D. R. (2014) "TRACE Code Application to Low Operating Pressure Research Reactor Safety Analysis" in Proceedings of the 16th Meeting of the International Group on Research Reactors (IGORR), San Carlos de Bariloche, Argentina, November 2014.

PROFESSIONAL TRAINING

- *EuroTech winter school on Integrated Approaches to Energy Systems* (Feb. 2015) Lausanne, Switzerland.
- *The Frédéric Joliot/Otto Hahn summer school on nuclear reactors Physics, fuels and systems* (Aug. 2014) Aix en Provence, France.
- *Materials Ageing Institute school* (Dec. 2012) EDF R&D. Site des Renardières, Ecuelles, France.
- *Energy Management summer program* (Jul. 2012) Grenoble École de Management, France.
- *Natural Gas Processing* (Nov. 2010) IAPG (Oil&Gas Argentine Institute), Buenos Aires, Argentina.
- *Introduction to Gas Industry* (Sep. 2010) IAPG (Oil&Gas Argentine Institute), Buenos Aires, Argentina.
- *Natural Gas Measurement* (Apr. 2010) IAPG (Oil&Gas Argentine Institute), Buenos Aires, Argentina.

COMPUTER AND TECHNICAL SKILLS

Engineering:

- SolidWorks (3D CAD), ANSYS Fluent (CFD)
- Monte Carlo computational algorithms
- Microsoft Project

General IT:

- ANSI C, Matlab, Python, Fortran 90, HTML
- MS Office packages
- Linux, Macintosh, Windows

MEMBERSHIPS AND ADVISING ACTIVITIES

- Member of the KIC InnoEnergy (European Institute of Innovation and Technology) Quality Assessment Board for Master and PhD school (2013 - 2014) KTH Royal Institute of Technology, Sweden.
- Member of the EPFL's Doctoral program in Energy (EDEY) Committee (2014 - 2017) EPFL, Switzerland.

AWARDS

- Full scholarship at Instituto Balseiro (2006 - 2009) obtained by academic records and exam based selection.
- KIC InnoEnergy scholarship (2011 - 2013) awarded to the best candidates applying to the EMINE program.